NASA Contractor Report 3818

Free-Jet Acoustic Investigation of High-Radius-Ratio Coannular Plug Nozzles

P. R. Knott, B. A. Janardan, R. K. Majjigi,
P. K. Bhutiani, and P. G. Vogt

General Electric Company
Cincinnati, Ohio

Prepared for
Lewis Research Center
under Contract NAS3-20619

[redacted]

National Aeronautics
and Space Administration

Scientific and Technical Information Branch

1984

TABLE OF CONTENTS

Section		Page
1.0	SUMMARY	1
2.0	INTRODUCTION	2
3.0	TEST APPARATUS AND DATA REDUCTION PROCEDURES	4
	3.1 General Electric Anechoic Jet Noise Facility	4
	3.1.1 General Arrangement and Operational Range	4
	3.1.2 Acoustic Data Acquisition and Reduction	4
	3.2 General Electric Laser Velocimeter	11
	3.2.1 General Arrangement	11
	3.2.2 LV Actuator and Seeding	13
	3.2.3 Signal Processing and Recording	13
	3.2.4 Laser Velocimeter Data Reduction and Typical Test Results	13
	3.3 Description of the Flight Transformation Technique	14
	3.3.1 Objective and Concept	14
	3.3.2 Algorithm Description	16
	3.3.3 Further Details	16
4.0	CONFIGURATION DESCRIPTION AND SCOPE OF TESTING	26
	4.1 Configuration Description	26
	4.2 Scope of Testing	28
	4.2.1 Acoustic Tests	28
	4.2.2 Laser Velocimeter Tests	28
5.0	TEST RESULTS AND DISCUSSION	29
	5.1 Acoustic Test Results	29
	5.1.1 Verification of High-Radius-Ratio Coannular Plug Nozzle Jet Noise Reduction in Simulated Flight	29
	5.1.2 Influence of Geometry on Coannular Plug Nozzle Acoustics	51
	5.1.3 Influence of Flow Variables on Static and Simulated Flight Acoustics of High-Radius-Ratio Coannular Plug Nozzles	74
	5.1.4 Special Remarks Regarding Shock Noise and Shock Noise Control for High-Radius-Ratio Coannular Plug Nozzles	119

TABLE OF CONTENTS (Concluded)

Section		Page
	5.2 Laser Velocimeter Test Results	130
	5.2.1 Exhaust Plume Characteristics of a Conic Nozzle	130
	5.2.2 Exhaust Plume Characteristics of a Coannular Plug Nozzle	136
	5.2.3 Influence of Outer Flowpath Termination on the Flow Characteristics	140
	5.2.4 Influence of Under/Overexpansion of Inner/Outer Streams on the Cell Structure	143
	5.2.5 Effect of Area Ratio and Outer Stream Radius Ratio on the Exhaust Plume Development	151
	5.2.6 Effect of Velocity Ratio on Plume Growth	154
	5.2.7 Influence of Struts on Mean and Turbulent Velocities	158
	5.2.8 A Rationale for the Observed Flow Asymmetry	158
	5.2.9 Summary of Observations	162
	5.3 A Unique Coannular Plug Nozzle Jet Noise Prediction Procedure	165
	5.3.1 The Basic Concept of the Procedure	165
	5.3.2 An Outline of the Prediction Procedure	166
	5.3.3 Comparison of Data and Predictions	181
6.0	CONCLUSIONS AND RECOMMENDATIONS	190
	6.1 Conclusions	190
	6.2 Recommendations	191
7.0	NOMENCLATURE	192
	REFERENCES	196
	APPENDIX A - Aerodynamic Test Conditions for the Acoustic Tests	199
	APPENDIX B - Aerodynamic Test Conditions for the Laser Velocimeter Tests	213

1.0 SUMMARY

This report, along with the companion Comprehensive Data Report, R81AEG212, summarizes the experimental and analytical results of a scale-model free-jet acoustic exploratory program performed by the General Electric Company under NASA-Lewis Research Center sponsorship on unsuppressed high-radius-ratio coannular plug nozzles with inverted velocity profiles. The nozzles selected for test were nozzles covering the range of geometry and class applicable to General Electric designs for dual-flow exhaust nozzles typical of a variable cycle engine (VCE) for advanced supersonic technology (AST).

In all, six high-radius ratio coannular plug nozzle models, along with a baseline conical nozzle, were tested for simulated flight acoustic evaluation in the General Electric Anechoic Free-Jet Acoustic Test Facility. The models tested were primarily at an outer nozzle radius ratio, R_r^o, of 0.853 and an inner-to-outer nozzle area ratio, A_r, of 0.2. A model with R_r^o = 0.902 and A_r = 0.53 was tested also. Some of the key geometry features studied were the influence of nozzle exhaust struts, a convergent-divergent flowpath on shock control, as well as effect of area ratio holding radius ratio fixed, and the effect of radius ratio holding area ratio fixed.

Some of the key results of this investigation were:

- In simulated flight, the high-radius-ratio coannular plug nozzle essentially maintained its jet noise and shock noise reduction feature observed under static conditions relative to a baseline conical nozzle.

- The presence of nozzle bypass struts will not significantly effect the acoustic characteristic of a General Electric-type nozzle design.

- A unique coannular plug nozzle spectral prediction method was evolved based on modern acoustic theories and significant static and simulated flight acoustic test results.

- Diagnostic acoustic and laser velocimeter tests were performed which led to observations regarding possible regions of the flow in which further coannular plus nozzle shock control research could evolve reduction of shock-cell noise.

2.0 INTRODUCTION

The General Electric Company under NASA Lewis Contract NAS3-18008 initiated an exploratory scale-model acoustic and aerodynamic performance test program to obtain parametric data on unsuppressed and suppressed coannular nozzles. That program was directed toward the development of high velocity jet noise technology for Advanced Supersonic Transport application. One of the findings of that program, results of which are in Reference 1, was that the unsuppressed coannular plug nozzle exhibited acoustic benefits with modest performance losses. A follow-on investigation was conducted under Contract NAS3-19777 (Reference 2) with the objective to determine the effects of key design variables of unsuppressed coannular plug nozzles through a systematic static acoustic and wind tunnel aerodynamic performance measurements. The variables considered were radius ratio, area ratio, inner stream plug geometry, inner and outer stream flow variables, and inner to outer stream velocity and weight-flow ratios. The measured data identified the mixed stream velocity V_j^{mix}, outer stream radius ratio R_r^o, inner-to-outer velocity ratio V_r, and inner-to-outer stream area ratio A_r as the parameters that had influence on the measured jet noise data. The current study was initiated with the objective to confirm the observed coannular nozzle acoustic benefits under simulated flight conditions. In addition, effort has been made to develop a semi-empirical spectral prediction method for coannular plug nozzles that will take into consideration the various noise generating mechanisms that have been identified in relevant studies (References 1-7).

To determine the effect of forward flight on the acoustic effectiveness of various coannular plug configurations, six coannular model nozzles along with a reference circular conic nozzle were tested under both static and simulated flight conditions. In addition, the influences of nozzle exhaust struts, area ratio and radius ratio on jet noise, and a convergent - divergent flowpath on shock-cell noise were investigated. The aerodynamic flow conditions for the coannular plug nozzle test points were selected to simulate a typical AST/VCE operating line and to yield an inverted velocity profile. Furthermore, the laser velocimeter was used with five of the test configurations to determine the jet plume mean and turbulent velocity distributions and to correalte these data with the acoustic results. The details of the configurations and scope of testing are summarized in Section 4.0 and the measured acoustic and LV data are presented and discussed in Section 5.0. Detailed acoustic and laser-velocimeter data are presented separately in the Comprehensive Data Report (Reference 8) of this program.

In addition to the relevance of the measured acoustic results in determining the effects of tested parameters on jet and shock-cell related noise of coannular plug nozzles, the data of this program were employed during the concept screening related to the selection of engine scale hardware for the YJ101/VCE tests. These engine tests are being conducted as a part of a multiphase, multiyear GE/NASA test-bed engine program to investigate key technology features applicable to an AST powerplant. Furthermore, selected model-nozzle

data, obtained during the tests are to be compared with the test-bed engine data in order to verify coannular nozzle acoustic data scaling procedures. Preliminary correlation of the full-scale engine and scale-model acoustic results and verification of the analytical prediction methodology developed during this program are reported in Reference 9.

3.0 TEST APPARATUS AND DATA REDUCTION PROCEDURES

All of the acoustic and laser velocimeter tests of this program were performed in the General Electric Anechoic Test Facility located at Evendale, Ohio. A brief description of the test apparatus, the data acquisition, and the data reduction procedures is presented in this section. Results of the tests conducted to determine (1) the acoustic characteristics of the anechoic chamber (e.g., inverse square law tests, background noise determination) and (2) the mean velocity and turbulence intensity distributions in the free jet, along with a detailed description of the aerodynamic/acoustic data acquisition and reduction systems are presented in the Comprehensive Data Report of this program (Reference 8).

3.1 GENERAL ELECTRIC ANECHOIC JET NOISE FACILITY

3.1.1 General Arrangement and Operational Range

The test facility, schematically and photographically shown in Figure 1, is a cylindrical chamber having a diameter of 13.1 m (43 ft) and a height of 21.95 m (72 ft). The inner surfaces of the chamber are lined with anechoic wedges made of fiberglass to yield a low frequency cutoff below 220 Hz and an absorption coefficient of 0.99 above 220 Hz.

The facility can accommodate model configurations up to 17.3 cm (6.8 in.) in diameter. The operating domains of this facility in terms of total temperature, pressure ratio, and jet velocity are indicated in Figure 2 for single and dual flow operation. The required streams of heated air that are produced by separate burners pass through acoustically treated plenum chambers for the suppression of flow and combustor noise.

A tertiary duct surrounds the model nozzles with the airflow in order to simulate a forward flight up to Mach 0.41. The tertiary air passes through a silencer plenum chamber before it is discharged through the 1.2 m (48 in.) free-jet exhaust. An overhead view of the tertiary exhaust surrounding a test conical nozzle is presented in Figure 3.

3.1.2 Acoustic Data Acquisition and Reduction

3.1.2.1 Acoustic Data Acquisition System

A schematic of the microphone data acquisition system used to obtain acoustic data during tests in the anechoic chamber is shown on Figure 4. This system is optimized for obtaining acoustic data up through 80 kHz 1/3-octave center frequency. The microphones used to obtain the far field data are the B&K 4135 6.4 mm (0.25 in.) condenser microphones. All the tests are conducted with the microphone grid caps removed to obtain the best frequency

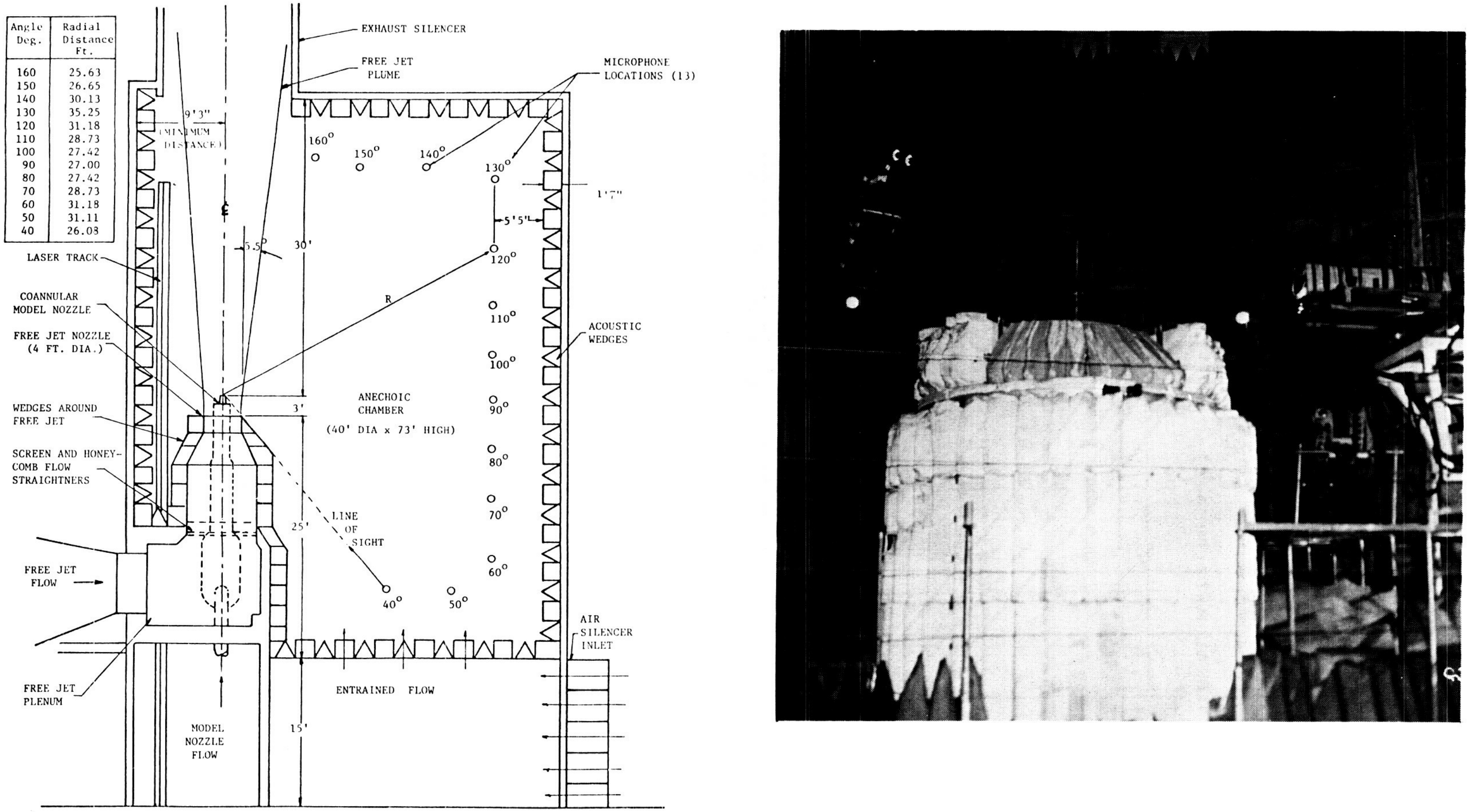

Angle Deg.	Radial Distance Ft.
160	25.63
150	26.65
140	30.13
130	35.25
120	31.18
110	28.73
100	27.42
90	27.00
80	27.42
70	28.73
60	31.18
50	31.11
40	26.03

(a) Schematic

(b) Photo

Figure 1. Free-Jet Arrangement in Anechoic Facility.

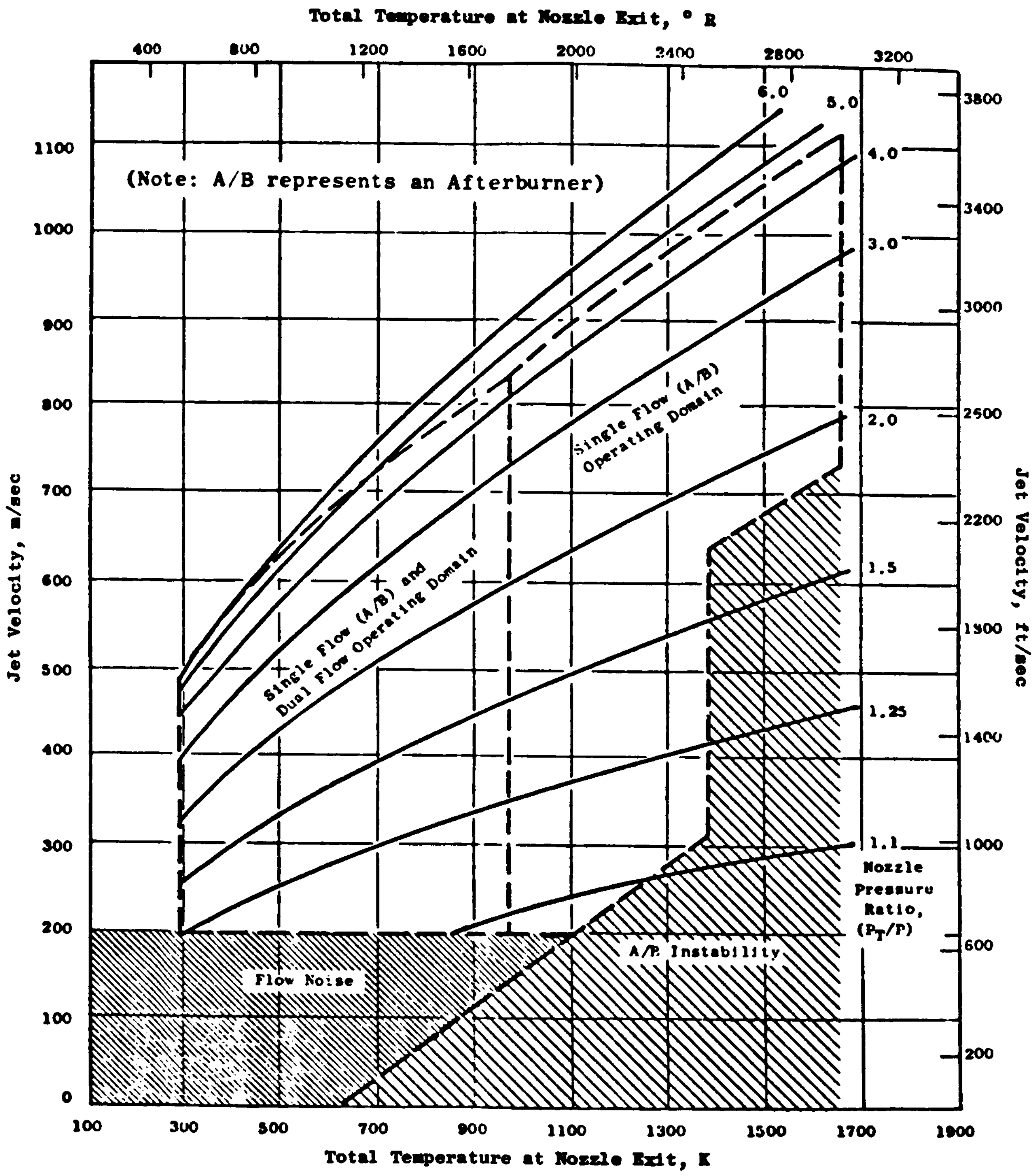

Figure 2. General Electric Anechoic Chamber Operating Domain.

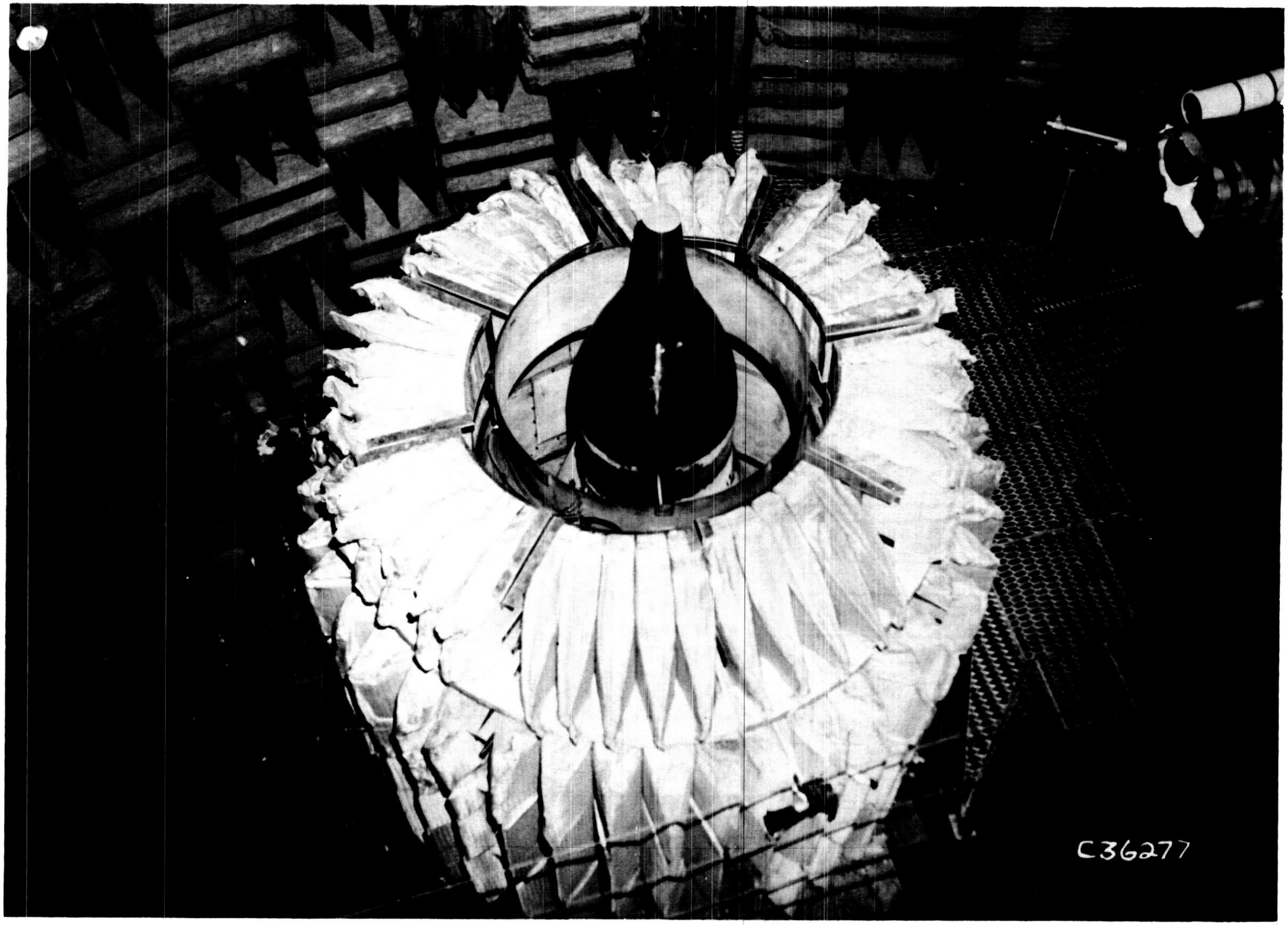

Figure 3. Overhead View of the Tertiary Exhaust with a Test Conical Nozzle.

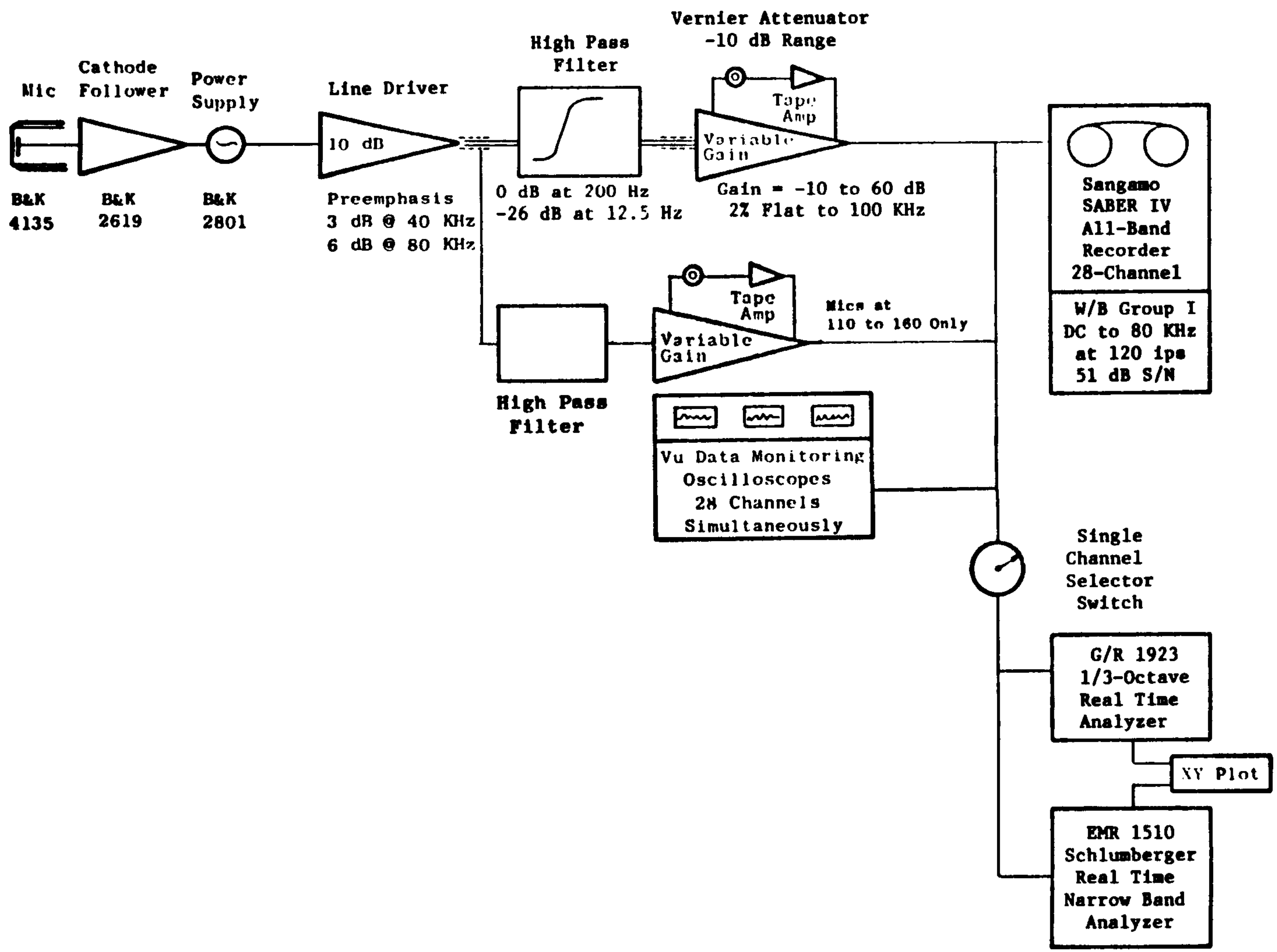

Figure 4. Acoustic Data Acquisition System.

response. The cathode followers are the transistorized B&K 2619 for optimum frequency response and lower inherent system noise characteristics relative to the 2615 cathode follower. All systems utilize the B&K 2801 power supply operated in the direct mode.

Power supply output is connected to a line driver adding 10 dB of amplification to the signal, as well as adding "preemphasis" to the high frequency portion of the spectrum. The net effect of this amplifier is a 10 dB gain at all frequencies, plus an additional 3 dB at 40 kHz and 6 dB at 80 kHz due to preemphasis. This procedure improves low amplitude, high frequency data. In order to remove low frequency noise, high pass filters with attenuations of approximately 26 dB at 12.5 Hz and decreasing to 0 dB at 200 Hz are installed in the system.

The tape recorder amplifiers have a variable gain from -10 dB to +60 dB in 10-dB steps and a gain trim capability for normalizing incoming signals. The prime system used for recording acoustic data is a Sangamo/Sabre IV, 28-track FM recorder. The system is set up for Wideband Group I (intermediate band double extended) at 120-in./sec tape speed. Operating at this speed provides a dynamic range that is necessary for obtaining satisfactory low-amplitude, high frequency acoustic signal. The tape recorder is set up for ±40% carrier deviation with a recording level of 8 volts peak-to-peak. During recording, the signal is displayed on a calibrated master oscilloscope, and the signal gain is adjusted to maximum without exceeding the 8-volt peak-to-peak level.

High pass filters are incorporated into the acoustic data acquisition systems to enhance the high-frequency data previously lost in the tape recorder electronic noise floor for microphones from 110° to 160°. The microphone signal below the 20-kHz 1/3-octave band is filtered out, and the gain is increased to boost the signal to noise ratio. For microphones from 110° to 160°, both filtered and unfiltered signals are recorded on tape. For data below 20 kHz, the unfiltered signal is used to calculate the sound pressure levels, while the filtered signal is employed for high frequencies. The entire jet noise spectrum at a given angle is obtained by computationally merging these two spectra.

3.1.2.2 Acoustic Data Reduction

Standard data reduction is conducted in the General Electric-AEBG Instrumentation and Data Room (IDR). As shown in Figure 5, the data tapes are played back on a CEC3700B tape deck with electronics capable of reproducing signal characteristics within the specifications indicated for Wideband Group I. An automatic shuttling control is included in the system. In normal operation, a tone is inserted on the recorder in the time slot designed for data analysis. The tape control automatically shuttles the tape, initiating an integration start signal to the analyzer at the tone as the tape moves in its forward motion. This motion continues until an "integration complete" signal is received from the analyzer at which time the tape direction is reversed;

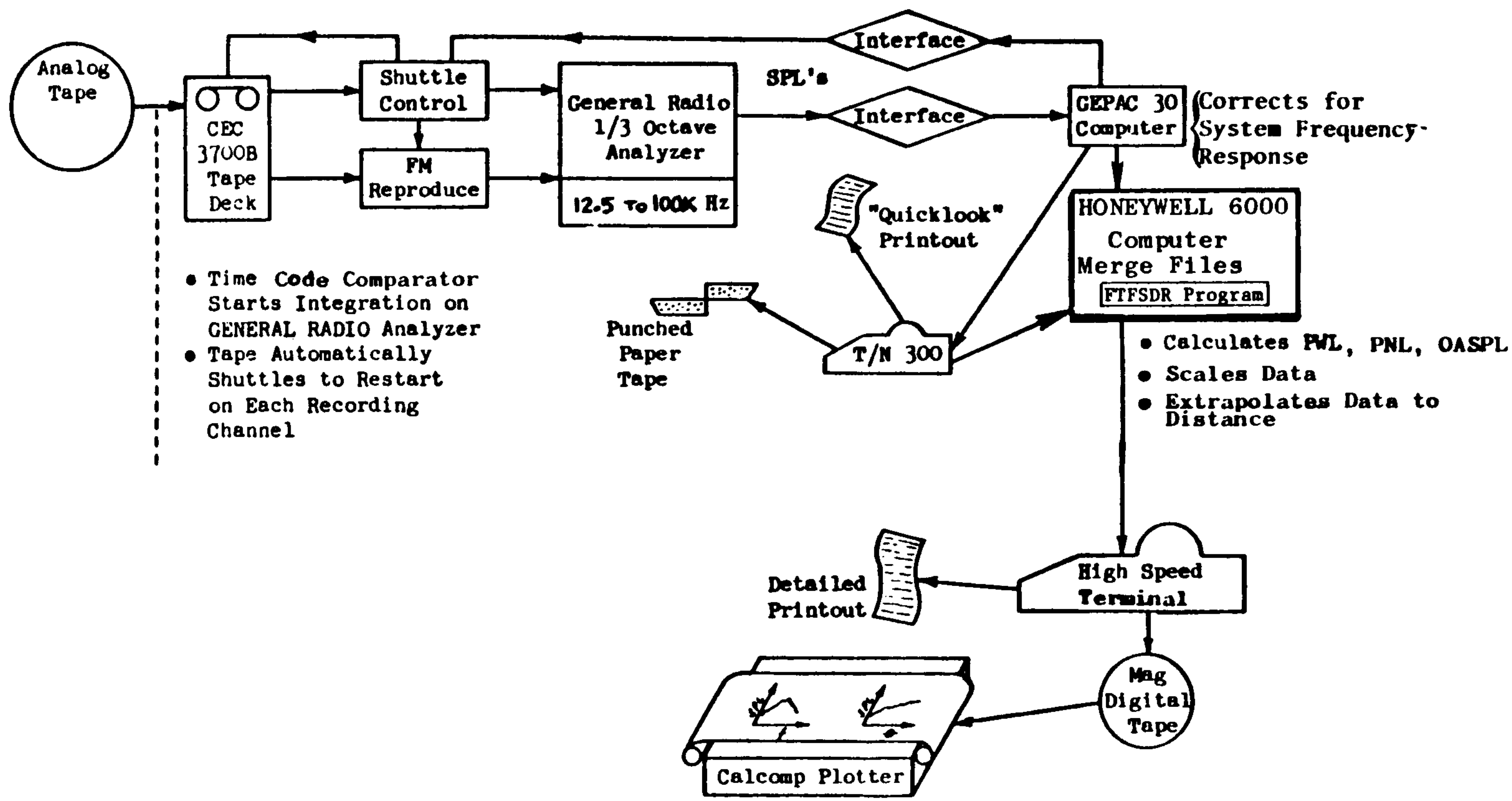

Figure 5. Acoustic Data Reduction System.

and at the tone, the tape restarts in the forward direction advancing to the next channel to be analyzed until all the channels have been processed. In addition, a time code generator is utilized to signal tape position as directed by the computer program control.

All 1/3-octave analyses are performed on a General Radio 1921 analyzer. Normal integration time is set for 32 seconds to ensure sufficient averaging time for the low frequency content. The analyzer has 1/3-octave filter sets from 12.5 Hz to 100 Hz, and has a rated accuracy of ±1/4 dB in each band. Each data channel is passed through an interface to the GEPAC 30 computer where the data are corrected for the frequency response of the microphone and the data acquisition system. Next, the data are corrected to standard day (15° C, 70% RH atmospheric attenuation conditions as recommended by Shields and Bass, Reference 10) and processed to calculate the perceived noise level (PNL) and the overall sound pressure level (OASPL) from the spectra. For calculation of acoustic power, scaling to other nozzle sizes, and/or extrapolation to different far field distances, the data are sent to the Honeywell 6000 computer for data processing. This is accomplished by transmitting the SPL via direct time-share link to the 6000 computer through a 1200 Band Modem. In the 6000 computer, the data are processed through the Flight Transformed Full-Scale Data Reduction (FTFSDR) Program where the appropriate calculations are performed. The data printout is accomplished on a high-speed "remote" terminal. The FTFSDR Program also writes a magnetic tape for CALCOMP plotting of the data. Detailed descriptions of the acoustic data reduction system are given in the Comprehensive Data Report (Reference 8).

3.2 GENERAL ELECTRIC LASER VELOCIMETER

3.2.1 General Arrangement

The laser velocimeter (LV) used is a system developed under a USAF/DOT-sponsored program and reported in detail in References 11 and 12. The basic optical system is a differential Doppler, backscatter, single package arrangement that has the proven feature of ruggedness for the severe environments encountered in high velocity and high temperature jets. Figure 6 shows a photograph of the LV system installed in the General Electric Anechoic Jet Noise Facility and Figure 7 indicates a schematic arrangement of the laser package. The laser beams are projected from below the lens, forming an angle that keeps the major axis of the control volume ellipsoid to a minimum. The dimensions of the control volume are 0.535 cm (0.21 inch) for the major axis and 0.0518 cm (0.020 in.) for the minor axis. The range of the LV control volume from the laser hardware is 2.16 m (85 in.). The three steering mirrors and the beam splitter are mounted on adjustable supports made from the same aluminum alloy in order to eliminate temperature alignment problems.

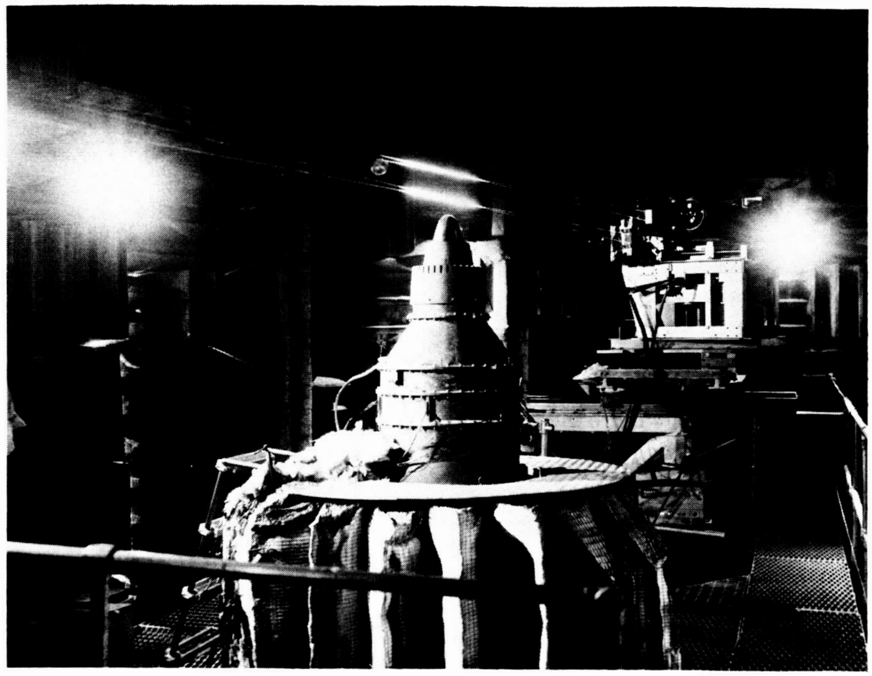

Figure 6. Two-Laser System in the GE Anechoic Jet Noise Test Facility.

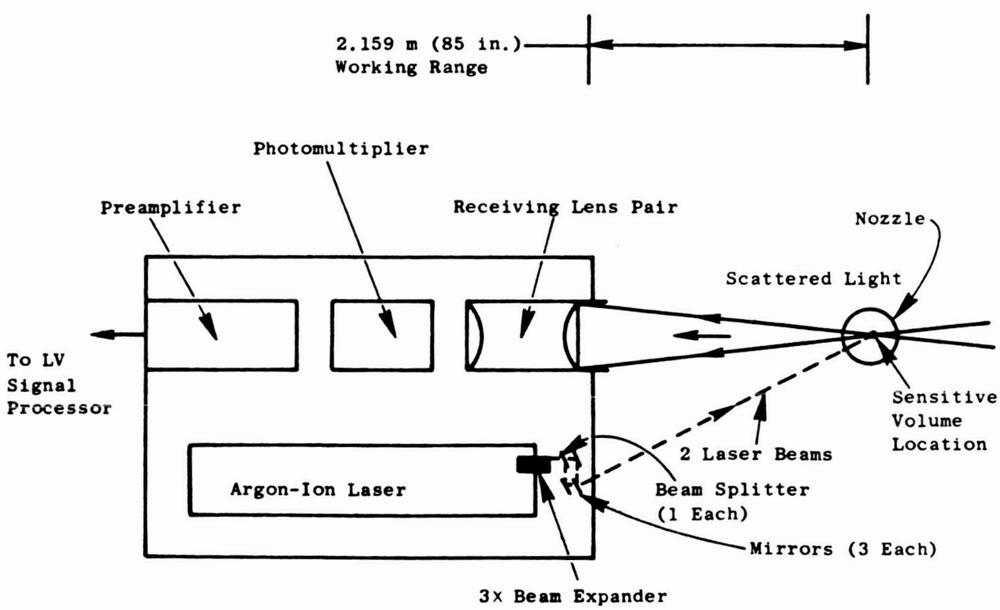

Figure 7. Laser Velocimeter Optics Package.

3.2.2 LV Actuator and Seeding

The remotely actuated platform has vertical, horizontal, and axial travel capabilities of 0.813 m (32 in.), 0.813 m (32 in.) and 5.79 m (228 in.), respectively. The resolution is ±0.1588 cm (0.0625 in.) for each axis except for the last 5.28 m (208 in.) of axial travel, which has a resolution of ±0.3175 cm (0.125 in.).

Seeding is by injection of nominal 1-μm diameter aluminum oxide (Al_2O_3) powder into the air supply to the burners and to the exit region of the tertiary duct so as to seed the entrained air. The seeding equipment used is described in Reference 11 (Chapter V, Section 3). However, the air supply to the fluidized bed column is currently heated to about 394° K (250° F) to prevent powder aggregation by moisture absorption.

3.2.3 Signal Processing and Recording

The LV signal processor is a direct-counter (time-domain) type similar to that reported in Reference 11, but with improvements. These improvements result in a lowered rate of false validations and improved linearity and resolution. Turbulent velocity probability distributions (histograms) are recorded by a NS633 pulse-height analyzer with 256 channels. The data acquired from the LV are transmitted to a minicomputer system (PDP 11/45) for storage on disk/tape and data reduction.

The processing capabilities of the General Electric LV system are as follows:

- Velocity range - 35 to 5000 ft/sec
- Random error for single particle accuracy (error associated with system inaccuracies such as fringe spacing, linearity, stability, burst noise) - 0.75%
- Bias error for mean velocity - 0.5%
- False data rejection capability (possibility of accepting bad data) - 0.0002%

The GE system uses a 16-fringe control volume where all of the 8 center fringes are used in the data acceptance/rejection testing.

3.2.4 Laser Velocimeter Data Reduction and Typical Test Results

The concept of using LV measurements for obtaining routine mean and turbulent velocity profiles can be described as follows. Two beams of monochromatic light intersect at a point in space and set up a fringe pattern of

known spacing. The flow is seeded with small particles which scatter the light while passing through the control volume. The scattered light is collected and the laser signal processor determines the time used by the particles to pass through each fringe. A knowledge of the distance and the time used by each validated particle enables the construction of the usual histogram. Then, by statistical techniques, the mean value (corresponding to the mean velocity) and the standard deviation (corresponding to the turbulent velocity) are constructed.

As with any large number of data samples, guidelines for estimating the accuracy of the measured delay are needed. Tables I and II, respectively, provide estimates of the percent of error associated in measuring the mean and turbulent velocities for a 95% confidence level as a function of the number of data samples and level of turbulence. Between 2000 to 5000 data samples are taken during a routine measurement. For simple and quick diagnostic-type information, this number of samples is sufficient.

Although the principle of LV measurement is well known, the practical aspects of designing a reliable electronic processing unit in order to monitor valid particles are arduous. Earlier investigators have had great difficulty in performing measurements even in low velocity jets, and hence the successful use of a LV system in the heated supersonic jets of this program represents a major achievement. References 13 through 16 list some of the reference materials in which General Electric has demonstrated the capabilities of the LV system for measuring mean and turbulent velocities in high temperature jet exhaust plumes of supersonic conical and coannular nozzles.

3.3 DESCRIPTION OF THE FLIGHT TRANSFORMATION TECHNIQUE

3.3.1 Objective and Concept

The objective of the General Electric free-jet transformation process is to employ far field SPL spectra at various angles to the jet axis (typically) for $20° \leq \theta_I \leq 150°$ in increments of 10°) obtained in a free-jet experiment and transform them to yield SPL spectra as would be measured in a true moving frame experiment.

The concept employed is that with area ratios of 50:1 or so and with the primary nozzle exhaust plane displaced aft of the free-jet plane sufficiently to permit aquisition of acoustic data in the inlet arc (e.g. up to $\theta_I = 150°$), proper aerodynamic simulation of the effects of forward flight is achieved; but that in terms of the acoustic simulation of the effects of uniform flow over the primary jet plume noise sources, the free jet achieves this only to a limited extent. In other words, the free jet achieves the effect of the right source mix but radiating into an environment that more nearly approaches a static environment than the environment of sources shrouded by either a finite or infinite extent of uniform nonturbulent flow. (The basis of several previous investigations has been to assuem that a well-defined region of uniform, nonturbulent flow surrounds the sources. This well-defined region is taken as

Table I. Estimated Percent Error in the LV Measurement of Mean Velocity with 95% Confidence.

Number of Data Samples	$V'/\bar{V}_j$			
	0.2	0.1	0.05	0.025
10	14.1	7.0	3.5	1.76
20	9.3	4.7	2.3	1.20
30	7.4	3.7	1.9	0.93
40	6.3	3.2	1.6	0.80
60	5.0	2.6	1.3	0.65
120	3.6	1.8	0.9	0.45

Table II. Estimated Percent Error for LV Turbulent Velocity Measurements With 95% Confidence.

Number of Data Samples	Percent Error
20	31.5
40	21.8
60	17.8
120	12.6
240	9.12
480	6.45
960	4.56
5,000	2.0
25,000	0.89

a doubly infinite cylinder of constant circular section equal to the cross section of the free-jet exhaust plane.) The acoustic sources in a free jet, of course, do not radiate into a completely static environment and hence some propagation effects of the free-jet flow do have to be accounted for.

Based on the above picture, the broad outline of the procedure adopted is as follows. Defining as the "static" directivity, the directivity pattern (in various frequency bands) that the sources (of the primary jet exhaust plume altered by the effects of relative velocity due to imposition of the free jet) may be expected to produce if they radiated into a quiescent environment, we first deduce this static directivity from the measured free-jet experimental data by correcting the latter for propagation effects of the free jet. Since the free-jet flow field includes intensely turbulent shear layers through which the sound field of the sources must pass before it reaches the far field microphones (located in the quiescent ambient), some degree of empiricism (especially for the high frequency sound) is involved in attempting to account for these propagation effects.

Once such a static directivity is extracted, it still remains to deduce what the noise signature of the source distribution would be if the source distribution was not stationary relative to the ambient but moving relative to the ambient at the flight velocity. A multiple decomposition procedure suitable for the broad band jet noise problem which attempts to synthesize the static directivity by ascribing it to a mix of uncorrelated singularities was developed in order to enable the prediction of the flight noise. Once such a decomposition is completed, we simply apply the dynamic exponent applicable to each singularity to derive the flight noise signature.

In summary, the method starts with directivities from the free-jet experiment in various third octave bands, corrects these directivities for free-jet propagation effects in a frequency-dependent manner to retrieve the static directivity, synthesizes the static directivity by a suitable mix of uncorrelated singularities, and finally applies the dynamic effect appropriate to each singularity to predict the flight noise. It is an inherent feature of the method that it works separately with each third octave band directivity pattern. The final flight predictions can then be summed to yield either OASPL or PNL directivities or simply displayed as flight SPL spectra at various angles to the jet axis. (Doppler shift effects on the frequency are fully accounted for.)

3.3.2 Algorithm Description

A detailed algorithm description is shown in Figure 8 along with the applicable nomenclature. Complete description and discussion of this procedure can be found in Reference 17.

3.3.3 Further Details

The recommended procedure for transformation of free-jet noise to flight noise consists of extracting the "basic" directivity from the measured free-jet

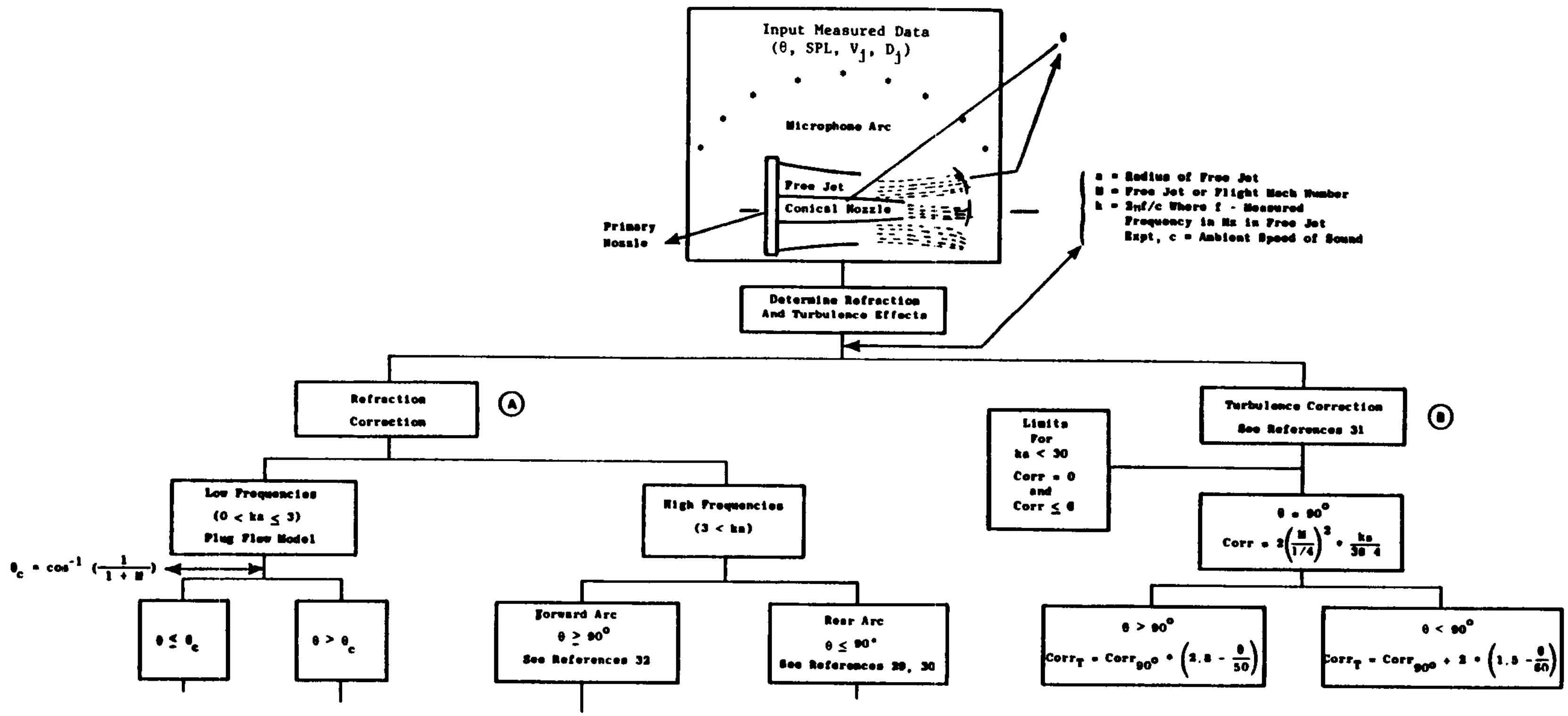

Figure 8. **Algorithm Description.**

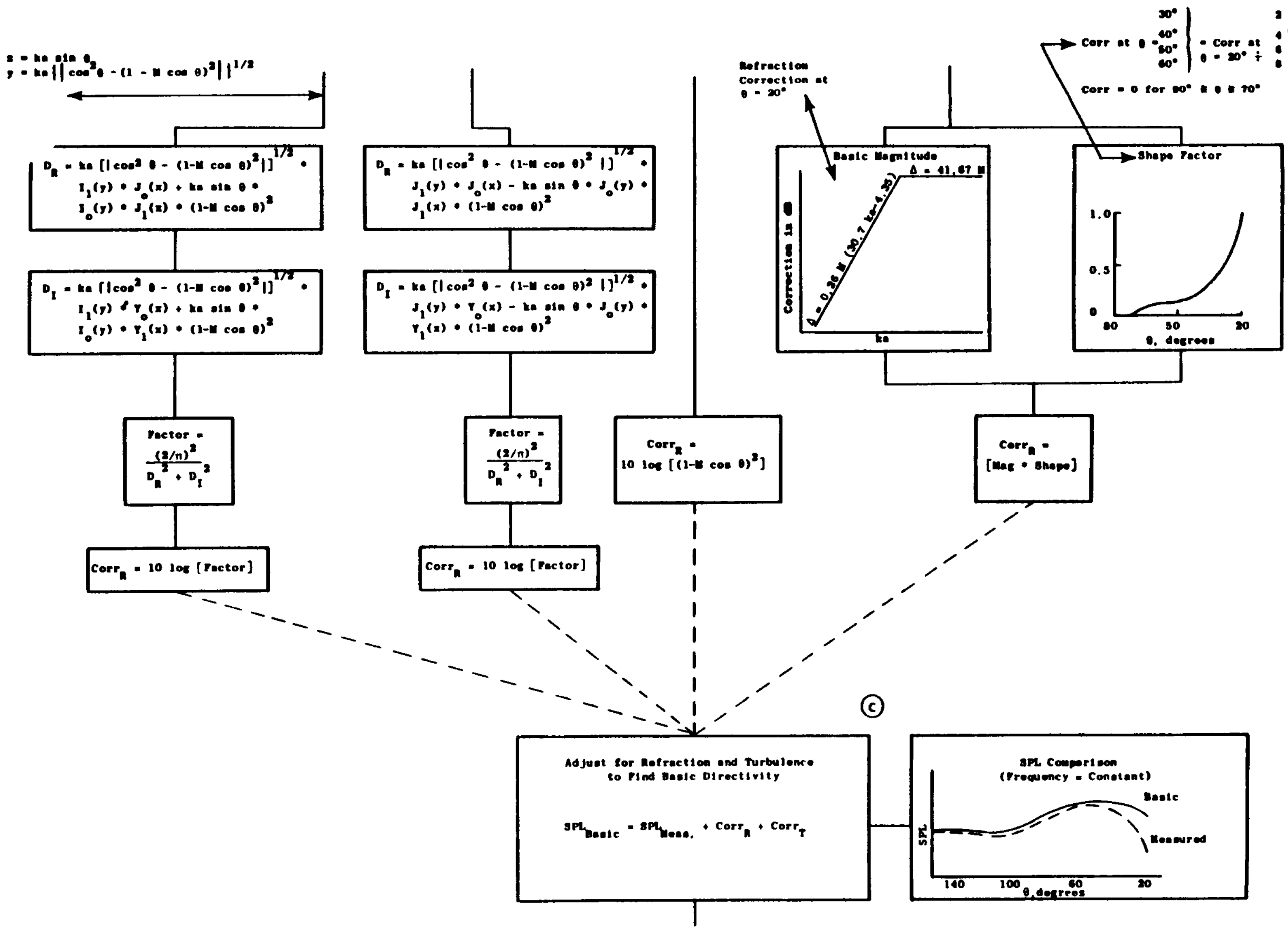

Figure 8. Algorithm Description (Continued).

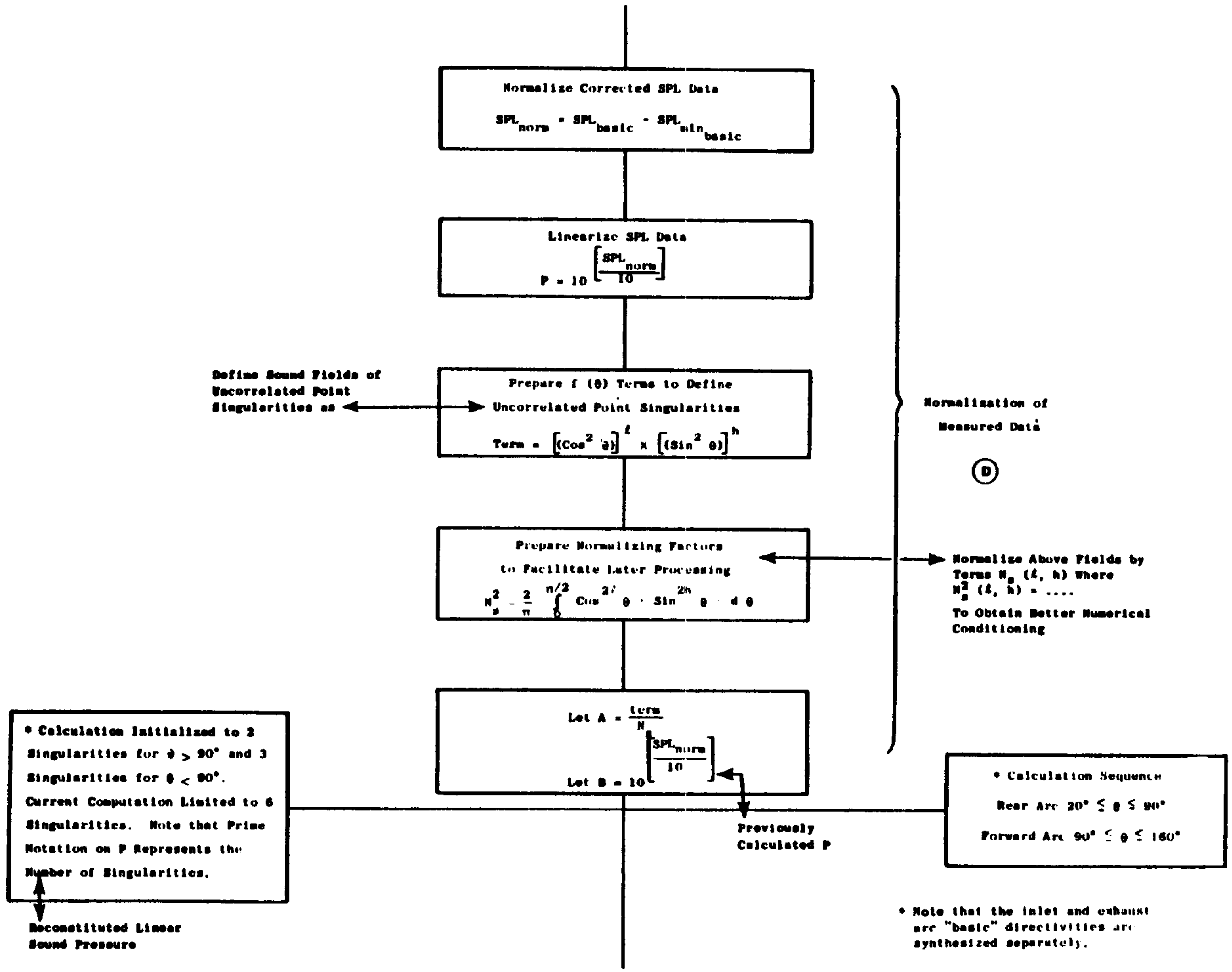

Figure 8. Algorithm Description (Continued).

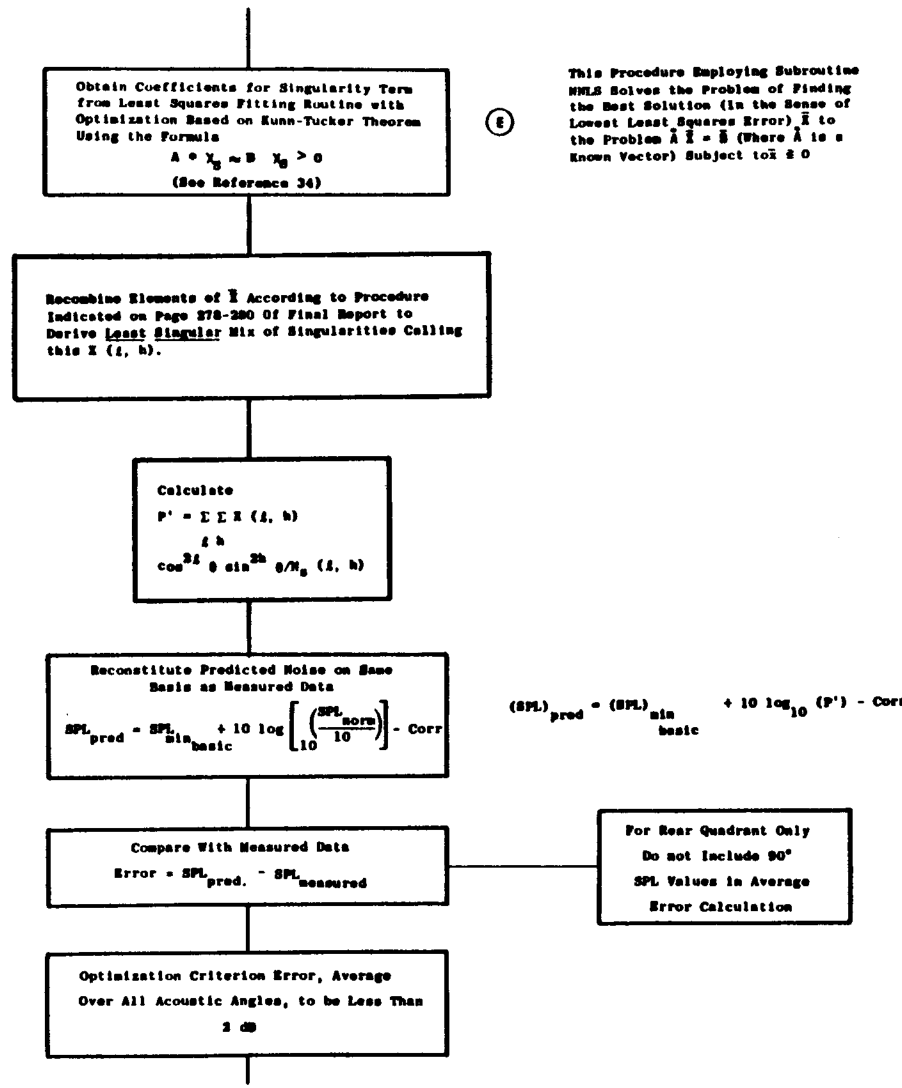

Figure 8. Algorithm Description (Continued).

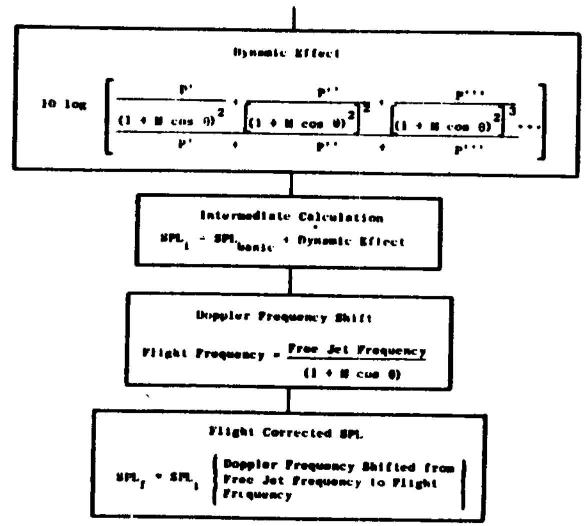

"F"

$$10 \log_{10}\left\{\left[\sum_{\ell}\sum_{h} X(\ell, h) \cos^{2\ell}(\theta) \cdot \sin^{2h}(\theta) / \left[N_s(\ell, h)\ (1 + M\cos\theta)^{2(\ell + h) + 2}\right) \div P'\right]\right.$$

List of Symbols

A	An Input Matrix to the Least Squares Fitting Procedure
B	An Input Vector to the Least Squares Fitting Procedure
Corr	An Acronym used to Identify the Refraction and/or Turbulence Correction
D_R	Real Root of Denominator Term in Solution of the Sound Pressure for the Plug Flow Model
D_I	Imaginary Root of Denominator Term in Solution of the Sound Pressure for the Plug Flow Model
F	Subscript for Flight Corrected SPL
h	Numerical Value Varies with Level of Singularity Considered
i	Subscript on SPL to Identify an Intermediate Calculation
$I_n(x)$	Modified Bessel Function of the First Kind of Order n, Argument in is x
$I_n(y)$	Modified Bessel Function of the First Kind of Order n, Argument in is y
$J_n(x)$	Bessel Function of the First Kind of Order n, Argument in is x
$J_n(y)$	Bessel Function of the First Kind of Order n, Argument in is y
ka	Frequency Parameter = (Free Jet Frequency Band of Interest in Radians per Second) × (Free Jet Radius in Feet) ÷ (Ambient Speed of Sound)
ℓ	Numerical Value Varies with Level of Singularity Considered
M	Mach Number = (Free Jet Velocity) ÷ (Ambient Speed of Sound)
$N_s(\ell, h)$	Normalizing Factor, Function of Singularity
P	Linear Sound Pressure
P_{ref}	0.0002 Microbars
R	Subscript for Refraction Correction
S	Singularity Subscript
SPL	Sound Pressure Level = 10 log (P^2/P^2_{ref})
T	Subscript for Turbulence Correction
Term	Acronym Used to Identify a Unique Algebraic Grouping
x	Bessel Function Argument, x = ka sin θ
X	A Vector Derived from Least Squares Fitting, Function of Singularity
y	Bessel Function Argument, y = ka $[\cos^2\theta - (1 - M\cos\theta)^2]^{1/2}$
$Y_n(x)$	Bessel Function of the Second Kind of Order n, Argument x
θ	Angle from the Jet Axis Referred to the Exhaust
θ_c	Critical Angle that Defines the Jet Zone of Silence = $\cos^{-1}(1/1 + M)$

Figure 8. Algorithm Description (Concluded).

data and then applying the "dynamic" effects to determine the noise in flight. The basic directivity is the directivity that the sources associated with the primary nozzle plume would create, if they radiated into a static rather than the free-jet environment.

Two phenomena are involved that change the directivity of the noise radiated by the sources associated with the jet plume when the jet is exhausting into a free-jet environment as opposed to a static environment. These are:

a. Refractive Effects of the Free-Jet Flows

To deduce the refractive effects of the free-jet flow, the following procedure is adopted:

1. At low frequencies ($k_oc < 3$), the plug flow model solution for a point pressure source is used

$$p' \propto (1 - M_{fj} \mathrm{Cos}\ \theta)^{-2}$$

2. At high frequencies ($k_oc > 3$), the asymptotic high frequency solution for a pressure source is used

$$p' \simeq (1 - M_{fj} \mathrm{Cos}\ \theta)^{-1}$$

At these values of the frequency parameter ($k_oc < 3$), the exhaust arc was used to deduce the refractive effect following the method due to Schubert (Reference 18). In this method:

- First, the refractive dip in dB along the jet exhaust axis is determined as being product of the jet Mach number and the frequency parameter.

- Then, a shape factor that is essentially Mach number and frequency indpendent is used to determine the refractive dip at other angles. For the range $3 < k_oc < 6$, Ribner's results were used with a linear extrapolation in the range $6 > k_oc > 1.25$.

- Based on experimental data, the refractive dip in the exhaust arc for $k_oc > 6$ was considered independent of k_oc, but still linearly proportional to M_{fj}.

b. Absorptive Effects of the Fine Grain Turbulence in the Shear Layer of the Free-Jet

This relates to the fact that fine-grained turbulence in the shear layer of the free jet can absorb sound, expecially at high frequencies. This correction is based on Crow's theory that states that the effective absorption

coefficient is proportional to the frequency, distance the sound traveled in the shear layer, and the square of the Mach number.

$$a_{\text{absorption coefficient}} \propto f\, M^2_{fj} l$$

where M_{fj} = free jet Mach number
l = path length

Based on the path length that the sound has to traverse, the absorption coefficient is assumed to vary with θ_I as shown in the following sketch:

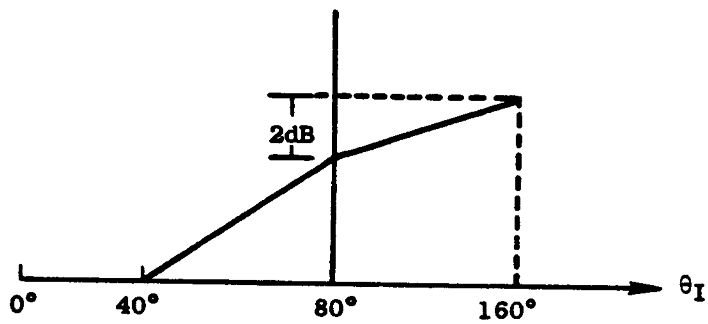

The absorption was calculated assuming an eddy viscosity

$$\varepsilon_{\text{eddy viscosity}} = 70\ \mu \text{ for } M_{fj} = 0.25 \text{ and } f = 50 \text{ kHz}.$$

This yields corrections for $k_o c > 30$. The actual expressions used were

$$\left. \text{Corr}_T \right|_{\theta_I = 90^\circ} = \begin{cases} 2 \left(\dfrac{M}{1/4}\right)^2 \times \dfrac{kc}{38.4} & \text{for } kc \geq 30 \\ 0 & \text{for } kc < 30 \end{cases}$$

where M = free-jet Mach number

$$k = \frac{2\pi f}{c_a}$$

a = Radius of the free jet

$$\mathrm{Corr}_T\Big|_{\theta_I > 90^\circ} = \mathrm{Corr}_T\Big|_{\theta_I = 90^\circ} \times \left(1.5 - \frac{180 - \theta_I}{180}\right)$$

$$\mathrm{Corr}_T\Big|_{\theta_I > 90^\circ} = \mathrm{Corr}_T\Big|_{\theta_I = 90^\circ} \times \left(2.8 - \frac{180 - \theta_I}{50}\right)$$

From the measured free-jet data, the refraction and turbulences absorption corrections are added to obtain the basic directivity of the sources.

The basic directivity obtained above is assumed to be generated by a set of singularities F_o, F_x, F_y, etc., such that the sound field is a solution to

$$\nabla^2_p + k_o^2\, p = Fo\ \delta(x)\ \delta(y)\ \delta(z) + F\alpha'\ (x)\ \delta(y)\ \delta(z) + Fy\ \delta(X)\ \delta(y)\ \delta(z)$$

where F_o, F_x, F_y ..... are mutually uncorrelated, so that they contribute to the far field only additively. As the mean square pressure of any singularity is symmetric about both $\theta = 0^\circ$ and $\theta = 90^\circ$, the inlet and exhaust arc are synthesized separately.

The procedure adopted to determine the dynamic effect is as follows:

1. From the basic directivity pattern, obtain the normalized SPL's based on the least singular fit in both the forward and aft quadrants.

2. Determine the linearized levels using the equation

$$\overline{p^2} = 10^{\frac{SPL-SPL_{min}}{10}}$$

3. Decide on a level of fitting using the criterion that the data ought to be reconstructed to within an error of 2 dB on the average. Then, assuming that the data ought to be reconstructed with the least singular distribution of uncorrelated sources possible, the problem simplifies to one of solving a least squares problem of the type find $\bar{x}$ to minimize $|\bar{r}| = (A\bar{x} - b)$ subject to nonnegative constraining $\bar{x} \geq 0$. This is done using an algorithm based on the Kuhn-Tucker theroem of optimization theory.

4. The singularities obtained using the Kuhn-Tucker theorem are then combined to obtain the least singular decomposition of the sources.

5. The appropriate dynamic effect is then applied to each singularity type to determine the correction that is applied to the measured free-jet data corrected for refraction and turbulence absorption. If the mean square of the sound pressure is obtained by adding the singularities as

$$P_\theta'^2 = F_o\ C^6 + F_1 C^4\ S^2 + F_2\ C^2\ S^4 + F_3\ S^4$$

where $C = \text{Cos } \theta$

$S = \text{Sin } \theta$

the dynamic effect is calculated using the relation

$$\text{Dynamic Effect} = 10 \log_{10} \frac{P_F'^2}{P_S'^2} = 10 \log_{10} \frac{\dfrac{F_o C^6}{k^8} + \dfrac{F_1 C^4 S^2}{k^8} + \dfrac{F_2 C^2 S^4}{k^8} + \dfrac{F_3 S^4}{k^6}}{P_S'^2}$$

where $k = (1 + M_{fj}\ \text{Cos } \theta)$

6. The levels are then corrected to:

$$\underset{\substack{\text{flight at} \\ \text{free-jet} \\ \text{frequency}}}{SPL_i} = SPL_{basic} + \text{dynamic effect}$$

7. Doppler frequency shift results in the flight frequency given by:

$$f_F = \frac{f_j}{1 + M_{fj}\ \text{Cos } \theta}$$

8. Hence $SPL_F = SPL_i$ Doppler shifted from free jet to flight.

Thus, using the above transformation, the free-jet data can be transformed into flight data. Further discussion of this procedure is found in Reference 17.

4.0 CONFIGURATION DESCRIPTION AND SCOPE OF TESTING

To determine the effect of forward flight on the acoustic effectiveness of various coanular plug nozzle configurations, six coannular plug nozzles along with a reference conical nozzle were tested during this program in the General Electric anechoic facility. Furthermore, the laser velocimeter system was used with five of these configurations to determine the jet plume mean velocity and turbulence intensity distributions and to correlate these data with the acoustic results. The details of the nozzle configurations and the aerodynamic flow conditions of the tests are presented in this section.

4.1 CONFIGURATION DESCRIPTION

Table III summarizes the significant geometric parameters of the test configurations. Models 1A through 4 basically are geometrically scaled versions of the General Electric VCE/AST test-bed nozzle designs. In particular, Models 1A and 2 (both having a C-D outer termination and an inner-to-outer area ratio A_r = 0.2) are identical in all respects except that Model 1A has eight internal struts similar to the VCE/AST test-bed design while Model 2 has no struts. Model 3 (A_r = 0.2) is similar to Model 2 except that it has a convergent termination in the outer stream. Finally, Model 4 with an area ratio A_r = 0.53 is obtained from Model 3 by removing a spacer. The design features of these four nozzles are such that (1) the influence of the eight internal struts in the outer stream on the far field acoustic measurements, (2) the influence of a convergent and C-D terminated outer nozzle on the measured shock noise, and (3) the effect of the area ratio (test range = 0.2 → 0.53 with an outer stream radius ratio R_r^o = 0.853) on the acoustic effectiveness of the VCE/AST design can be determined.

The Model 5 configuration is a single stream conical reference nozzle. The remaining nozzle configurations, namely, Models 6 and 7, were selected for flight simulated tests for the following reasons:

- They were tested earlier under static conditions (Reference 2, referred to therein as Configurations 6 and 7) over a wide range of aerodynamic flow conditions and, hence, a large data base is available on these two models for a comparison with the corresponding flight data from this study.

- These nozzles have a small area ratio and a large outer stream (Reference 2) radius ratio. The static tests have indicated that these geometric features are key coannular nozzle suppression parameters.

Detailed drawings of the test hardware are presented in the Comprehensive Data Report of this contract (Reference 8).

Table III. Significant Geometric Details of Test Configurations.

Model	h^o, in.	h^i, in.	R_1^o, in.	R_2^o, in.	R_1^i, in.	R_2^i, in.	R_r^o	A^o, in.^{2}	A^i, in.^{2}	A^i/A^o	x^o, in.	x^o/h^o	θ_s^1	θ_s^2	Internal Struts	Termination Outer	Termination Inner
1A	0.675	0.200	3.918	4.593	---	---	0.853	18.049	3.610	0.20	3.417	5.06	15°	15°	Yes	C-D	Convergent
2	0.675	0.200	3.918	4.593	---	---	0.853	18.049	3.610	0.20	3.417	5.06	15°	15°	No	C-D	Convergent
3	0.675	0.200	3.918	4.593	---	---	0.853	18.049	3.610	0.20	3.971	5.88	15°	15°	No	Conv.	Convergent
4	0.675	0.583	3.918	4.593	---	---	0.853	18.049	9.566	0.53	3.971	5.88	15°	15°	No	Conv.	Convergent
5	---	---	---	2.547	---	---	---	20.380	---	---	---	---	---	---	No	Conv.	Convergent
6	0.426	0.311	3.918	4.344	2.858	3.168	0.902	11.057	5.878	0.53	3.089	7.25	11°	15°	No	Conv.	Convergent
7	0.675	0.311	3.918	4.593	2.858	3.168	0.853	18.049	4.878	0.33	3.063	4.54	11°	15°	No	Conv.	Convergent

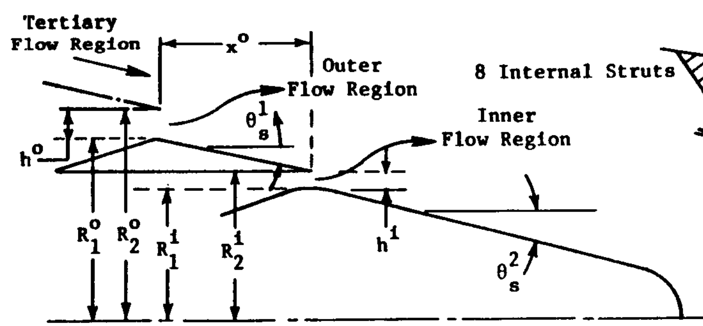

Schematic of Models 6 and 7 and Definition of Parameters

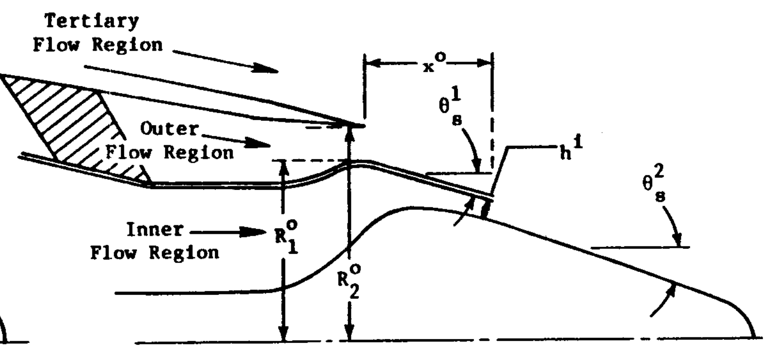

Schematic of Models 1 Through 4 and Definition of Parameters

4.2 SCOPE OF TESTING

The aerodynamic flow conditions for the coannular plug nozzle test points were selected to simulate a typical VCE/AST operating line and to yield an inverted velocity profile wherein the outer annulus flow is at a higher velocity and temperature than the inner stream. To the extent possible, identical inner and outer stream conditions were set during those tests that involved determining the effect of different geometries and velocity ratios on the acoustic characteristics of the nozzles.

4.2.1 Acoustic Tests

The total number of static and flight acoustic tests performed with the seven selected nozzle configurations was 196. Details of the tests are given in Appendix A. These tables list the inner, outer, and mixed stream conditions of the test points along with the PNL measured at θ_I = 50°, 70°, 90°, 110°, 130°, and 140°, and the OAPWL. PNL data have been scaled and extrapolated to a 1400 in.^{2} nozzle exhaust area and a 2400 ft sideline. Detailed acoustic test results, including spectral data for each of the test points, are presented in the Comprehensive Data Report.

4.2.2 Laser Velocimeter Tests

The aerodynamic flow conditions of the LV tests are presented in Appendix B.

5.0 TEST RESULTS AND DISCUSSION

The analyses of the acoustic and laser velocimeter measurements obtained with the annular plug nozzle configurations of this program are discussed in this section. Descriptions of the nozzle configurations and the range of test conditions were presented in Section 4.0.

This section consists of three main subsections. Subsection 5.1 contains a discussion of the static and simulated flight acoustic data with emphasis on the influences of various coannular plug nozzle geometries and aerodynamic flow conditions. The measured shock noise data of coannular plug nozzles also are discussed in this subsection. Subsection 5.2 contains a discussion of the mean and turbulent velocity measurements taken with the LV. In conclusion, Subsection 5.3 describes a unique coannular spectral prediction method developed as a part of this contract effort.

5.1 ACOUSTIC TEST RESULTS

5.1.1 Verification of High-Radius-Ratio Coannular Plug Nozzle Jet Noise Reduction in Simulated Flight

Earlier experimental investigations reported in References 2 and 17 showed that significant jet and shock noise reductions were obtained for high-radius-ratio coannular plug nozzles relative to a conical nozzle at the same specific thrust in a static environment. A key objective of this investigation was to verify this important noise reduction feature under a simulated flight environment.

In the course of the discussion of results presented in this section, a number of flight influences will be illustrated for different geometric or thermodynamic flow variations. In addition, general results that verify in simulated flight the high-radius-ratio coannular plug nozzle jet and shock noise reductions previously measured statically are presented.

The first illustration of the verification of high-radius-ratio coannular plug nozzle total jet noise reduction in flight is a plot of the measured PNL directivity for a conical nozzle and a coannular plug nozzle of radius ratio 0.853, an inner-to-outer area ratio of approximately 0.2, and at the same specific thrust for a simulated flight speed of approximately 390 fps. The coannular plug nozzle chosen for the comparisons is the nozzle with struts (Model 1A) which is representative of the similitude YJ101 nozzle configuration. This model nozzle has been designed based on one-dimensional Mach number simulation of the exhaust nozzle flowpath of the baseline coannular YJ101 nozzle. Details of the engine nozzle and summary of the measured data are in Reference 9. The comparison of this model d

conical nozzle is presented in Figure 9. The results are scaled to a typical supersonic cruise engine size of 1400 in.^{2} at a 2400 foot sideline distance. The sample case is for a typical AST/VCE

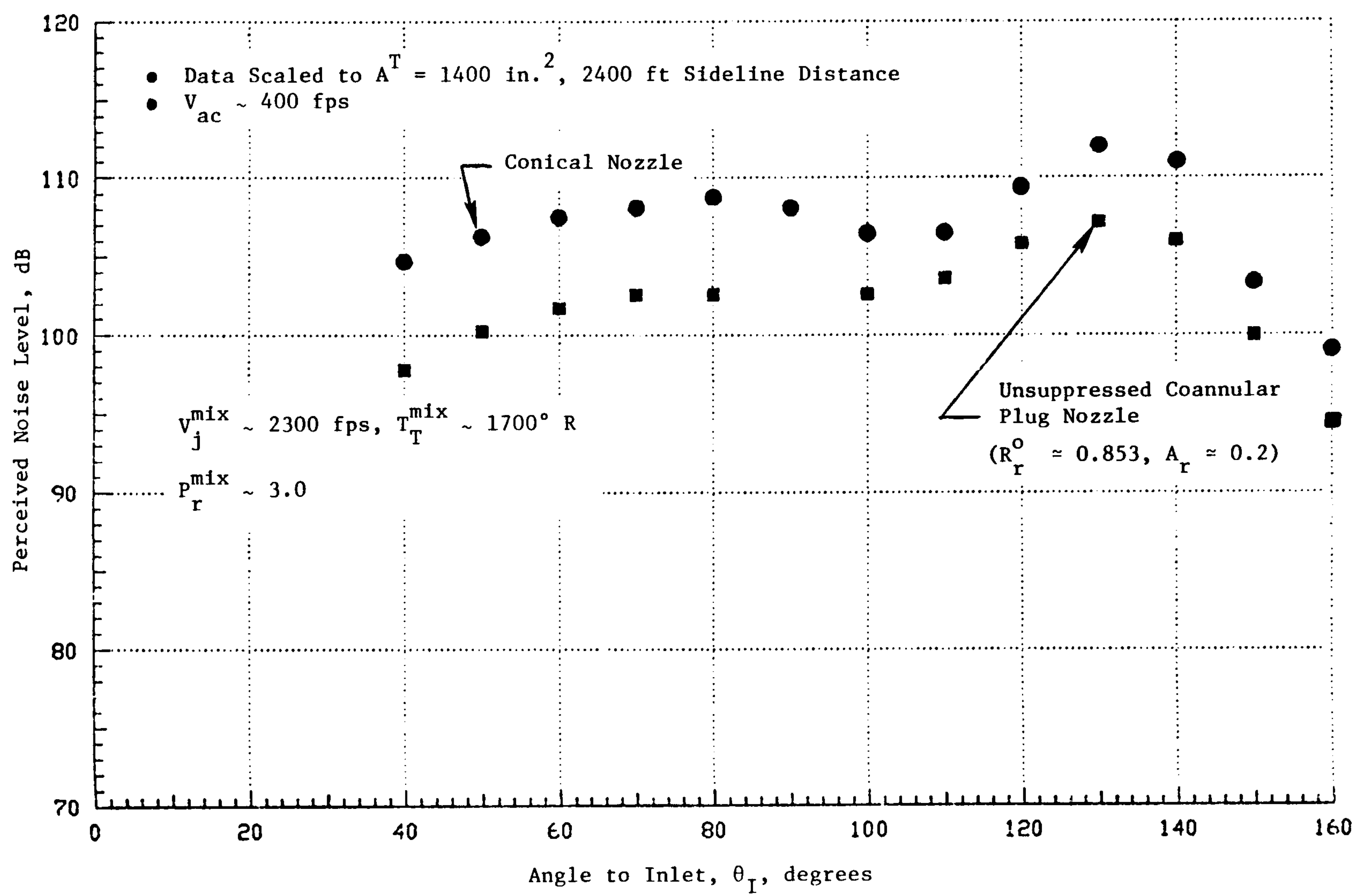

Figure 9. Verification of High Radius Ratio Coannular Plug Nozzle PNL Directivity: Jet and Shock Noise Reduction at Typical Takeoff Sideline Engine Cycle and Flight Conditions.

takeoff sideline engine cycle operating condition (V_j^{mix} ~ 2300 fps and p_r^{mix} ~ 3.0). This result shows that, in simulated flight, the high-radius-ratio coannular plug nozzle has maintained jet noise and shock noise reduction relative to a conical convergent circular nozzle at equivalent specific thrust (V_j^{mix}) and nozzle pressure ratio (p_r^{mix}). The peak angle jet noise reduction measured for this case is 5 PNdB at θ_I = 130°, and 6 PNdB shock noise or forward radiated noise at θ_I = 60°. The OASPL directivity for this case is shown in Figure 10. For this measurement, the peak jet noise angle is 140°, but the relative jet noise reduction at the peak angle is also 5 dB. In the forward quadrant at θ_I = 60°, the shock noise or forward quadrant noise reduction on a OASPL basis is as high as 8 dB.

Comparisons of the coannular plug nozzle acoustic spectral distribution with those of conical nozzle for observation locations from angle to the inlet, θ_I, of 40° to 160° are shown in Figure 11. These test measurements show that at a simulated flight condition of ~390 fps, the forward quadrant shock noise is considerably reduced - up to 12 dB on a peak spectral basis. In the aft quadrant, where jet mixing noise is the dominant exhaust noise mechanism, the high-radius-ratio coannular plug nozzle noise reduction is observed to occur nearly over all the measured frequency bands. Figures 12 through 17 illustrate the general static and simulated flight results measured for the typical takeoff sideline AST/VCE engine cycle condition.

Figures 12 and 13 show the static-to-simulated flight PNL and OASPL directivity characteristics for the circular conical convergent exhaust nozzle. What can be observed from these comparisons is that in the aft microphone observation angles the jet mixing noise has been reduced inflight. In the forward quadrant, or shallow observation angles, a shock associated noise "lift" is observed. The measurements indicate a 4 PNdB noise reduction due to flight at the peak aft quadrant noise angle, but a corresponding 4 PNdB forward quadrant amplification of noise at θ_I = 60°.

The spectral static-to-flight comparisons for the conical nozzle are shown in Figure 14. These results show that in the forward quadrant there is a Doppler shift of the shock associated noise toward higher frequencies associated with a general noise amplification. In the aft jet noise measurement angles, there is a general reduction in the noise signature over all frequency bands.

A comparison set of static-to-simulated flight acoustic measurements for the high-radius-ratio coannular plug nozzle is shown in Figures 15 through 17. As we generally observed with the conic nozzle, the high-radius-ratio coannular plug nozzle also shows for this case that in the aft quadrant at the peak noise angle there was a reduction in the jet noise with flight. In the forward quadrant (e.g., at θ_I = 60°), an amplification of the shock associated noise is observed again. At the peak jet noise angle, the coannular plug nozzle jet noise was reduced by 3.5 PNdB due to flight, while the forward quadrant lift was observed to be about 4.5 dB at θ_I = 60° (Figure 15).

The spectral static-to-simulated-flight acoustic test results for the unsuppressed coannular plug nozzle are shown in Figure 17. In the forward obser-

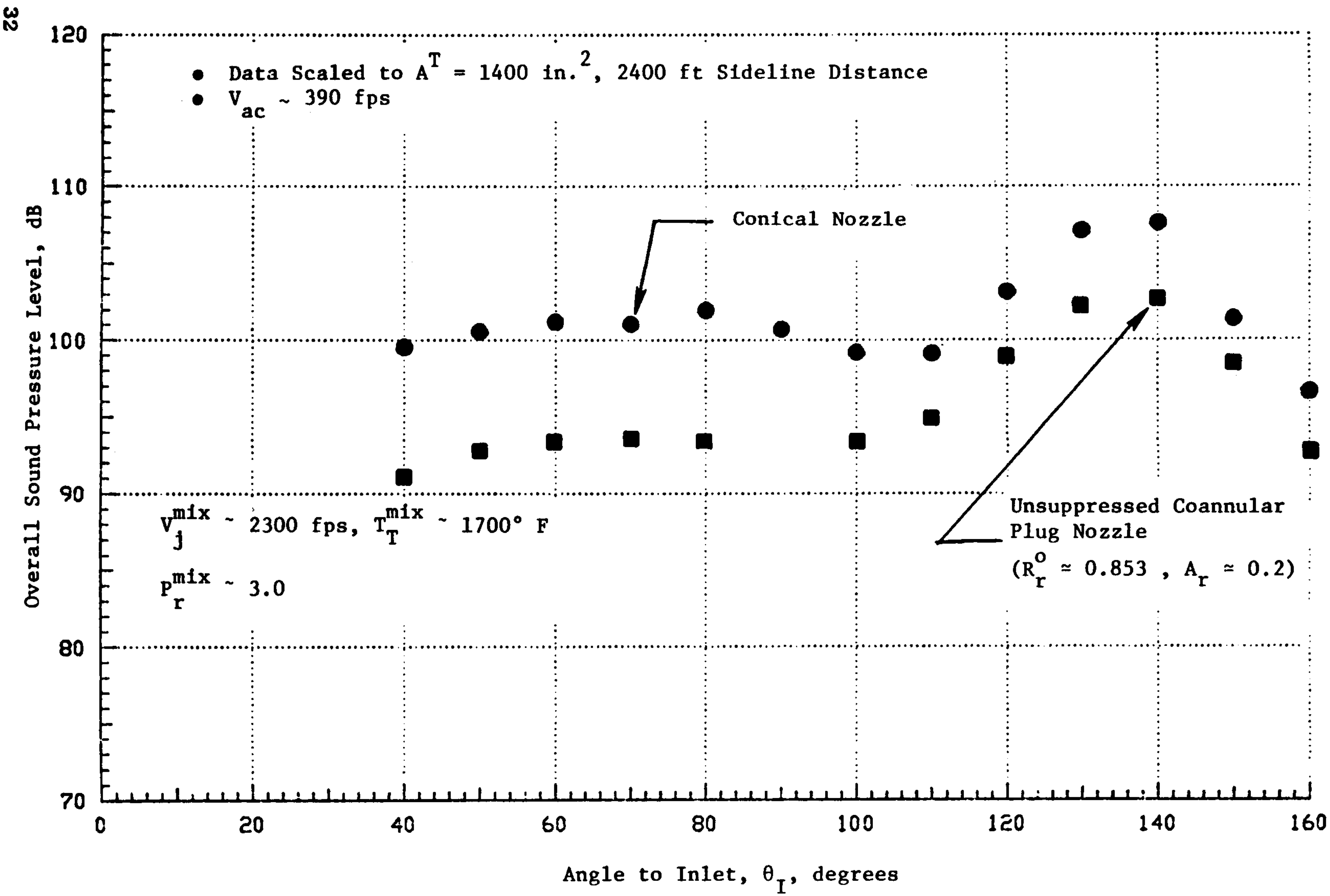

Figure 10. Verification of High Radius Ratio Coannular Plug Nozzle OASPL Directivity: Jet and Shock Noise Reduction at Typical Takeoff Sideline Engine Cycle and Flight Conditions.

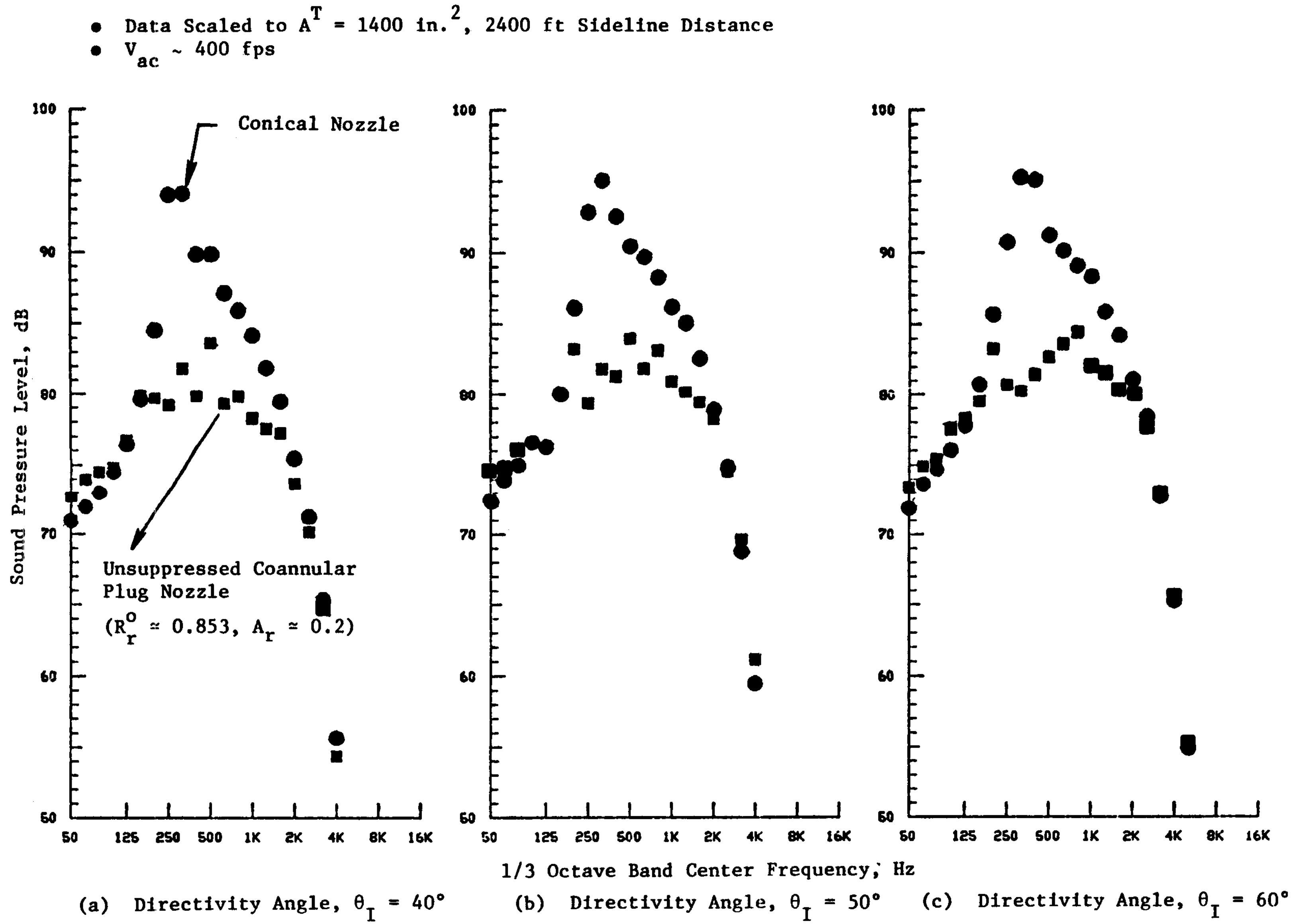

Figure 11. Verification of High Radius Ratio Coannular Plug Nozzle Jet and Shock Noise Spectral Distribution at Typical Takeoff Sideline Engine Cycle and Flight Conditions.

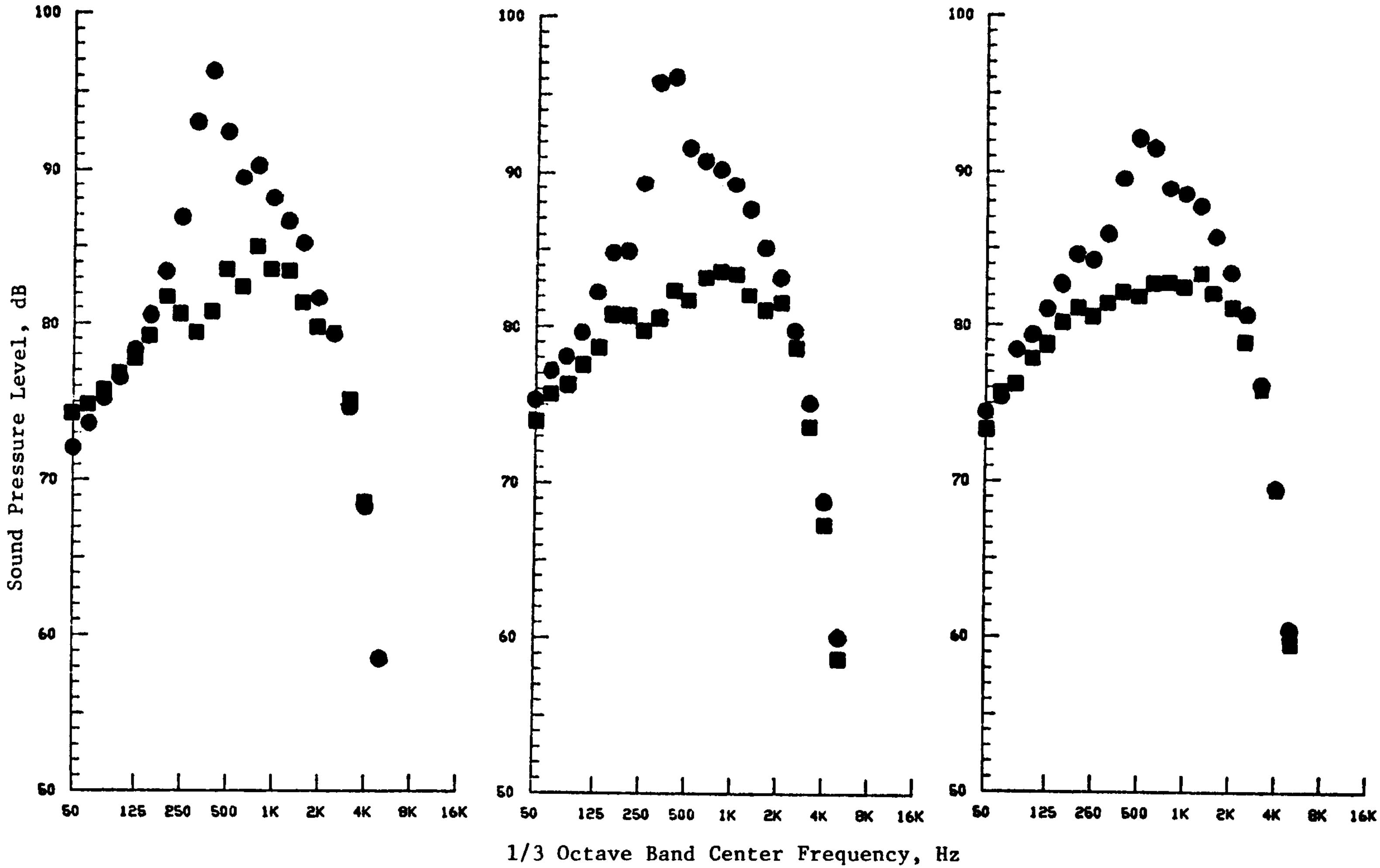

(d) Directivity Angle, $\theta_I = 70°$ (e) Directivity Angle, $\theta_I = 80°$ (f) Directivity Angle, $\theta_I = 100°$

Figure 11. Verification of High Radius Ratio Coannular Plug Nozzle Jet and Shock Noise Spectral Distribution at Typical Takeoff Sideline Engine Cycle and Flight Conditions (Continued):

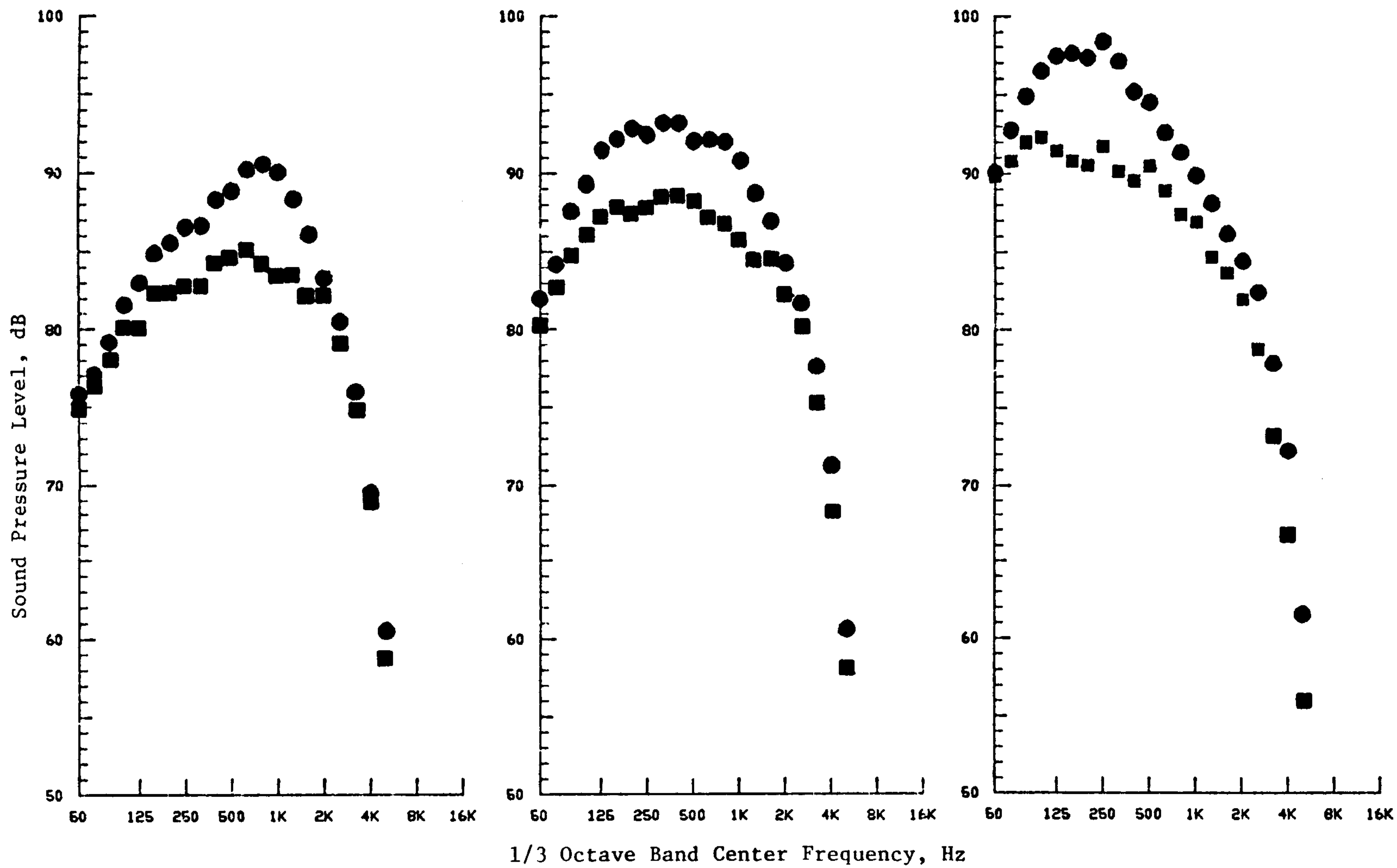

(g) Directivity Angle, θ_I = 110° (h) Directivity Angle, θ_I = 120° (i) Directivity Angle, θ_I = 130°

Figure 11. Verification of High Radius Ratio Coannular Plug Nozzle Jet and Shock Noise Spectral Distribution at Typical Takeoff Sideline Engine Cycle and Flight Conditions (Continued).

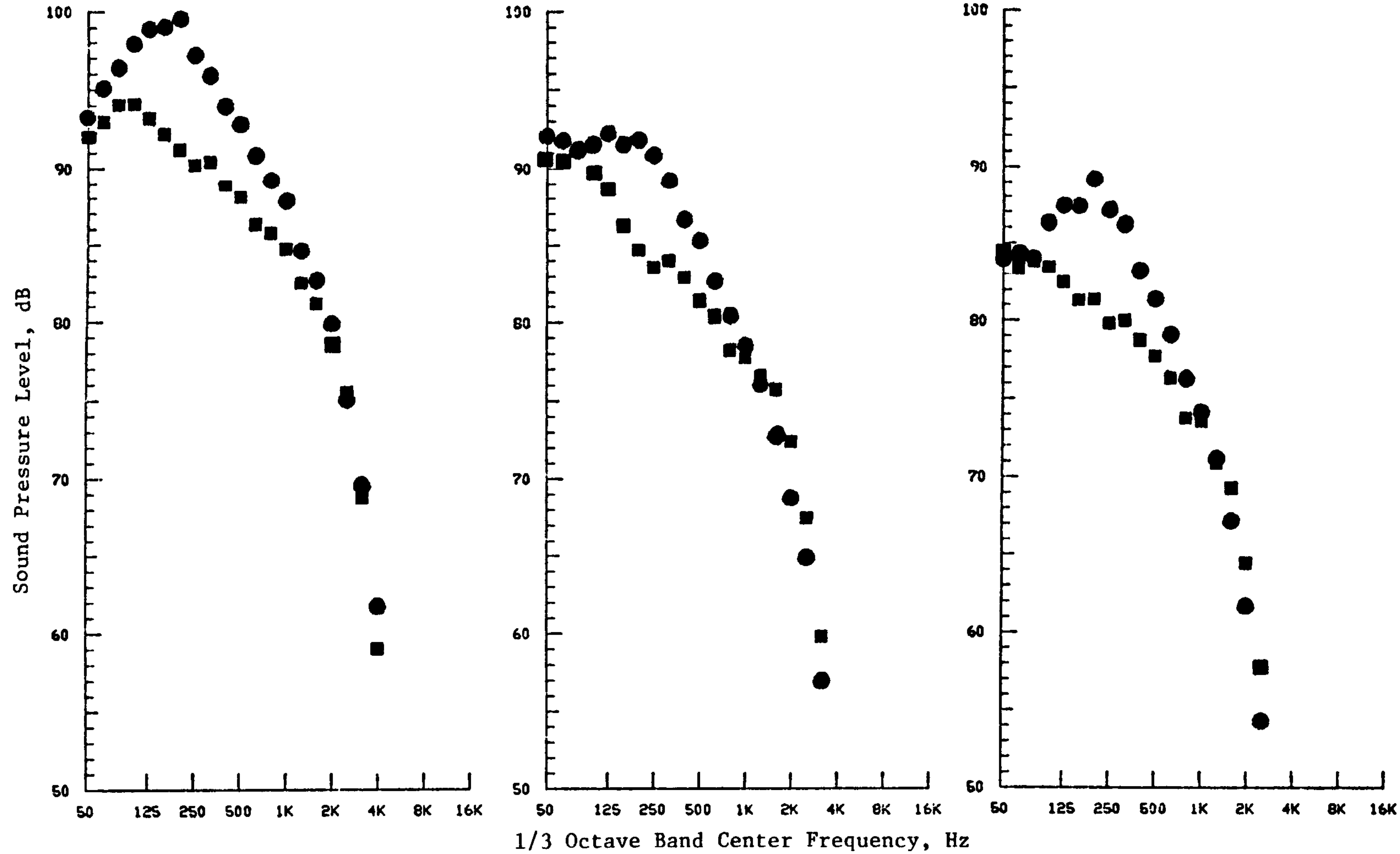

(j) Directivity Angle, θ_I = 140° (k) Directivity Angle, θ_I = 150° (l) Directivity Angle, θ_I = 160°

Figure 11. Verification of High Radius Ratio Coannular Plug Nozzle Jet and Shock Noise Spectral Distribution at Typical Takeoff Sideline Engine Cycle and Flight Conditions (Concluded).

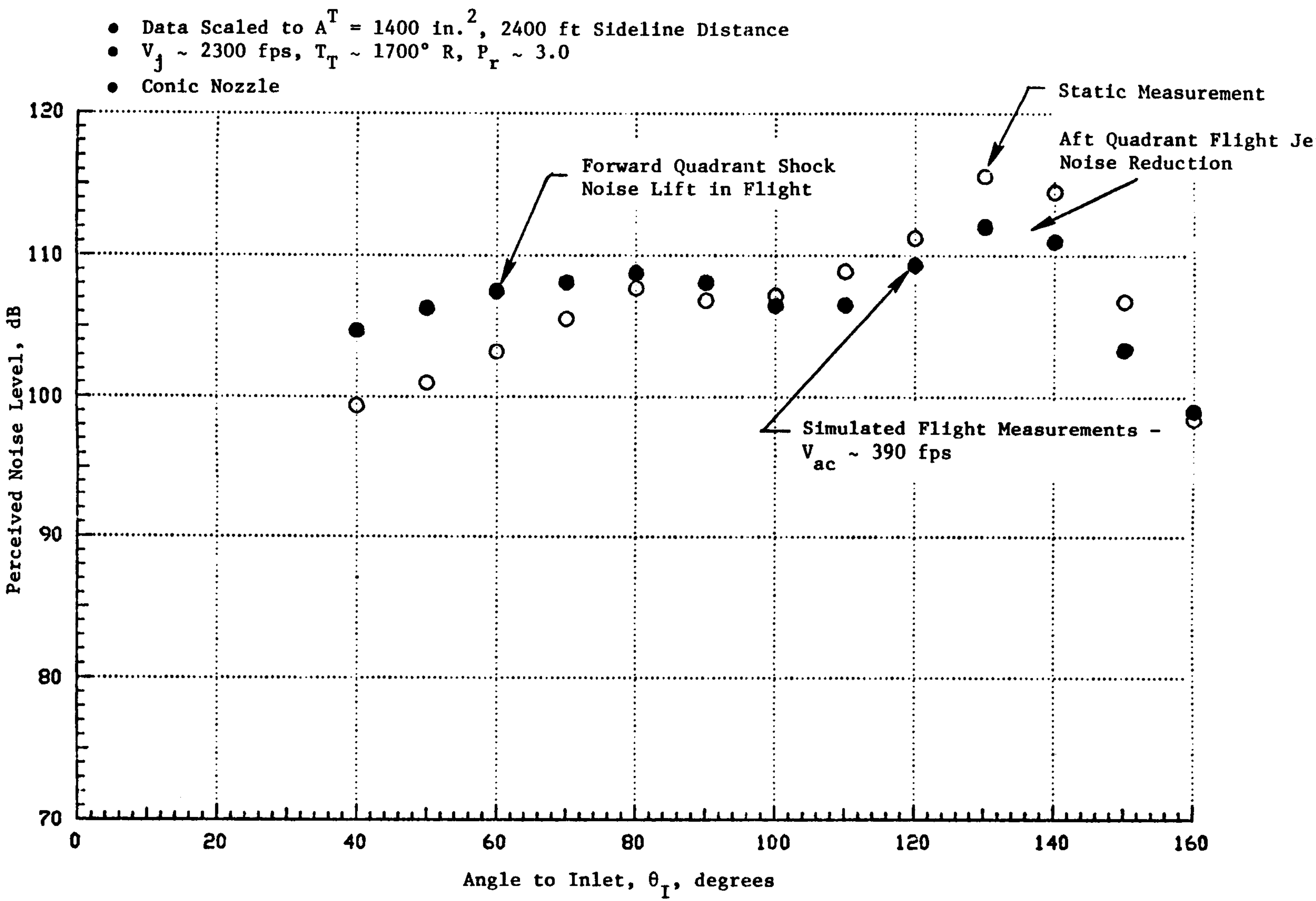

Figure 12. Comparison of Measured Static and Simulated Flight PNL Directivity of a Conic Nozzle at a Typical Takeoff Sideline AST/VCE Cycle Condition.

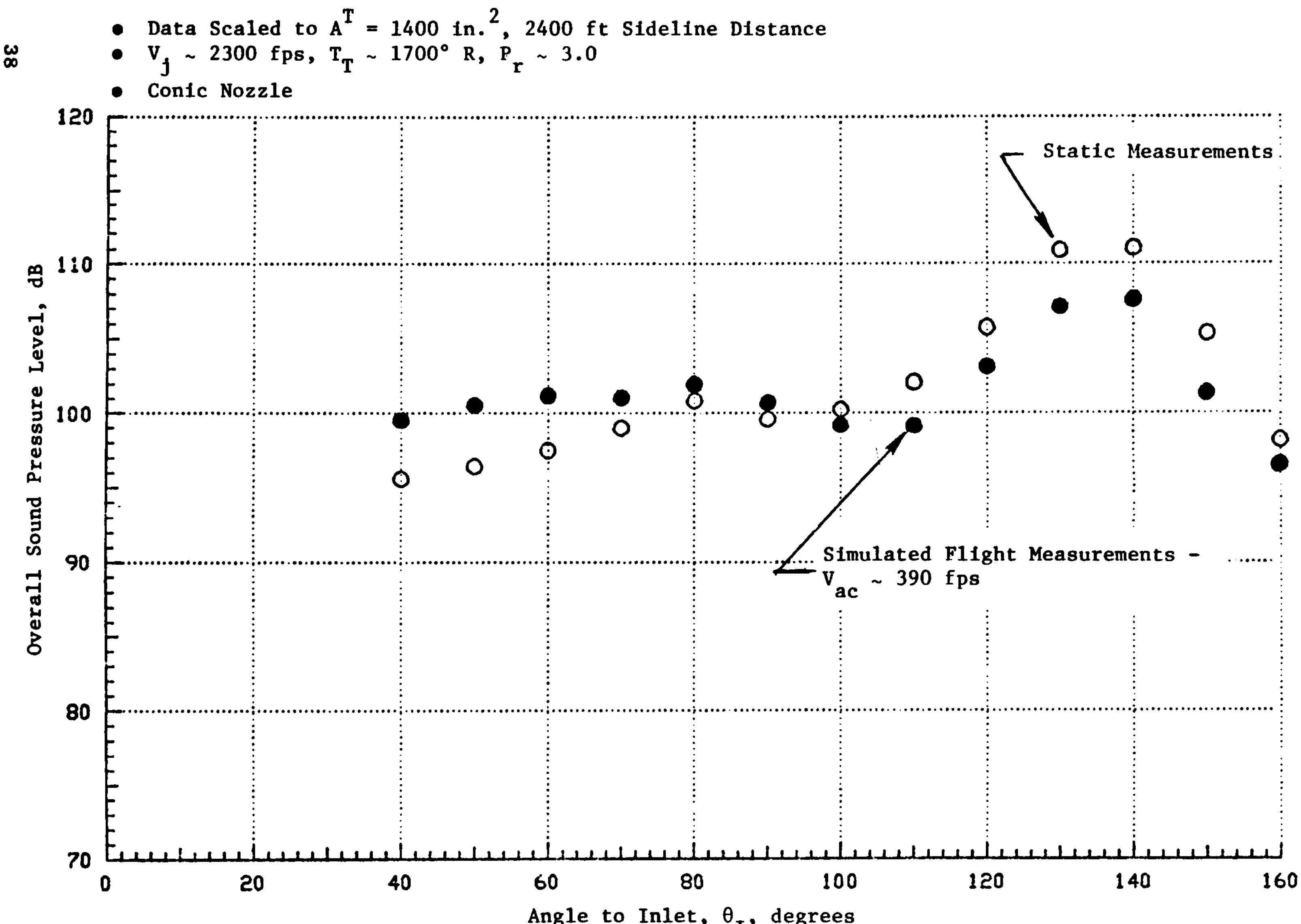

Figure 13. Comparison of Measured Static and Simulated Flight OASPL Directivity of a Conic Nozzle at a Typical Takeoff Sideline AST/VCE Cycle Condition.

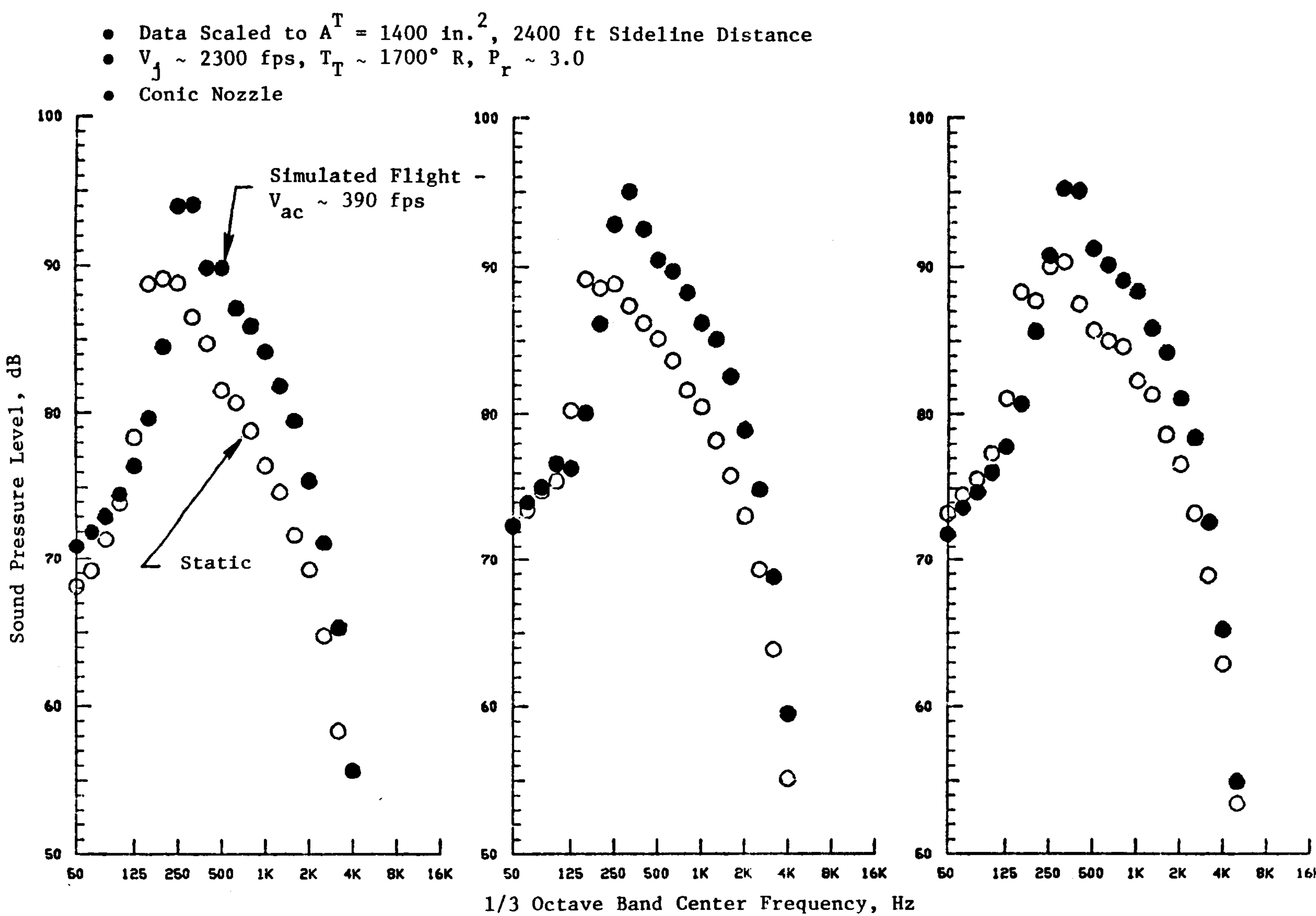

(a) Directivity Angle, θ_I, = 40° (b) Directivity Angle, θ_I, = 50° (c) Directivity Angle, θ_I, = 60°

Figure 14. Comparison of Measured Static and Simulated Flight Acoustic Spectra for a Conic Nozzle - Typical Takeoff Sideline AST/VCE Cycle Conditions.

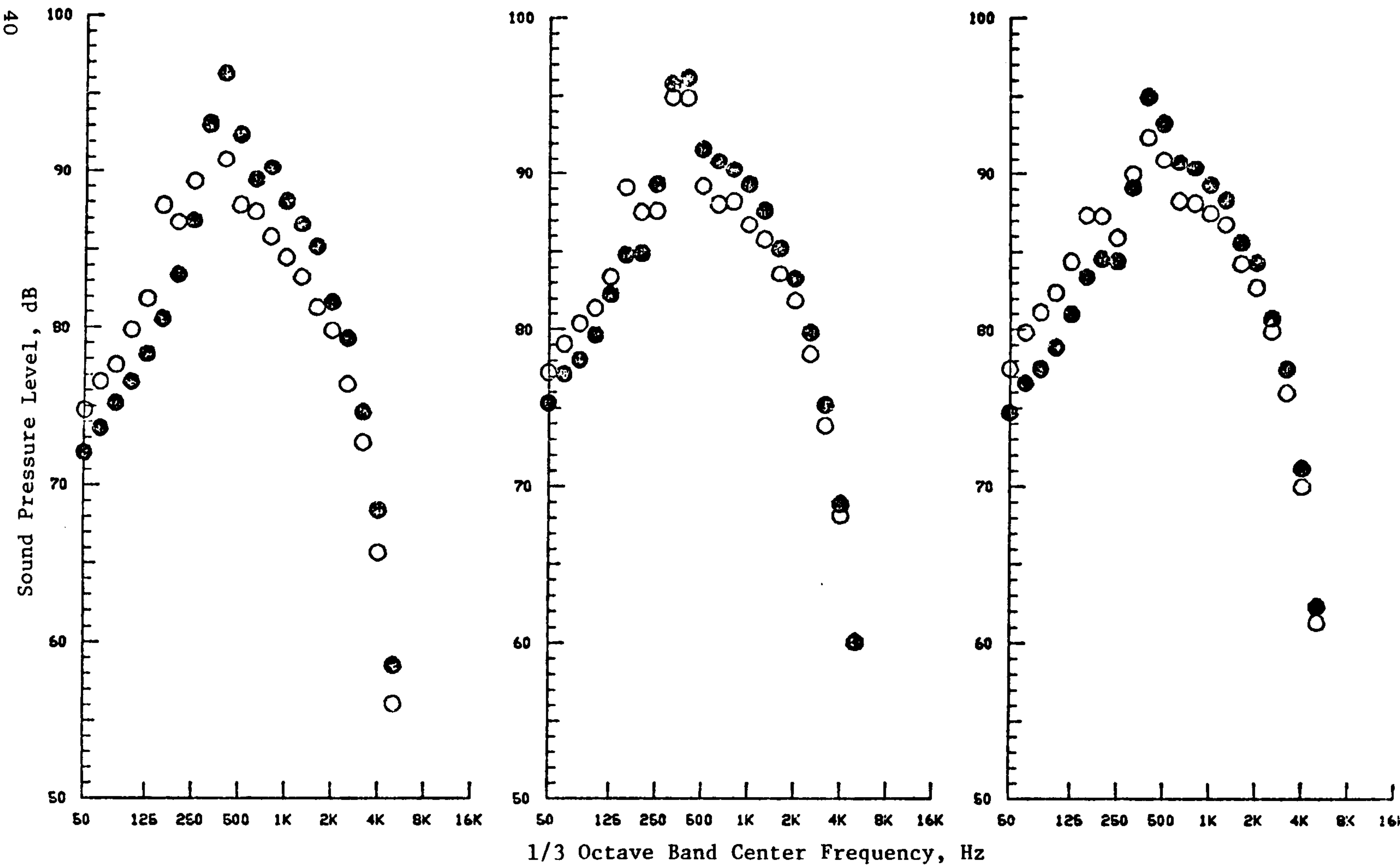

(d) Directivity Angle, θ_I, = 70°   (e) Directivity Angle, θ_I, = 80°   (f) Directivity Angle, θ_I, = 90°

Figure 14. Comparison of Measured Static and Simulated Flight Acoustic Spectra for a Conic Nozzle - Typical Takeoff Sideline AST/VCE Cycle Conditions (Continued).

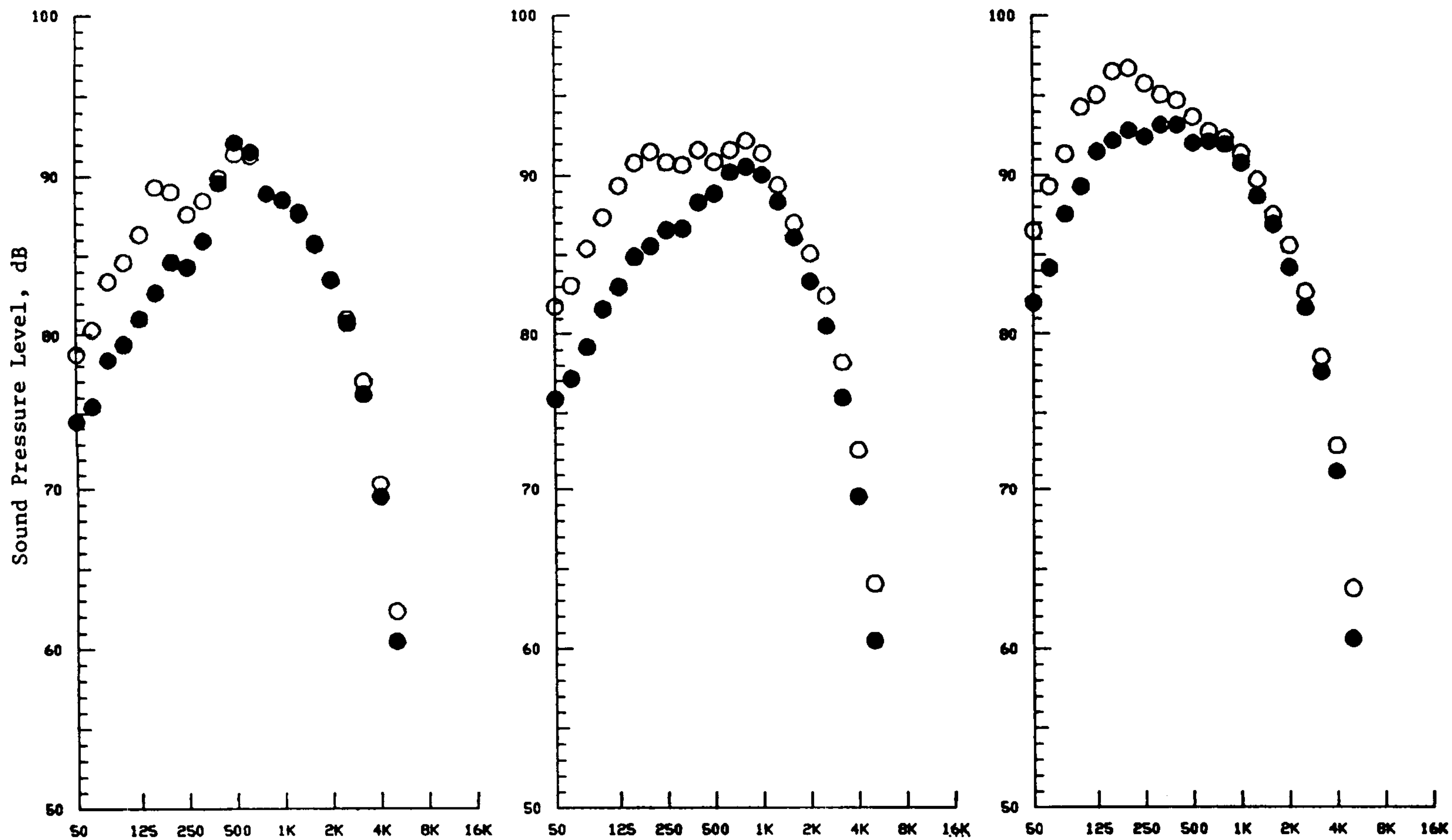

(g) Directivity Angle, θ_I, = 100° (h) Directivity Angle, θ_I, = 110° (i) Directivity Angle, θ_I, = 120°

Figure 14. Comparison of Measured Static and Simulated Flight Acoustic Spectra for a Conic Nozzle - Typical Takeoff Sideline AST/VCE Cycle Conditions (Continued).

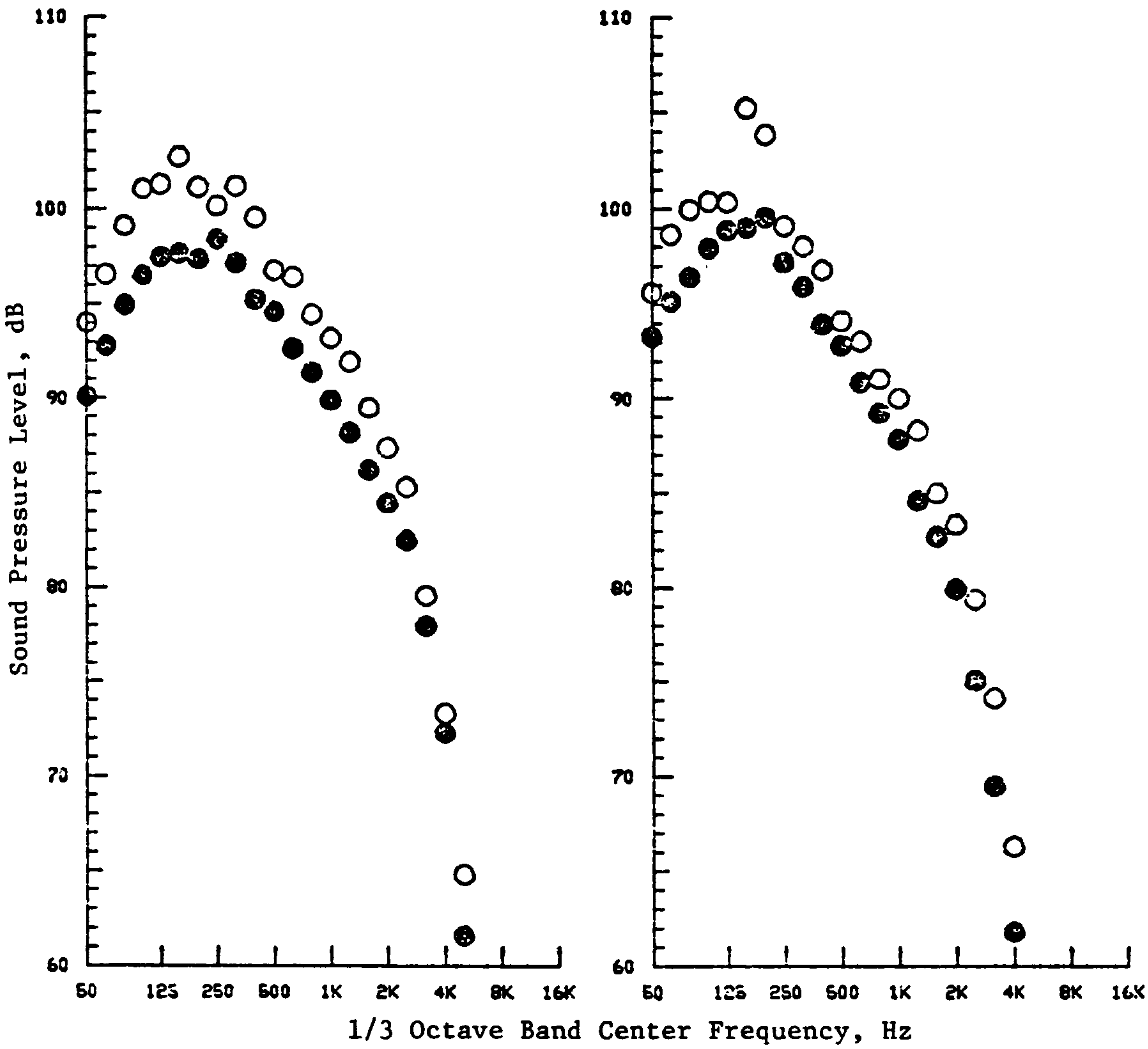

(j) Directivity Angle, θ_I, = 130°   (k) Directivity Angle, θ_I, = 140°

Figure 14. Comparison of Measured Static and Simulated Flight Acoustic Spectra for a Conic Nozzle - Typical Takeoff Sideline AST/VSE Cycle Conditions (Continued).

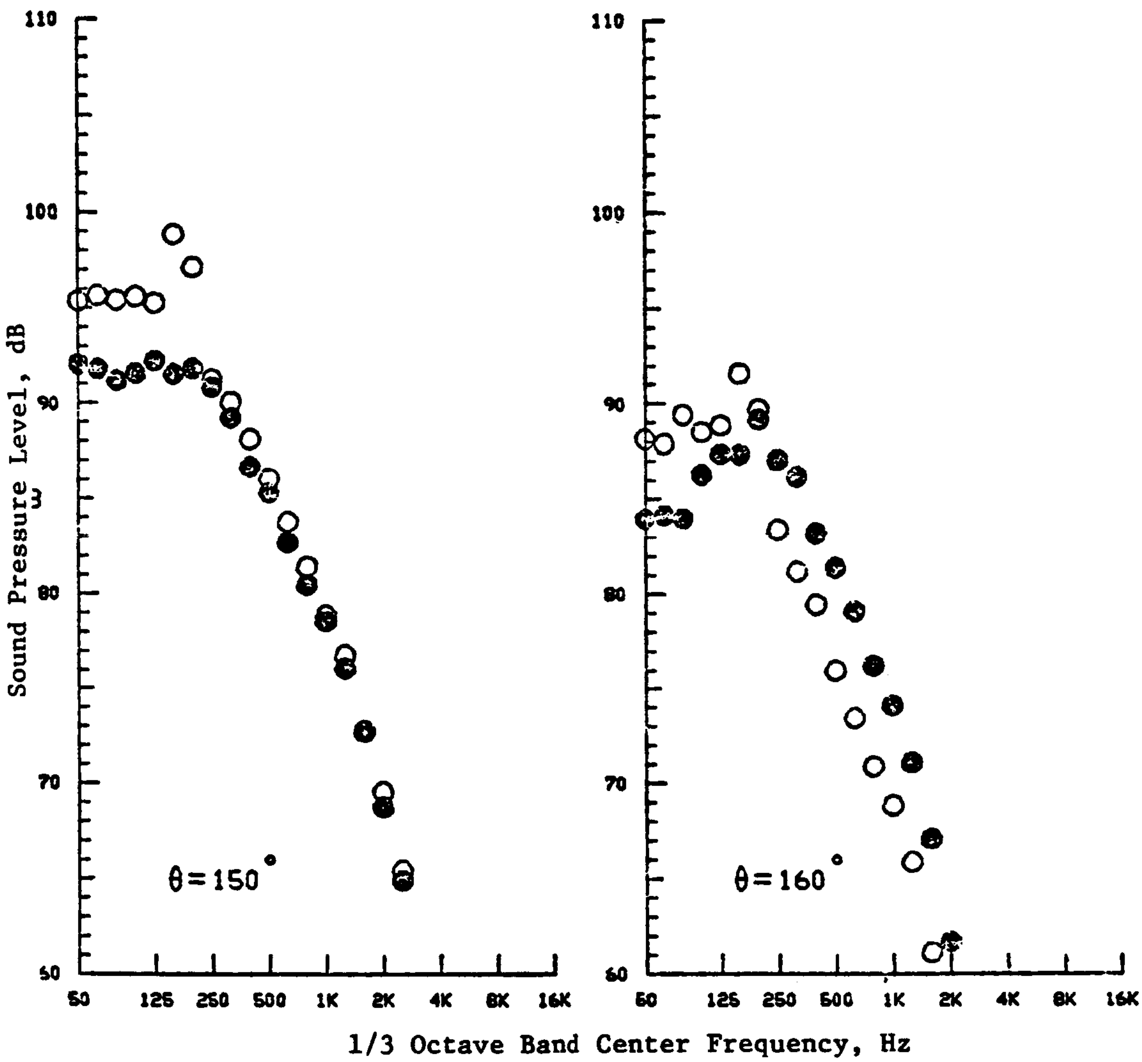

(l) Directivity Angle, θ_I, = 150°   (m) Directivity Angle, θ_I, = 160°

Figure 14. Comparison of Measured Static and Simulated Flight Acoustic Spectra for a Conic Nozzle - Typical Takeoff Sideline AST/VCE Cycle Conditions (Concluded).

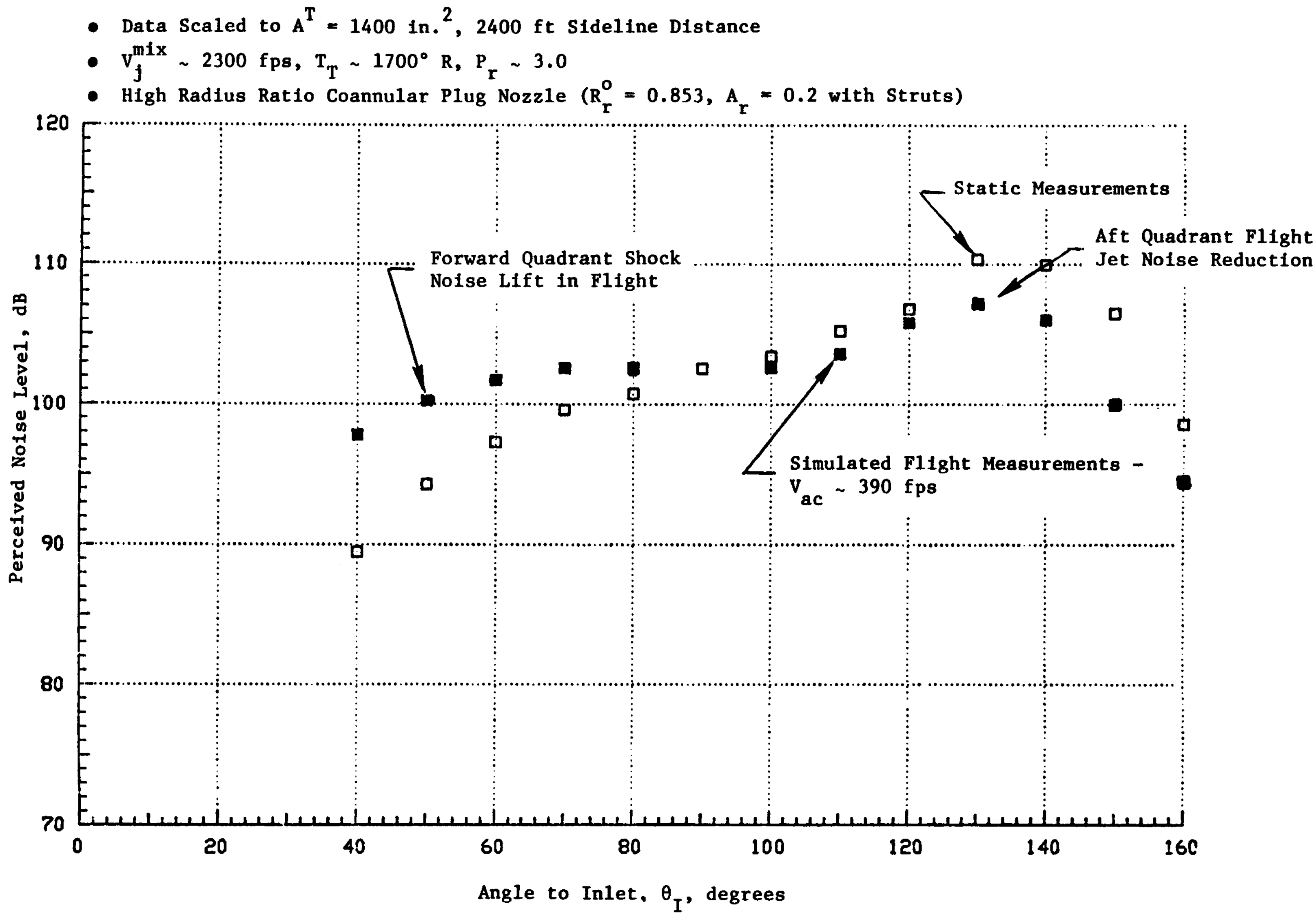

Figure 15. Comparison of Measured Static and Simulated Flight PNL Directivity of a Coannular Plug Nozzle at a Typical Takeoff Sideline AST/VCE Cycle Condition.

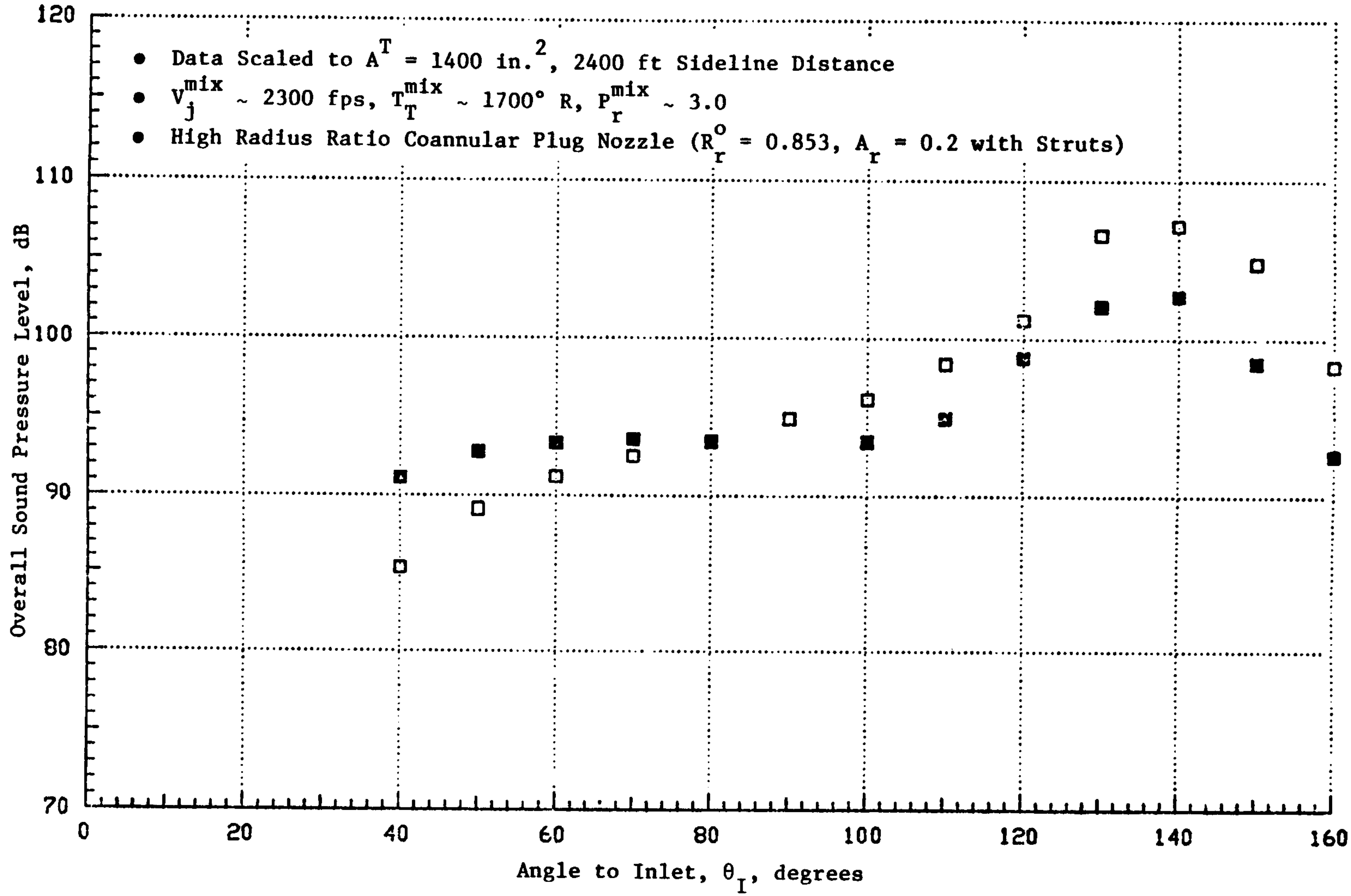

Figure 16. Comparison of Measured Static and Simulated Flight OASPL Directivity of a Coannular Plug Nozzle at a Typical Takeoff Sideline AST/VCE Cycle Condition.

- Data Scaled to $A^T = 1400\ in.^2$, 2400 ft Sideline Distance
- $V_m^{mix} \sim 2300$ fps, $T_T^{mix} \sim 1700°$ R, $P_r^{mix} \sim 3.0$
- High Radius Ratio Coannular Plug Nozzle ($R_r^o = 0.853$, $A_r = 0.2$ with Struts)

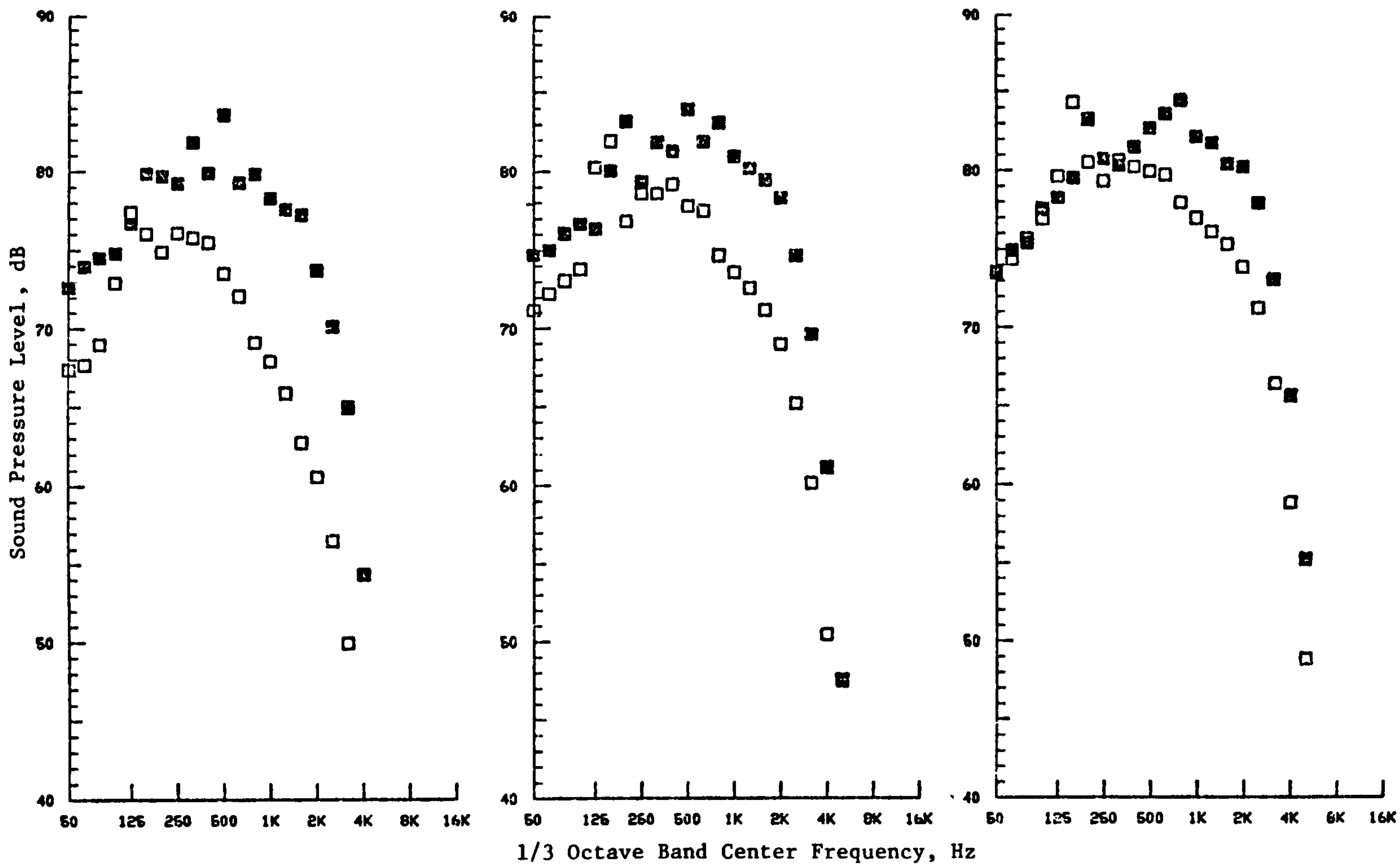

(a) Directivity Angle, θ_I, = 40° (b) Directivity Angle, θ_I = 50° (c) Directivity Angle, θ_I = 60°

Figure 17. Comparison of Measured Static and Simulated Flight Acoustic Spectra for a Coannular Plug Nozzle at Typical Takeoff Sideline AST/VCE Cycle Conditions.

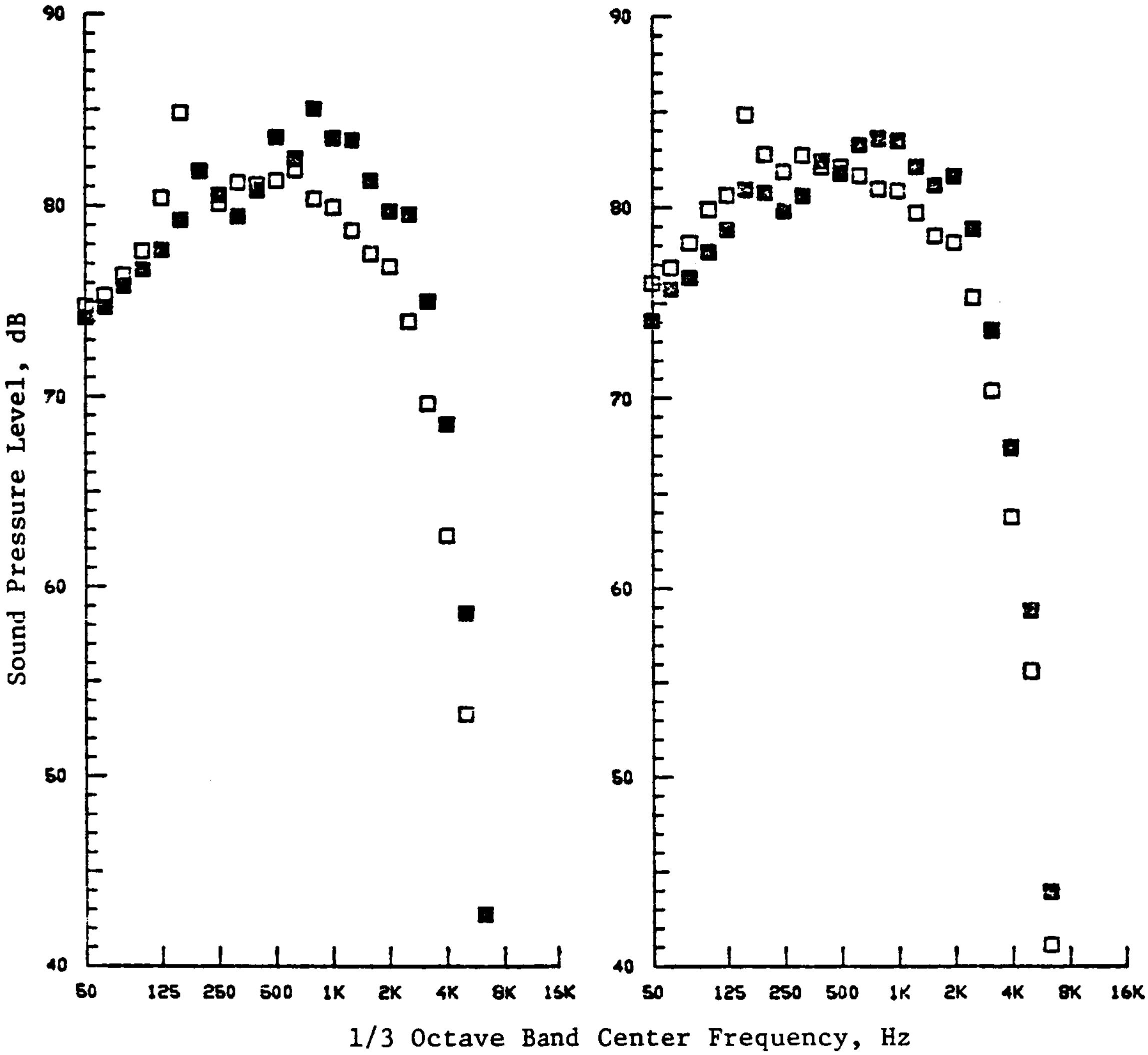

(d) Directivity Angle, θ_I = 70°   (e) Directivity Angle, θ_I = 80°

Figure 17. Comparison of Measured Static and Simulated Flight Acoustic Spectra for a Coannular Plug Nozzle at Typical Takeoff Sideline AST/VCE Cycle Conditions (Continued).

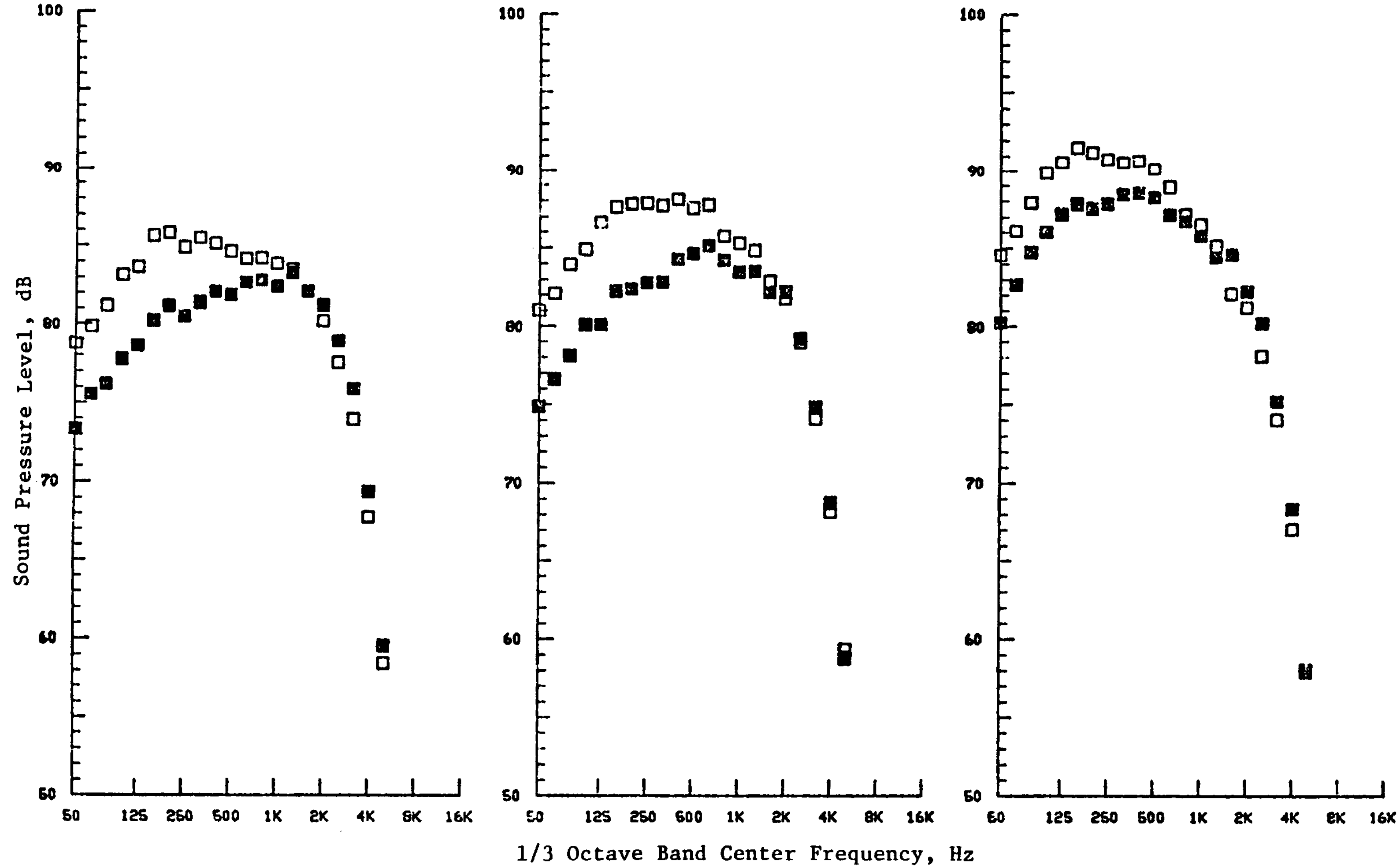

(f) Directivity Angle, θ_I = 100° (g) Directivity Angle, θ_I = 110° (h) Directivity Angle, θ_I = 120°

Figure 17. Comparison of Measured Static and Simulated Flight Acoustic Spectra for a Coannular Plug Nozzle at Typical Takeoff Sideline AST/VCE Cycle Conditions (Continued).

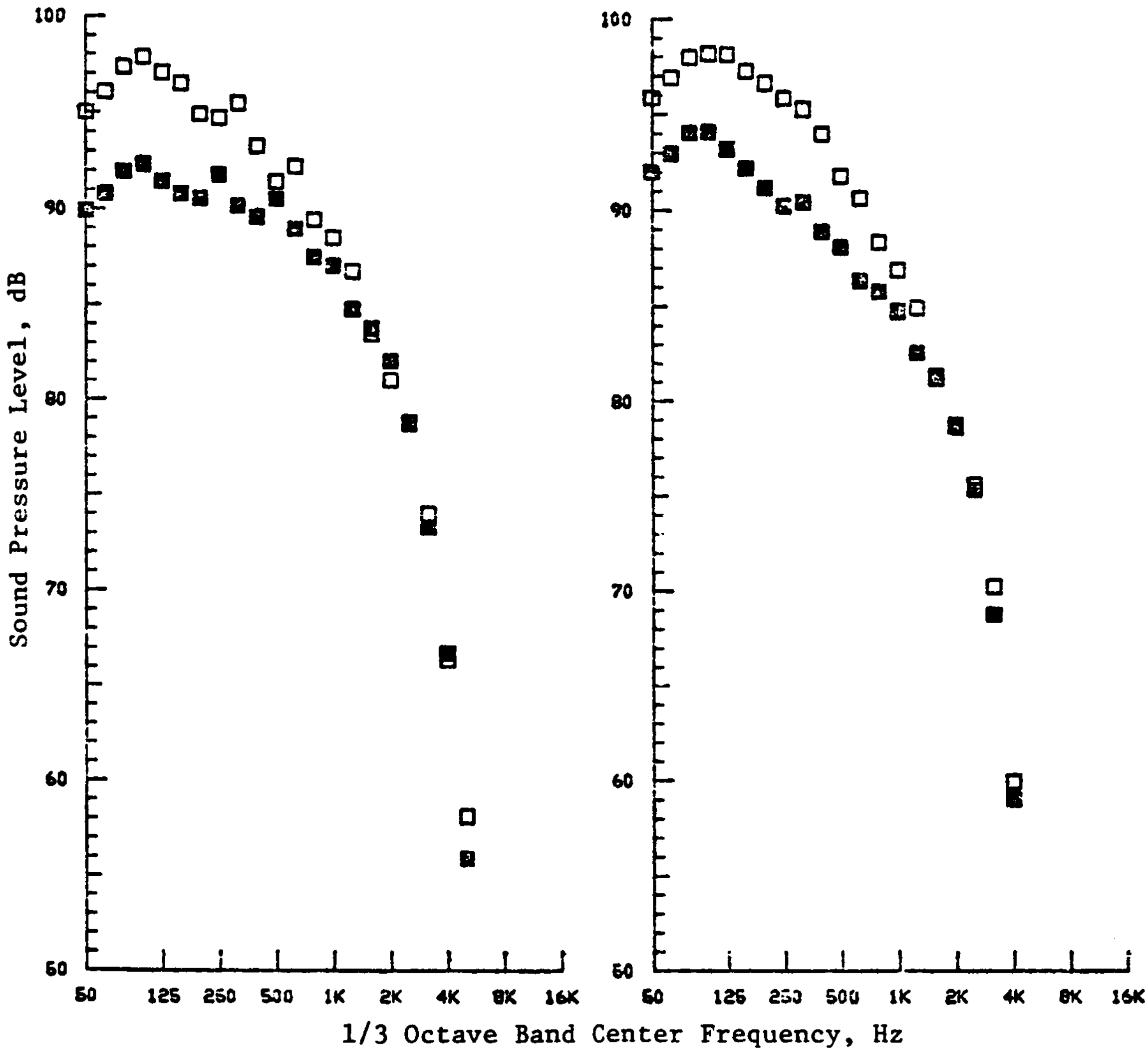

(i) Directivity Angle, θ_I = 130°

(j) Directivity Angle, θ_I = 140°

Figure 17. Comparison of Measured Static and Simulated Flight Acoustic Spectra for a Coannular Plug Nozzle at Typical Takeoff Sideline AST/VCE Cycle Conditions (Continued).

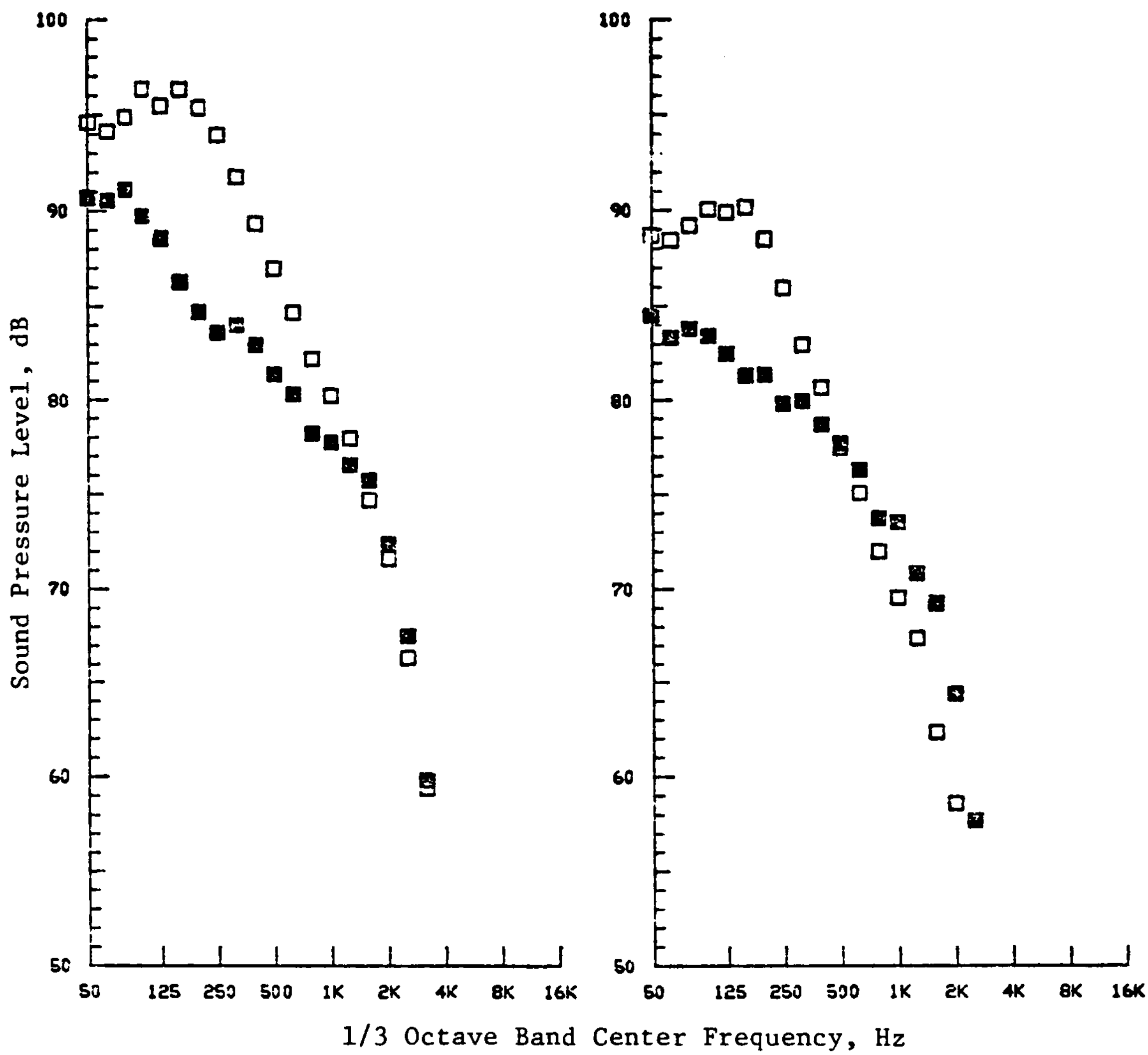

(k) Directivity Angle, θ_I = 150°   (l) Directivity Angle, θ_I = 160°

Figure 17. Comparison of Measured Static and Simulated Flight Acoustic Spectra for a Coannular Plug Nozzle at Typical Takeoff Sideline AST/VCE Cycle Conditions (Concluded).

vation angles, the amplification of the coannular shock associated noise over the entire spectral range is observed. In the aft quadrant, the flight noise reduction is observed to be primarily associated with the lower frequency bands of the scaled data (50 Hz to 2000 Hz); while at the higher frequencies, the static and flight spectrum are about the same or actually slightly higher for the flight conditions.

As a final general observation from this data set, Figure 18 shows a relative PNL and OASPL differences between the static and flight measurements in the forward quadrant for the conic and high-radius-ratio coannular plug nozzle in order to evaluate the forward quadrant shock noise lift. Shown on the figure is a predicted dynamic effect [$-40 \log (1 - M_{ac} \cos \theta_I)$] for shock noise. In general, the results seem to be in fair agreement with the simple dynamic effect prediction for the conic nozzle and the coannular plug nozzle measurements.

5.1.2 Influence of Geometry on Coannular Plug Nozzle Acoustics

5.1.2.1 Influence of Internal Struts

In order to study the influence of the eight internal struts in the outer stream of the VCE/AST test-bed nozzle on the measured far-field noise data, tests were conducted with Models 1A and 2 that are geometrically scaled versions of the test-bed nozzle but designed with and without struts, respectively. The measured static and simulated flight (V_{ac} = 390 ft/sec) normalized PNL_{max} data that are scaled to a 2400-ft sideline, 59° F standard day and a 1400 in.^{2} nozzle exhaust area are presented in Figure 19 as a function of 10 $\log(V_j^{mix}/c_a)$. An examination of this figure indicates that the PNL_{max} data with and without struts generally agree. Further, the normalized PNL_{max} data obtained from the YJ101 engine static tests with a nozzle similar to Model 1A are presented in Figure 19. Good agreement between the engine and model data is noted.

The PNL directivity patterns of Models 1A and 2 at a typical takeoff condition (V_j^{mix} = 2250 ft/sec, P_r^o = 3.2), measured under static and simulated flight conditions, are presented in Figure 20. Even though the data with/without struts reasonably agree in the aft quadrant, Figure 20 indicates that the nozzle with struts is less noisy in the forward quadrants. Such is the case from the data presented in Figure 21 comparing the frequency spectra at θ_I = 60° and 130° for Models 1A and 2 and at the typical takeoff condition. Furthermore, Figure 21 indicates that the forward angle SPL of Model 2 (without struts) is usually greater than that of Model 1A (With Struts) for all 1/3-octave band frequencies that are greater than 200 Hz.

Observations similar to those made earlier at the typical takeoff condition were noted at the underexpanded (V_j^{mix} ~ 2380 ft/sec, P_r^o = 3.8) test case. However, no significant differences in the with/without strut data were observed for the overexpanded cutback case (V_j^{mix} ~ 1920 ft/sec, P_r^o = 2.3).

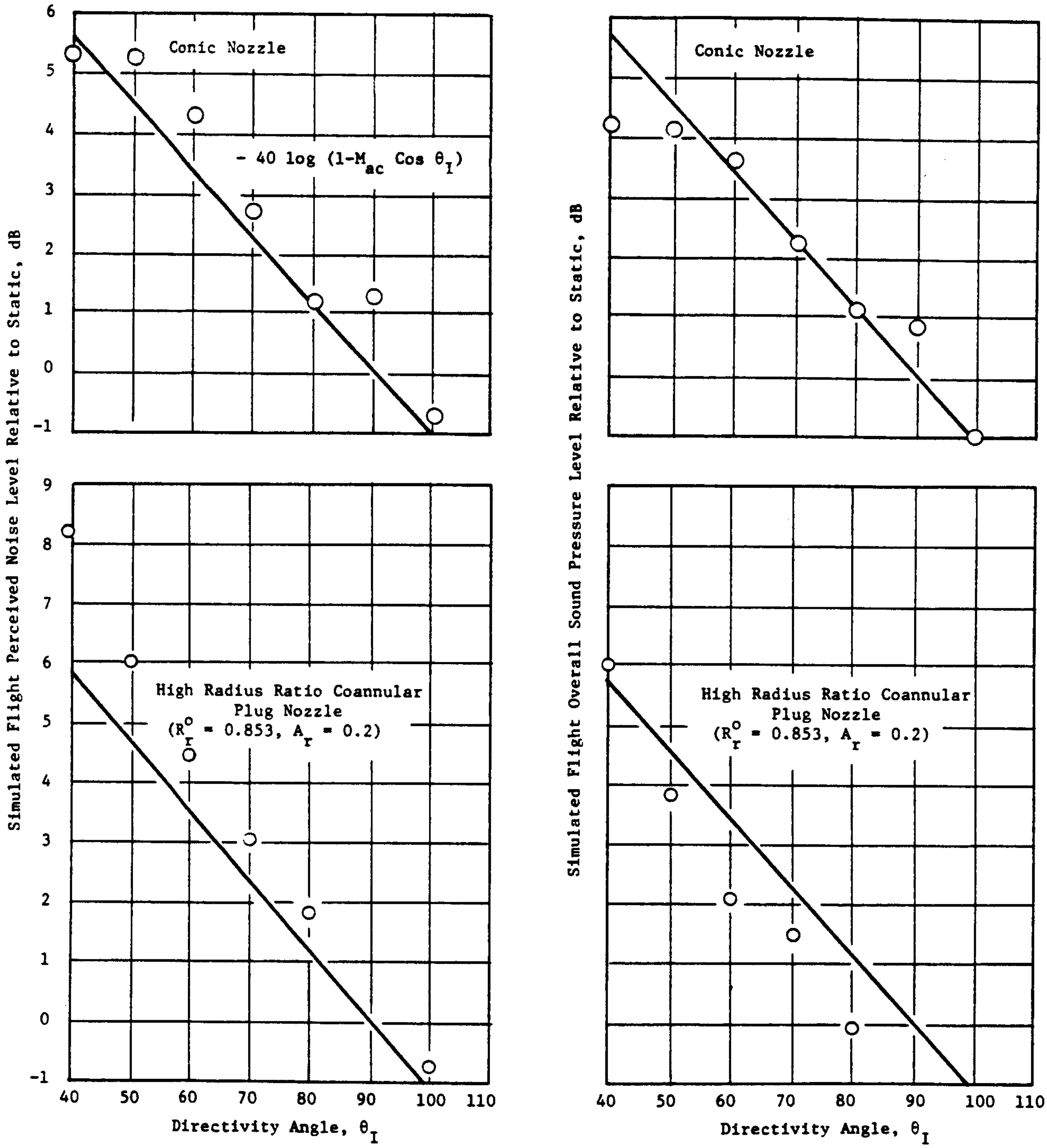

Figure 18. Simulated Flight PNL and OASPL Relative to Static Levels in Forward Quadrant.

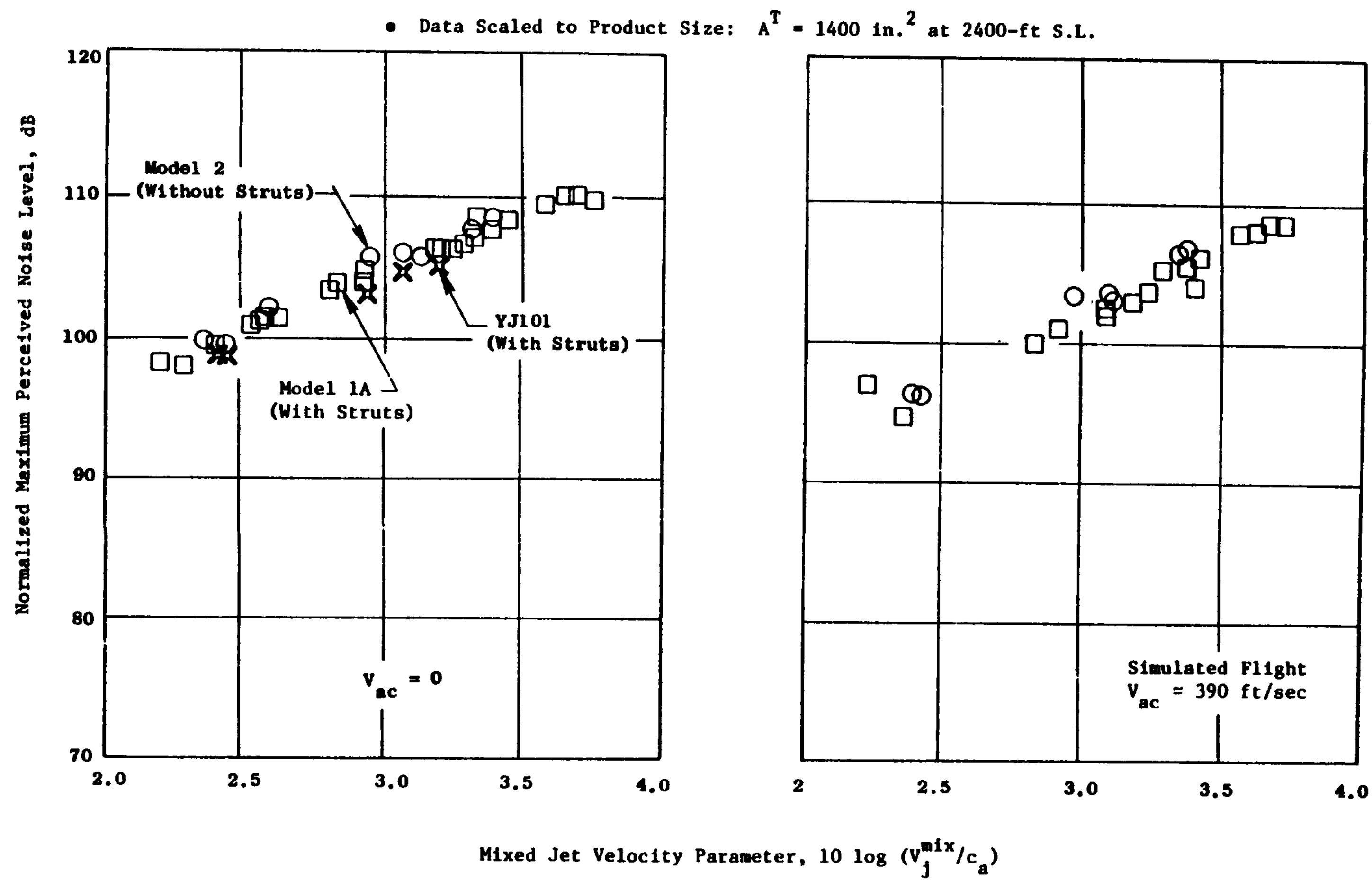

Figure 19. Normalized Maximum Perceived Noise Level Results for Model 1A (With Struts) and Model 2 (Without Struts).

Symb	Model	Test Point	V_j^o ft/sec	T_T^o °R	P_r^o	V_j^i ft/sec	T_T^i °R	P_r^i	V_j^{mix} ft/sec	T_T^{mix} °R	P_r^{mix}
□	1A	101	2411	1678	3.23	1636	789	3.19	2239	1482	3.15
○	2	201	2422	1720	3.16	1643	793	3.21	2247	1512	3.09

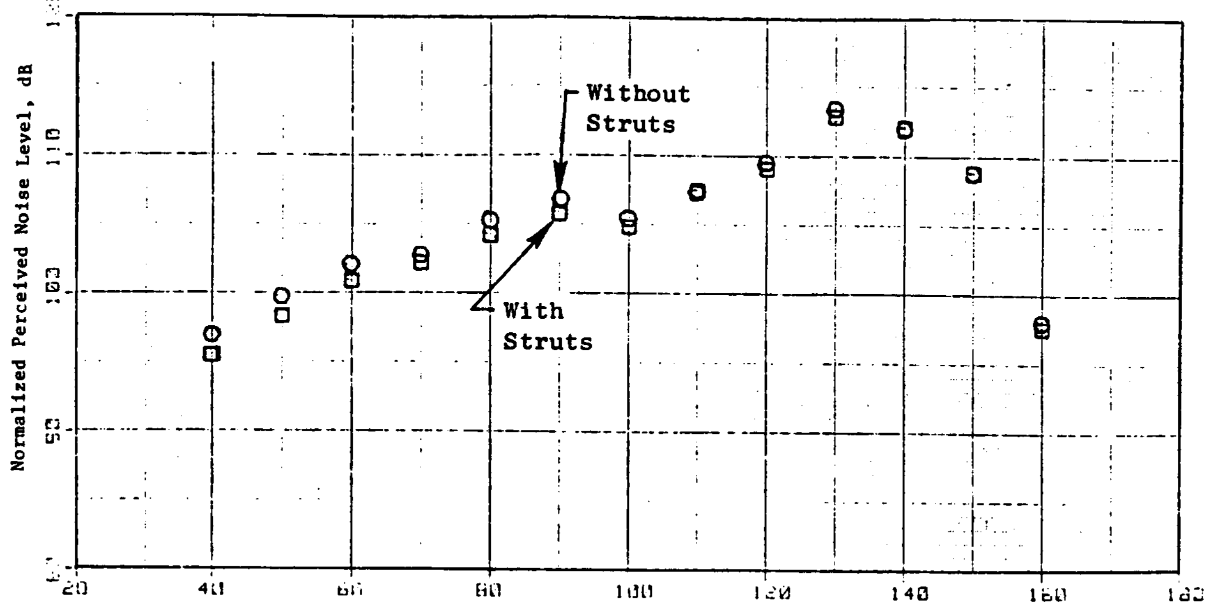

(a) Static

Symb	Model	Test Point	V_j^o ft/sec	T_T^o °R	P_r^o	V_j^i ft/sec	T_T^i °R	P_r^i	V_j^{mix} ft/sec	T_T^{mix} °R	P_r^{mix}
□	1A	103	2453	1735	3.23	1656	804	3.22	2275	1527	3.15
○	2	203	2425	1714	3.19	1651	801	3.21	2253	1511	3.11

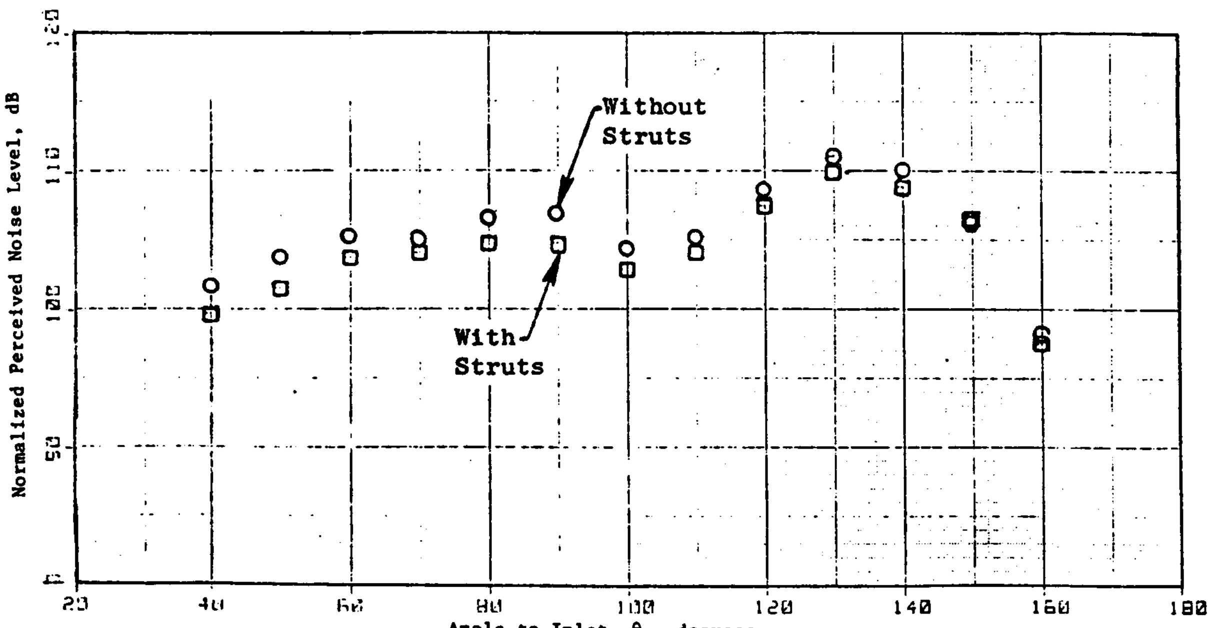

(b) Simulated Flight, $V_{ac} \approx 390$ ft/s

Figure 20. Comparison of Normalized PNL Directivity of Nozzles With and Without Struts; Typical Takeoff, $V_j^{mix} \approx 2250$ Ft/S, $P_r^o = 3.2$.

Symb	Model	Test Point	V_j^o ft/sec	T_T^o °R	P_r^o	V_j^i ft/sec	T_T^i °R	P_r^i	V_j^{mix} ft/sec	T_T^{mix} °R	P_r^{mix}
□	1A	103	2453	1735	3.23	1656	804	3.22	2275	1527	3.15
○	2	203	2425	1714	3.19	1651	801	3.21	2253	1511	3.11

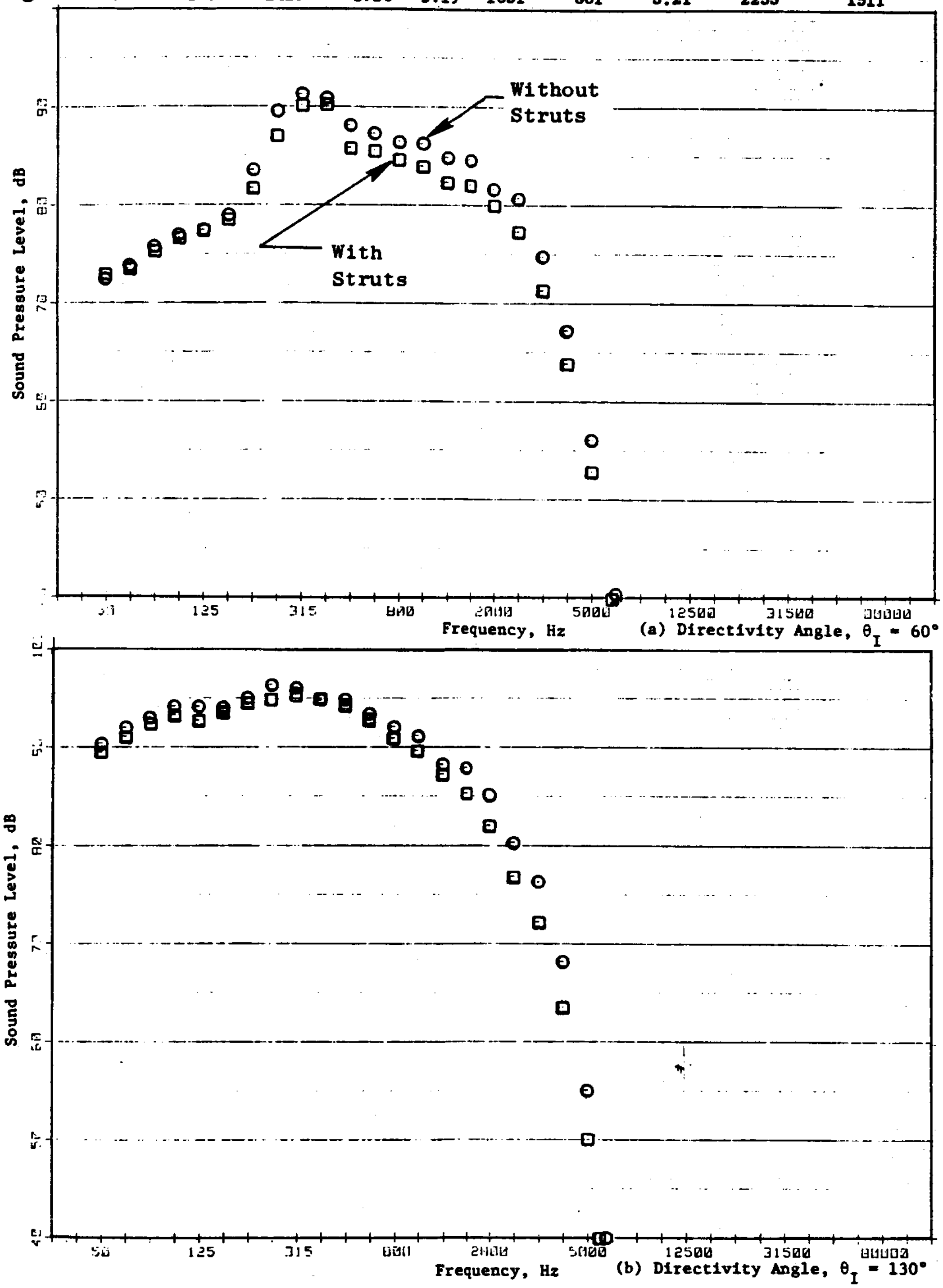

Figure 21. Comparison of Frequency Spectra of Model 1A (With Struts) and Model 2 (Without Struts), Simulated Flight $V_{ac} \simeq 390$ Ft/S at Typical Takeoff.

5.1.2.2 Influence of Outer Stream Termination

To determine the effect of forward flight on the acoustic effectiveness of a convergent-divergent (C-D) termination in the outer stream of the VCE/AST test-bed scale model, tests were conducted with a Model 2 nozzle having a C-D outer termination that is designed for a typical takeoff condition (P_r^o = 3.21). The measured static and flight acoustic data are presented in Figures 22 and 23 and are compared with the corresponding data obtained with Model 3 which has its outer stream terminated at the throat in order to yield a convergent termination. An examination of the figures indicates no significant differences, under both static and simulated flight conditions, in the forward quadrant acoustic data of C-D and convergent terminated nozzle configurations. But, in the aft quadrant, the convergent terminated configuration is observed to be beneficial, particularly during simulated flight. This aft quadrant benefit with the convergent terminated nozzle and with no significant differences in the forward quadrant data of the two nozzles is observed to be not only at the C-D optimum design pressure ratio but also at the other overexpanded/underexpanded test cases. This is made clear from the data presented in Figure 24 that compares the PNL_{60} and the normalized PNL_{max} data of Model 2 with that of Model 3 over a range of V_j^{mix} = 2380 → 1900 ft/sec and P_r^o = 3.8 → 2.3.

5.1.2.3 Influences of Outer Stream Radius Ratio and Nozzle Area Ratio

The objectives of this study are to determine, under static and simulated flight conditions, (1) the effect of the outer stream radius ratio R_r^o for a given nozzle area ratio A_r (defined = A^i/A^o) and (2) the effect of nozzle area ratio for a constant outer stream radius ratio on the acoustic characteristics of coannular plug nozzles. The measured data are presented in this section.

(1) Radius Ratio Effect

The configurations employed for this study are:

Model	A_r	R_r^o	Outer Termination
4	0.53	0.853	Convergent
6	0.53	0.902	Convergent

The tests included a series where the inner-to-outer stream velocity ratio was varied. This was achieved by holding the outer stream velocity constant at V_j^o ~ 2300 ft/sec and regulating the inner stream velocity V_j^i so as to obtain velocity ratios of 0.16 to 0.70.

The measured normalized PNL_{max} data are summarized in Figure 25. The data indicate that, under both static and simulated flight conditions and for a given area ratio, an increase in the radius ratio of the outer annular nozzle

Symb	Model	Test Point	V_j^o ft/sec	T_T^o °R	P_r^o	V_j^i ft/sec	T_T^i, °R	P_r^i	V_j^{mix} ft/sec	T_T^{mix} °R	P_r^{mix}
○	2	201	2422	1720	3.16	1643	793	3.21	2247	1512	3.09
□	3	301	2427	1719	3.18	1634	784	3.21	2247	1507	3.10

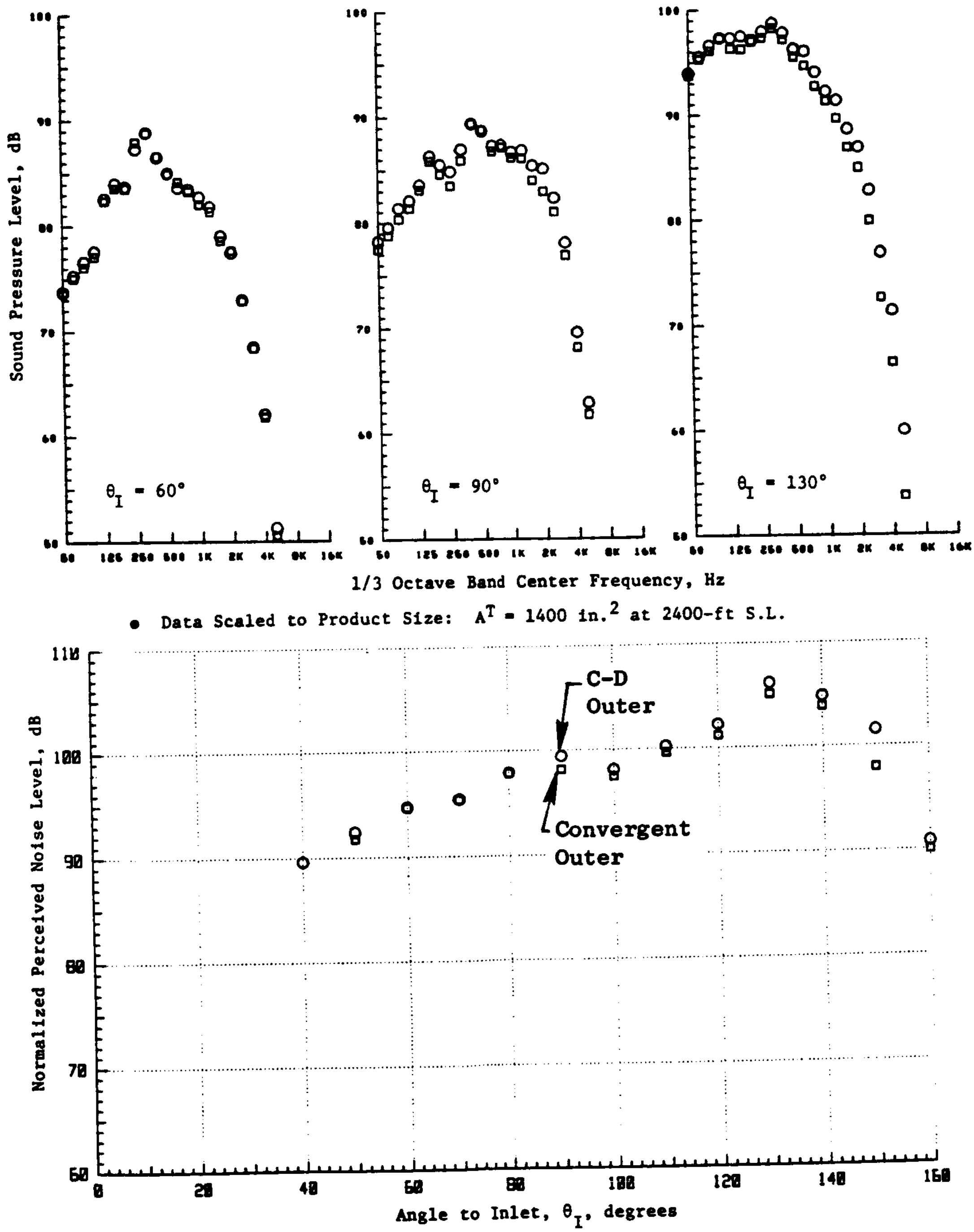

Figure 22. Comparison of Acoustic Data for Models 2 (C-D Outer Termination) and 3 (Convergent Outer Termination) at Typical Takeoff Condition at Design P_r^o = 3.21 (Static).

Symb	Model	Test Point	V_j^o ft/sec	T_T^o, °R	P_r^o	V_j^i ft/sec	T_T^i, °R	P_r^i	V_j^{mix} ft/sec	T_T^{mix} °R	P_r^{mix}
○	2	203	2425	1714	3.19	1651	801	3.21	2253	1511	3.11
□	3	303	2438	1724	3.21	1636	786	3.21	2257	1512	3.12

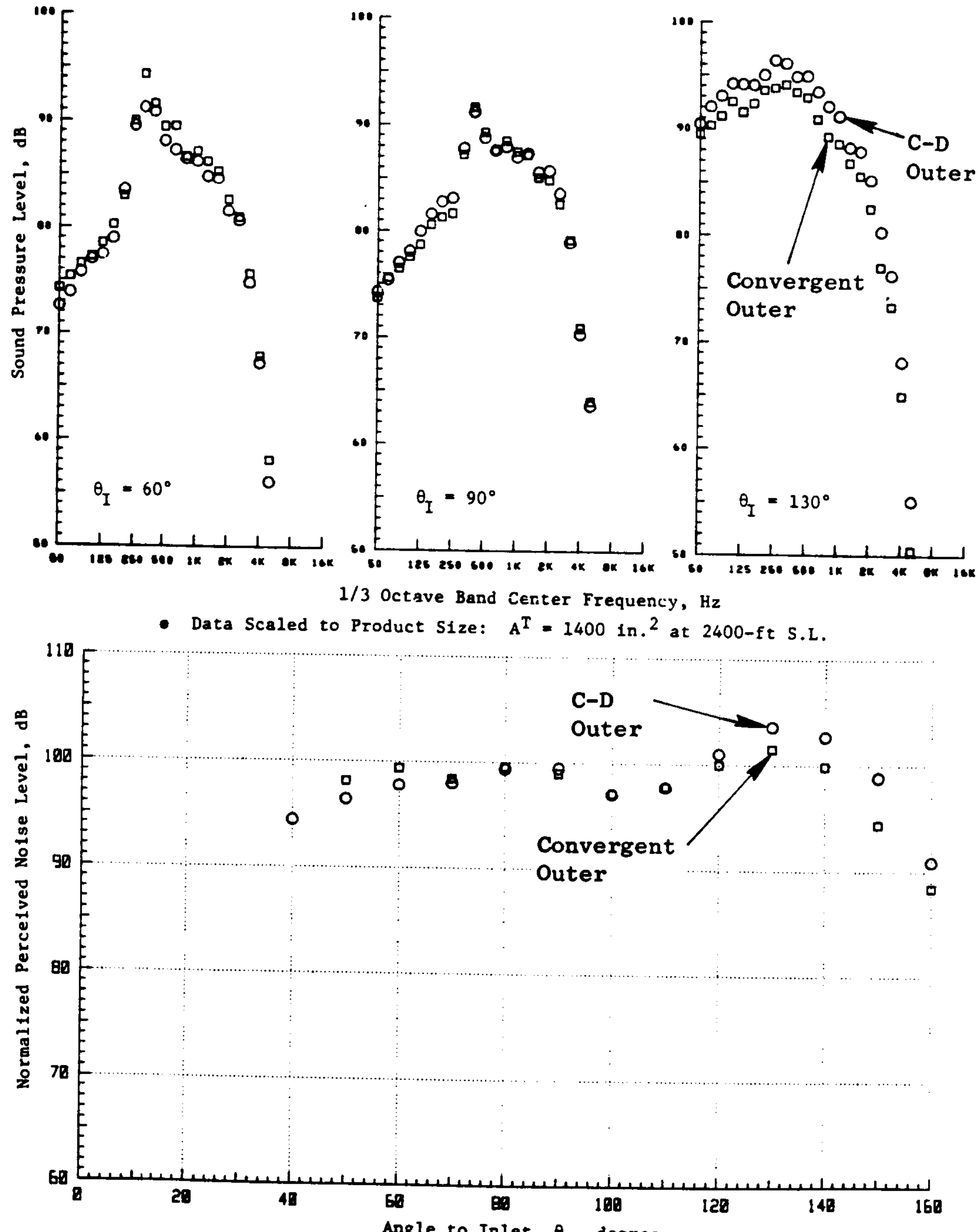

Figure 23. Comparison of Acoustic Data for Models 2 (C-D Outer Termination) and 3 (Convergent Outer Termination) at Typical Takeoff Condition at Design P_r^o = 3.21, Simulated Flight V_{ac} ≃ 390 Ft/S.

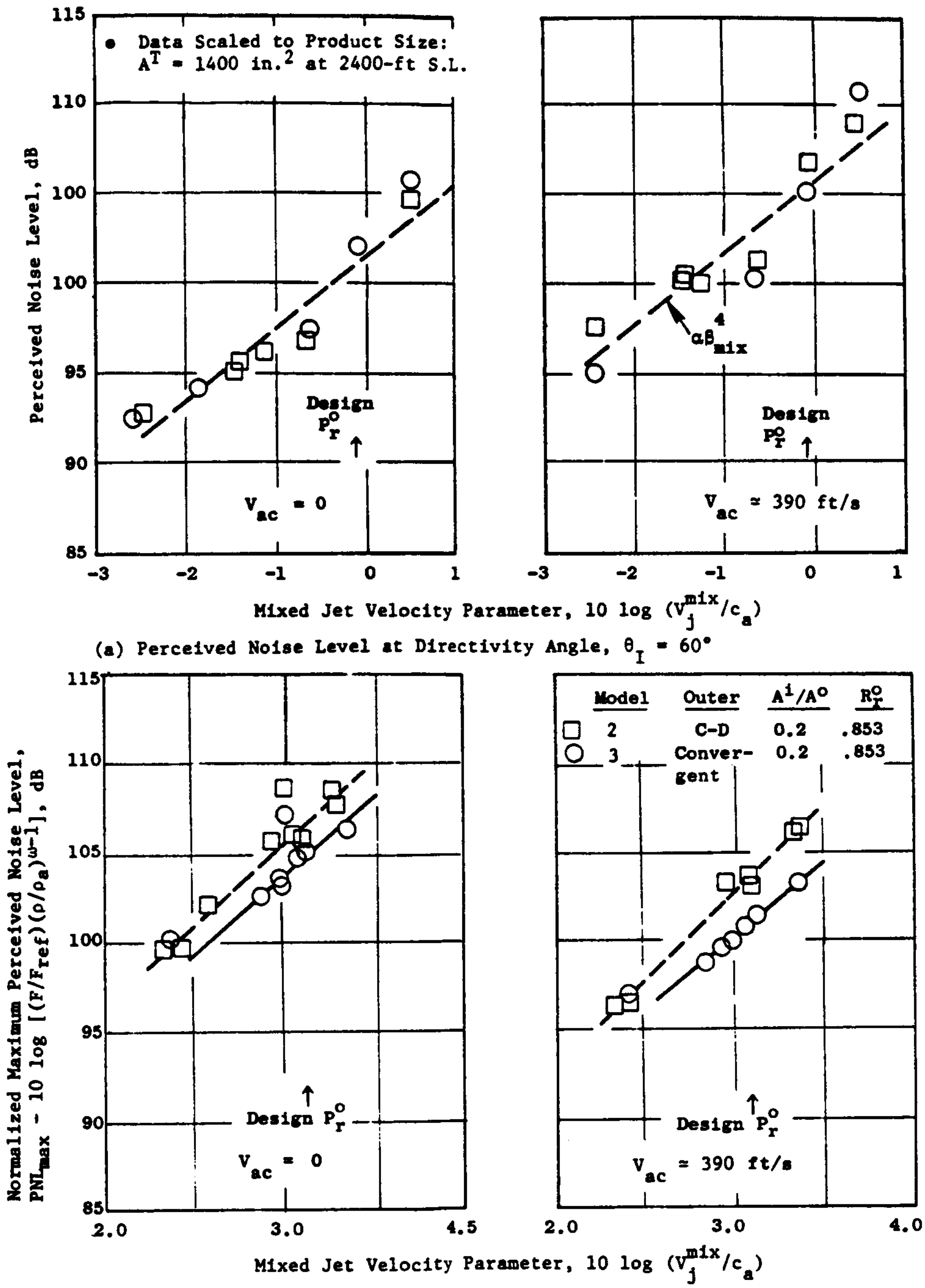

(b) Normalized Maximum Perceived Noise Level

Figure 24. Perceived Noise Levels as a Function of Mixed Jet Velocity Parameter for Models 2 (C-D Terminated) and 3 (Convergent Terminated).

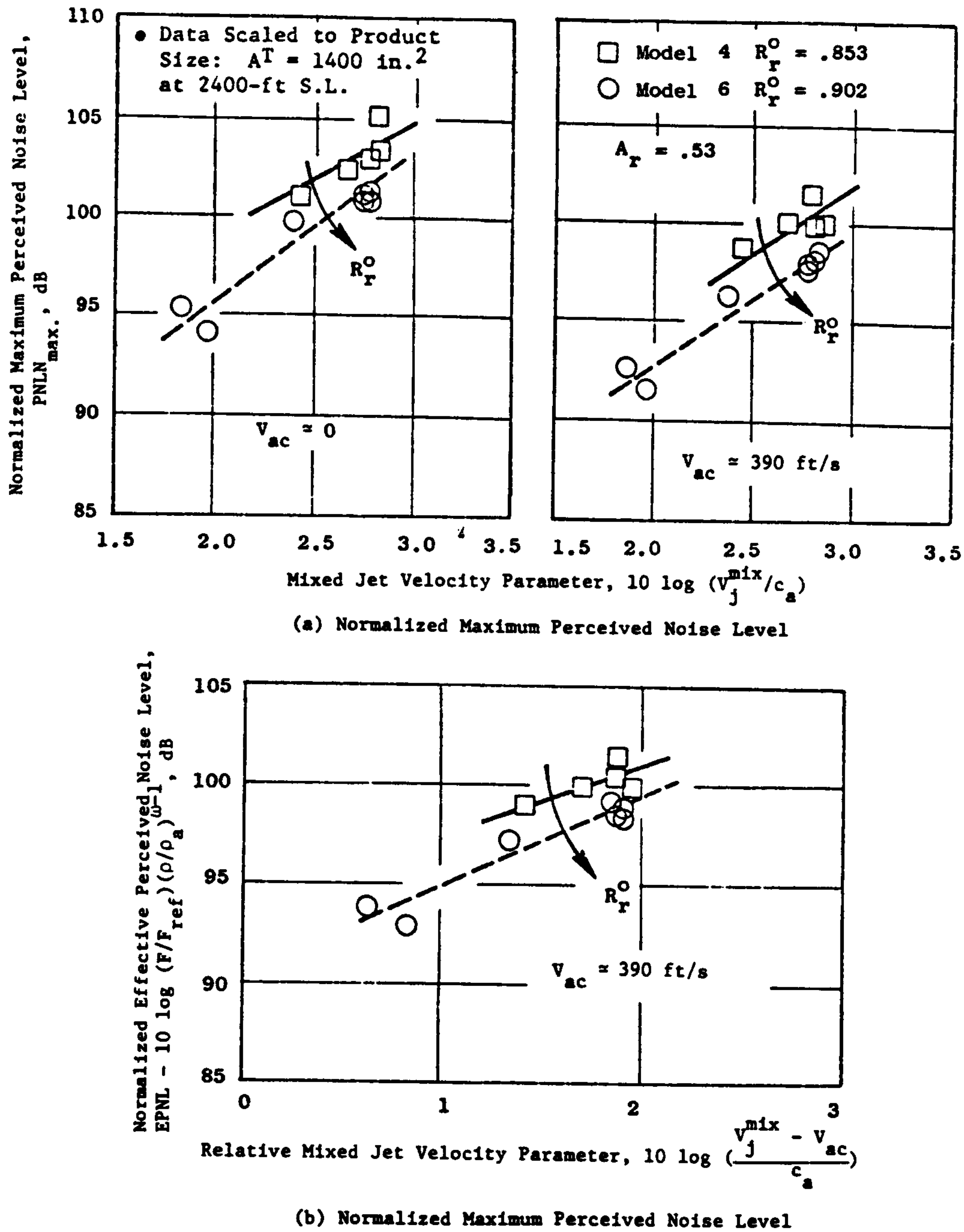

Figure 25. Influence of Outer Stream Radius Ratio on Normalized PNL_{max} and EPNL; Inner-to-Outer Area Ratio = 0.53.

is significantly beneficial in the test velocity range of V_j^{mix} = 1800 to 2200 ft/sec. This is indicated also on a normalized EPNL basis in Figure 25.

The data obtained from the tests involving variation in the inner-to-outer-stream velocity ratio are presented in Figure 26. The figure indicates that the PNL_{max} benefit due to a high outer stream radius ratio is maintained over the test velocity ratio range and under both static and simulated flight conditions.

Typical frequency spectra (at θ_r = 60°, 90°, and 130°/140°) and normalized PNL directivities that compare Models 4 and 6 static and flight data at V_j^{mix} = 2100 ($V_r \simeq$ 0.2, 0.7) and 1900 ft/sec ($V_r \simeq$ 0.4) are presented in Figures 27 through 29. An examination of the PNL directivities indicates that, while under static conditions, only aft angles benefit from a higher outer radius ratio; beneficial acoustic characteristics are observed at all angles in simulated flight. In general, the higher radius ratio nozzle results in a lower SPL at all frequencies.

(2) Area Ratio Effect

The configurations employed for this study are:

Model	R_r^o	A_r	Outer Termination
3	0.853	0.20	Convergent
7	0.853	0.33	Convergent
4	0.853	0.53	Convergent

The measured normalized PNL_{max} data of this study are presented in Figure 30 along with YJ101 engine static data obtained with a convergent terminated coannular plug nozzle having A_r = 0.2 and R_r^o = 0.853. These data indicate that, for a fixed outer stream radius ratio and V_j^{mix}, PNL_{max} decreases with a decrease in the nozzle area ratio. Also, over the test velocity range of V_j^{mix} = 1800 → 2400 ft/sec and under static and simulated flight situations, the configuration with A_r = 0.2 yielded the lowest measured aft quadrant, PNL_{max} data.

Typical frequency spectra (θ_I = 60°, 90°, and 130°/140°) and normalized PNL directivities of Models 3, 4, and 7 are presented in Figures 31 and 32. While in Figure 31 the data are plotted from tests having identical outer and mixed flow conditions (V_j^o ~ 2300 and V_j^{mix} ~ 2100 ft/sec), the data presented in Figure 32 were obtained from tests having constant outer and inner conditions (and, hence, a constant V_r). An examination of the data indicates that a change in the area ratio had no significant effect on the front quadrant acoustics for all of the test cases. In the aft quadrant, although the nozzle with the smaller area ratio (0.2) yielded beneficial results for given outer and mixed stream conditions (due to a favorable V_r), the nozzle with the larger area ratio (0.53) yielded beneficial results for given inner and outer conditions (due to the smaller V_j^{mix}).

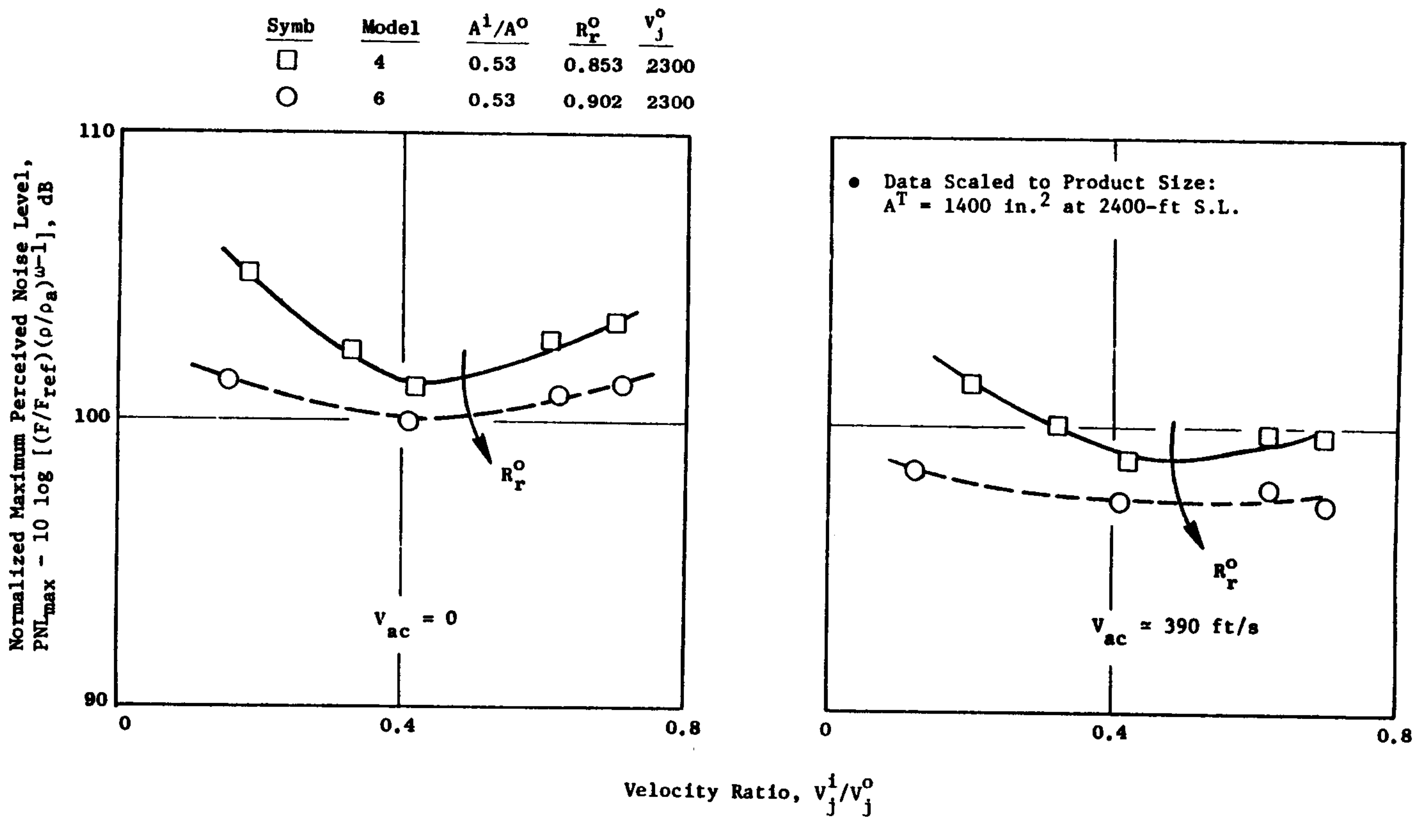

Figure 26. Influence of Outer Stream Radius Ratio on Normalized Maximum Perceived Noise Level at Different Inner-to-Outer Stream Velocity Ratios; Inner-to-Outer Stream Area Ratio = 0.53.

Symb	Model	Test Point	V_j^o ft/sec	T_T^o °R	P_r^o	V_j^i ft/sec	T_T^i °R	P_r^i	V_j^{mix} ft/sec	T_T^{mix} °R	P_r^{mix}
○	4	481	2313	1736	2.78	425	980	1.06	2104	1552	2.39
□	6	3006	2316	1741	2.78	371	637	1.07	2039	1584	2.35

• Data Scaled to Product Size: A^T = 1400 in.^{2} at 2400-ft S.L.

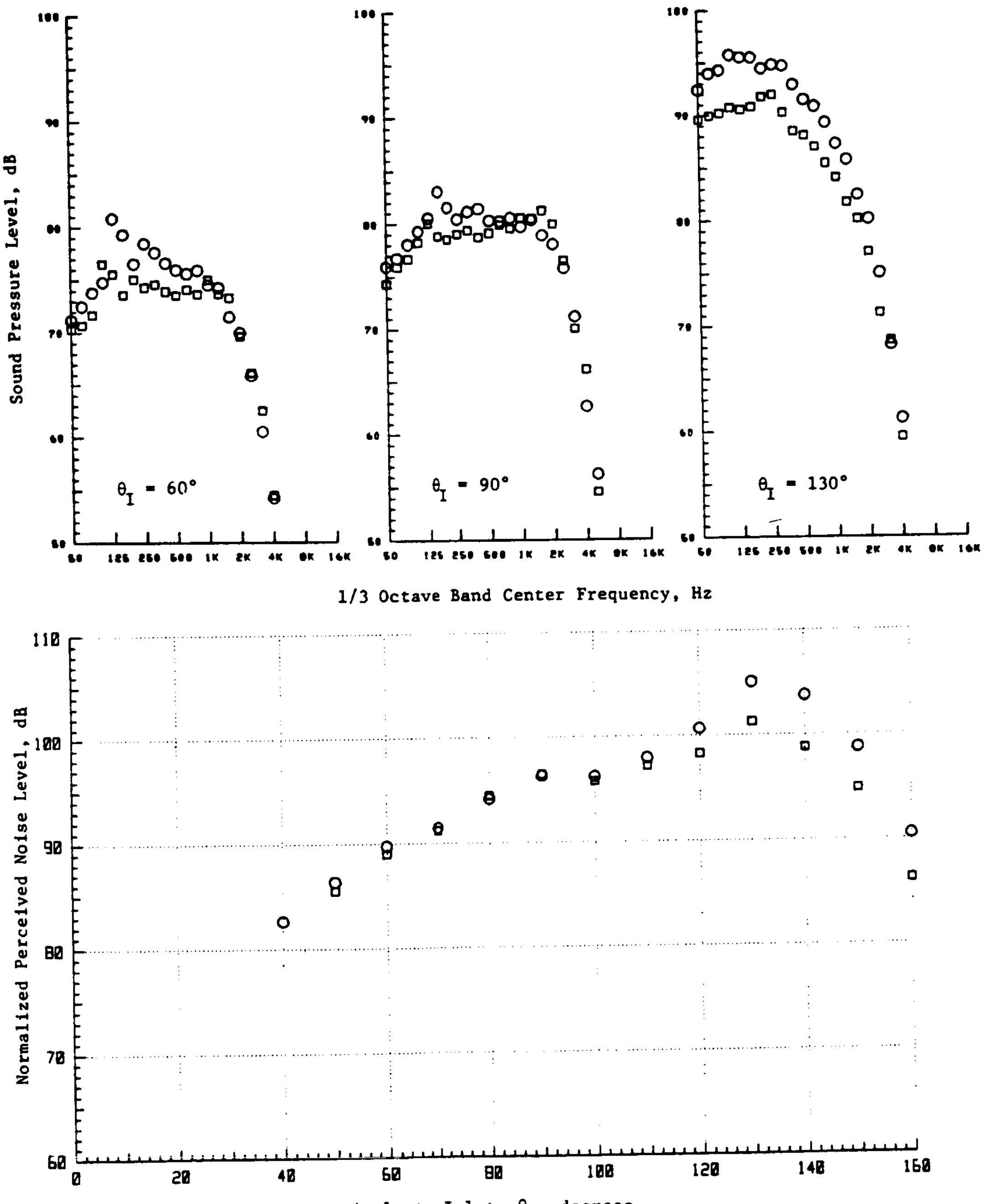

(a) Static

Figure 27. Comparison of Model 4 (R_r^o = 0.853) and Model 6 (R_r^o = 0.902) Frequency Spectrum and PNL Directivity at V_j^{mix} ≃ 2100 ft/s, V_r ≃ 0.2, A_r = 0.53.

Symb	Model	Test Point	V_j^o ft/sec	T_T^o °R	P_r^o	V_j^i ft/sec	T_T^i °R	P_r^i	V_j^{mix} ft/sec	T_T^{mix} °R	P_r^{mix}	EPNL
○	4	402	2285	1689	2.79	464	1026	1.06	2079	1614	2.39	101.2
□	6	3008	2302	1711	2.80	272	709	1.03	2106	1614	2.46	98.6

• Data Scaled to Product Size: A^T = 1400 in.^{2} at 2400-ft S.L.

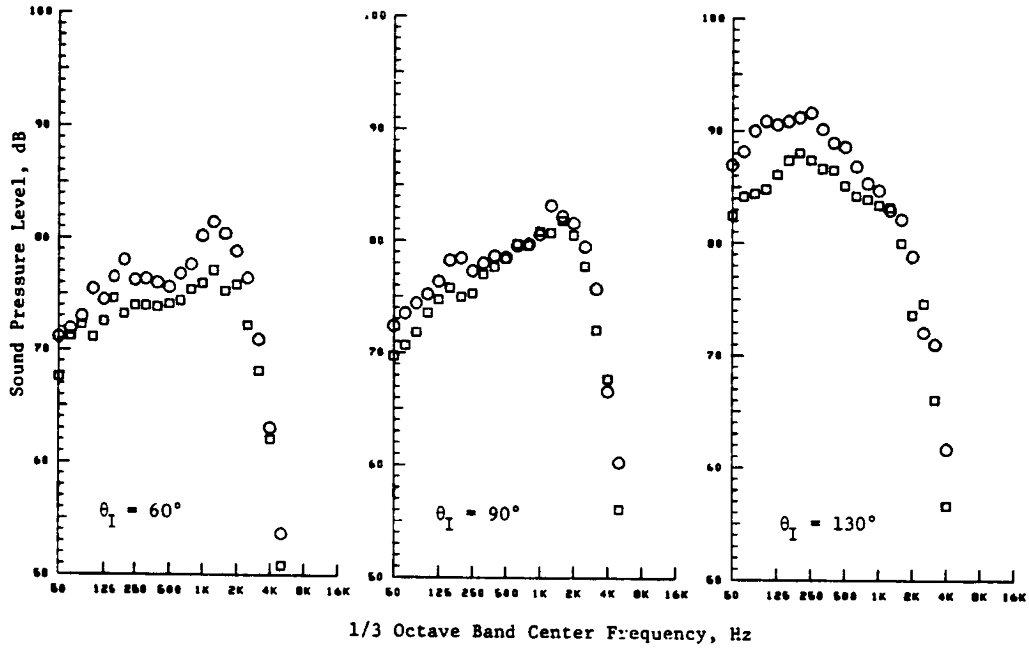

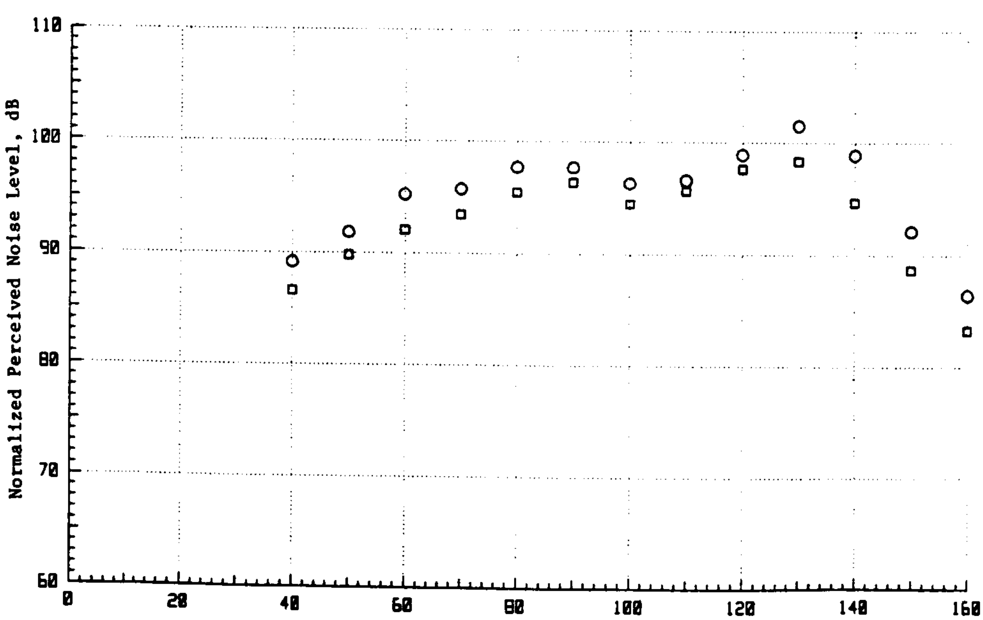

(b) Simulated Flight, V_{ac} ≈ 390 ft/s

Figure 27. Comparison of Model 4 (R_r^o = 0.853) and Model 6 (R_r^o = 0.902) Frequency Spectrum and PNL Directivity at V_j^{mix} ≈ 2100 Ft/Sec, V_r ≈ 0.2, A_r = 0.53 (Concluded).

Symb	Model	Test Point	V_j^o ft/sec	T_T^o °R	P_r^o	V_j^i ft/sec	T_T^i °R	P_r^i	V_j^{mix} ft/sec	T_T^{mix} °R	P_r^{mix}
○	4	409	2318	1742	2.78	1626	1258	1.95	2107	1594	2.49
□	6	3018	2276	1697	2.75	1616	1243	1.95	2076	1559	2.47

• Data Scaled to Product Size: A^T = 1400 in.^{2} at 2400-ft S.L.

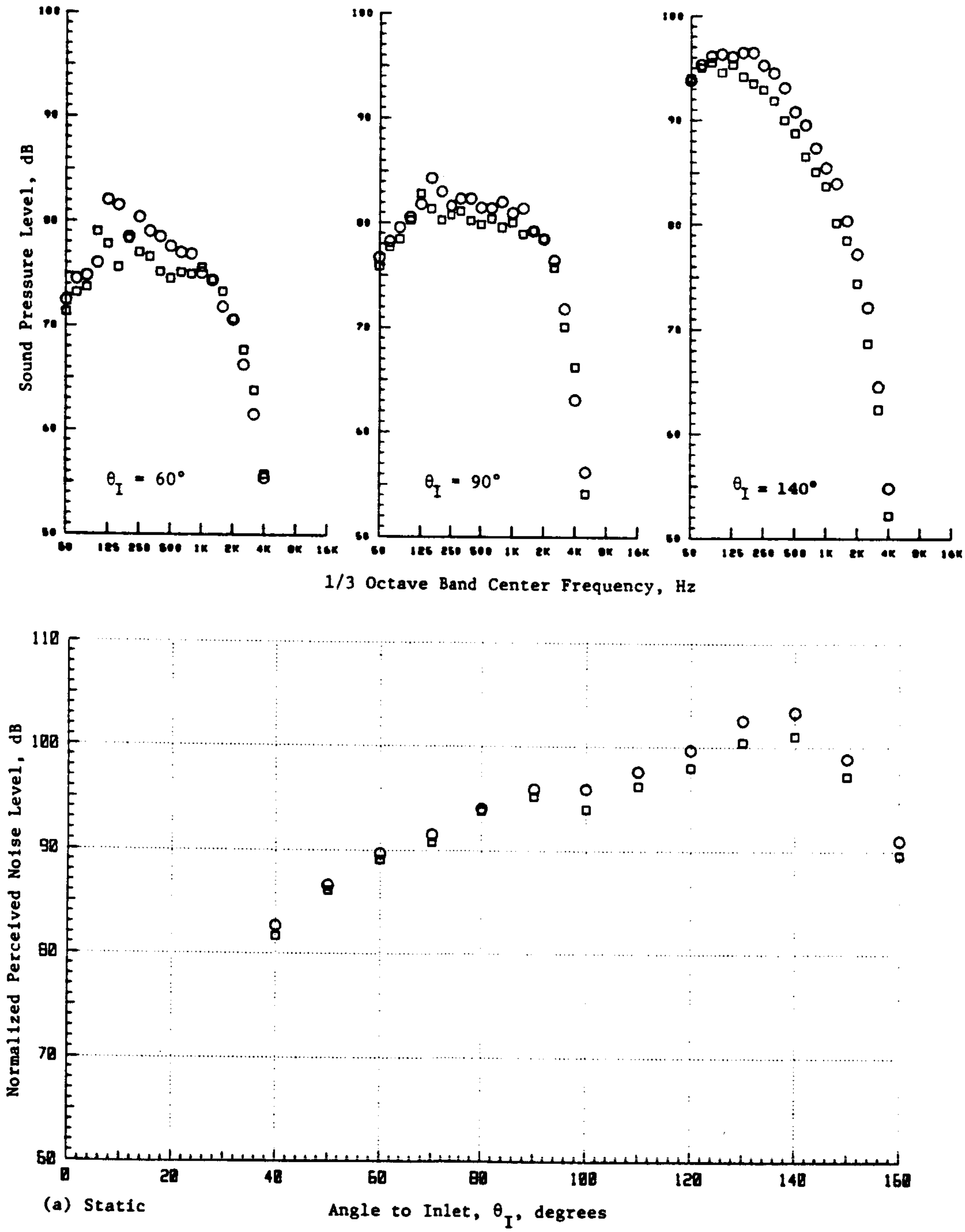

Figure 28. Comparison of Model 4 (R_r^o = 0.853) and Model 6 (R_r^o = 0.902) Frequency Spectrum and PNL Directivity at V_j^{mix} ≈ 2100 Ft/Sec, V_r ≈ 0.7, A_r = 0.53.

Symb	Model	Test Point	V_j^o, ft/sec	T_T^o, °R	P_r^o	V_j^i, ft/sec	T_T^i, °R	P_r^i	V_j^{mix}, ft/sec	T_T^{mix}, °R	P_r^{mix}	EPNL
○	4	410	2319	1734	2.80	1625	1257	1.95	2109	1590	2.50	99.8
□	6	3020	2322	1761	2.76	1622	1237	1.97	2105	1599	2.48	98.1

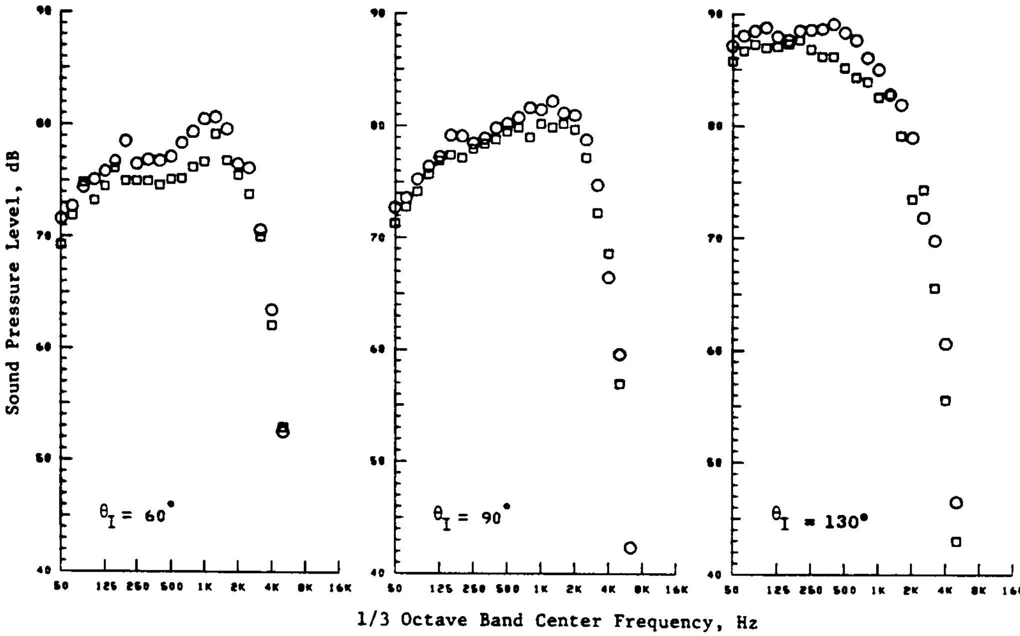

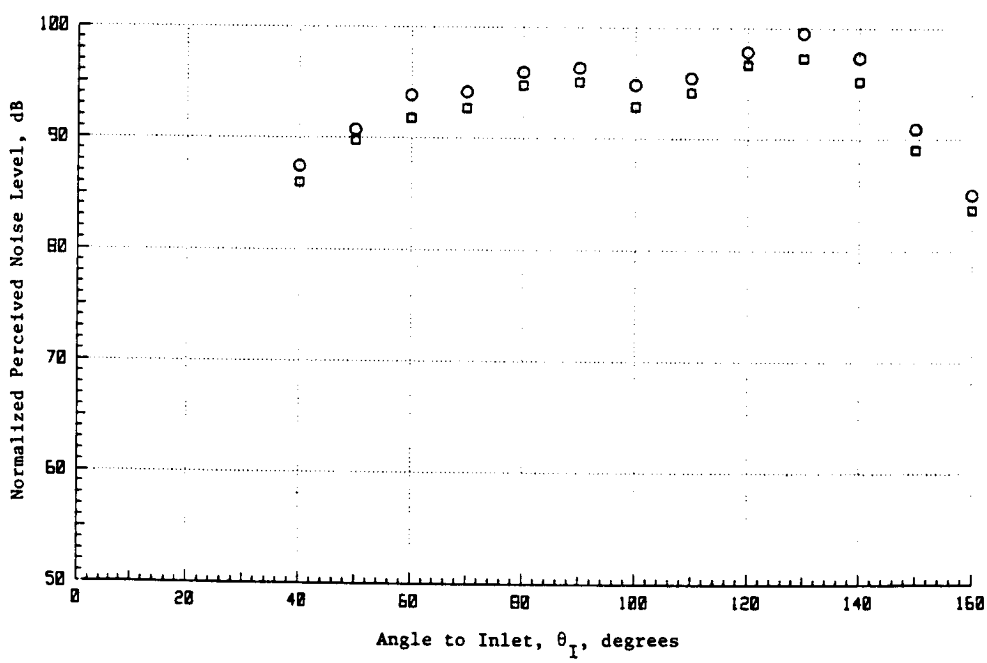

(b) Simulated Flight,
$V_{ac} \simeq 390$ ft/s

Figure 28. Comparison of Model 4 ($R_r^o = 0.853$) and Model 6 ($R_r^o = 0.902$) Frequency Spectrum and PNL Directivity at $V_j^{mix} \simeq 2100$ Ft/Sec, $V_r \simeq 0.7$, $A_r = 0.53$ (Concluded).

Symb	Model	Test Point	V_j^o ft/sec	T_T^o °R	P_r^o	V_j^i ft/sec	T_T^i °R	P_r^i	V_j^{mix} ft/sec	T_T^{mix} °R	P_r^{mix}
○	4	405	2298	1730	2.75	957	746	1.46	1960	1445	2.27
□	6	3012	2274	1694	2.75	935	747	1.43	1900	1430	2.27

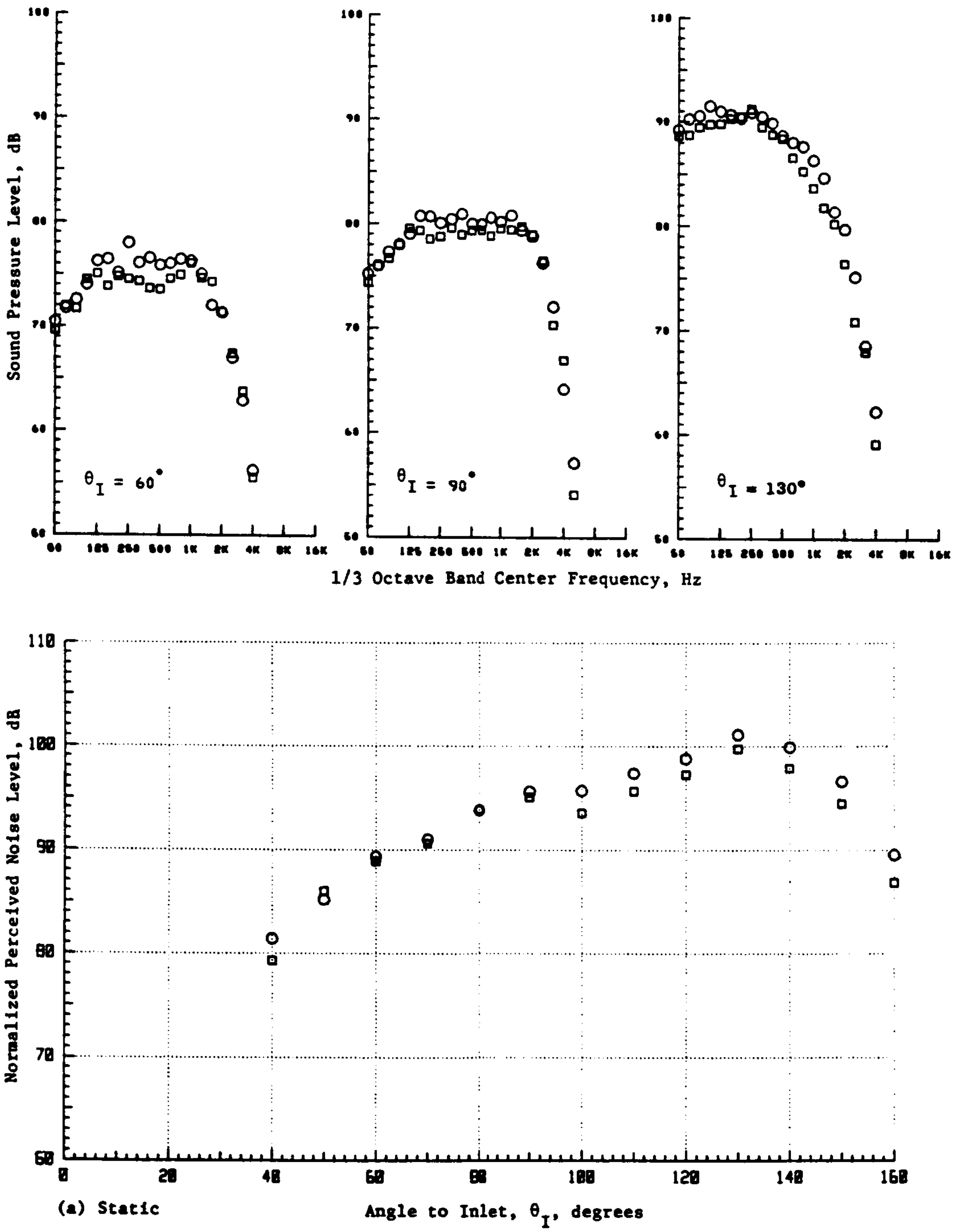

Figure 29. Comparison of Model 4 (R_r^o = 0.853) and Model 6 (R_r^o = 0.902) Frequency Spectrum and PNL Directivity at $V_j^{mix} \simeq$ 1900 Ft/Sec, $V_r \simeq 0.4$, $A_r = 0.53$.

Symb	Model	Test Point	V_j^o ft/sec	T_T^o °R	P_r^o	V_j^i ft/sec	T_T^i °R	P_r^i	V_j^{mix} ft/sec	T_T^{mix} °R	P_r^{mix}	EPNL
○	4	406	2297	1727	2.75	965	762	1.46	1916	1451	2.27	98.7
□	6	3014	2279	1697	2.76	943	726	1.46	1895	1418	2.28	97.1

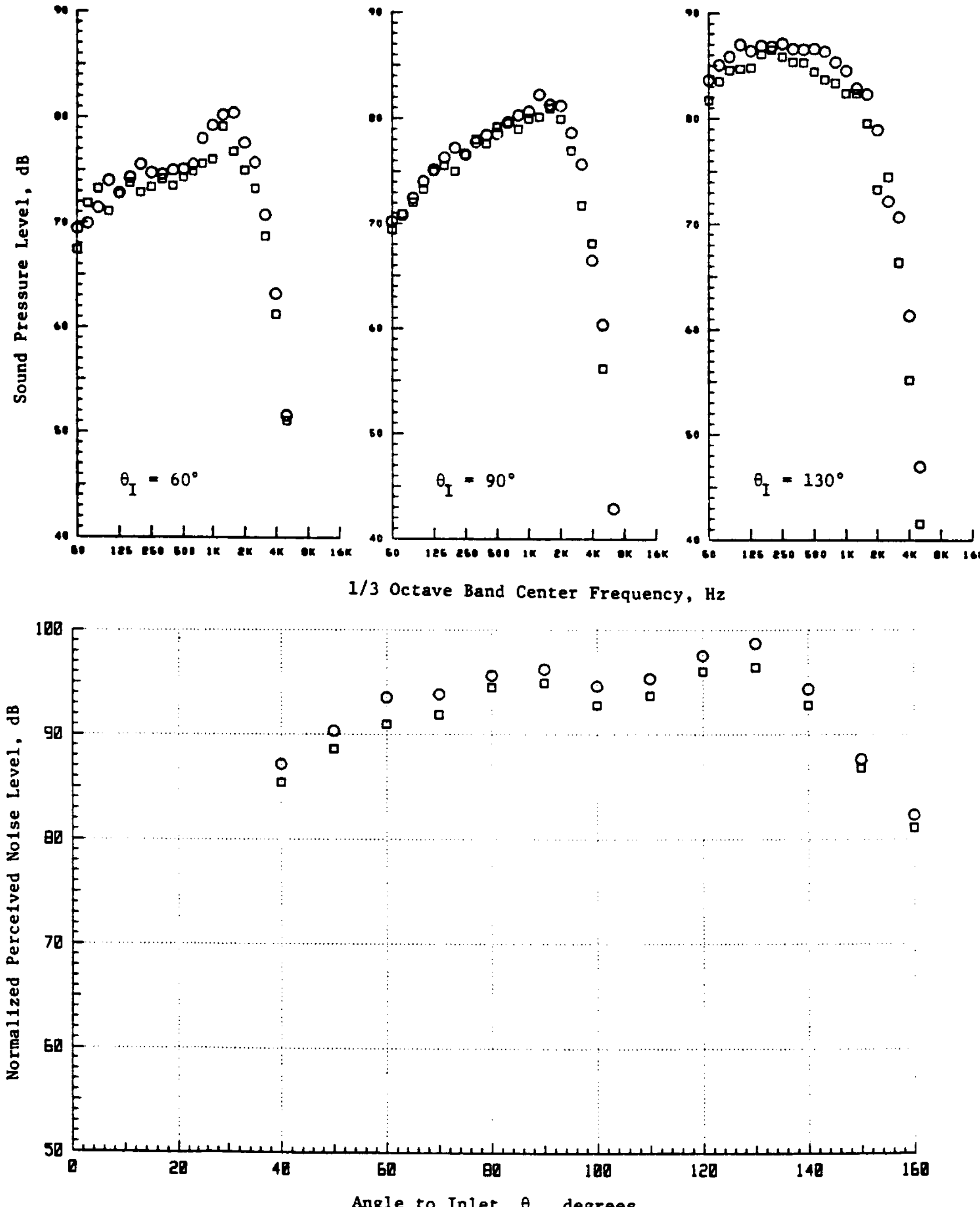

(b) Simulated Flight,
$V_{ac} \simeq 390$ ft/s

Figure 29. Comparison of Model 4 ($R_r^o = 0.853$) and Model 6 ($R_r^o = 0.902$) Frequency Spectrum and PNL Directivity at $V_j^{mix} \simeq 1900$ Ft/Sec, $V_r \simeq 0.4$, $A_r = 0.53$ (Concluded).

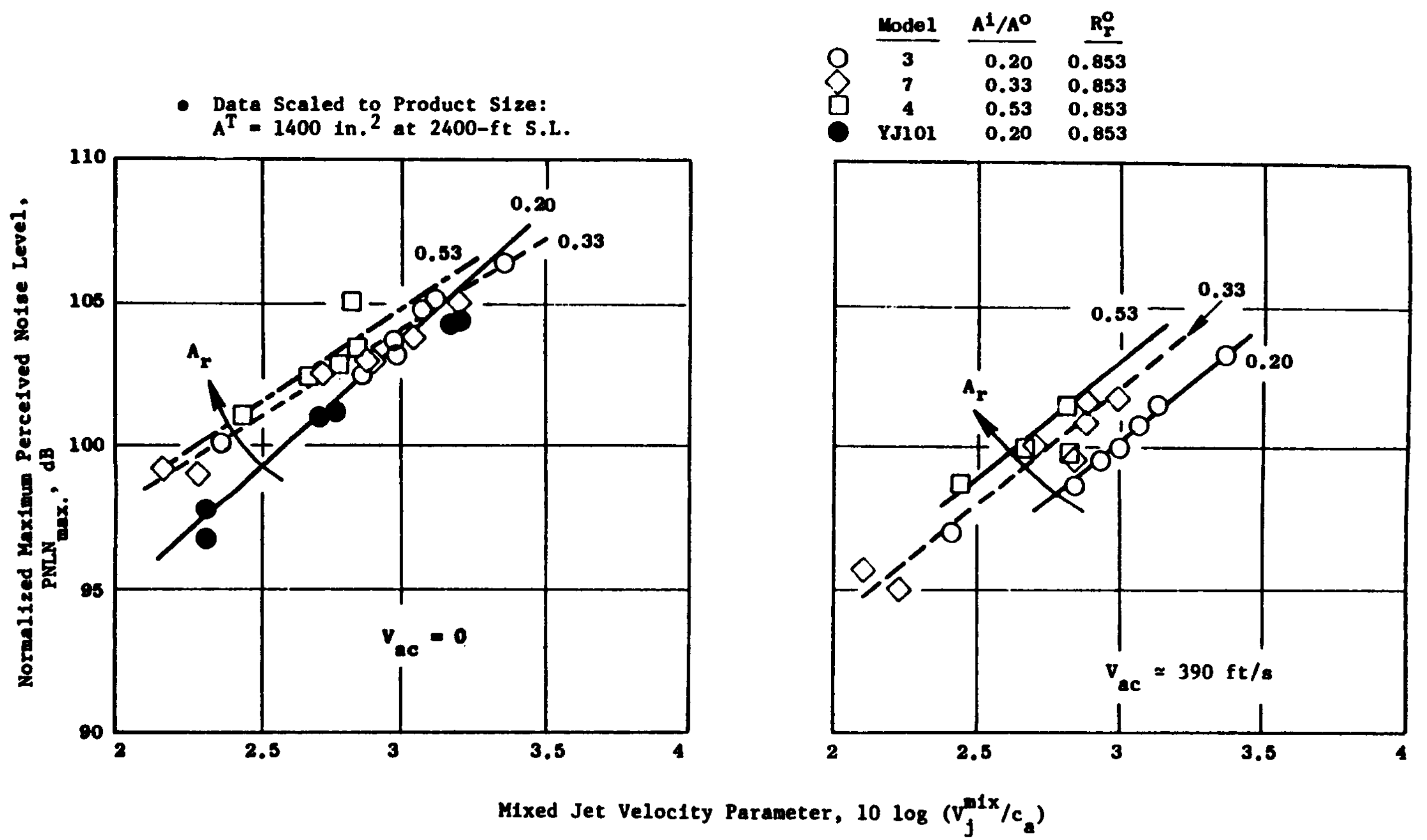

Figure 30. Effect of Area Ratio on PNL_{max} for a Given Radius Ratio.

Symb	Model	Test Point	V_j^o ft/sec	T_T^o °R	P_r^o	V_j^i ft/sec	T_T^i °R	P_r^i	V_j^{mix} ft/sec.	T_T^{mix} °R	P_r^{mix}	V_r
○	3	315	2286	1712	2.75	946	726	1.46	2110	1582	2.52	0.41
□	4	409	2318	1742	2.78	1626	1258	1.95	2107	1594	2.50	0.70
◇	7	7015	2290	1734	2.72	1396	1039	1.81	2094	1581	2.50	0.61

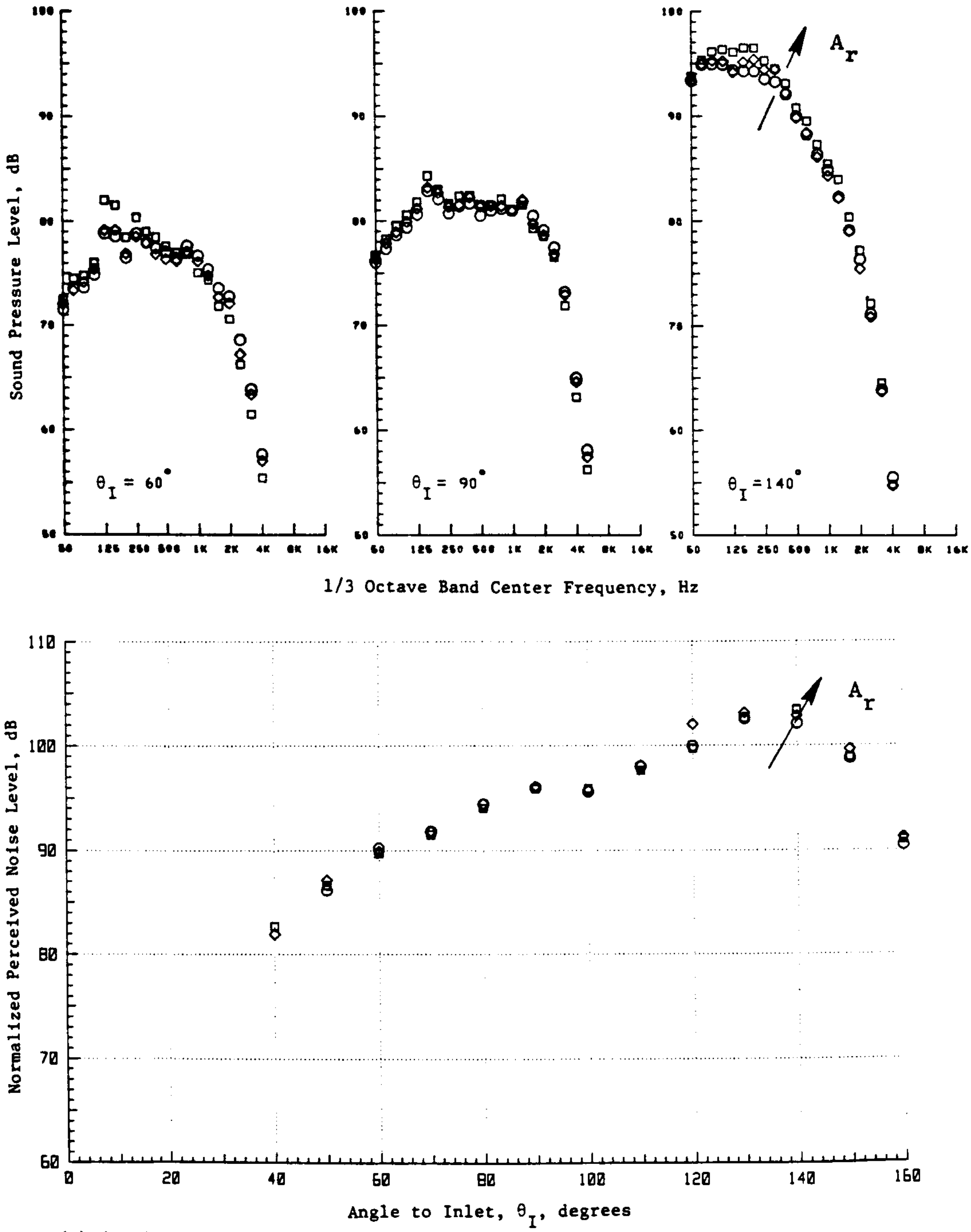

(a) Static

Figure 31. Effect of Area Ratio for a Given Radius Ratio (0.853) and Fixed Outer and Mixed Conditions.

Symb	Model	Test Point	V_j^o ft/sec	T_T^o °R	P_r^o	V_j^i ft/sec	T_T^i °R	P_r^i	V_j^{mix} ft/sec	T_T^{mix} °R	P_r^{mix}	V_r
○	3	316	2287	1726	2.75	962	767	1.45	2117	1603	2.50	0.42
□	4	410	2319	1734	2.80	1625	1257	1.95	2109	1590	2.50	0.70
◇	7	7017	2291	1724	2.74	1421	1063	1.82	2102	1581	2.50	0.62

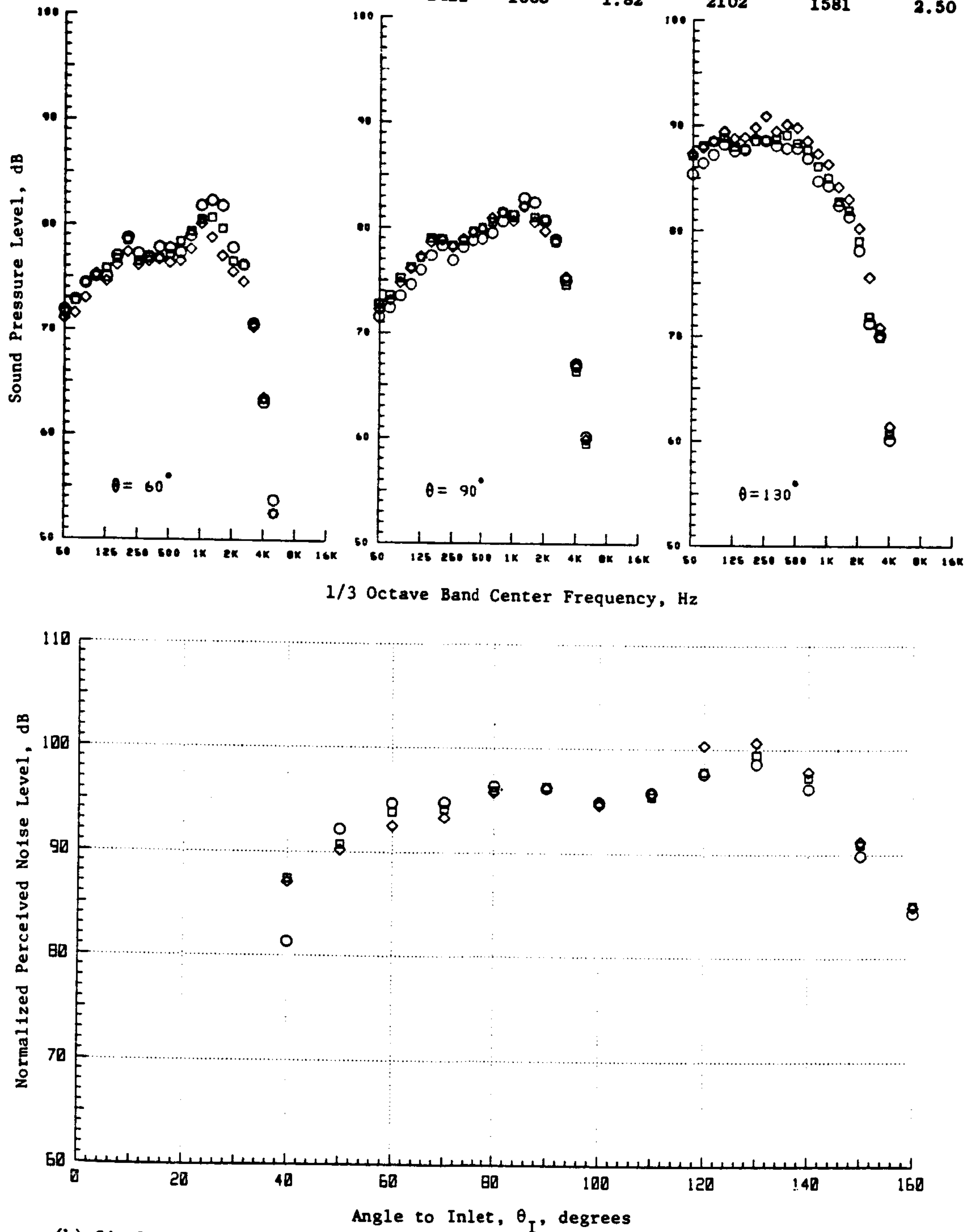

(b) Simulated Flight,
V_{ac} = 390 ft/s

Figure 31. Effect of Area Ratio for a Given Radius Ratio (0.853) and Fixed Outer and Mixed Conditions (Concluded).

Symb	Model	Test Point	V_j^o ft/sec	T_T^o °R	P_r^o	V_j^i ft/sec	T_T^i °R	P_r^i	V_j^{mix} ft/sec	T_T^{mix} °R	P_r^{mix}	V_r
○	3	315	2286	1712	2.75	946	726	1.46	2110	1582	2.52	0.41
□	4	405	2298	1730	2.75	957	746	1.46	1909	1445	2.27	0.42
◇	7	7012	2287	1721	2.73	936	711	1.46	2011	1514	2.39	0.41

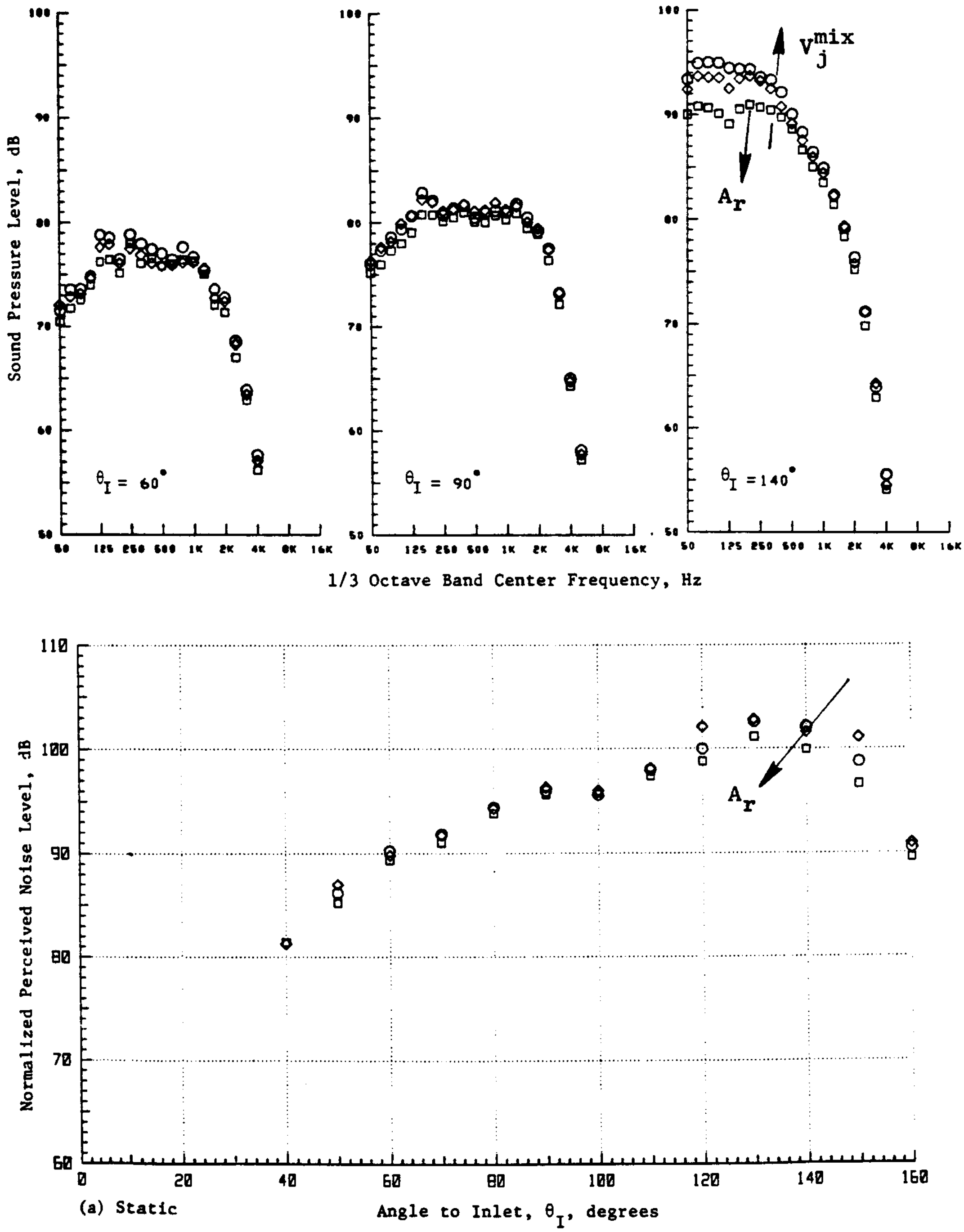

Figure 32. Effect of Area Ratio for a Given Radius Ratio (0.853) and Fixed Inner and Outer Conditions.

Symb	Model	Test Point	V_j^o, ft/sec	T_T^o, °R	P_r^o	V_j^i, ft/sec	T_T^i, °R	P_r^i	V_j^{mix}, ft/sec	T_T^{mix}, °R	P_r^{mix}	V_r
○	3	316	2287	1726	2.73	962	767	1.45	2117	1603	2.50	0.42
□	4	406	2297	1727	2.75	965	762	1.46	1916	1451	2.27	0.42
◇	7	7014	2263	1713	2.74	943	738	1.45	2017	1520	2.40	0.41

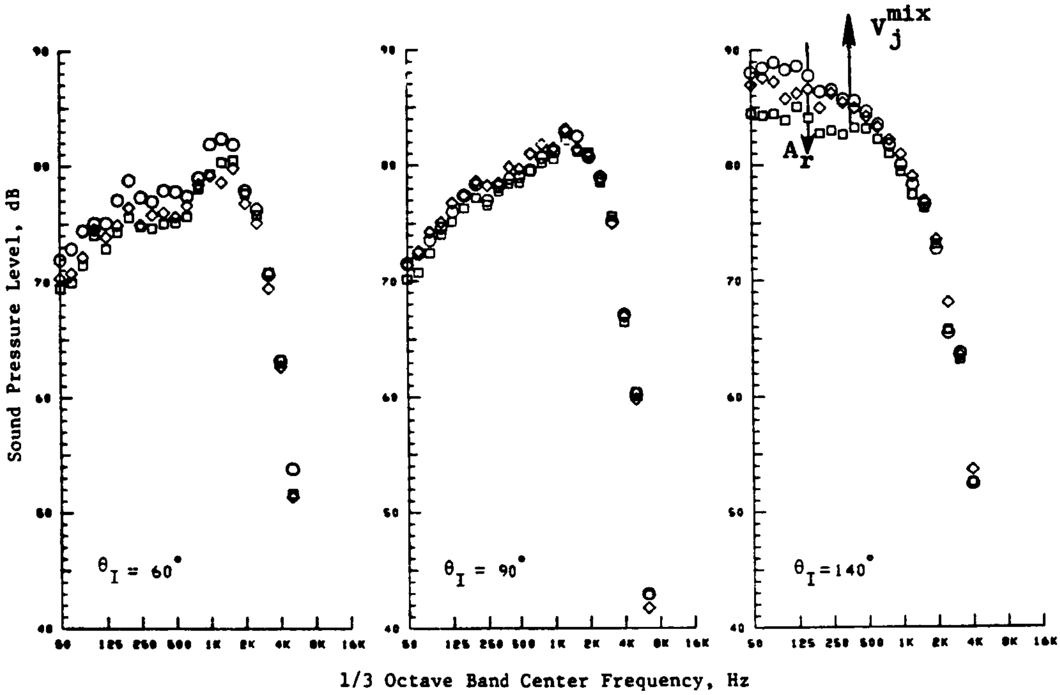

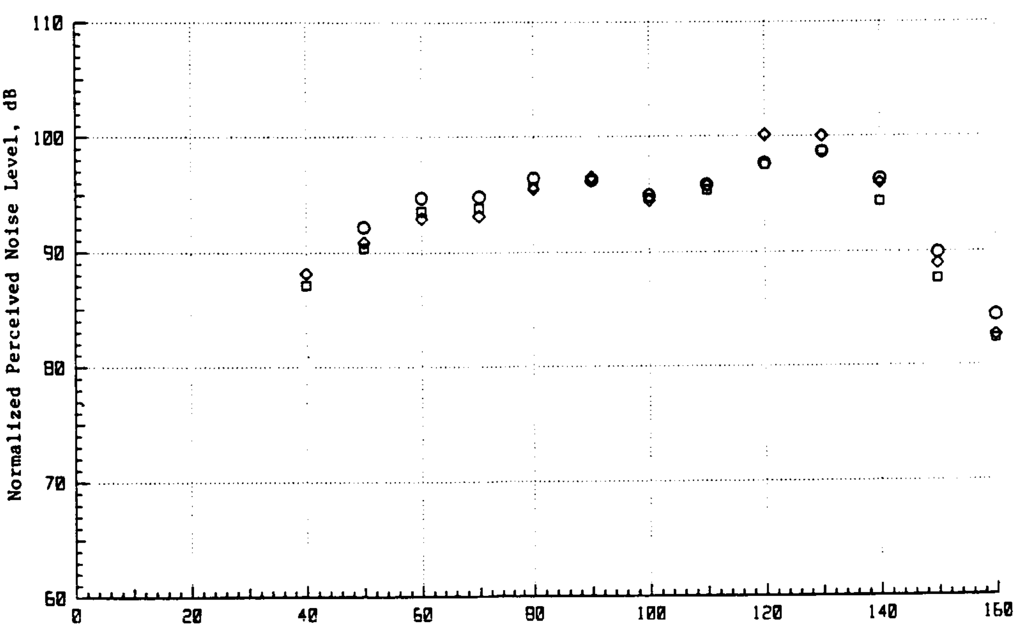

(b) Simulated Flight, $V_{ac} \approx 390$ ft/s

Figure 32. **Effect of Area Ratio for a Given Radius Ratio (0.853) and Fixed Inner and Outer Conditions (Concluded).**

5.1.3 Influence of Flow Variables on Static and Simulated Flight Acoustics of High-Radius-Ratio Coannular Plug Nozzles

Within this subsection, several aspects regarding the influence of the free stream and the various nozzle flow variables on the acoustics of a typical high-radius-ratio coannular plug nozzle are discussed. Discussion of the acoustic data measured with Model 7 ($R_r^o \approx 0.853$, $A_r \approx 0.2$) will cover (1) variation in free-stream velocity holding V_j^{mix} or V_j^o fixed, (2) static and free-jet measurements with variations in V_j^{mix} holding V_j^o, T_T^o and T_T^{mix} fixed, (3) static and free-jet measurements of variations with V_j^o holding V_j^{mix}, T_T^{mix}, T_j^o constant, (4) nozzle temperature effects, and (5) inner-to-outer velocity ratio effects.

5.1.3.1 Influence of Free-Jet Velocity for a Constant V_j^o, T_j^{mix}, and T_j^o

Free-Jet Velocity Influence on PNL_{max} and PNL_{60}

Several tests with variations in the specific thrust (V_j^{mix}) were run while holding the outer stream velocity (V_j^o), the outer stream static temperature (T_j^o), and the mixed stream static temperature (T_j^{mix}) nearly constant. These correspond to Test Points 7101 through 7114 having the test conditions defined in Section 4.2.1. Figures 33 and 34 illustrate the static and simulated flight acoustic test results, respectively, at θ_I that corresponds to the maximum noise angle in the aft quadrant and at $\theta_I = 60°$ for the following range of test conditions: V_j^{mix} ranges from 1500 to 2400 ft/sec; $V_j^o \approx 1700$, 2100, and 2500 ft/sec; $T_j^o \approx 1200°$ R, $T_j^{mix} \approx 1100°$ R.

Figure 33 illustrates the influence of flight on the normalized PNL_{max} plotted against $10 \log_{10} (V_j^{mix}/C_a)$. All test results are scaled to a typical product engine size. The basic trend of the data is that flight decreases the peak angle noise at all the tested conditions. At the lower V_j^{mix} conditions, the influence of flight on peak angle noise reduction is observed to be larger than at the higher V_j^{mix} conditions.

In the forward quadrant where shock noise exists, the influence of flight is to enhance the noise. These results are shown in Figure 34. The range of mixed pressure ratios is $P_r^{mix} \approx 1.9$ to 3.5. Roughly, a 3- to 4.5-PNdB forward quadrant lift is observed over the range of test conditions. It is likely that these measurements are influenced by jet mixing noise. However, there should not be any influence of temperature since the static temperatures for all the tests were approximately constant. Later in Section 5.1.4, some of these issues concerning the shock noise will be discussed.

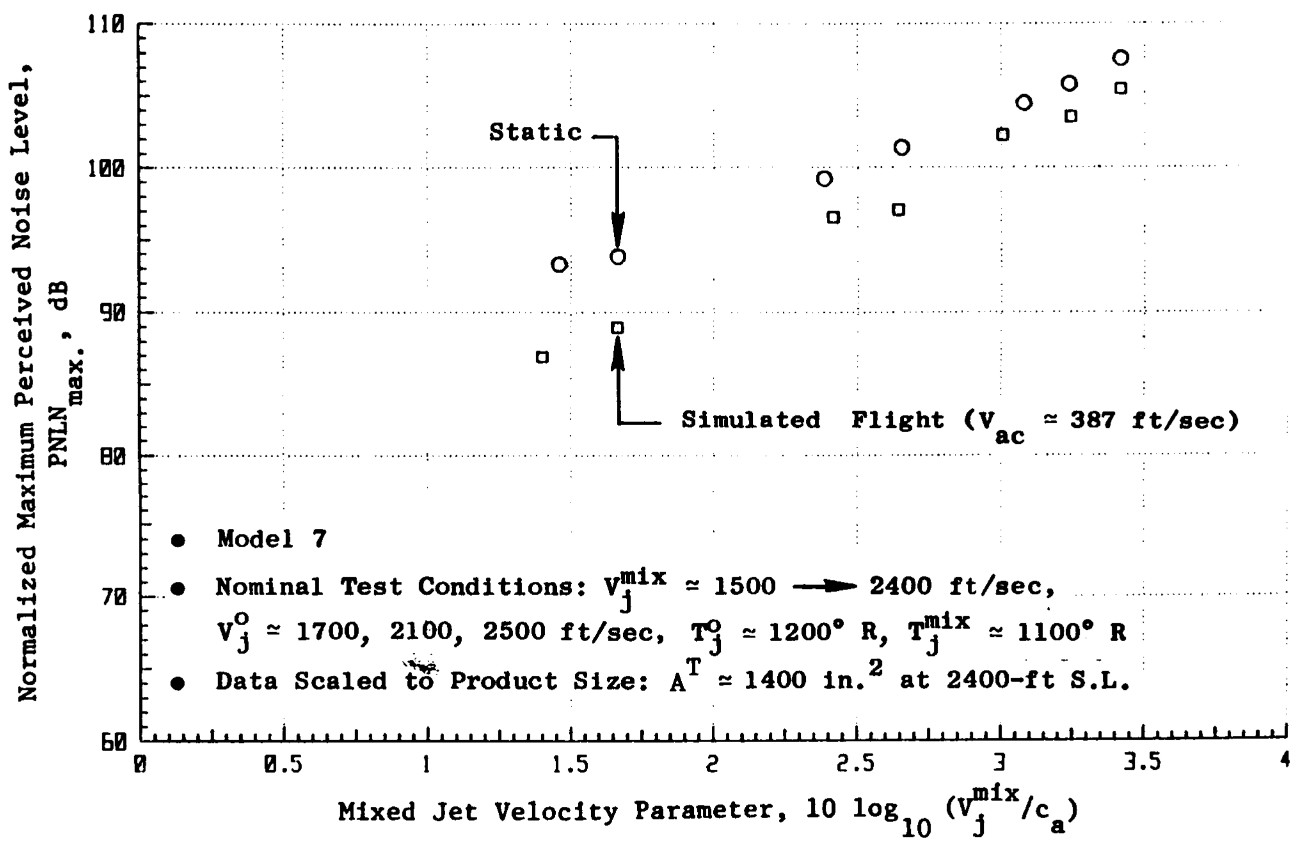

Figure 33. Influence of Free-Jet Velocity on Normalized PNL_{max}.

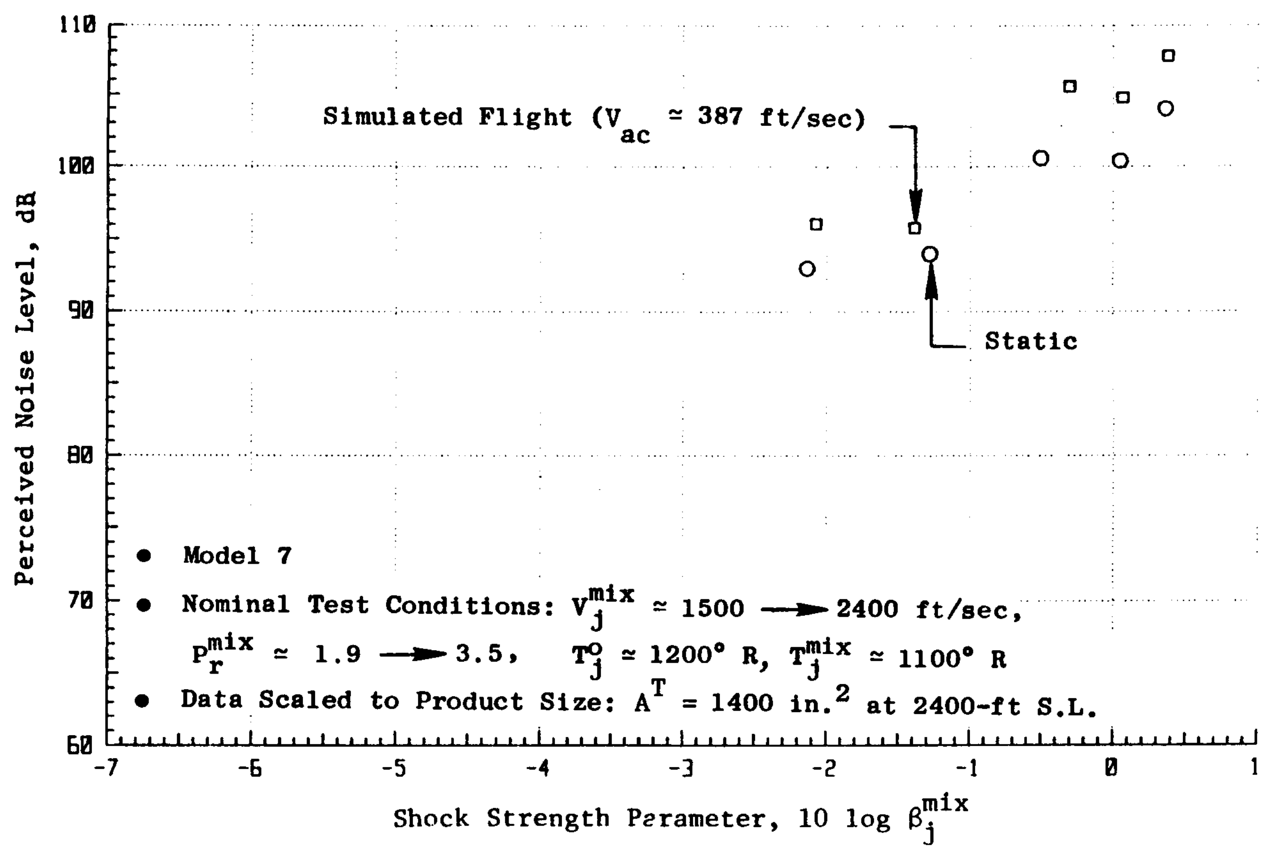

Figure 34. **Influence of Free-Jet Velocity on PNL_{60}.**

Free-Jet Velocity Influence on Directivity and Spectra

For the full range of test conditions, the static and simulated flight acoustic PNL directivity, SPL spectra at $\theta_I = 60°$, $90°$, and the maximum noise angle are shown in Figures 35 through 38. Figures 35 and 36 show the static and simulated flight PNL directivities, and Figures 37 and 38 show the corresponding SPL spectra. In general, the results show coannular plug nozzle trends described earlier in this section. But, it is worth noting the strong influence of flight on shock noise. The results indicate that in-flight shock noise may be influencing the coannular plug nozzle acoustic spectra up to $\theta_I \approx 110°$. This observation is viewed more clearly when comparing the static and simulated flight data on one graph. Figures 39 and 40 compare static and simulated flight results when $V_j^{mix} \approx 2000$ ft/sec and $P_r^{mix} \approx 2.56$; Figures 41 and 42 compare static and simulated flight results when $V_j^{mix} \approx 2400$ ft/sec and $P_r^{mix} \approx 3.5$.

As an example of subcritical flow conditions, Figures 43 and 44 are shown ($V_j^{mix} \approx 1500$ ft/sec, $P_r^{mix} \approx 1.75$). As a rule, the subcritical tests show a greater range of beneficial flight effects on aft angle directivity and spectra as compared with the supercritical tests shown in Figures 39 to 42. The flight benefit extends beyond $\theta_I = 70°$ on a directivity basis. The simulated flight spectra shown at $\theta_I = 90°$ and the maximum jet noise angle show reduction at nearly all frequencies.

5.1.3.2 Influence of Free-Jet Velocity for a Constant V_j^{mix}, T_j^o, and T_j^{mix}

General Results

A series of test points was run where the specific thrust V_j^{mix}, mixed static temperature T_j^{mix}, and the outer stream temperature T_j^o were held approximately constant ($V_j^{mix} \approx 2250$ ft/sec, $T_j^{mix} \approx 1250°$ R, $T_j^o \approx 1275°$ R) while the outer/inner stream flows were appropriately varied, as well as the free-stream velocity. Figures 45 and 46 show typical static test results, and Figures 47 and 48 show typical simulated flight results at $V_{ac} \approx 387$ ft/sec.

The results of Figures 45 and 46 show that, although the outer stream velocity ranged from approximately 2300 to 2500 ft/sec (with V_j^{mix} fixed), the jet mixing noise in terms of coannular plug nozzle PNL levels are relatively the same. On a spectral basis, Figure 46 shows that at $\theta_I \approx 60°$ and $90°$ the shock noise spectral signature differs with the various combinations of P_r^o and P_r^i, even though P_r^{mix} (or 10 logβ^{mix}) is maintained, approximately constant. In simulated flight (Figures 47 and 48), the trends noted above statically are observed also. However, for the test point with the highest outer stream pressure ratio ($P_r^o \approx 3.3$), greater shock noise amplification is observed. It is also worth mentioning here that for $\theta_I > \approx 120°$ the static

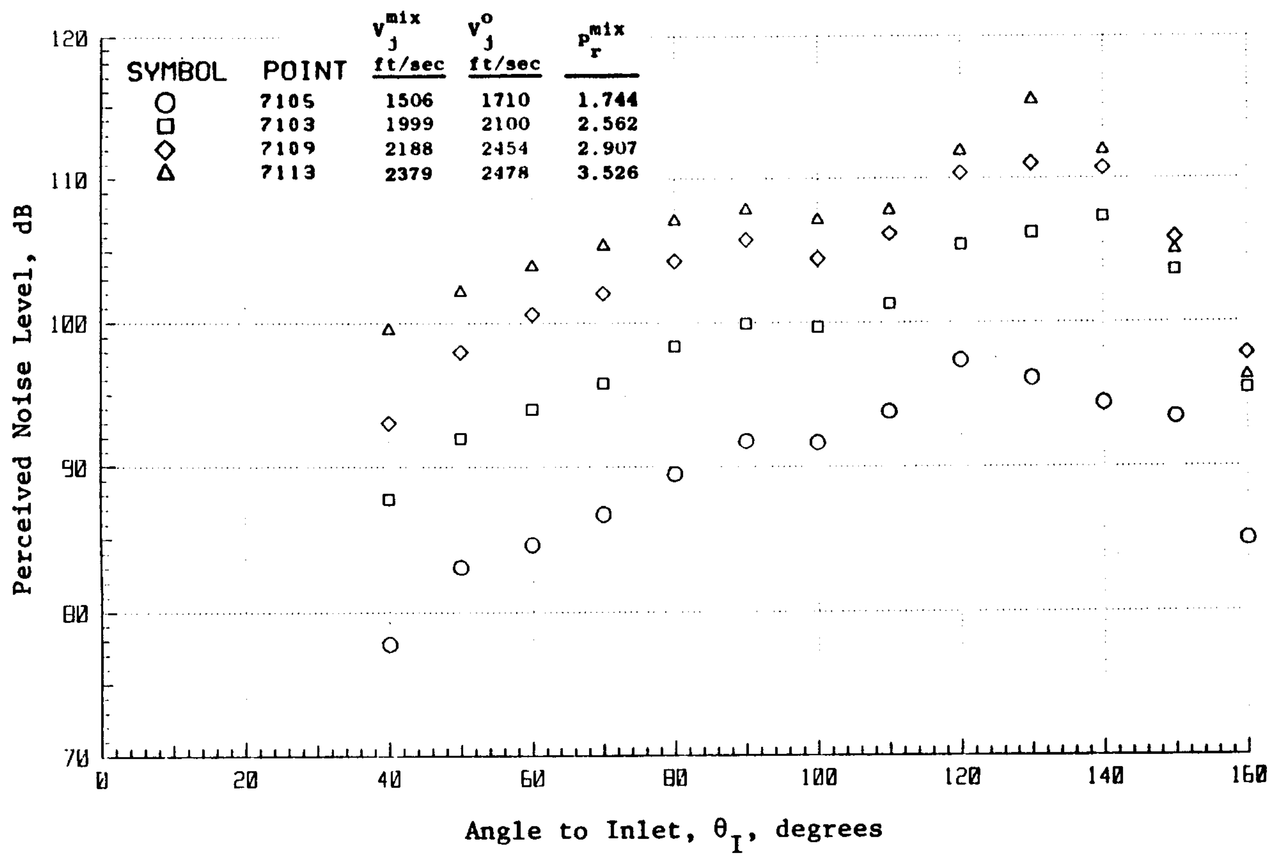

Figure 35. Comparison of Static PNL Directivities at $V_j^{mix} \approx 1500, 2000,$ 2200, and 2400 Ft/Sec.

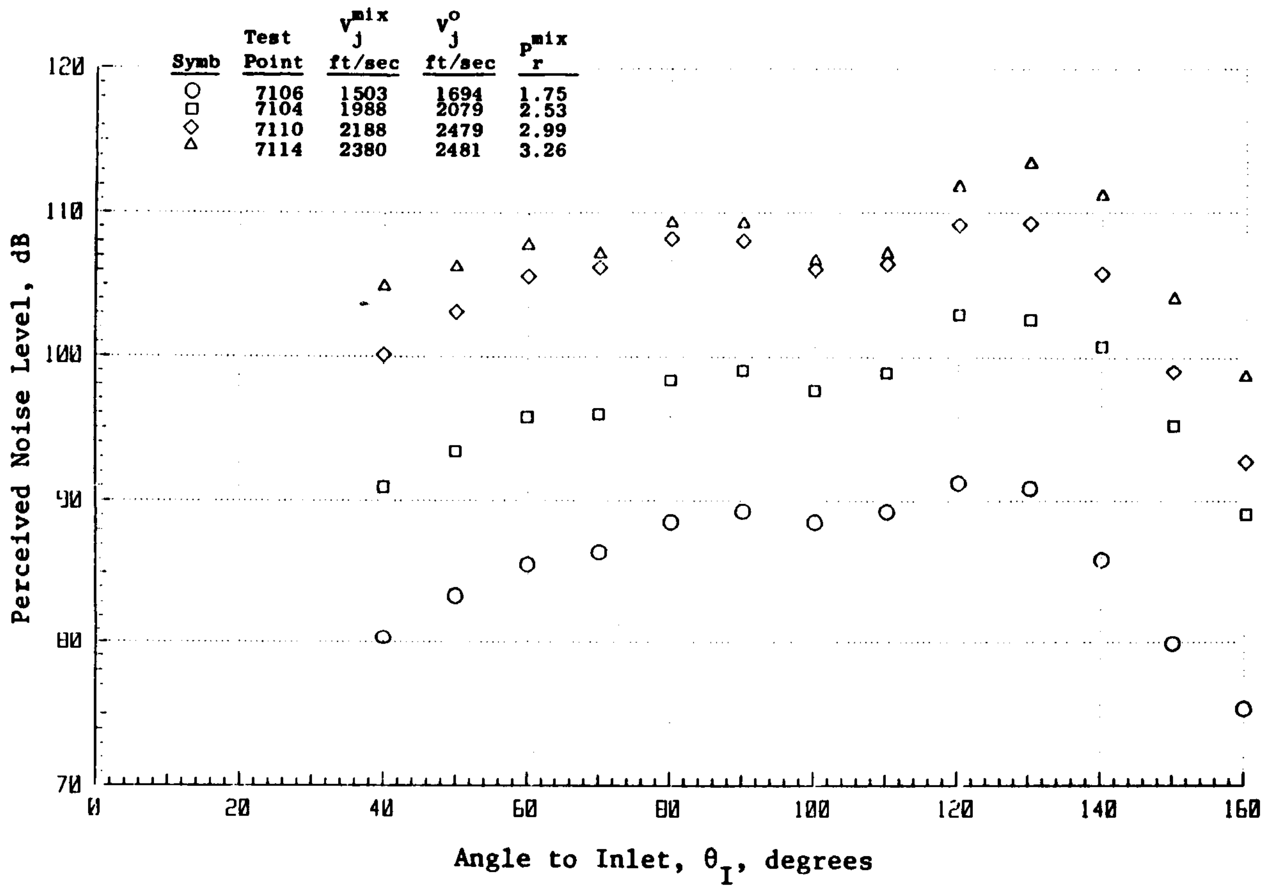

Figure 36. Comparison of Simulated Flight PNL Directivities at $V_j^{mix} \approx 1500$, 2000, 2200, and 2400 Ft/Sec.

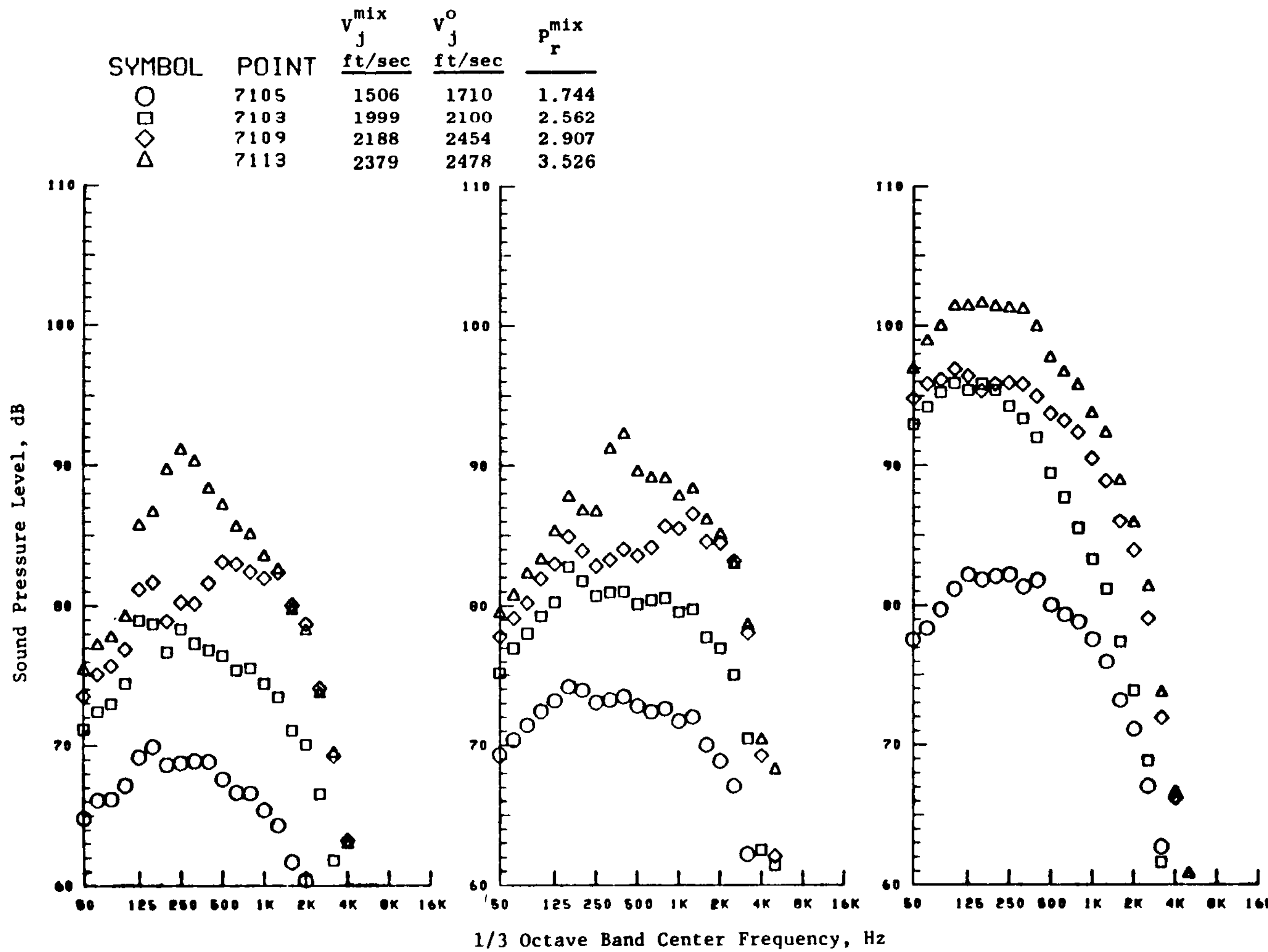

(a) Directivity Angle, $\theta_I = 60°$

(b) Directivity Angle, $\theta_I = 90°$

(c) Peak Noise Angle

Figure 37. Comparison of Static SPL Spectra at $V_j^{mix} \simeq 1500$, 2000, 2200, and 2400 Ft/Sec.

Symb	Test Point	V_j^{mix} ft/sec	V_j^o ft/sec	P_r^{mix}
○	7106	1503	1694	1.75
□	7104	1988	2079	2.53
◇	7110	2188	2479	2.99
△	7114	2380	2481	3.26

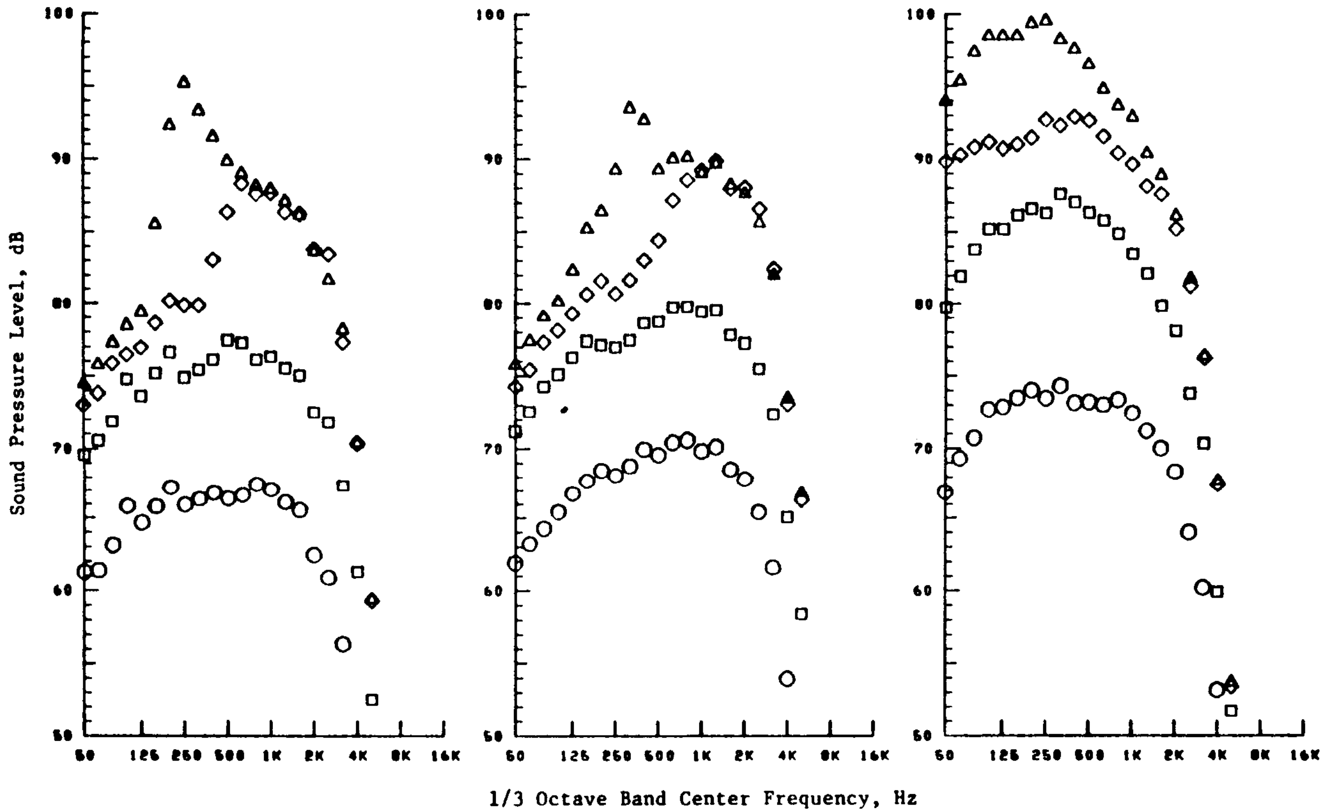

(a) Directivity Angle, $\theta_I = 60°$

(b) Directivity Angle, $\theta_I = 90°$

(c) Peak Noise Angle

Figure 38. Comparison of Simulated Flight SPL Spectra at $V_j^{mix} \simeq 1500$, 2000, 2200, and 2400 Ft/Sec.

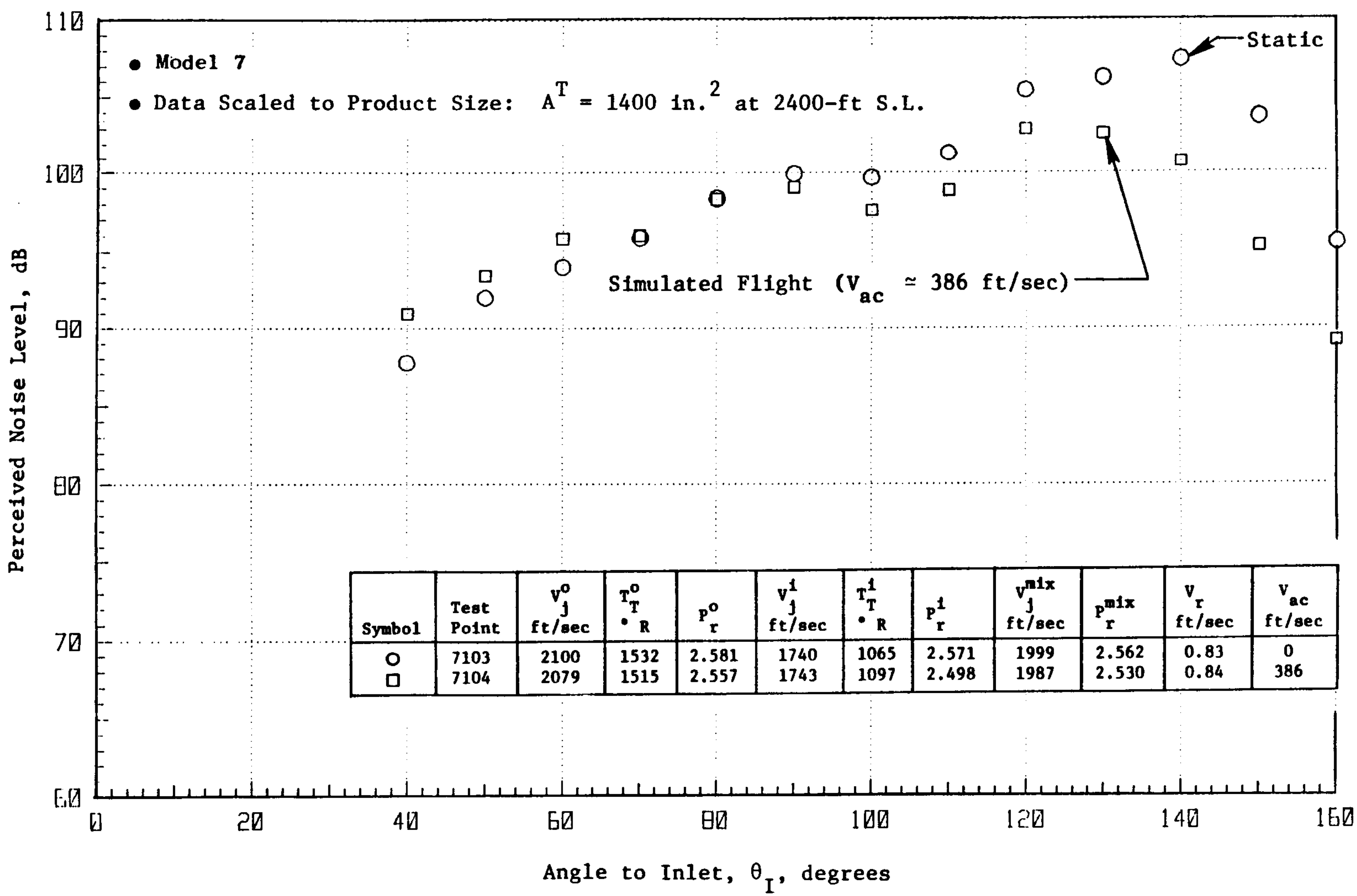

Symbol	Test Point	V_j^o ft/sec	T_T^o °R	P_r^o	V_j^i ft/sec	T_T^i °R	P_r^i	V_j^{mix} ft/sec	P_r^{mix}	V_r ft/sec	V_{ac} ft/sec
○	7103	2100	1532	2.581	1740	1065	2.571	1999	2.562	0.83	0
□	7104	2079	1515	2.557	1743	1097	2.498	1987	2.530	0.84	386

Figure 39. Comparison of Static and Simulated Flight PNL Directivity at V_j^{mix} ≃ 2000 Ft/Sec, P_r^{mix} ≃ 2.56.

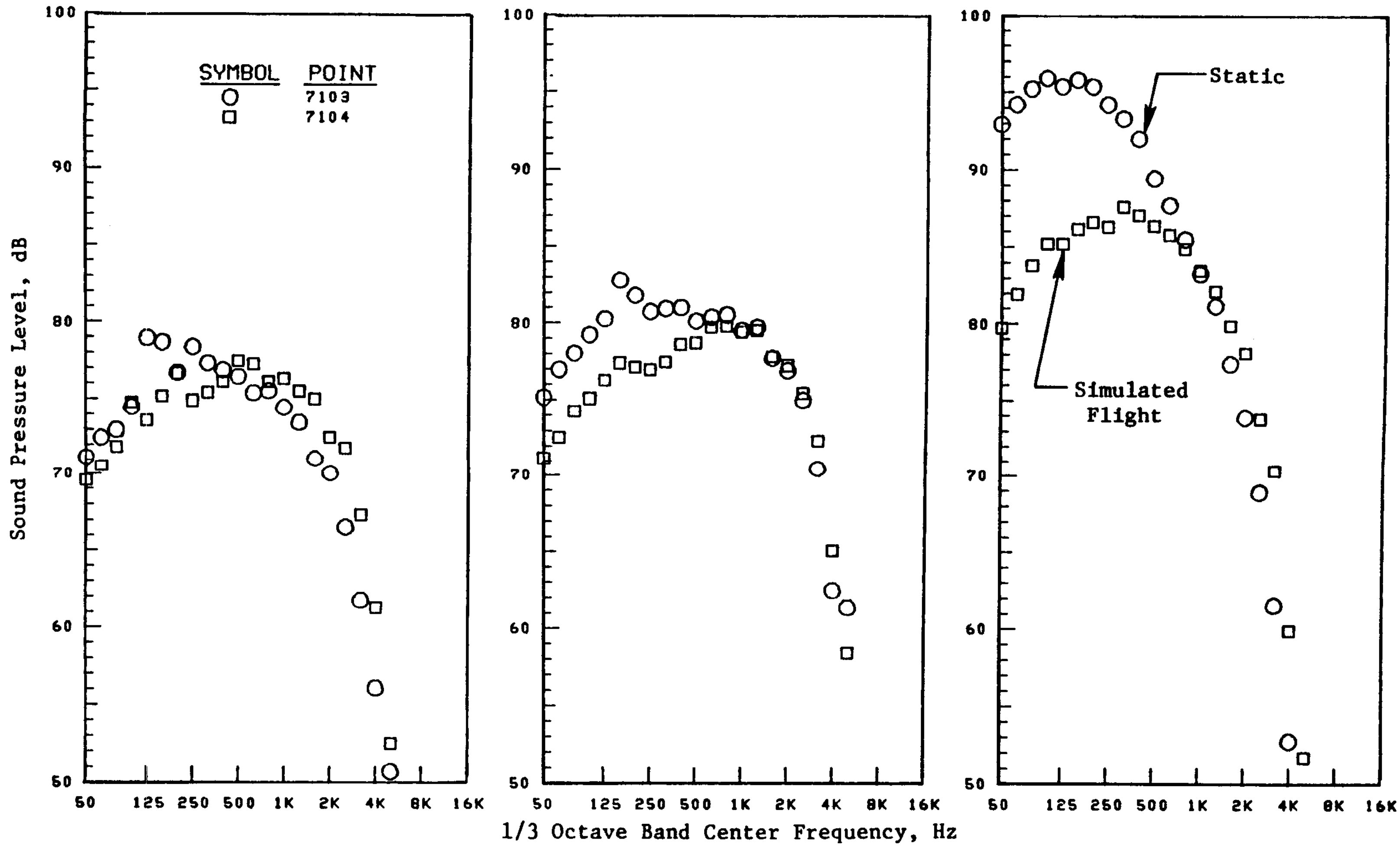

(a) Directivity Angle, $\theta_I = 60°$ (b) Directivity Angle, $\theta_I = 90°$ (c) Peak Noise Angle

Figure 40. Comparison of Static and Simulated Flight SPL Spectra at $V_j^{mix} \simeq$ 2000 Ft/Sec, $P_r^{mix} \simeq$ 2.56.

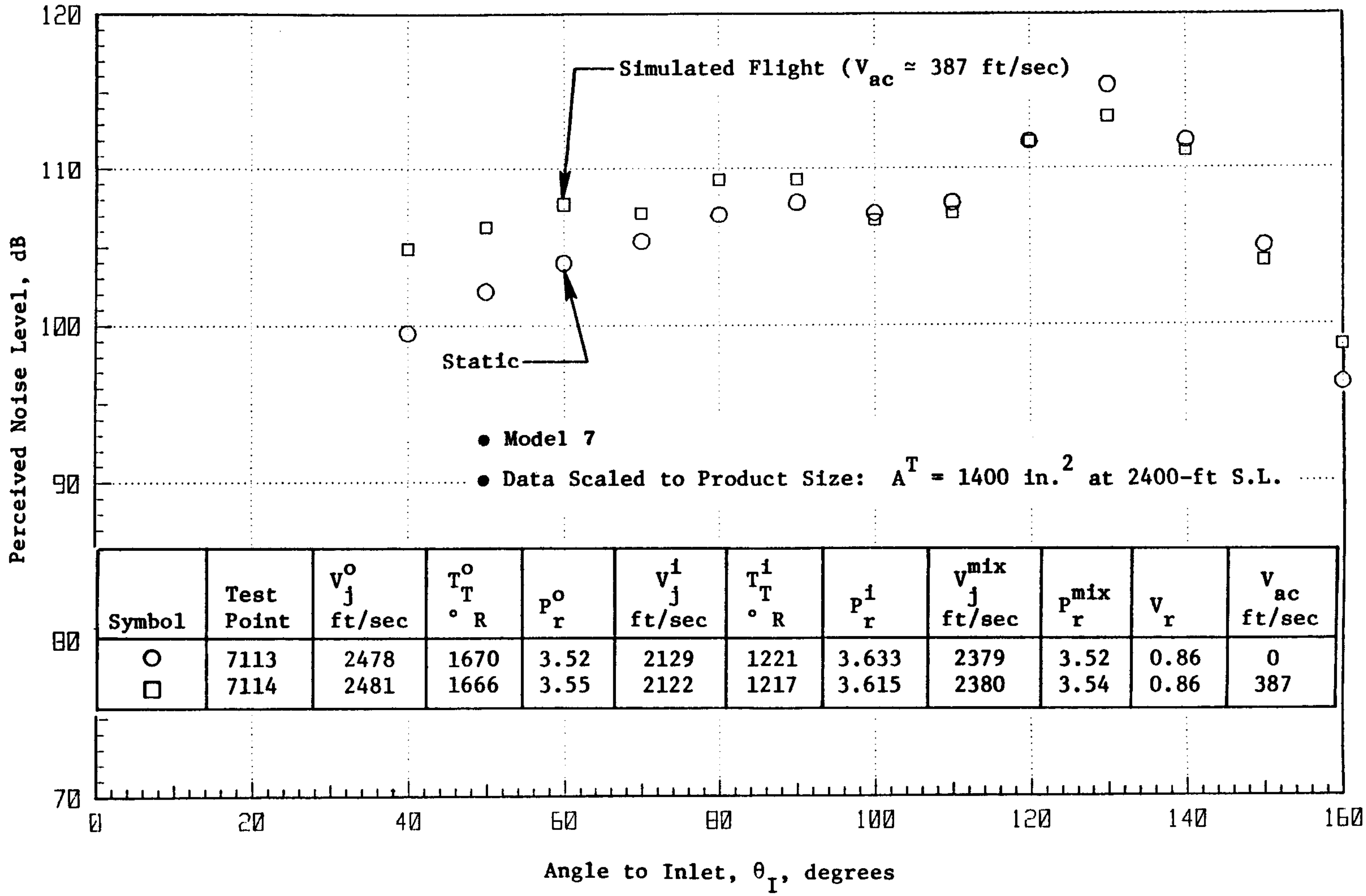

Symbol	Test Point	V_j^o ft/sec	T_T^o °R	P_r^o	V_j^i ft/sec	T_T^i °R	P_r^i	V_j^{mix} ft/sec	P_r^{mix}	V_r	V_{ac} ft/sec
○	7113	2478	1670	3.52	2129	1221	3.633	2379	3.52	0.86	0
□	7114	2481	1666	3.55	2122	1217	3.615	2380	3.54	0.86	387

Figure 41. Comparison of Static and Simulated Flight PNL Directivity at $V_j^{mix} \approx 2400$ Ft/Sec, $P_r^{mix} \approx 3.5$.

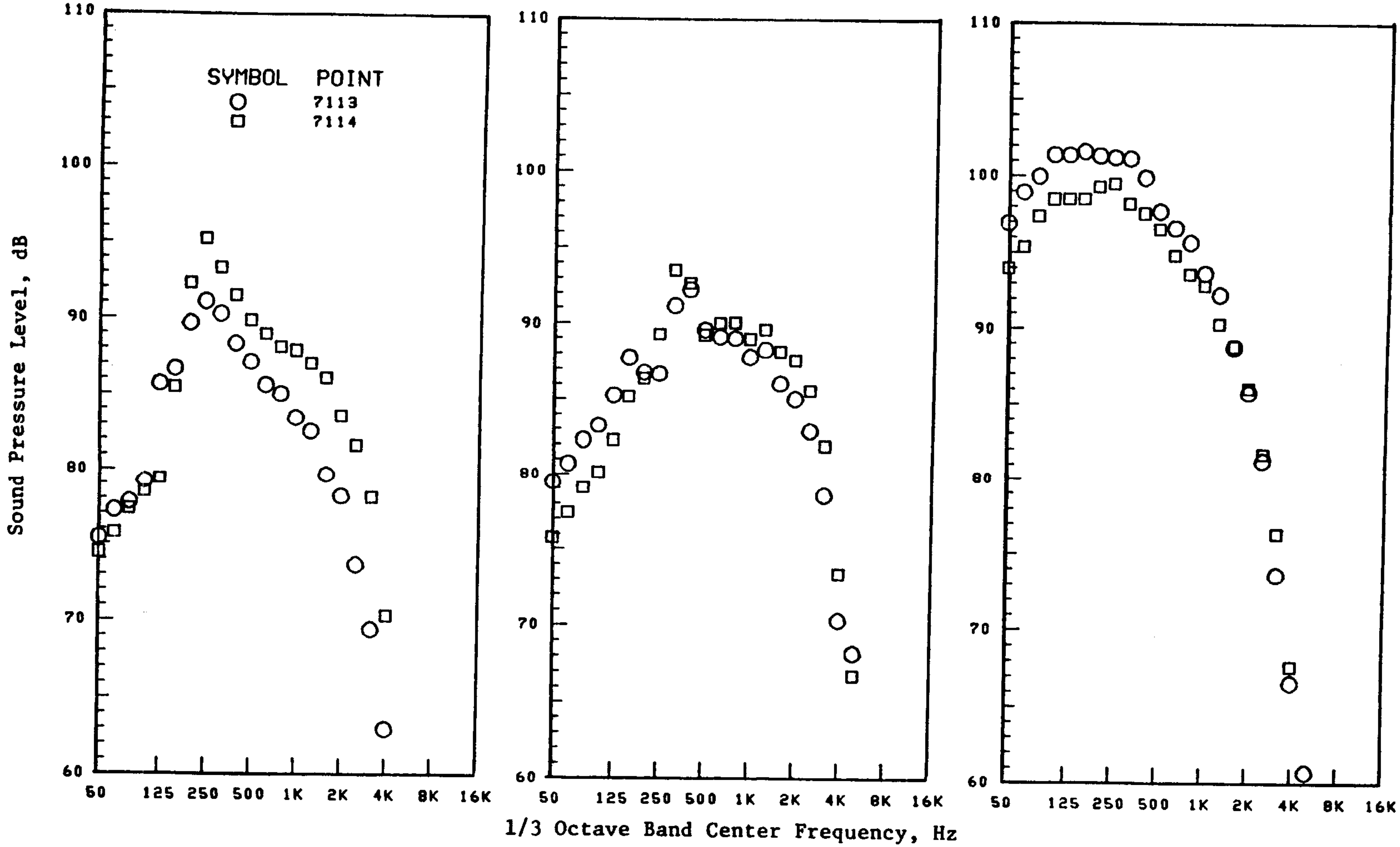

(a) Directivity Angle, $\theta_I = 60°$

(b) Directivity Angle, $\theta_I = 90°$

(c) Peak Noise Angle

Figure 42. Comparison of Static and Simulated Flight SPL Spectra at $V_j^{mix} \simeq 2400$ Ft/Sec, $P_r^{mix} \simeq 3.5$.

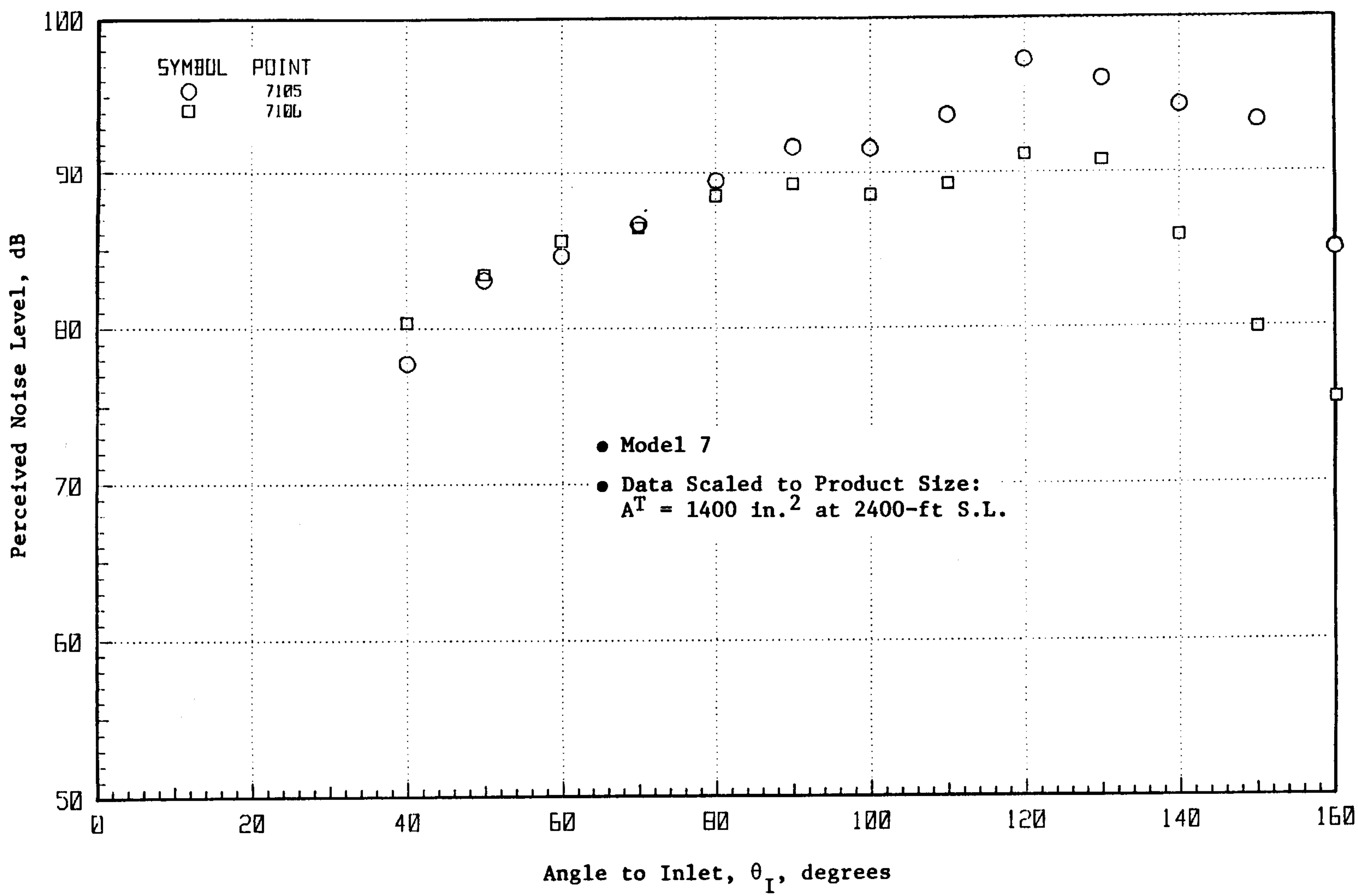

Figure 43. Comparison of Static and Simulated Flight PNL Directivity at $V_j^{mix} \simeq 1500$ Ft/Sec, $P_r^{mix} \simeq 1.75$.

Symb	Test Point	V_j^o ft/sec	T_T^o °R	P_r^o	V_j^i ft/sec	T_T^i °R	P_r^i	V_j^{mix} ft/sec	P_r^{mix}	V_r	V_{ac} ft/sec
○	7105	1710	1428	1.914	643	654	1.20	1506	1.74	0.38	0
□	7106	1694	1404	1.912	680	696	1.22	1502	1.75	0.40	386

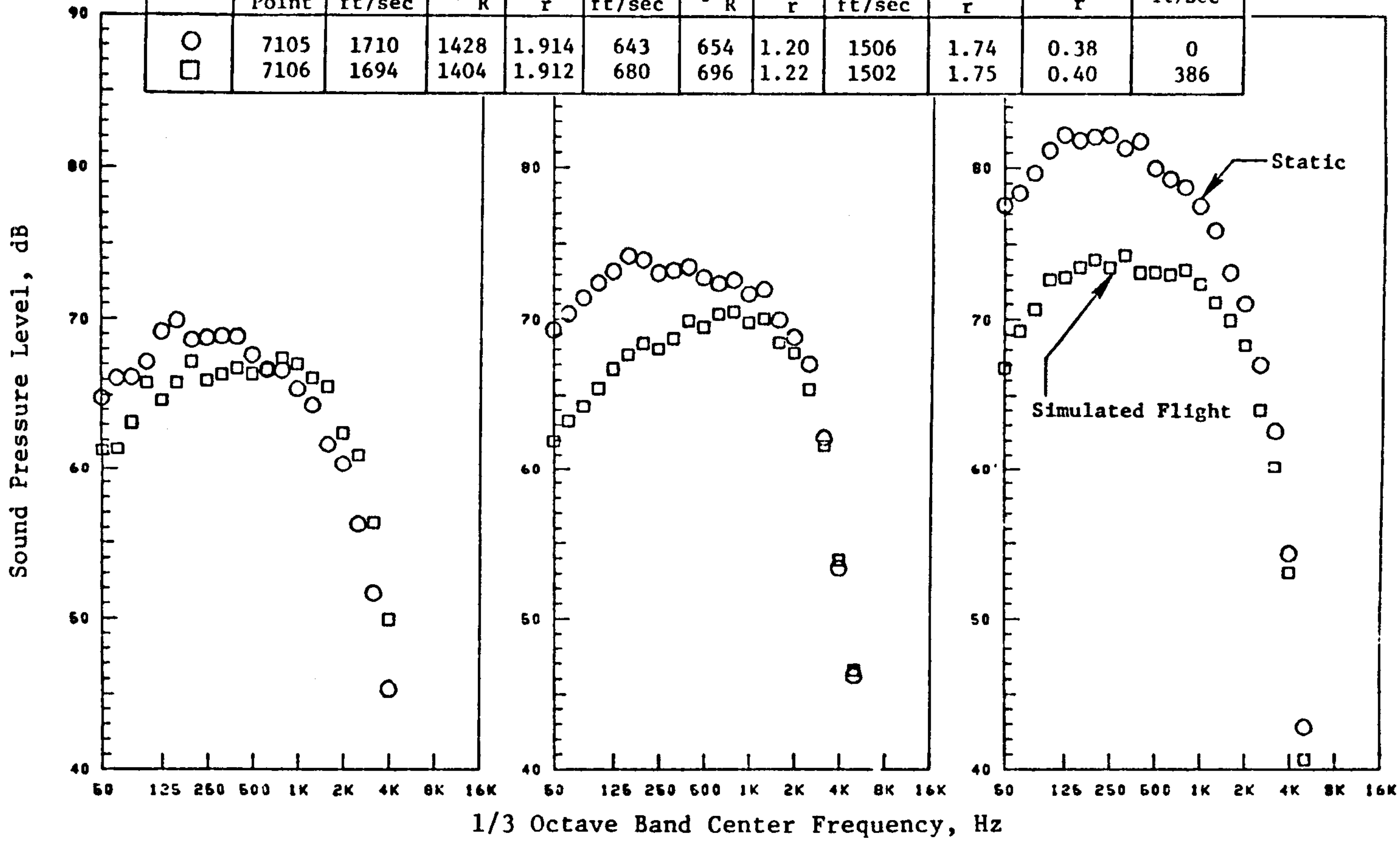

(a) Directivity Angle, $\theta_I = 60°$

(b) Directivity Angle, $\theta_I = 90°$

(c) Peak Noise Angle

Figure 44. Comparison of Static and Simulated Flight SPL Spectra at $V_j^{mix} \simeq 1500$ Ft/Sec, $P_r^{mix} \simeq 1.75$.

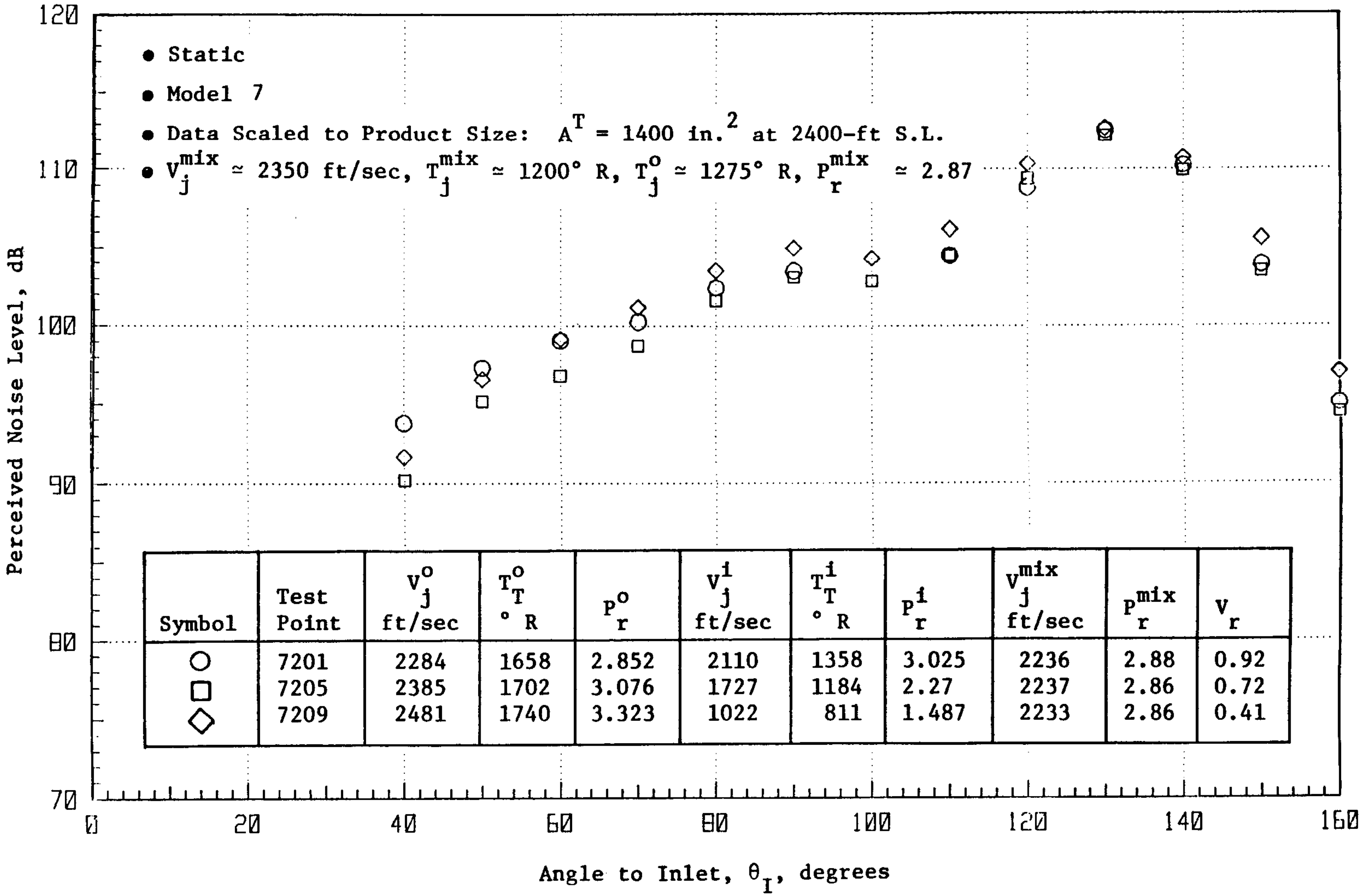

Symbol	Test Point	V_j^o ft/sec	T_T^o ° R	P_r^o	V_j^i ft/sec	T_T^i ° R	P_r^i	V_j^{mix} ft/sec	P_r^{mix}	V_r
○	7201	2284	1658	2.852	2110	1358	3.025	2236	2.88	0.92
□	7205	2385	1702	3.076	1727	1184	2.27	2237	2.86	0.72
◇	7209	2481	1740	3.323	1022	811	1.487	2233	2.86	0.41

Figure 45. Static PNL Directivity for $V_j^o \simeq$ 2300, 2400, and 2500 Ft/Sec Holding V_j^{mix}, T_j^{mix}, T_j^o, and P_r^{mix} Constant.

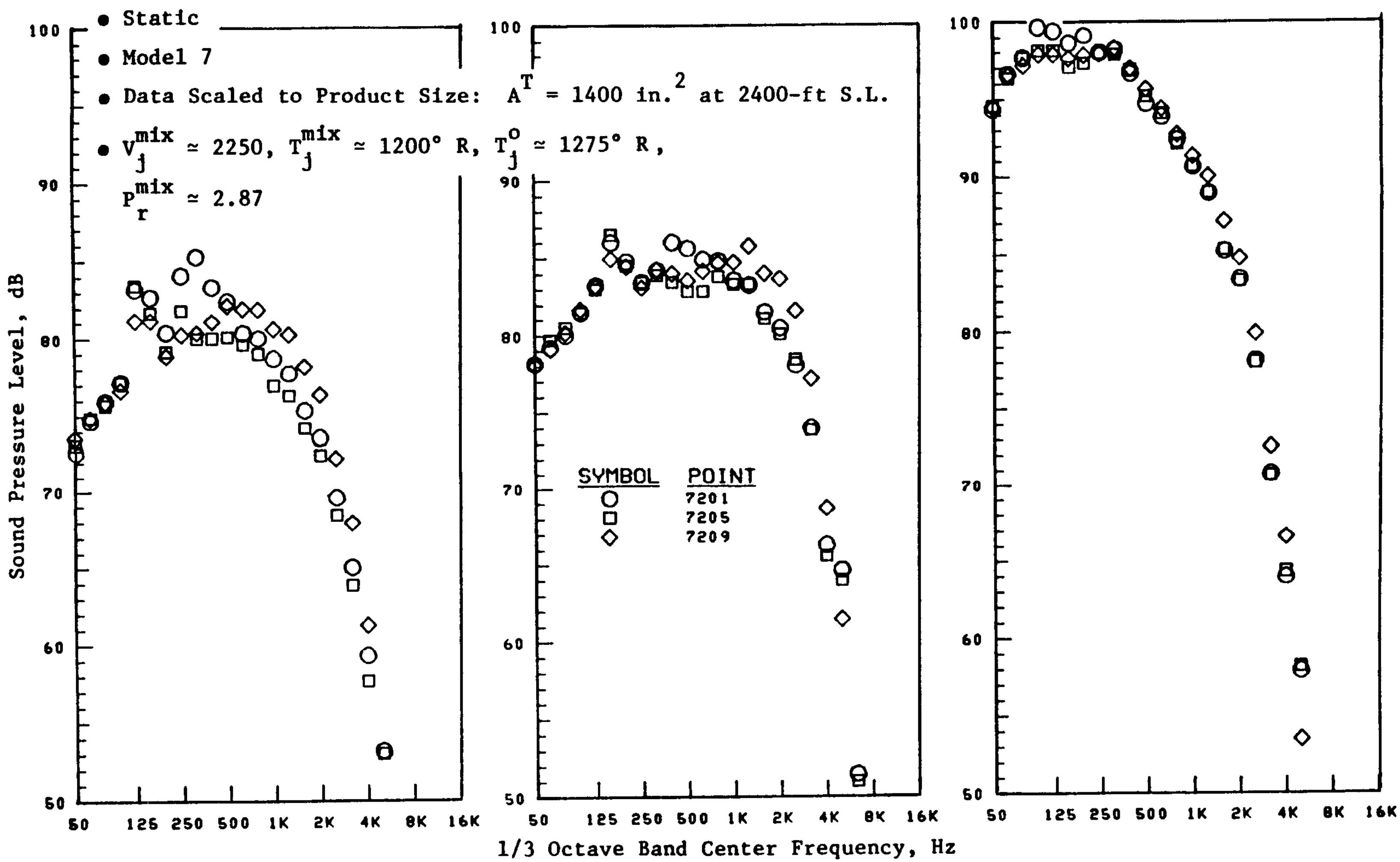

(a) Directivity Angle, $\theta_I = 60°$ (b) Directivity Angle, $\theta_I = 90°$ (c) Peak Noise Angle

Figure 46. Static SPL Spectra for $V_j^o \simeq 2300$, 2400, and 2500 Ft/Sec Holding V_j^{mix}, T_j^{mix}, T_j^o, and P_r^{mix} Constant.

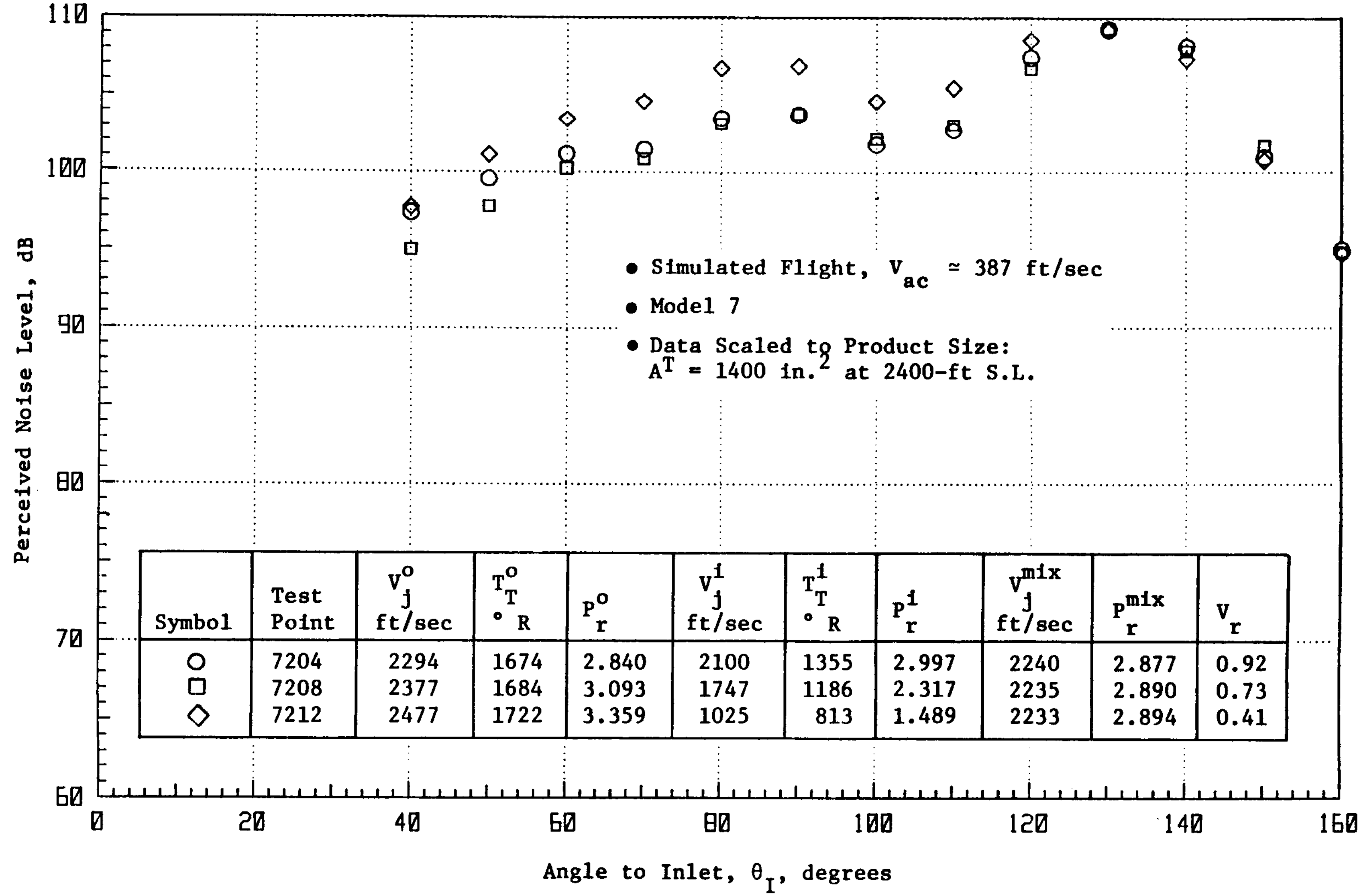

Symbol	Test Point	V_j^o ft/sec	T_T^o °R	P_r^o	V_j^i ft/sec	T_T^i °R	P_r^i	V_j^{mix} ft/sec	P_r^{mix}	V_r
○	7204	2294	1674	2.840	2100	1355	2.997	2240	2.877	0.92
□	7208	2377	1684	3.093	1747	1186	2.317	2235	2.890	0.73
◇	7212	2477	1722	3.359	1025	813	1.489	2233	2.894	0.41

Figure 47. Simulated Flight PNL Directivity for $V_j^o \approx$ 2300, 2400, and 2500 Ft/Sec Holding V_j^{mix}, T_j^{mix}, T_j^o, and P_r^{mix} Constant.

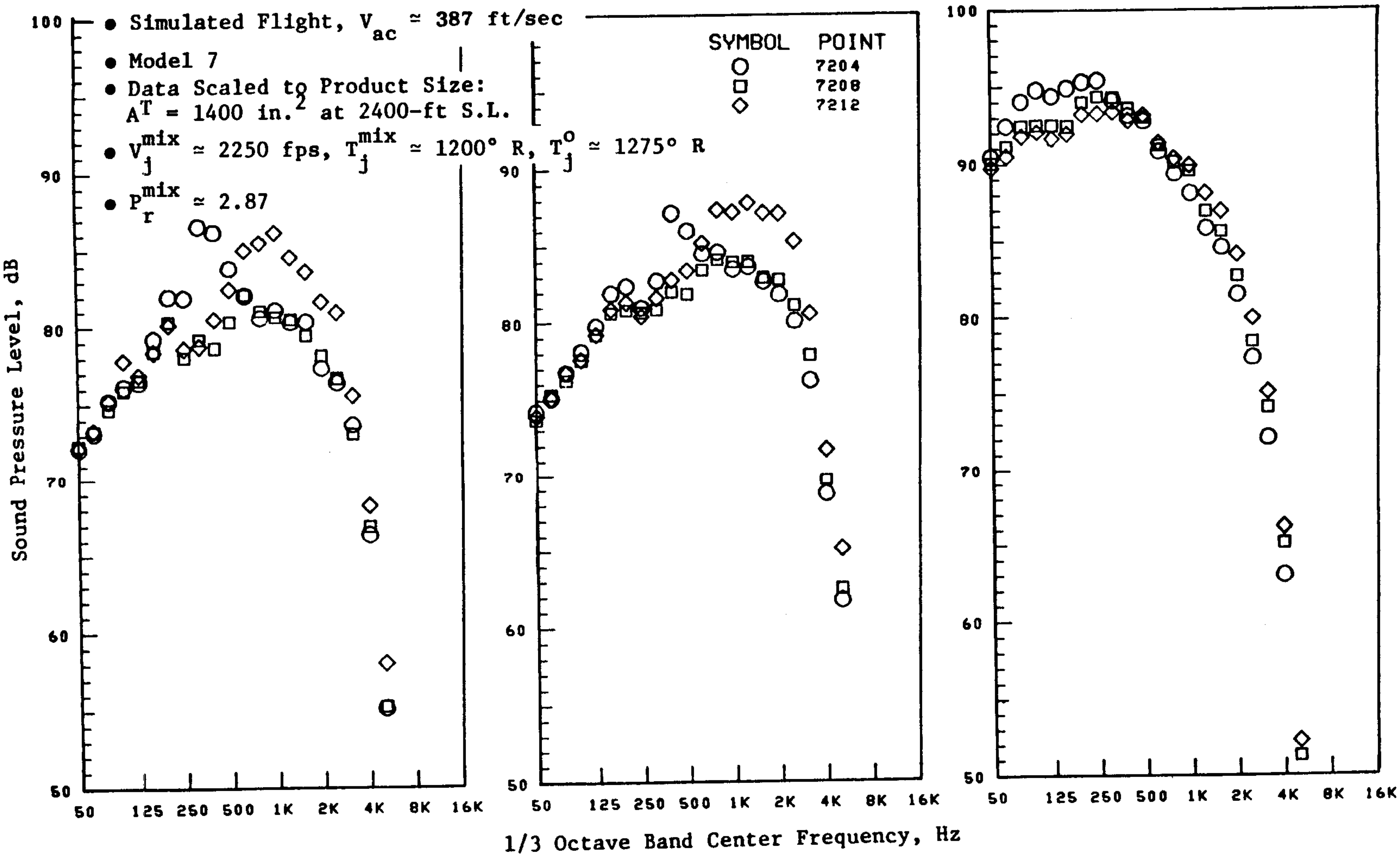

(a) Directivity Angle, $\theta_I = 60°$

(b) Directivity Angle, $\theta_I = 90°$

(c) Peak Noise Angle

Figure 48. Simulated Flight SPL Spectra for $V_j^o \simeq 2300$, 2400, and 2500 Ft/Sec Holding V_j^{mix}, T_j^{mix}, P_r^{mix} Constant.

and simulated flight aft angle overall noise levels remained relatively insensitive to inner-to-outer velocity ratio (V_r) changes from 0.41 to 0.92. Further studies on velocity ratio effects are discussed in Subsection 5.1.3.5, but the general trend is that for a low inner-to-outer stream area ratio (A_r) coannular plug nozzle suppression is maintained over a broad range of V_r at a fixed specific thrust.

Variation With Free-Jet Velocity

During this test series, acoustic free-jet data were obtained with Model 7 at $V_{ac} \approx 0$, 150, 300, and 400 ft/sec. Figures 49 and 50 illustrate these results. Shown in Figure 49 is the PNL directivity at the four free-jet speeds. Figure 50 shows the corresponding comparison of the spectral characteristics at $\theta_I = 60°$, 90°, and at the maximum noise angle. The nozzle flow conditions are $V_j^{mix} \sim 2250$ ft/sec, $P_r^{mix} \sim 2.87$, and $V_j^o \sim 2400$ ft/sec, and $V_r \sim 0.72$.

Figure 49 shows that as the flight velocity is increased the aft angle noise progressively decreases. However, in the forward quadrant, an opposite trend is observed, i.e., as the flight velocity is increased, so does the forward quadrant noise. From the spectral results shown in Figure 50, it is observed that as forward speed is increased the spectral level at θ_{max} decreases over the frequency range of 50 to 4 kHz. Thereafter, the classical flight effect is not observed. The maximum effect of flight is observed at the lower frequencies. At $\theta_I \approx 90°$ and 60°, observations show that at the lower frequencies (< 2 kHz), the jet noise decreases with an increase in forward speed. At the higher frequencies, an amplification of coannular plug nozzle noise is observed. This is due to the shock-noise forward quadrant amplification with an increase in flight velocity. Other flight tests performed with $V_j^o \approx 2300$ and 2500 ft/sec yielded acoustic results similar to the above discussed data.

5.1.3.3 Variation in V_j^o Holding V_j^{mix}, T_j^{mix}, T_j^o Constant

In order to study the effects of outer stream velocity on coannular plug nozzle acoustics, a series of test points were run where V_j^o was varied with V_j^{mix}, T_j^{mix}, and T_j^o held approximately constant. Under these conditions, it is of interest to examine the effect on the static and flight measured high frequency noise spectra.

Static Test Results

Figures 51 through 54 illustrate the results for two specific thrust conditions ($V_j^{mix} \approx 1900$ and 2250 ft/sec) for outer stream velocities of V_j^o 2000, 2100, 2200, 2300, 2400, and 2500 ft/sec.

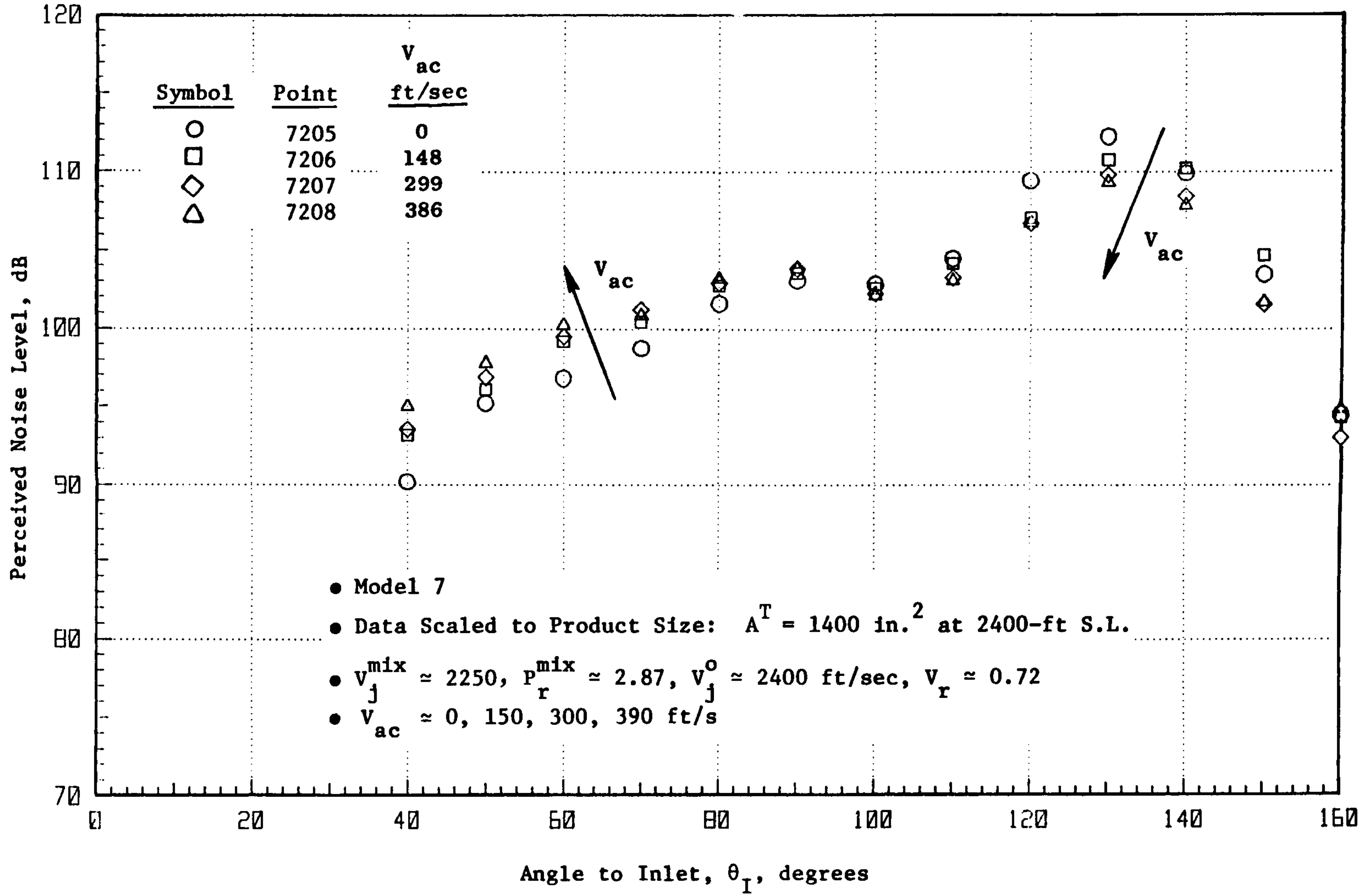

Figure 49. Influence of Free-Jet Velocity on Coannular Plug Nozzle PNL Directivity.

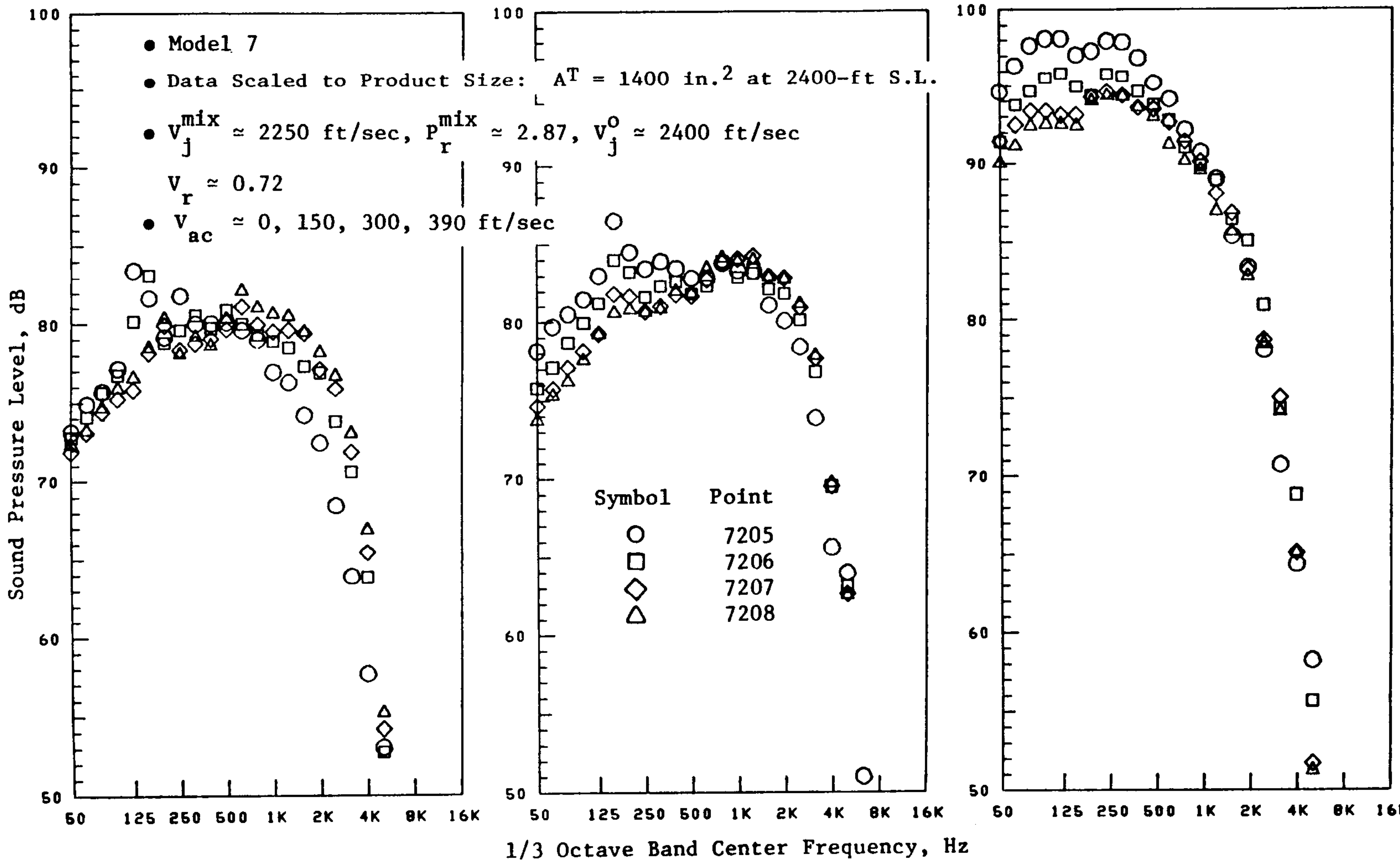

(a) Directivity Angle, $\theta_I = 60°$ (b) Directivity Angle, $\theta_I = 90°$ (c) Peak Noise Angle

Figure 50. Influence of Free-Jet Velocity on Coannular Plug Nozzle SPL Spectra.

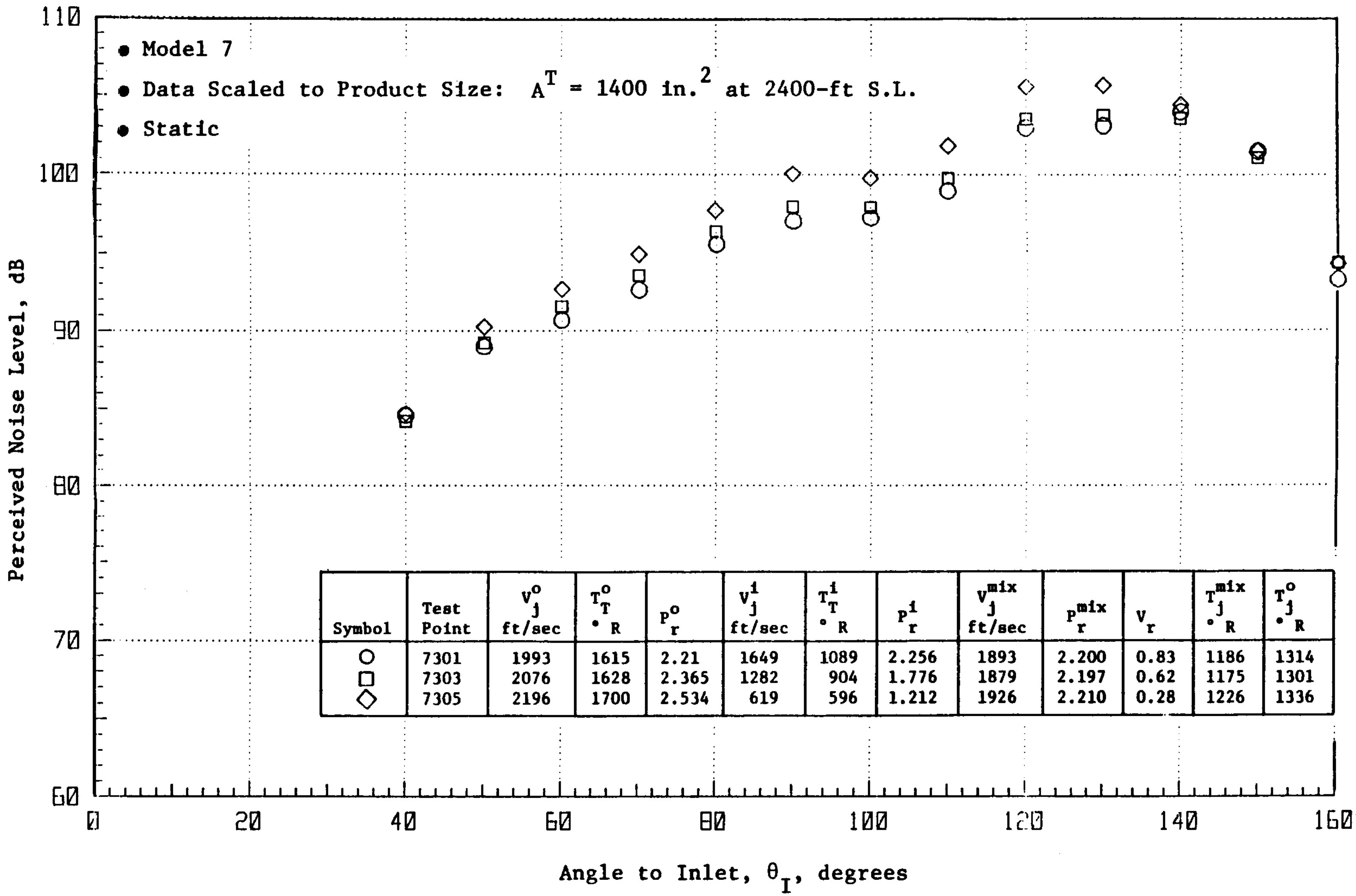

Symbol	Test Point	V_j^o ft/sec	T_T^o °R	P_r^o	V_j^i ft/sec	T_T^i °R	P_r^i	V_j^{mix} ft/sec	P_r^{mix}	V_r	T_j^{mix} °R	T_j^o °R
○	7301	1993	1615	2.21	1649	1089	2.256	1893	2.200	0.83	1186	1314
□	7303	2076	1628	2.365	1282	904	1.776	1879	2.197	0.62	1175	1301
◇	7305	2196	1700	2.534	619	596	1.212	1926	2.210	0.28	1226	1336

Figure 51. Static PNL Directivity for $V_j^o \approx$ 2000, 2100 and 2200 ft/s Holding V_j^{mix}, P_r^{mix}, T_j^{mix} and T_j^o Approximately Constant.

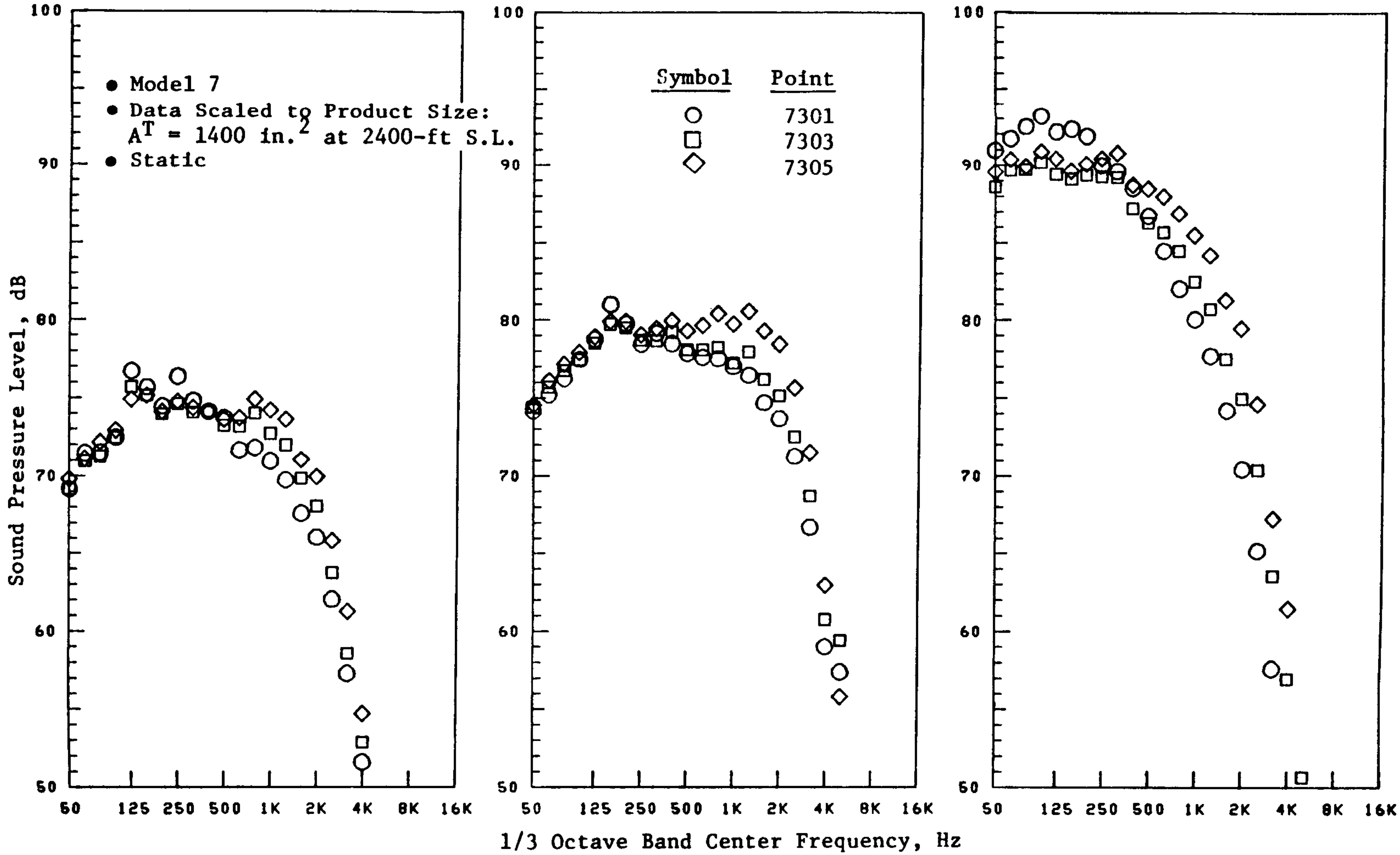

(a) Directivity Angle, θ_I = 60°

(b) Directivity Angle, θ_I = 90°

(c) Peak Noise Angle

Figure 52. Static SPL Spectra for $V_j^o \simeq$ 2000, 2100 and 2200 ft/s Holding V_j^{mix}, P_r^{mix}, T_j^{mix} and T_j^o Approximately Constant.

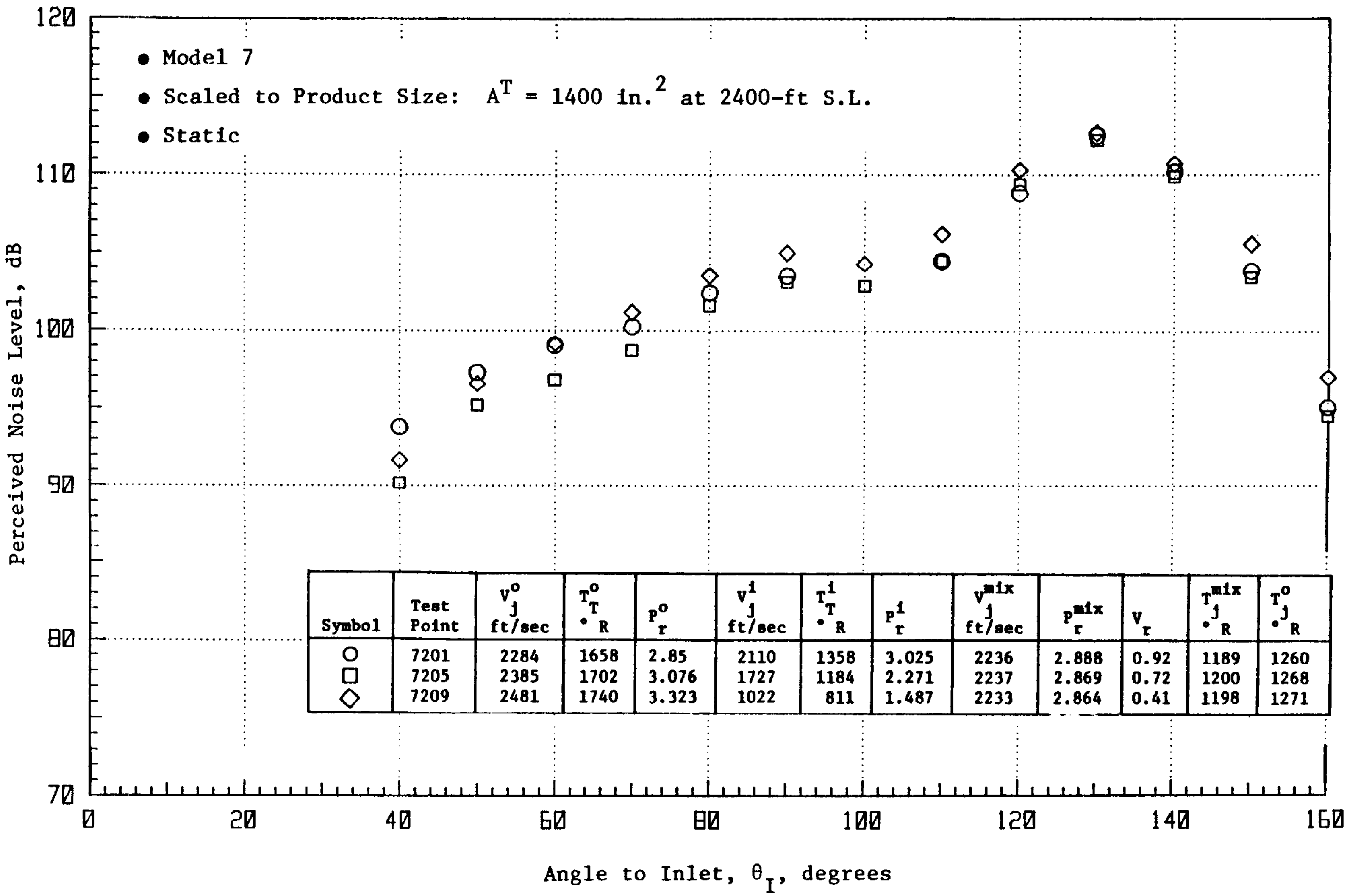

Symbol	Test Point	V_j^o ft/sec	T_T^o °R	P_r^o	V_j^i ft/sec	T_T^i °R	P_r^i	V_j^{mix} ft/sec	P_r^{mix}	V_r	T_j^{mix} °R	T_j^o °R
○	7201	2284	1658	2.85	2110	1358	3.025	2236	2.888	0.92	1189	1260
□	7205	2385	1702	3.076	1727	1184	2.271	2237	2.869	0.72	1200	1268
◇	7209	2481	1740	3.323	1022	811	1.487	2233	2.864	0.41	1198	1271

Figure 53. Static PNL Directivity for $V_j^o \simeq$ 2300, 2400 and 2500 ft/s Holding V_j^{mix}, P_r^{mix}, T_j^{mix} and T_j^o Approximately Constant.

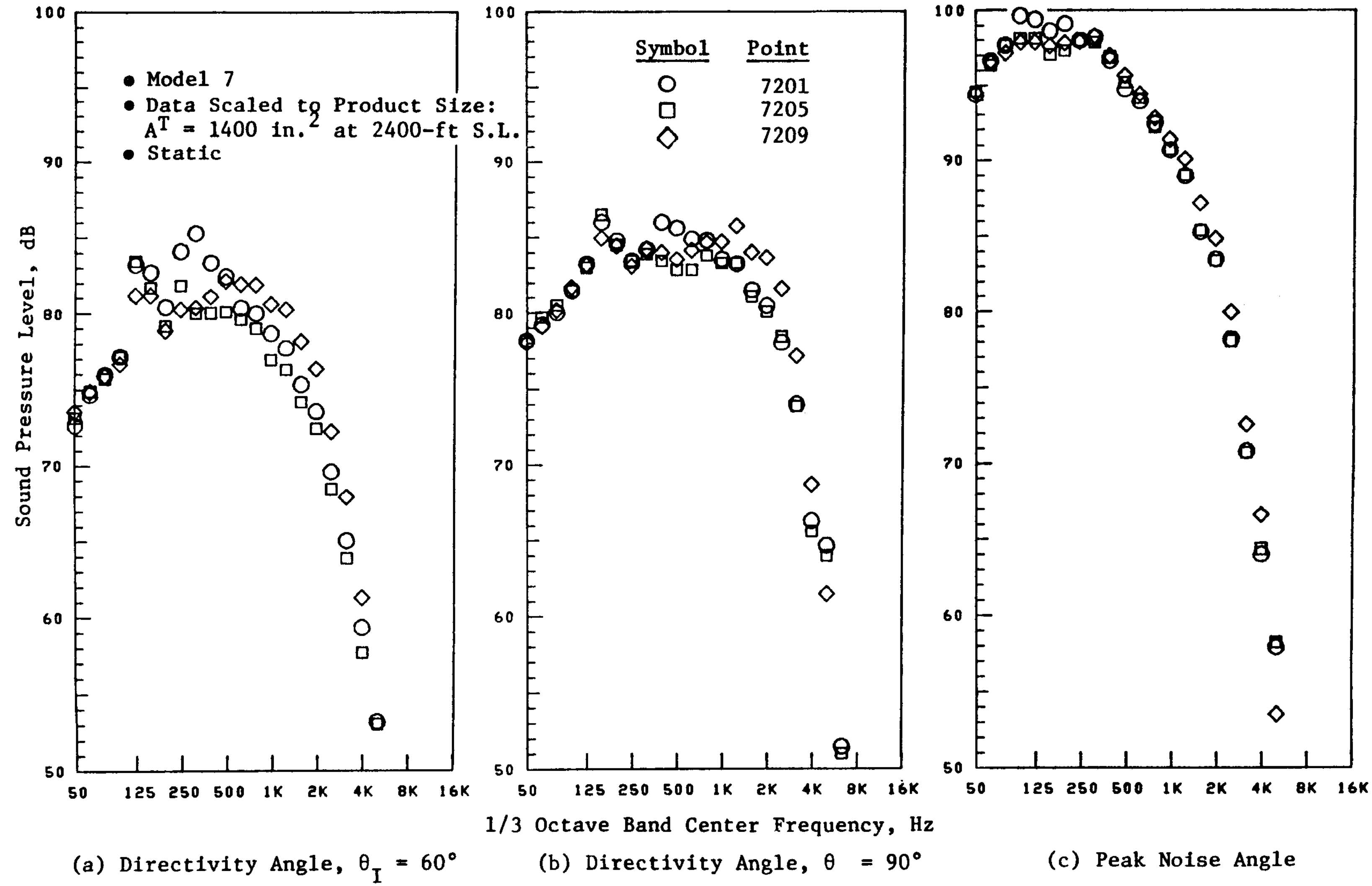

Figure 54. Static SPL Spectra for $V_j^o \approx$ 2300, 2400 and 2500 Ft/S Holding V_j^{mix}, P_r^{mix}, T_j^{mix} and T_j^o Approximately Constant.

Shown in Figures 51 and 52 are the PNL directivity and SPL spectra for the case where $V_i^{mix} \approx 1900$ ft/sec and V_j^o is 2000, 2100, and 2200 ft/sec. The results show that while the PNL levels appear to differ the same for the three test points the differences can be due mainly to the variation in V_r and to a smaller extent in V_j^{mix}. On a spectral basis, Figure 52 demonstrates that as V_j^o increases, the high frequency noise (f > 2000 Hz) increases while the low frequency noise remains nearly the same. As V_j^o was increased so was P_r^o, although P_r^{mix} remained approximately constant. The change and/or increase in P_r^o is observed particularly for the case where P_r^i was subcritical, and the outer stream pressure ratio, P_r^o, was at its highest value for this test point ($P_r^o \approx 2.534$). The amount of influence of shock noise versus jet noise is not easily assessed here. This effect will be discussed separately in Section 5.1.4.

Figures 53 and 54 illustrate the results when $V_j^{mix} \approx 2250$ ft/sec and V_j^o is ~ 2300, 2400, and 2500 ft/sec. At this higher V_j^{mix} condition, the V_j^o variation does not indicate the strong influence of V_j^o on the high frequency noise spectrum at θ_{max} as was observed in the previous case. Nonetheless, it is observed that the low frequency noise remained approximately constant and the high frequency noise increased with an increase in V_j^o. In the forward quadrant, the change in shock noise spectrum with increases in P_r^o is seen again. However, a significant change and an amplification are noticed when the inner stream is subsonic and the outer stream is fully supercritical ($P_r^o \approx 3.3$). For this case, which is representative of a typical AST takeoff sideline condition, it appears that it would be acoustically preferable to run at a reduced outer stream velocity with both streams supercritical rather than at a high outer stream velocity and inner stream subcritical for a given specific thrust and mixed pressure ratio.

Simulated Flight Acoustic Results

The simulated flight acoustic test results are illustrated in Figures 55 and 56. Results shown here are for the case where $V_j^{mix} \approx 2250$ ft/sec, $P_r^{mix} \approx 2.88$, and $V_j^o \approx 2350$, 2400, and 2500 ft/sec, with T_j^{mix} and T_j^o approximately constant at 1200° and 1275° R, respectively. The results show that increasing the outer stream velocity at a fixed specific thrust does tend to increase the high frequency portion of the θ_{max} spectra. However, PNL_{max} is relatively insensitive to the variations in V_j^o and is governed by changes in V_j^{mix} and contributions from lower frequency noise. In the forward quadrant and for the case when the inner stream was subsonic and the outer stream supersonic, an appreciable increase in shock noise occurred. The benefit of running both streams at supercritical conditions rather than just the outer stream supercritical (for a given P_r^{mix}) is reaffirmed and even more true in flight. Still, the effect of these changes on the shock structure for the two cases is not understood at this time.

Symb	Point	V_j^o ft/sec	T_T^o °R	P_r^o	V_j^i ft/sec	T_T^i °R	P_r^i	V_j^{mix} ft/sec	P_r^{mix}	V_r	T_j^{mix} °R	T_j^o °R
○	7204	2294	1674	2.848	2100	1355	2.917	2240	2.877	0.92	1199	1273
□	7208	2377	1684	3.093	1747	1186	2.317	2235	2.893	0.72	1186	1252
◇	7212	2477	1722	3.359	1025	813	1.489	2233	2.894	0.41	1184	1253

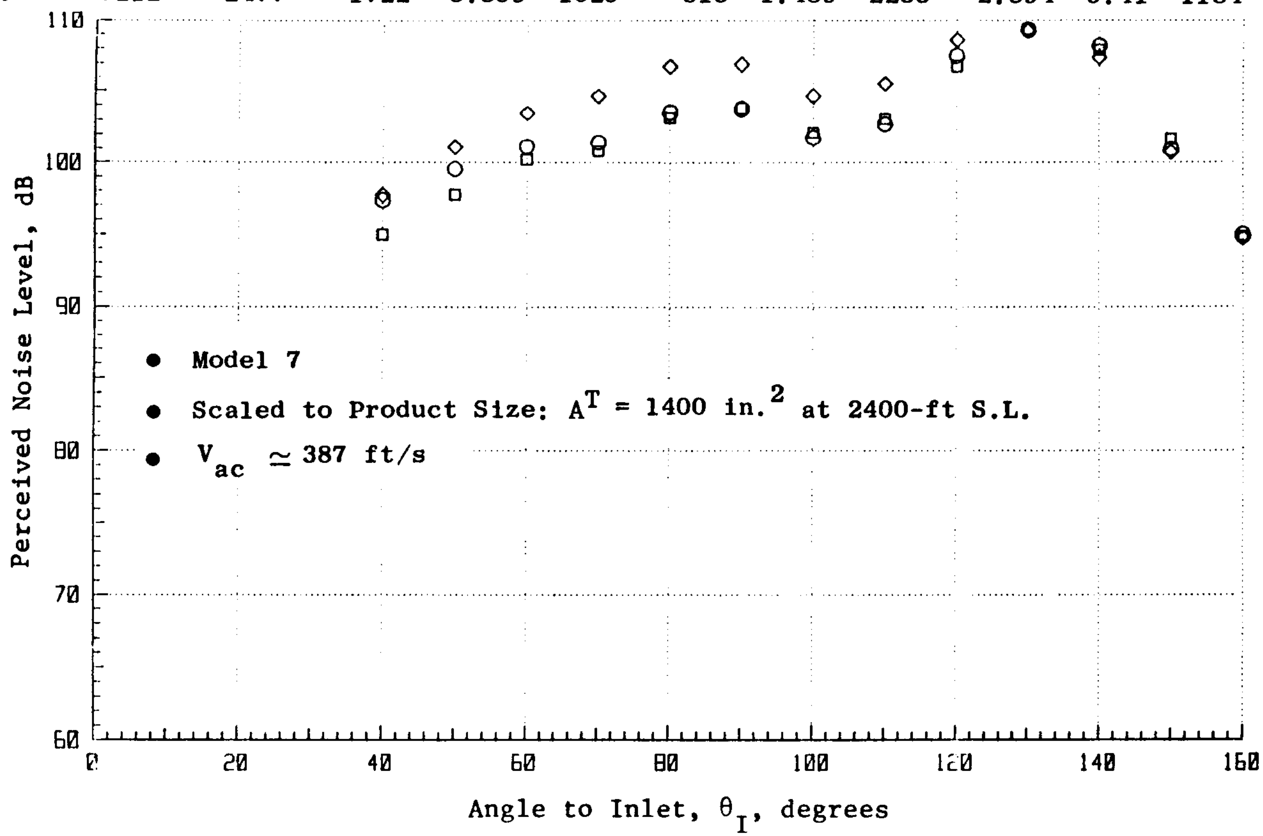

Figure 55. Simulated Flight PNL Directivity for $V_j^o \simeq$ 2300, 2400 and 2500 Ft/S Holding V_j^{mix}, P_r^{mix}, T_j^{mix} and T_j^o Approximately Constant.

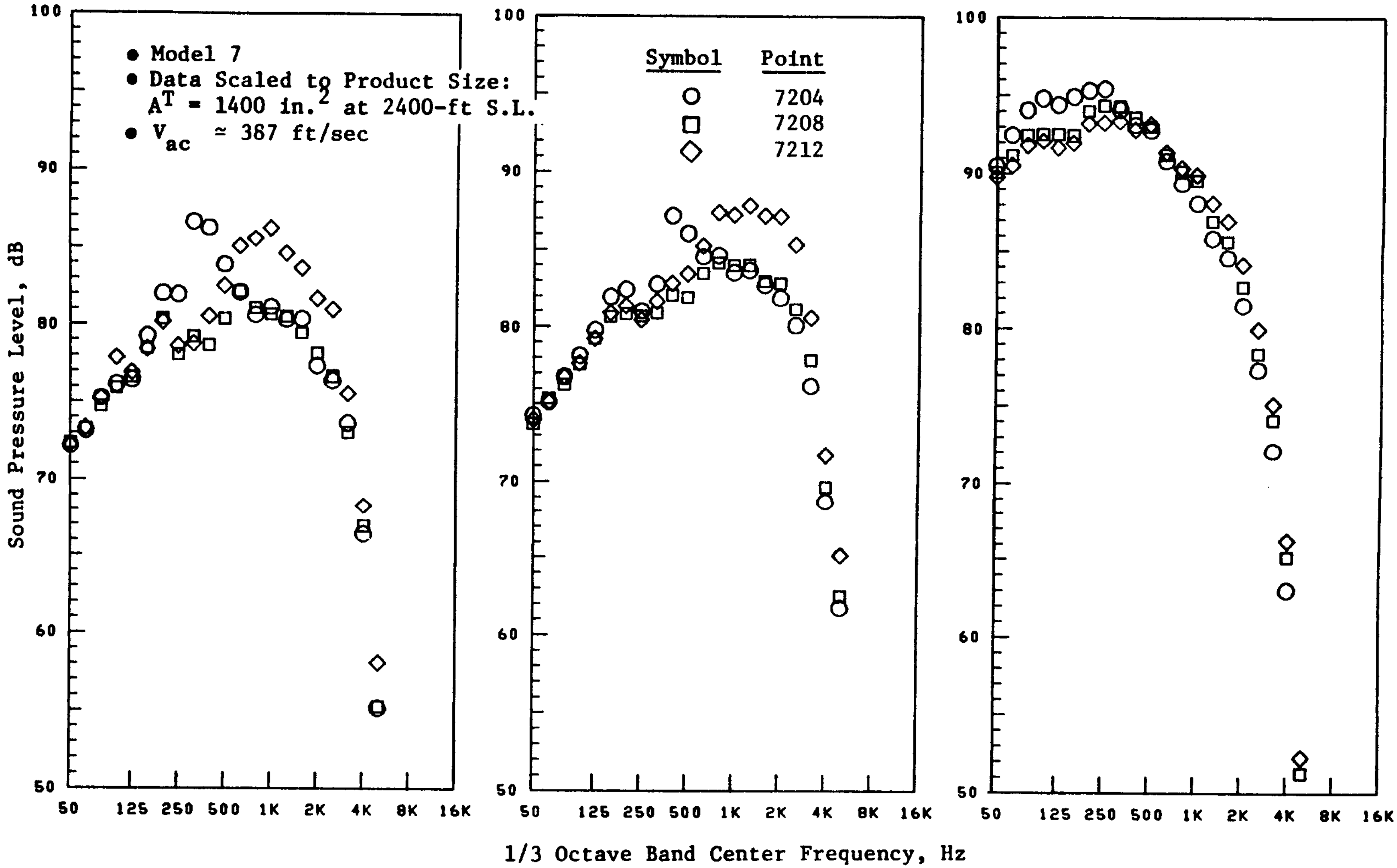

(a) Directivity Angle, θ_I = 60°   (b) Directivity Angle, θ = 90°   (c) Peak Noise Angle

Figure 56. Simulated Flight Spectra for $V_j^o \simeq 2300$, 2400 and 2500 Ft/S Holding V_j^{mix}, P_r^{mix}, T_j^{mix} and T_j^o Approximately Constant.

The last illustrative example of test results for this subsection is presented in Figures 57 and 58. These figures compare the static and simulated flight acoustic measurements at $V_j^o \approx 2387$ ft/sec, $V_j^{mix} \approx 2250$ ft/sec, $P_r^{mix} \approx 2.87$, and $V_r \approx 0.72$ (typical VCE takeoff sideline conditions). The data show that the aft quadrant jet noise is reduced and the forward quadrant shock-associated noise is amplified with increase in flight velocity. By and large, a significant reduction in low-frequency jet noise occurs with flight, offset to some extent by an increase in the high frequency shock-associated noise.

5.1.3.4 Temperature Effects

In order to assess the influence of temperature on coannular plug nozzle static and simulated flight acoustics, a few test points were run in which the outer stream velocity V_j^o, the inner stream static temperature T_j^i, and the inner stream pressure ratio P_r^i were fixed and the outer stream temperature T_j^o was varied. These tests were performed on Model 7. The nominal conditions were as follows:

Test Point	V_j^o, ft/sec	T_T^o, °R	T_j^o, °R	P_r^o	V_j^i, ft/sec	T_T^i, °R	T_j^i °R	P_r^i	V_j^{mix} ft/sec	T_j^{mix}, °R	P_r^{mix}
7501	2000	1200	860	3.05	1340	830	680	2.01	1840	825	2.80
2000	2000	1730	1440	2.08	1350	830	680	2.02	1790	1205	2.03

Thus, with V_j^o fixed and V_j^{mix} differing only slightly, the expected influences due to temperature changes are on the jet mixing noise in the aft quadrant. However, the forward quadrant noise will be influenced significantly by the large change in the pressure ratio. Figures 59 through 61 illustrate the measured results.

Figures 59 and 60 show the static test measurements for the two test points. Figure 59 compares the static directivities. The results show that by increasing the static mixed stream temperature from $T_j^{mix} \approx 826$ to 1205° R, but V_j^{mix} changing from 1840 to 1790 ft/sec, alters the angle of maximum noise from $\theta_I = 140°$ to 120°. Associated with this shift in θ_{max}, there is also a reduction in PNL_{max} of $\approx$ 4 dB. An 80 $\log_{10} V_j^{mix}$ and a 20 log T_j^{mix}-type of correlation could account for this change in PNL. In the forward quadrant, there exists a 10-dB noise reduction. Based on a 40 log β^{mix}, there would be a predicted 13.8 dB reduction. Since there is also a significant amount of jet mixing noise in the forward quadrant, it is expected that the jet mixing noise is holding up some of the forward quadrant noise levels. To better illustrate the temperature effect on the aft quadrant noise, SPL spectra results at $\theta_I = 130°$, 140°, and 150° are presented in Figure 61. Figure 60 illustrated the influence of temperature at θ_{max}, but θ_{max} was different for the two test conditions. Figure 61 compares the results at equal values of

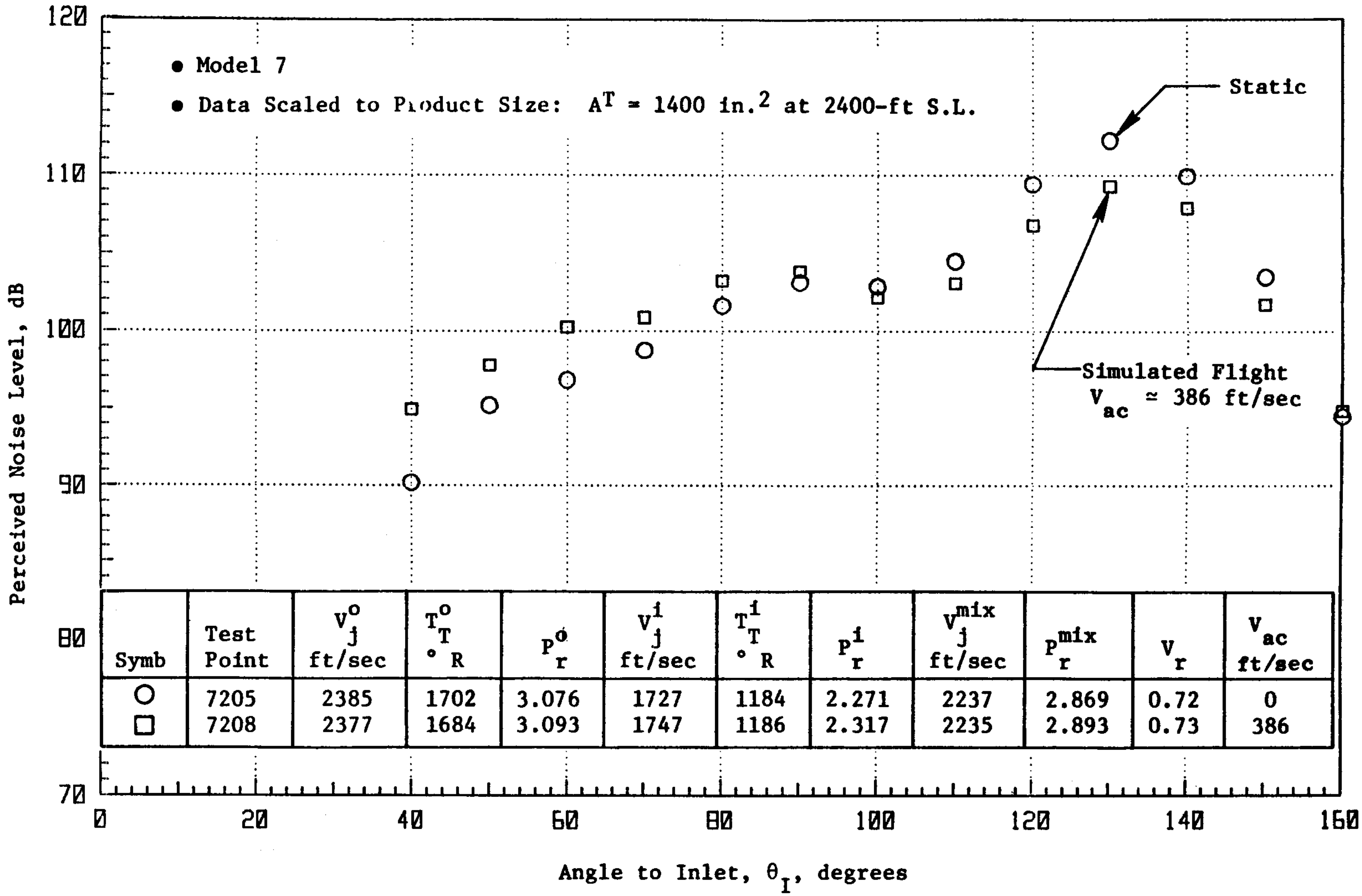

Symb	Test Point	V_j^o ft/sec	T_T^o °R	P_r^o	V_j^i ft/sec	T_T^i °R	P_r^i	V_j^{mix} ft/sec	P_r^{mix}	V_r	V_{ac} ft/sec
○	7205	2385	1702	3.076	1727	1184	2.271	2237	2.869	0.72	0
□	7208	2377	1684	3.093	1747	1186	2.317	2235	2.893	0.73	386

Figure 57, Static and Simulated Flight PNL Directivity Comparison for $V_j^{mix} \simeq 2250$ ft/s, $P_r^{mix} \simeq 2.87$ and $V_r \simeq 0.72$.

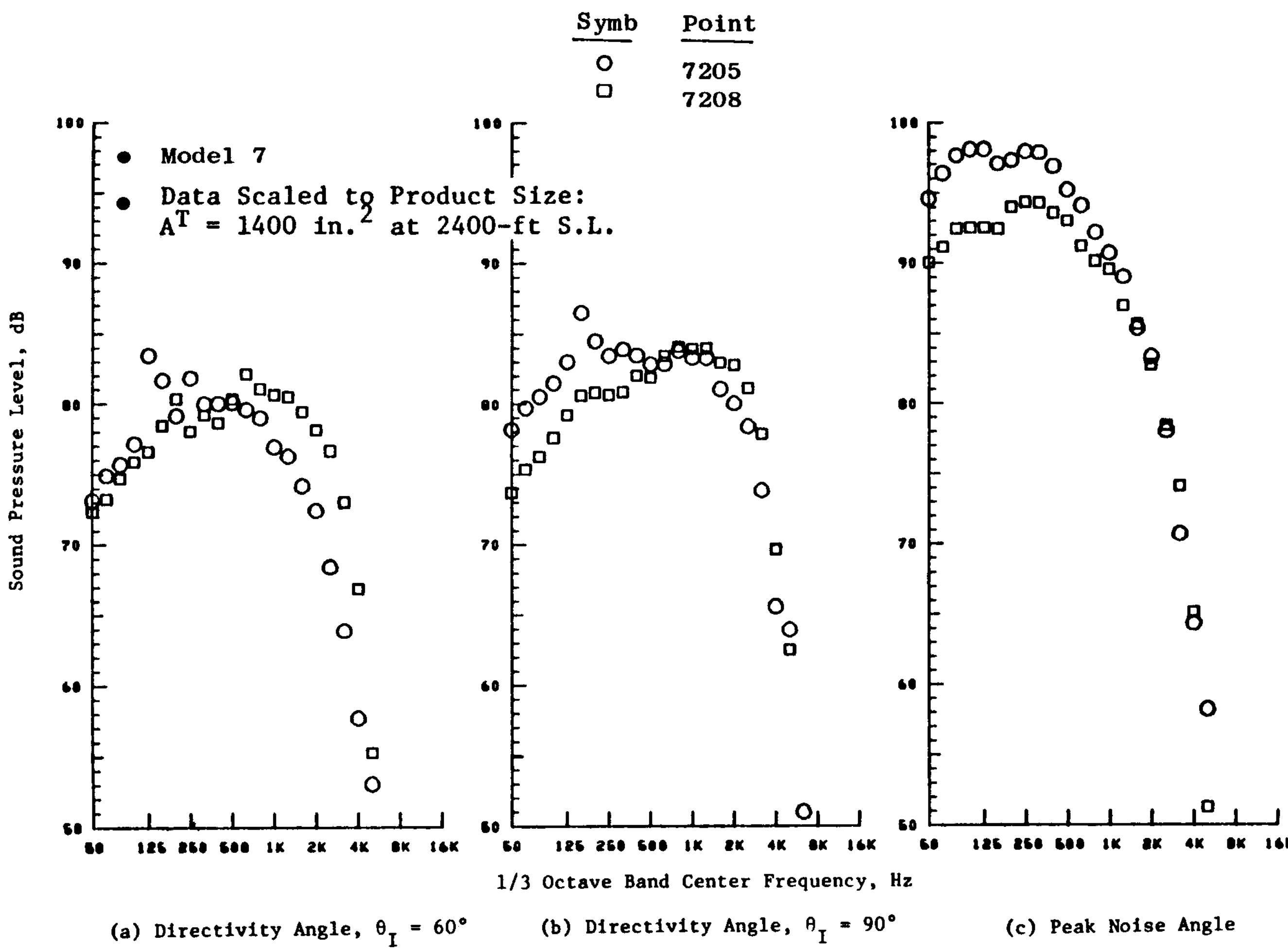

Figure 58. Static and Simulated Flight Spectral Comparison for $V_j^{mix} \simeq 2250$ ft/s, $P_r^{mix} \simeq 2.87$ and $V_r \simeq 0.72$.

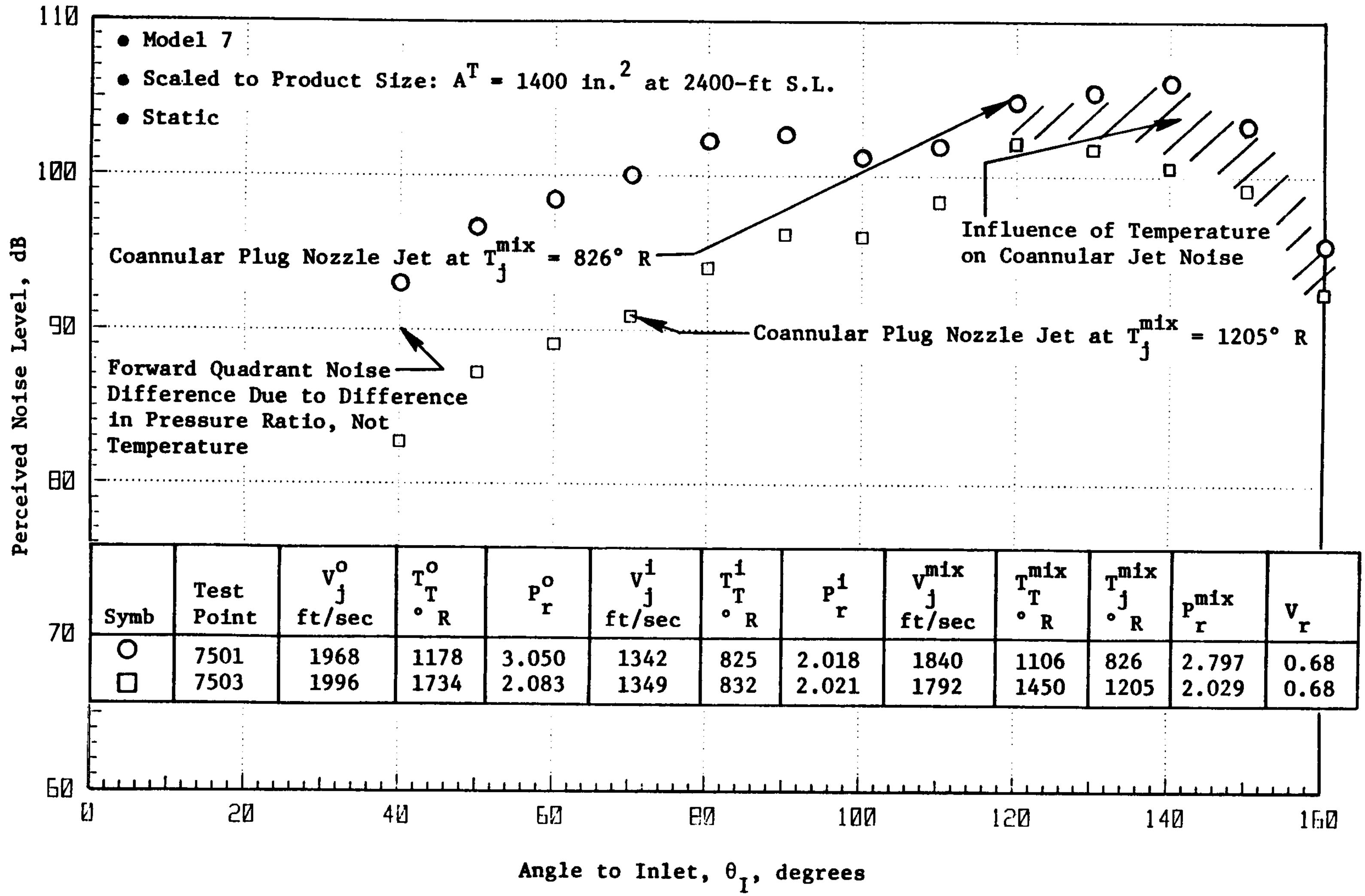

Symb	Test Point	V_j^o ft/sec	T_T^o °R	P_r^o	V_j^i ft/sec	T_T^i °R	P_r^i	V_j^{mix} ft/sec	T_T^{mix} °R	T_j^{mix} °R	P_r^{mix}	V_r
○	7501	1968	1178	3.050	1342	825	2.018	1840	1106	826	2.797	0.68
□	7503	1996	1734	2.083	1349	832	2.021	1792	1450	1205	2.029	0.68

Figure 59. Influence of Temperature on Coannular Plug Nozzle Jet Noise Directivity for $V_j^{mix} \simeq$ 1800 Ft/Sec, Static Tests.

Symbol	Test Point	V_j^o ft/sec	T_T^o °R	P_r^o	V_j^i ft/sec	T_T^i °R	P_r^i	V_j^{mix} ft/sec	T_T^{mix} °R	P_r^{mix}	V_r	T_j^{mix} °R
○	7501	1968	1178	3.050	1342	825	2.018	1840	1106	2.797	0.68	826
□	7503	1996	1734	2.083	1349	832	2.021	1792	1450	2.029	0.68	1205

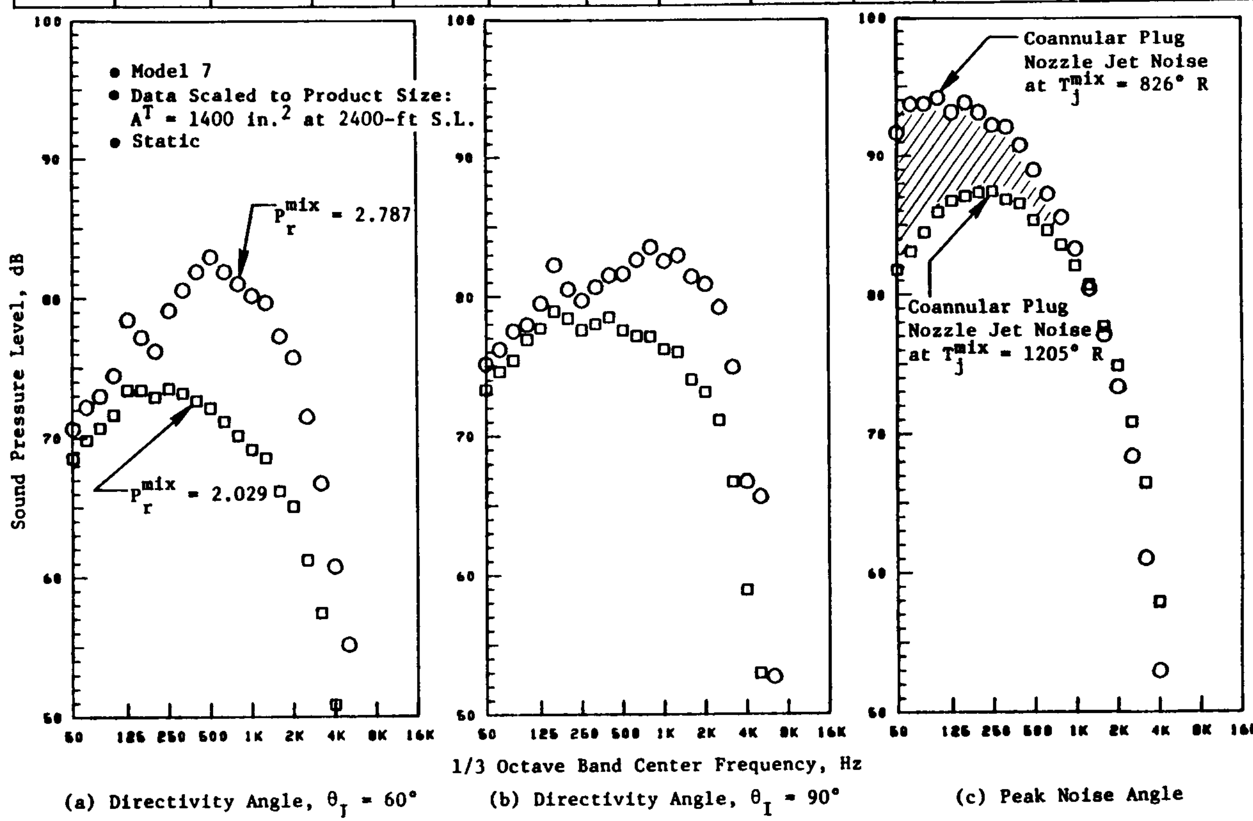

(a) Directivity Angle, θ_I = 60°　(b) Directivity Angle, θ_I = 90°　(c) Peak Noise Angle

Figure 60. Influence of Temperature on Coannular Plug Nozzle SPL Spectra for $V_j^{mix} \simeq$ 1800 Ft/Sec, Static Tests.

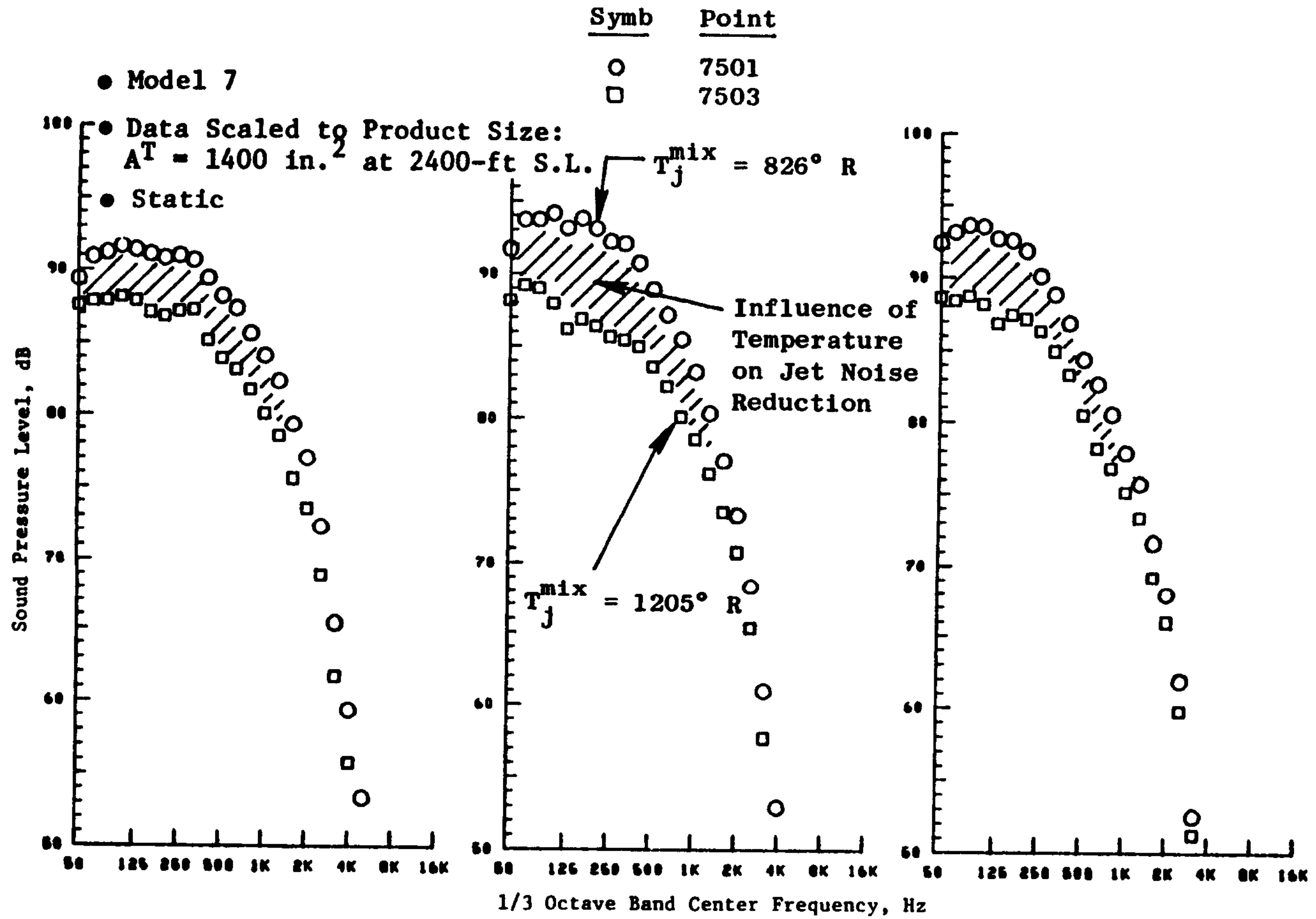

(a) Directivity Angle, θ_I = 130° (b) Directivity Angle, θ_I = 140° (c) Directivity Angle, θ_I = 150°

Figure 61. Influence of Temperature on Coannular Plug Nozzle SPL Spectra at θ_I = 130°, 140° and 150° for $V_j^{mix} \simeq 1800$ Ft/S, Static Tests.

θ_I and it indicates that the reduction in the aft quadrant jet noise is observed at all frequencies and that the relative amount of reduction increases as θ_I increases.

The corresponding simulated flight acoustic results are presented in Figures 62 through 64. The PNL directivity results are shown in Figure 62, which indicates that the angles corresponding to a peak PNL in the aft quadrant are now the same. However, the actual peak angle for the $T_j^{mix} \approx 825°$ R test case now occurs at $\theta_I \approx 90°$. This is due to the strong shock noise contribution for this test case, whereas the heated test ($T_j^{mix} \approx 1205°$ R) is barely supercritical and has relatively little coannular shock noise. The next observation is that the amount of peak aft quadrant noise reduction due to increased temperatures is somewhat greater in simulated flight than was observed statically. The simulated flight SPL spectra comparisons at $\theta_I = 130°$, 140°, and 150° that are shown in Figure 64 illustrate the broad range of spectral reductions due to temperature effects, as was observed in the static test results.

5.1.3.5 Effect of Ratio of Inner-to-Outer Velocities

In order to determine the effect of the velocity ratio on the noise characteristics of coannular plug nozzles (Models 3, 4, 6, and 7), tests were conducted where the ratio of inner-to-outer stream velocity was varied. This was achieved by holding the outer stream velocity constant at $V_j^o \approx 2300$ ft/sec and regulating the inner stream velocity V_j^i so that velocity ratios of 0.1 to 0.7 were obtained. The normalized PNL_{max} static and flight data (scaled to 2400 ft sideline and 1400 in.^{2} exhaust area) that were measured during these tests are presented in Figure 65(a). An examination of this figure indicates that the measured PNL_{max} for each of the test configurations is a minimum at a velocity ratio between 0.4 and 0.5. The data further indicate that the variation in the PNL_{max} with the velocity ratio is more significant for Models 3, 4, and 7 ($R_r^o = 0.853$) when compared to that of the high-radius-ratio Model 6 ($R_r^o = 0.902$).

The corresponding mixed stream velocities are presented in Figure 65(b). An examination of the data along with the acoustic data indicates that both the PNL_{max} and the mixed stream velocities vary with the velocity ratio in an identical manner for each of the test configurations. A similar observation has been made during an earlier NASA-supported static study (Reference 2) on a family of coannular plug nozzles. Moreover, after accounting for the different values of V_j^{mix}, it was shown during that study that the noise levels of nozzles with an area ratio <1 are not affected significantly by a variation in the velocity ratio.

For the purpose of making similar analyses with the static and flight data of this study, a linear regression of normalized PNL_{max} as a function of 10 log (V_j^{mix}/c_a) for each of the four configurations was conducted and

Symb	Point	V_j^o ft/sec	T_T^o ° R	P_r^o	V_j^i ft/sec	T_T^i ° R	P_r^i	V_j^{mix} ft/sec	T_T^{mix} ° R	T_j^{mix} ft/sec	P_r^{mix}	V_r
○	7502	1973	1180	3.07	1361	849	2.02	1850	1114	831	2.81	0.69
□	7504	2004	1732	2.10	1363	845	2.03	1804	1456	1205	2.04	0.68

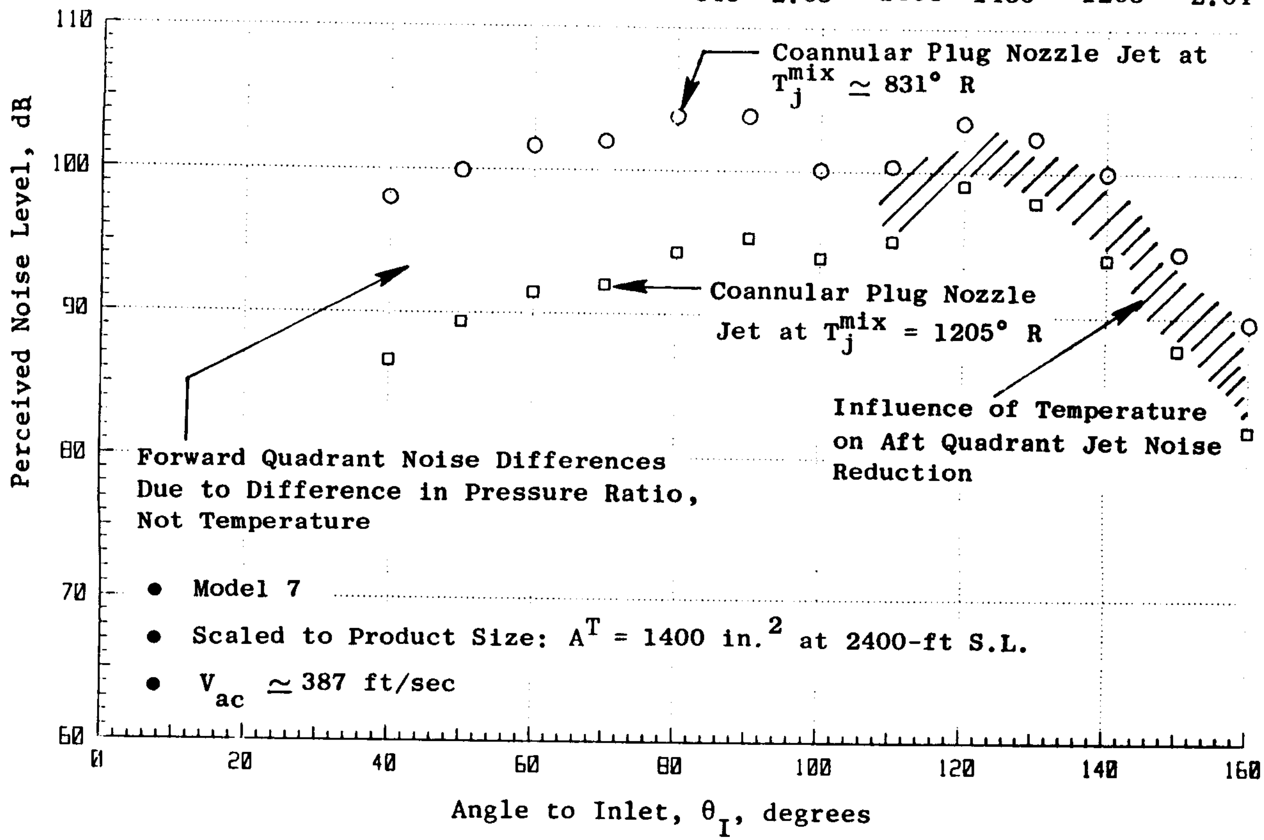

Figure 62. Influence of Temperature on Coannular Plug Nozzle Jet Noise Directivity for $V_j^{mix} \simeq 1800$ Ft/Sec, Simulated Flight at $V_{ac} \simeq 387$ Ft/Sec.

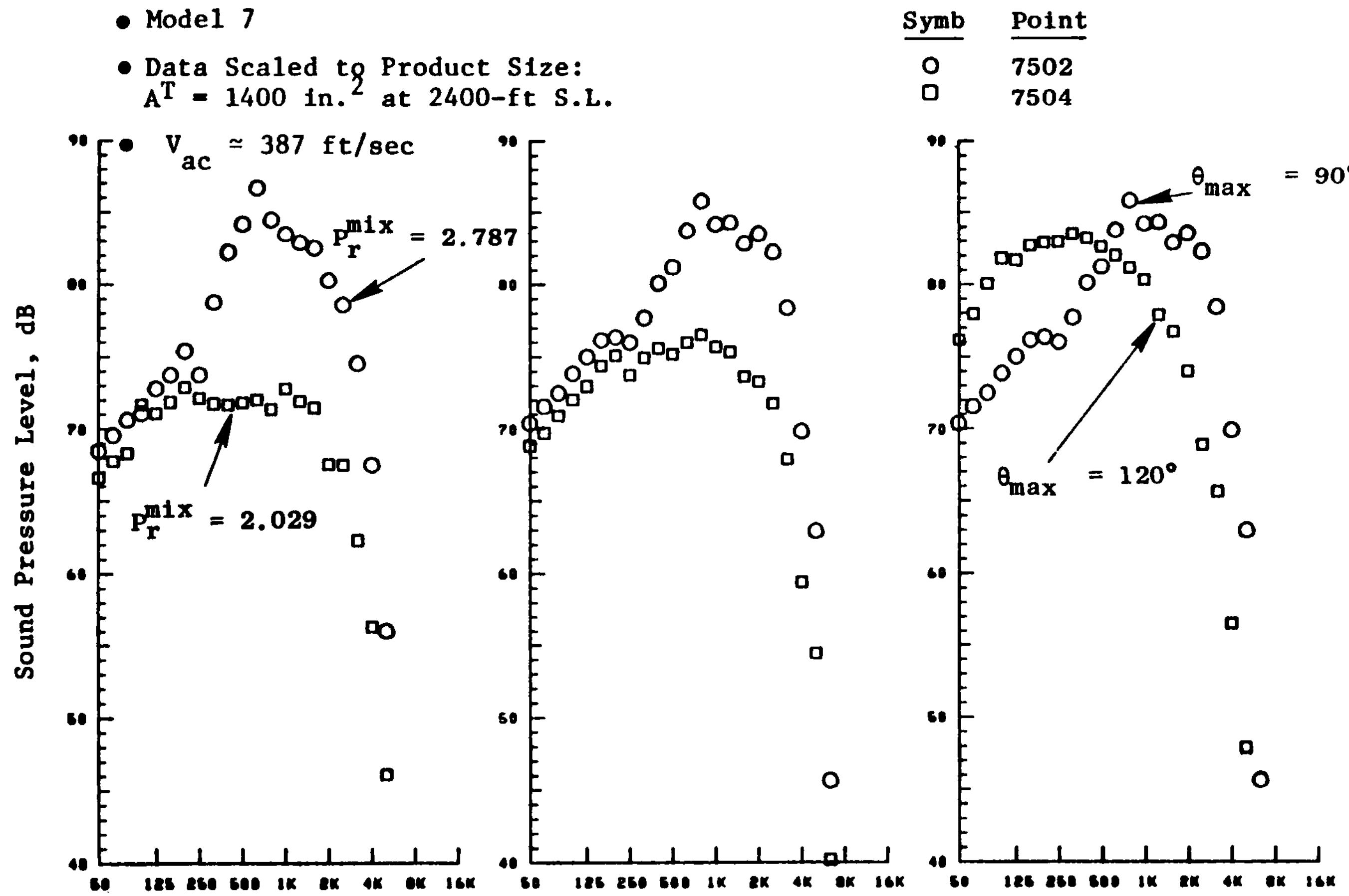

(a) Directivity Angle, θ_I = 60°

(b) Directivity Angle, θ_I = 90°

(c) Peak Noise Angle

Figure 63. Influence of Temperature on Coannular Plug Nozzle SPL Spectra for V_j^{mix} ≈ 1800 Ft/Sec, V_{ac} ≈ 387 Ft/Sec.

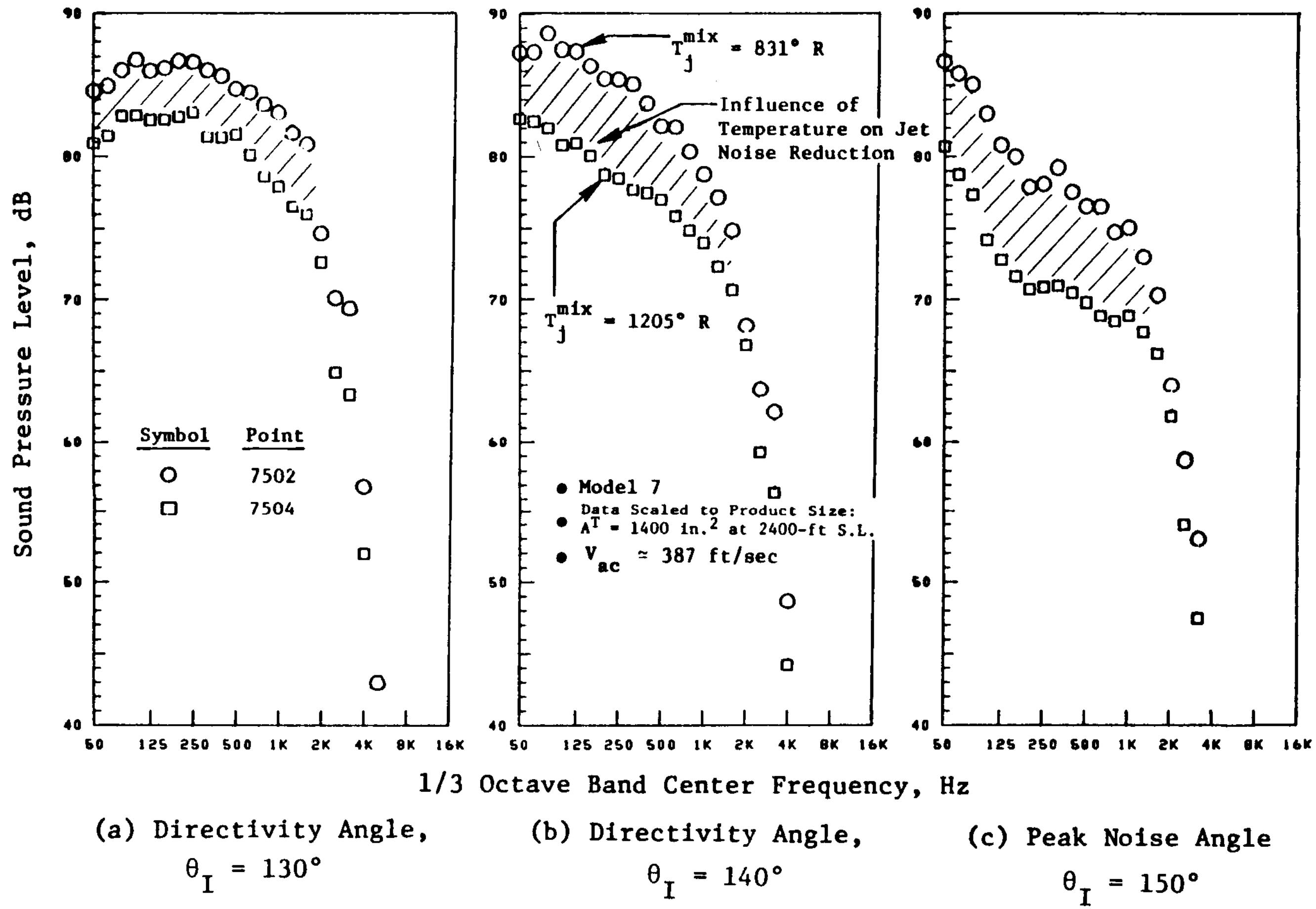

Figure 64. Influence of Temperature on Coannular Plug Nozzle SPL Spectra at $\theta_I = 130°$, 140°, and 150° for $V_j^{mix} \simeq 1800$ Ft/S; $V_{ac} \simeq 387$ Ft/S.

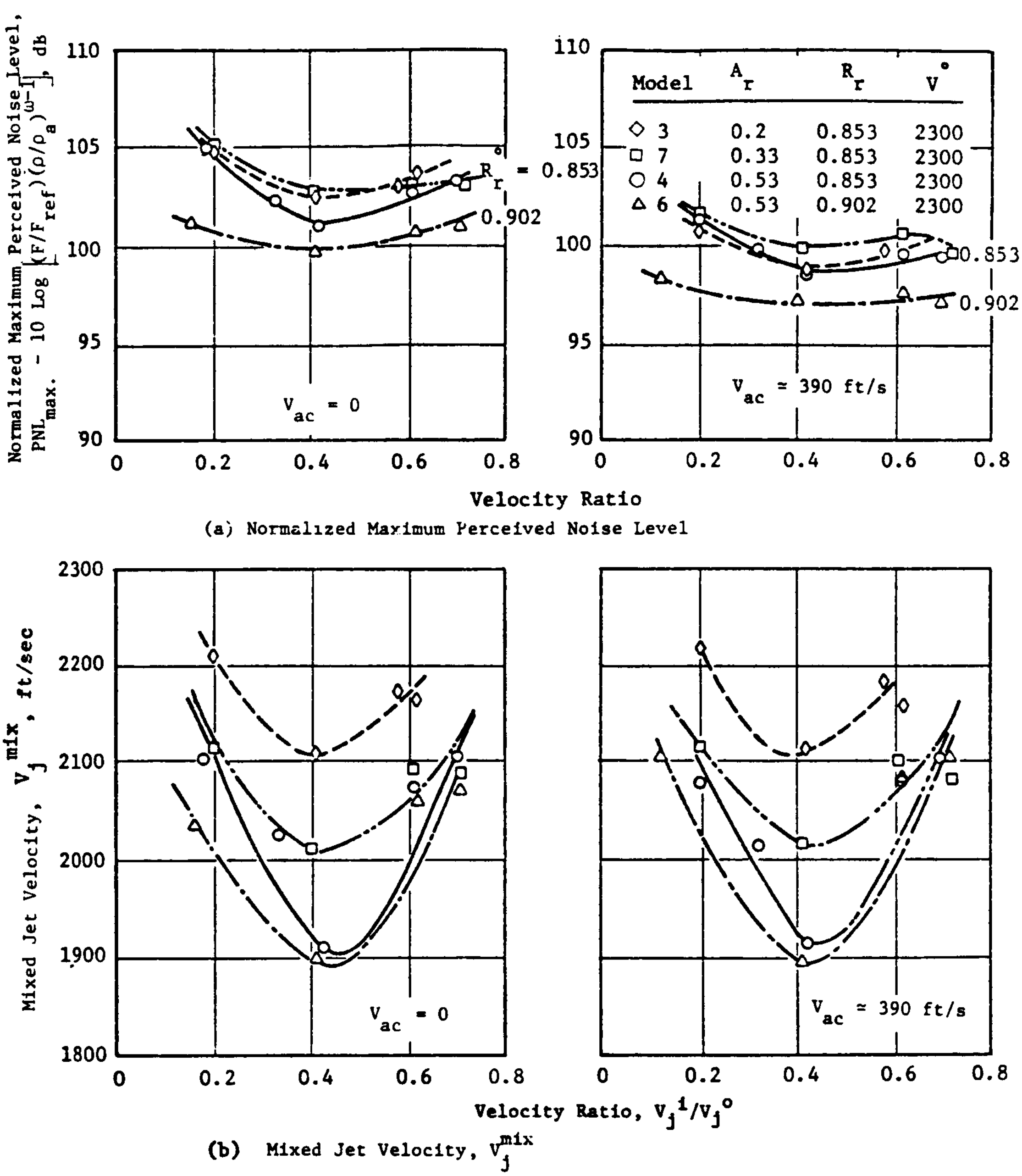

Figure 65. Effect of Velocity Ratio on the Acoustic Characteristics of Coannular Nozzles (Models 3, 4, 6, and 7).

the following expressions obtained (data are summarized in Figure 30 under the area ratio study):

$$PNLN_{max.} = \alpha_1 + \alpha_2 \left[10 \log \left(V_m^{mix}/c_a \right) \right]$$

the coefficients A and B are

Model	3		4		5		6	
V_{ac} ft/sec	0	400	0	400	0	400	0	400
α_1	85.050	79.520	82.98	90.610	81.960	81.040	82.260	74.740
α_2	6.304	6.956	7.34	3.407	7.016	5.981	7.311	8.272
σ_{xy}	0.650	0.810	2.65	2.970	0.930	0.780	0.200	0.270

The data of Figure 65(a) were then normalized to account for the different values of V_j^{mix}. The data so obtained are presented in Figure 66; they indicate that (1) the acoustic characteristics of the tested nozzles are not significantly affected by a change in the velocity ratio, and (2) the considerable variation in the data observed in Figure 67(a) is mainly due to the different values of V_j^{mix}.

The spectral characteristics (at θ_I = 60°, 90°, 130°) and the PNL directivities obtained during the velocity ratio study with Models 3 and 4 are presented in Figures 67 and 68. Reduction in aft angle acoustic data at velocity ratios that correspond to the smallest V_j^{mix} of the test series is indicated. Similar data were obtained with the other coannular Models 6 and 7 of this study.

An optimum velocity ratio, at which V_j^{mix} is a minimum, can be estimated from the definition of the mixed velocity as follows:

$$V_j^{mix} = \frac{\rho^o A^o \left(V_j^o\right)^2 + \rho^i A^i \left(V_j^i\right)^2}{\rho^o A^o V_j^o + \rho^i A^i V_j^i}$$

This can be rewritten as

$$V_j^{mix} = V_j^o \ \frac{1 + \rho_r A_r V_r^2}{1 + \rho_r A_r V_r} \qquad \text{where } \rho_r = \frac{\rho^i}{\rho^o},\ V_r = \frac{V_j^i}{V_j^o},\ A_r = \frac{A^i}{A^o}$$

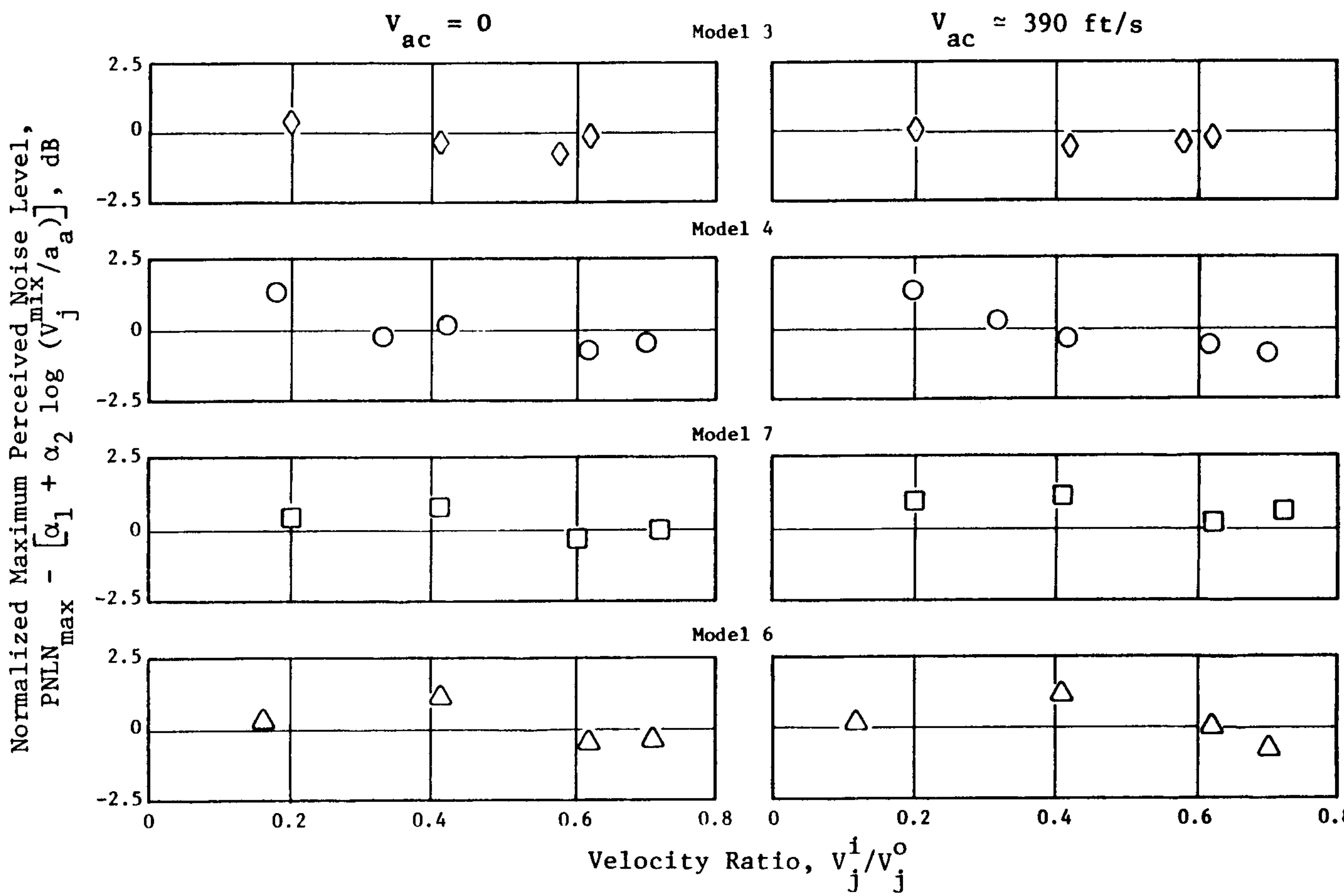

Figure 66. Effect of Velocity Ratio on a Normalized PNL_{max} of Models 3, 4, 6, and 7; Data Normalized to a Constant Mixed Stream Velocity.

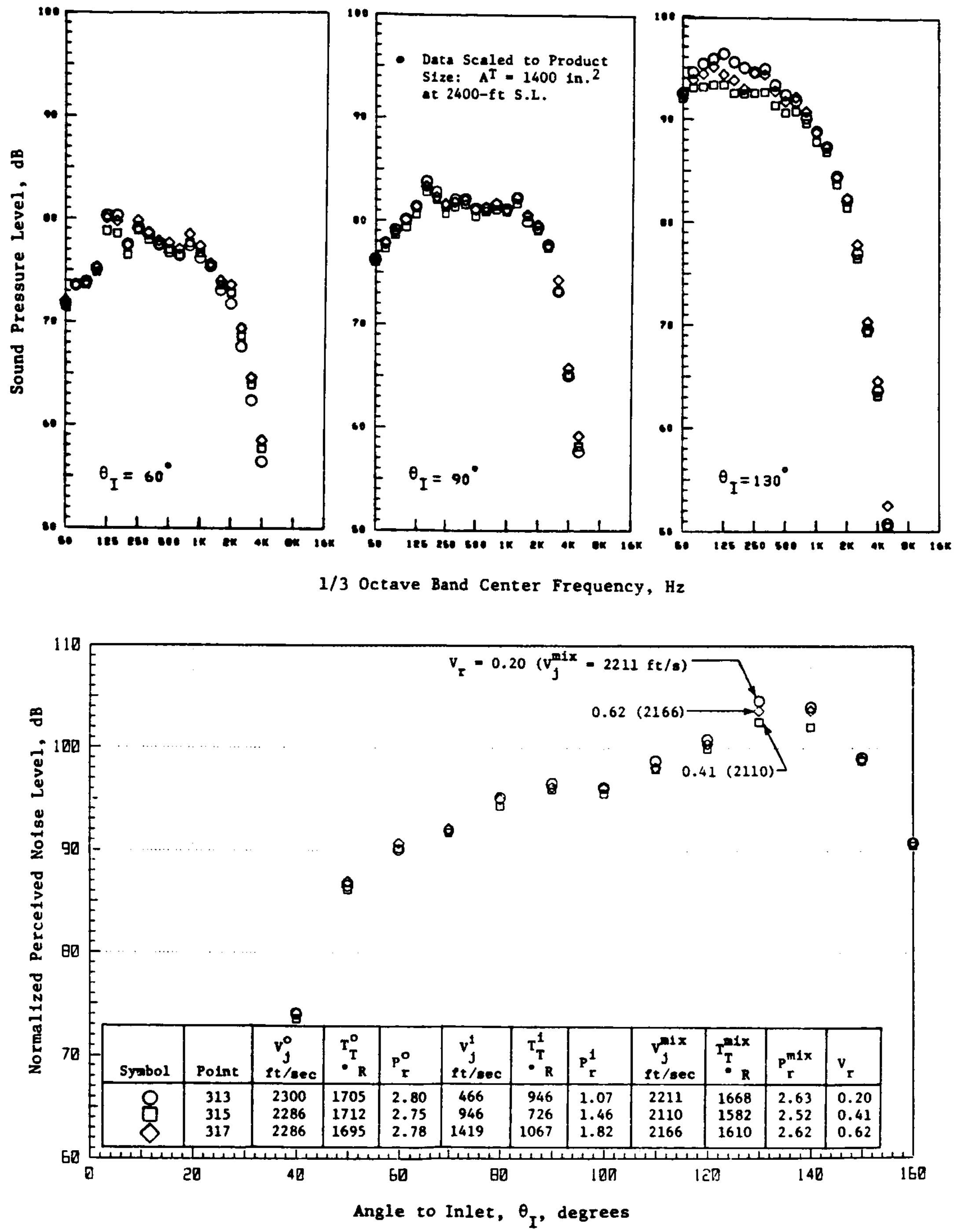

Symbol	Point	V_j^o ft/sec	T_T^o °R	P_r^o	V_j^i ft/sec	T_T^i °R	P_r^i	V_j^{mix} ft/sec	T_T^{mix} °R	P_r^{mix}	V_r
○	313	2300	1705	2.80	466	946	1.07	2211	1668	2.63	0.20
□	315	2286	1712	2.75	946	726	1.46	2110	1582	2.52	0.41
◇	317	2286	1695	2.78	1419	1067	1.82	2166	1610	2.62	0.62

(a) Static

Figure 67. Spectral Characteristics and PNL Directivities of Model 3 Obtained at Different Velocity Ratios with $V_j^o \simeq 2300$ Ft/Sec.

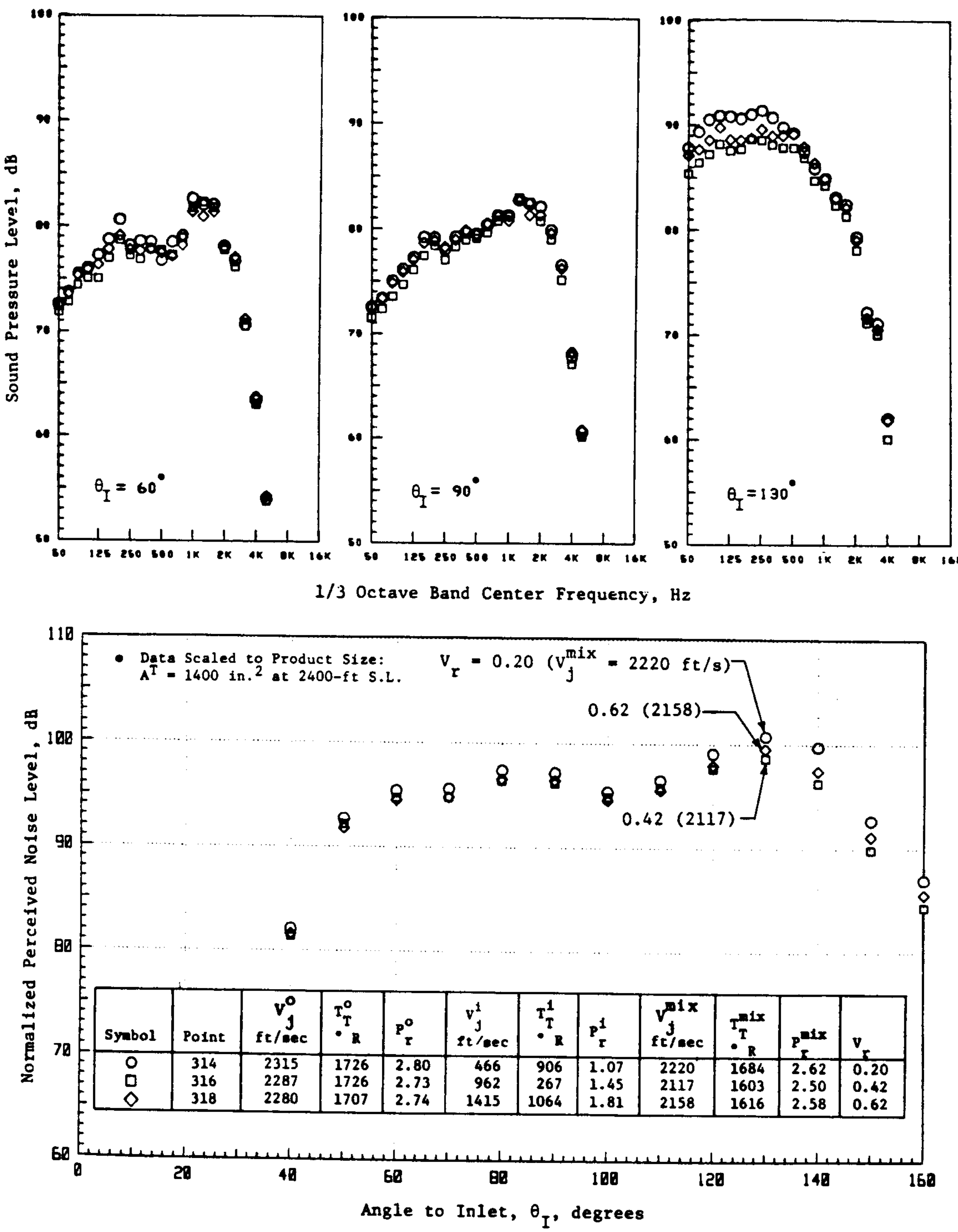

Symbol	Point	V_j^o ft/sec	T_T^o °R	P_r^o	V_j^i ft/sec	T_T^i °R	P_r^i	V_j^{mix} ft/sec	T_T^{mix} °R	P_r^{mix}	V_r
○	314	2315	1726	2.80	466	906	1.07	2220	1684	2.62	0.20
□	316	2287	1726	2.73	962	267	1.45	2117	1603	2.50	0.42
◇	318	2280	1707	2.74	1415	1064	1.81	2158	1616	2.58	0.62

(b) Flight, V_{ac} = 390 ft/s

Figure 67. Spectral Characteristics and PNL Directivities of Model 3 Obtained at Different Velocity Ratios with $V_j^o \simeq 2300$ Ft/Sec (Concluded).

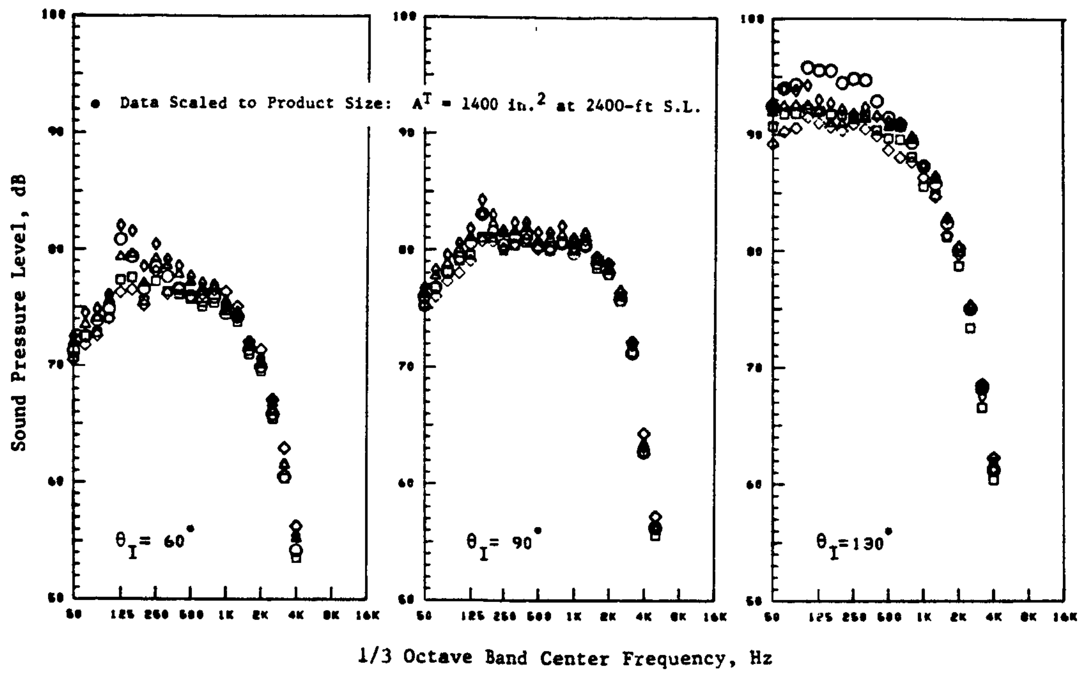

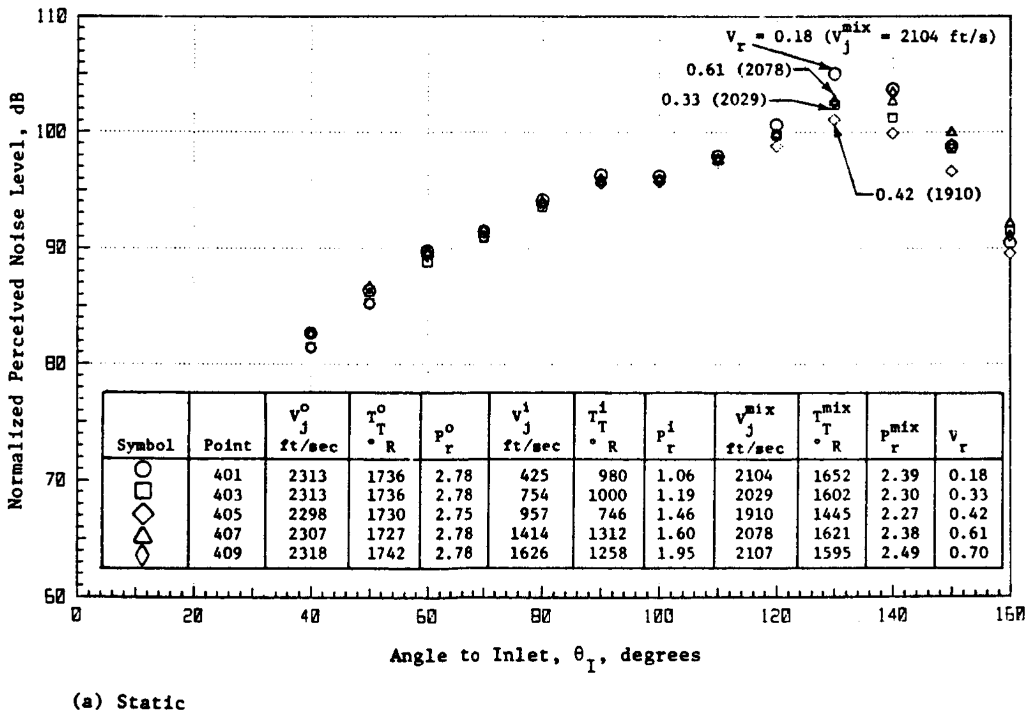

Symbol	Point	V_j^o ft/sec	T_T^o °R	P_r^o	V_j^i ft/sec	T_T^i °R	P_r^i	V_j^{mix} ft/sec	T_T^{mix} °R	P_r^{mix}	V_r
○	401	2313	1736	2.78	425	980	1.06	2104	1652	2.39	0.18
□	403	2313	1736	2.78	754	1000	1.19	2029	1602	2.30	0.33
◇	405	2298	1730	2.75	957	746	1.46	1910	1445	2.27	0.42
△	407	2307	1727	2.78	1414	1312	1.60	2078	1621	2.38	0.61
◊	409	2318	1742	2.78	1626	1258	1.95	2107	1595	2.49	0.70

(a) Static

Figure 68. Spectral Characteristics and PNL Directivities of Model 4 Obtained at Different Velocity Ratios with $V_j^o \simeq$ 2300 Ft/S.

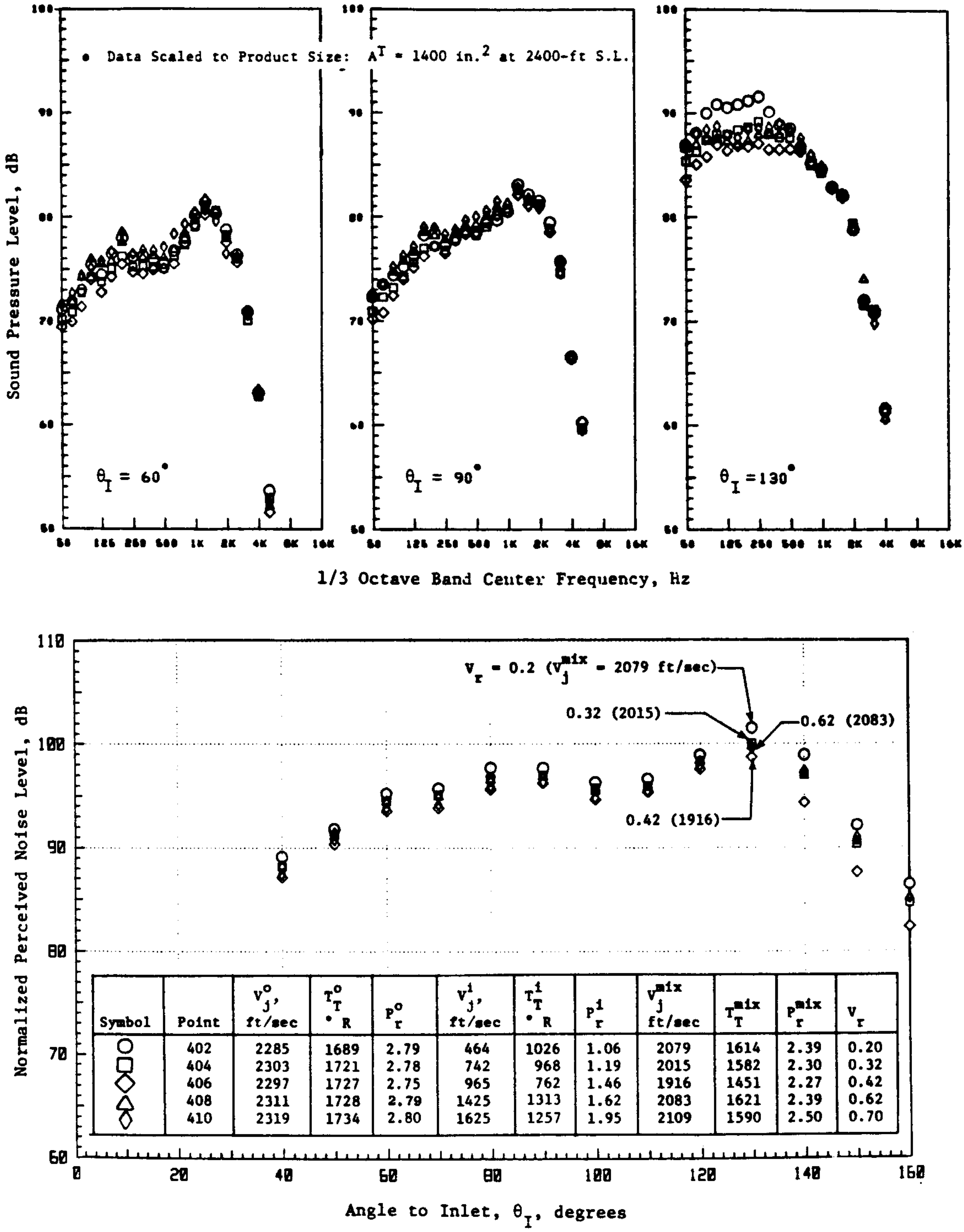

Symbol	Point	V_j^o, ft/sec	T_T^o °R	P_r^o	V_j^i, ft/sec	T_T^i °R	P_r^i	V_j^{mix} ft/sec	T_T^{mix}	P_r^{mix}	V_r
○	402	2285	1689	2.79	464	1026	1.06	2079	1614	2.39	0.20
□	404	2303	1721	2.78	742	968	1.19	2015	1582	2.30	0.32
◇	406	2297	1727	2.75	965	762	1.46	1916	1451	2.27	0.42
△	408	2311	1728	2.79	1425	1313	1.62	2083	1621	2.39	0.62
◇	410	2319	1734	2.80	1625	1257	1.95	2109	1590	2.50	0.70

(b) Simulated Flight,
$V_{ac} \simeq$ 390 ft/s

Figure 68. Spectral Characteristics and PNL Directivities of Model 4 Obtained at Different Velocity Ratios with $V_j^o \simeq$ 2300 Ft/S (Concluded).

For a given V_j^o and A_r and assuming that ρ_r is a constant (over the test series of this study ρ_r ranges from 1.5 to 2.0), the above expression for V_j^{mix} can be shown to result in a minimum value at

$$V_r = \frac{(1 + \rho_r A_r)^{1/2} - 1}{\rho_r A_r}$$

which approximates for small values of $\rho_r A_r$ to

$$V_r = 1/2 - 1/8 \, \rho_r A_r$$

For example, this expression defining V_r for a minimum in V_j^{mix} will yield $V_r = 0.38$ to 0.45 for the test nozzles of this study ($A_r = 0.2$ to 0.53, and $\rho_r = 1.5$ to 2.0). This confirms the data presented in Figure 65(b).

In conclusion, this study indicates that the noise levels of nozzles with $A_r < 1$ are not significantly affected by a variation in the inner-to-outer velocity ratio. But, for a maximum benefit in the aft angle noise data, the coannular plug nozzles should be operated at a value of V_r which yields a minimum V_j^{mix}.

5.1.4 Special Remarks Regarding Shock Noise and Shock Noise Control for High-Radius-Ratio Coannular Plug Nozzles

In the previous subsections, the general acoustic characteristics associated with coannular plug nozzles have been discussed for static and simulated flight conditions. This subsection describes other significant experimental results obtained in the General Electric anechoic test facility regarding the effectiveness of a convergent-divergent flowpath in shock noise control, the effect of temperature on shock noise, and the influence of downstream shock structure on the resultant shock noise signature and its control.

5.1.4.1 Influence of Contouring for Coannular Plug Nozzles

During earlier static experiments with high-radius-ratio-coannular plug nozzles (Reference .2), it was observed that substantial forward quadrant shock noise reduction was achieved with reference to a conical nozzle. Figure 69 is a summary illustration of this experimental observation. The data show that, at the same shock strength parameter, β^{eff} (as defined in the figure), there exists a forward quadrant lift in the static data due to the simulated flight, indicating that the coannular plug nozzle still results in shock cell generated exhaust nozzle noise. As pointed out earlier in flight, this shock-associated noise is amplified in the forward quadrant in simulated flight and thus additional noise reduction could be obtained is the shock cell pattern could be further mitigated or eliminated altogether.

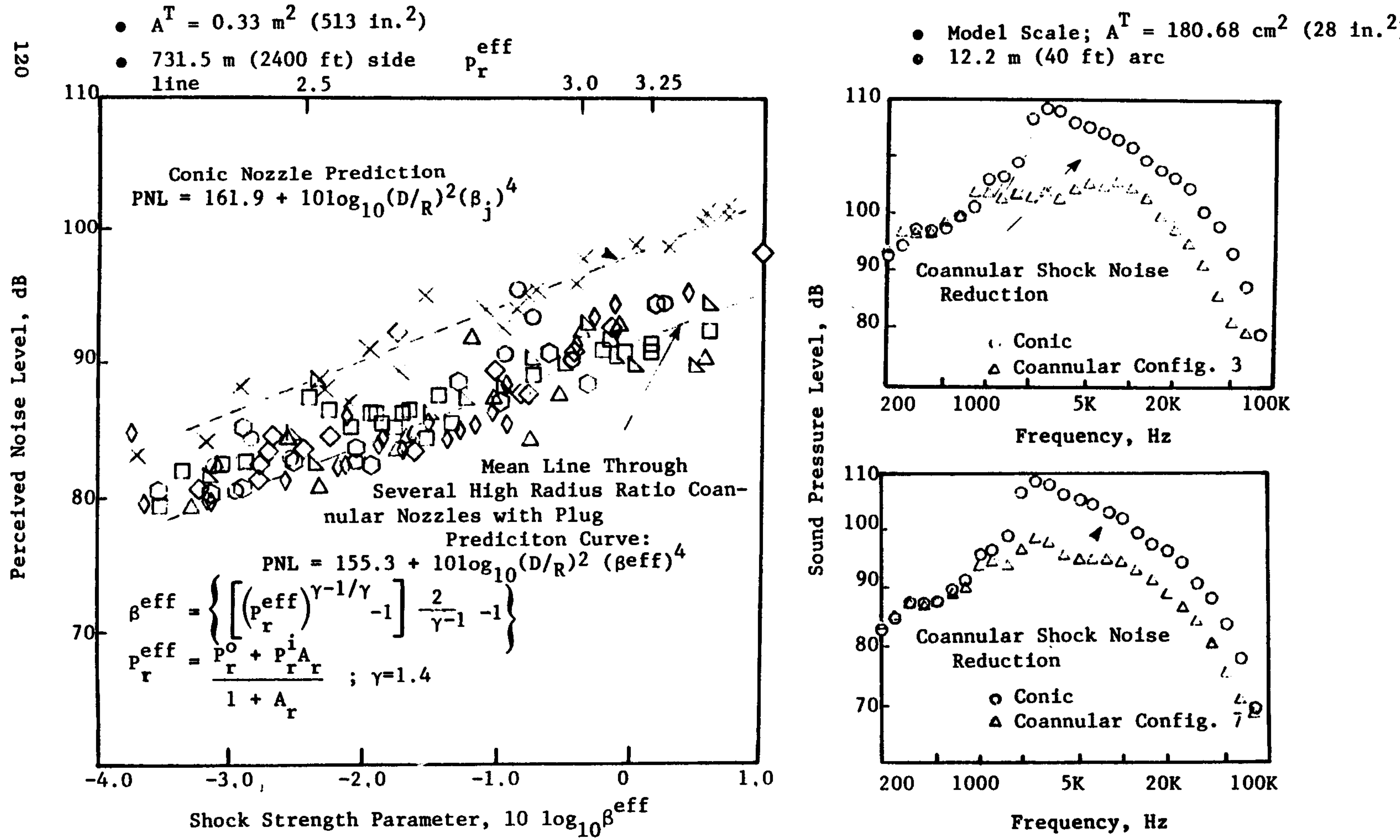

a) PNL Shock Noise Reduction at $\theta_I = 50°$ Between a Conic Nozzle and Several Coannular Plug Nozzles for a Wide Range of Operating Conditions.

b) Spectral Illustration of Coannular Plug Shock Noise Reduction at $\beta \sim 0.83$ and $\theta_I = 50°$.

Figure 69. Illustration of Coannular Plug Nozzle Shock Noise Reduction Relative to a Baseline Conical Nozzle (Reference 10).

As a first attempt toward obtaining reduced coannular nozzle shock noise, the outer shroud of the coannular plug nozzle was extended, holding the diameter of the shroud constant and obtaining a nozzle throat to exit plane area ratio which would correspond to convergent-divergent design area ratio for shock-free perfect expansion at $P_r^o \sim 3.2$. No special contouring was performed for this nozzle. To evaluate the convergent-divergent effectiveness of this simplistic design, a series of heated coannular flow static tests was performed. For this test sequence, the area ratio of the nozzle was $A_r \sim 0.2$, and the inner stream was held at a pressure ratio of $P_r \sim 1.6$. For the heated outer flow, the outer pressure ratio was slowly varied from 2.5 to 3.6. Figure 70 illustrates the results.

The results shown in Figure 70 indicate that shock control was not obtained. The PNL values at $\theta_I = 60°$ show that with a relatively fine grain outer nozzle pressure ratio variation over the design condition for perfect expansion no significant decrease in the forward quadrant shock noise was observed. These results indicate that in order to obtain perfect expansion for coannular or annular plug nozzle, proper care in the nozzle flowpath contour will be needed. It should be noted here that a subsequent contoured convergent-divergent nozzle has been successfully tested under a separate NASA contract effort.

5.1.4.2 Temperature Influences on Coannular Shock Noise

To determine the effect of temperature on coannular shock cell noise, two series of static acoustic tests have been performed. One test series was performed when both streams were heated, and the second series of tests was performed when both streams were at room temperature - but at nearly the same effective pressure ratio or shock strength condition. The results summarized in Figure 71 show two distinct levels of forward quadrant ($\theta_I = 60°$) shock-cell noise. Figures 72 and 73 illustrate PNL directivity and SPL spectra for selected test points at a $P_r^{mix} \sim 3.0$. These results indicate that forward quadrant as well as aft quadrant radiated noise was substantially reduced for the room temperature jets. It should be noted that room temperature jets are at considerably lower V_J^{mix} and, therefore, result in a lower jet mixing noise level. Nontheless, for circular nozzles, Tanna (Reference 19 has shown for similar temperature differences that there was no shock noise sensitivity with temperature. In actuality, the differences noted above could be temperature effects, jet mixing noise effects or a combination of these two effects on the shock noise. These diagnostic measurements are insufficient to separate each of the effects, but indicate that a temperature influence on the shock noise amplitude does exist. Further work in this important area is needed.

5.1.4.3 Influence of Downstream Shock Structure on the Resultant Shock Noise Signature

In specifying the levels of shock noise for any coannular or annular plug nozzle configuration, the shock region responsible for shock cell associated

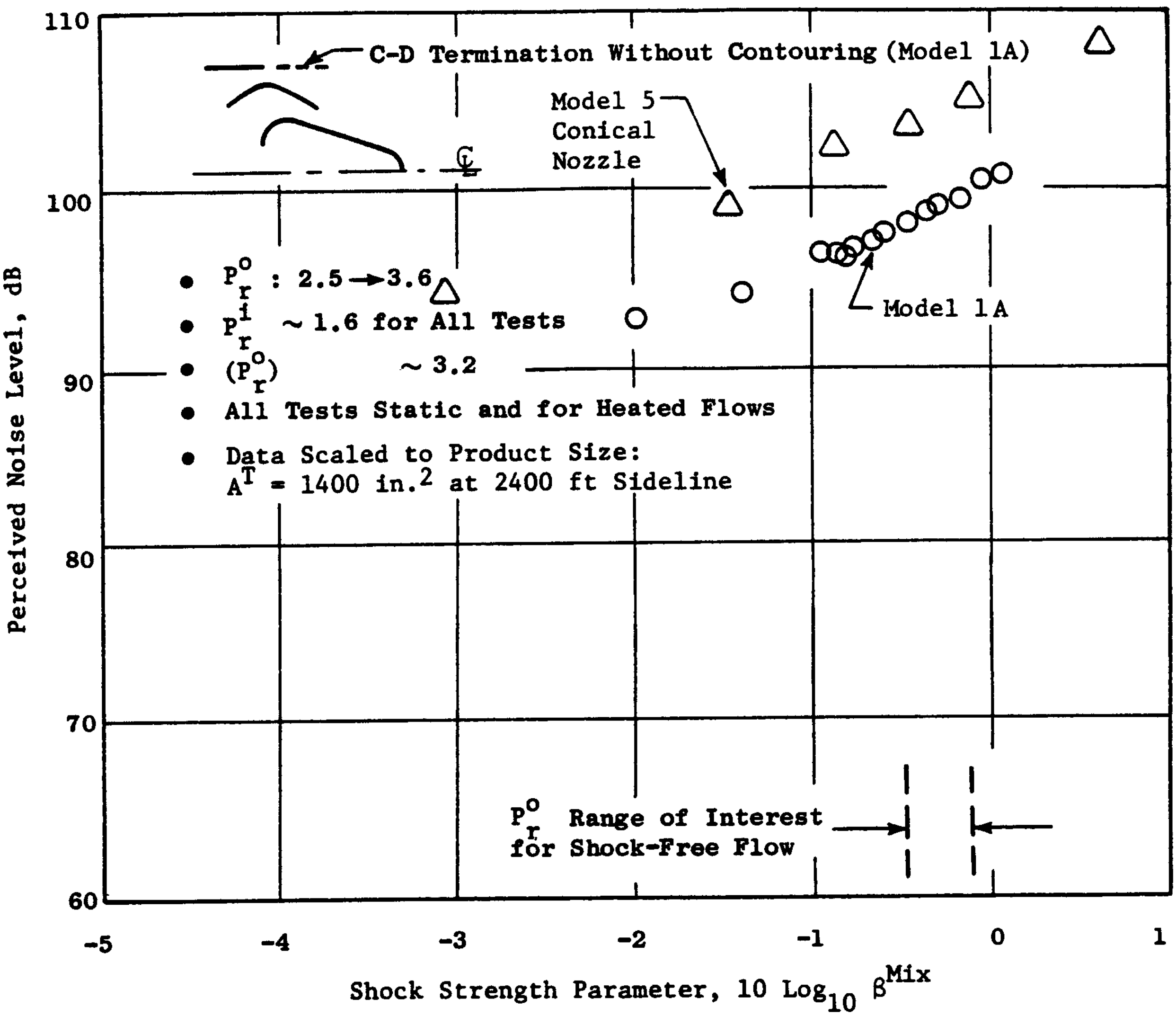

Figure 70. Coannular Plug Nozzle Acoustic Tests with Outer C-D Flow, Directivity Angle, θ_I = 60°.

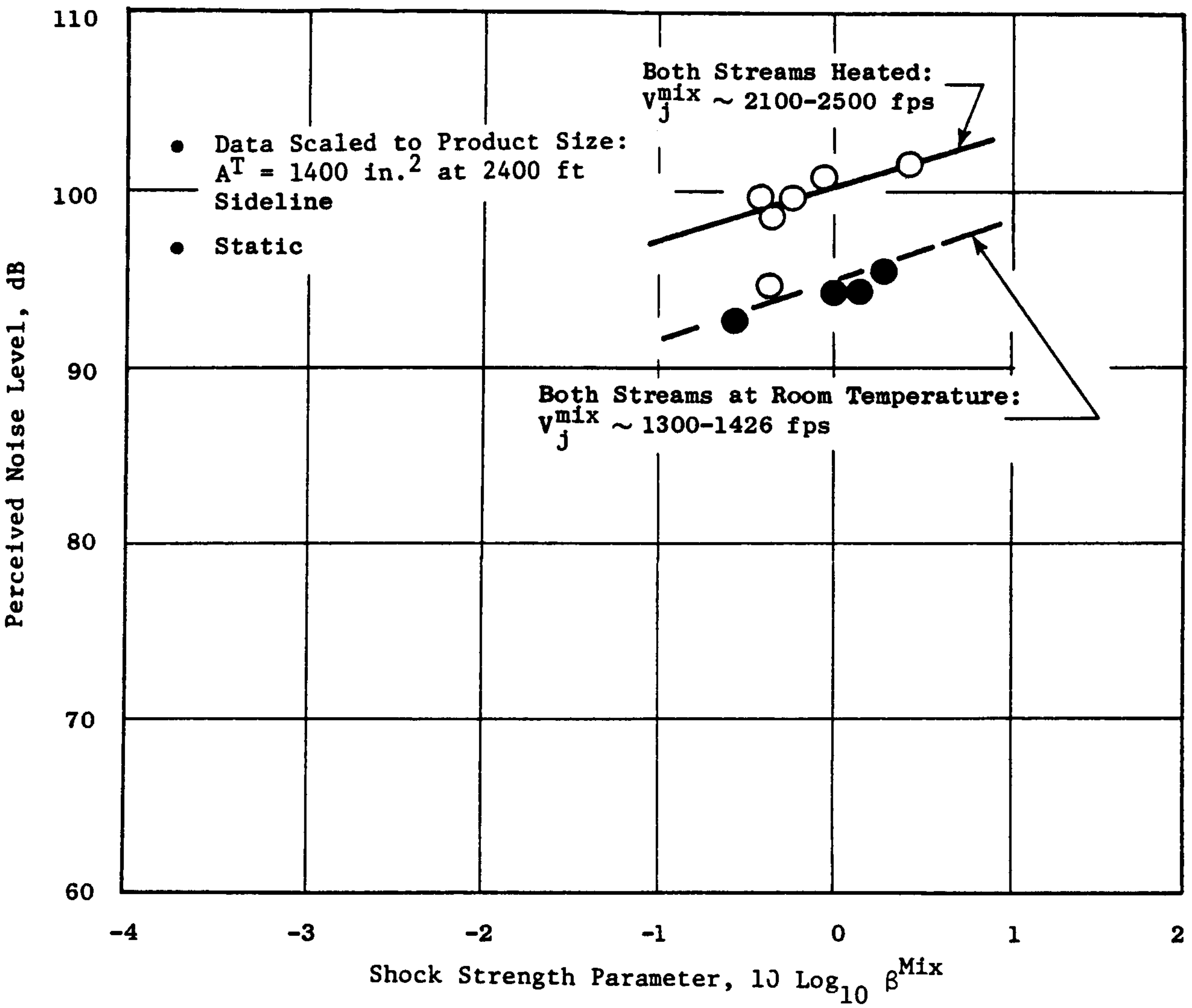

Figure 71. Coannular Plug Nozzle Data at θ_I = 60° for Heated and Room Temperature Jets Over the Same Pressure Ratio Range.

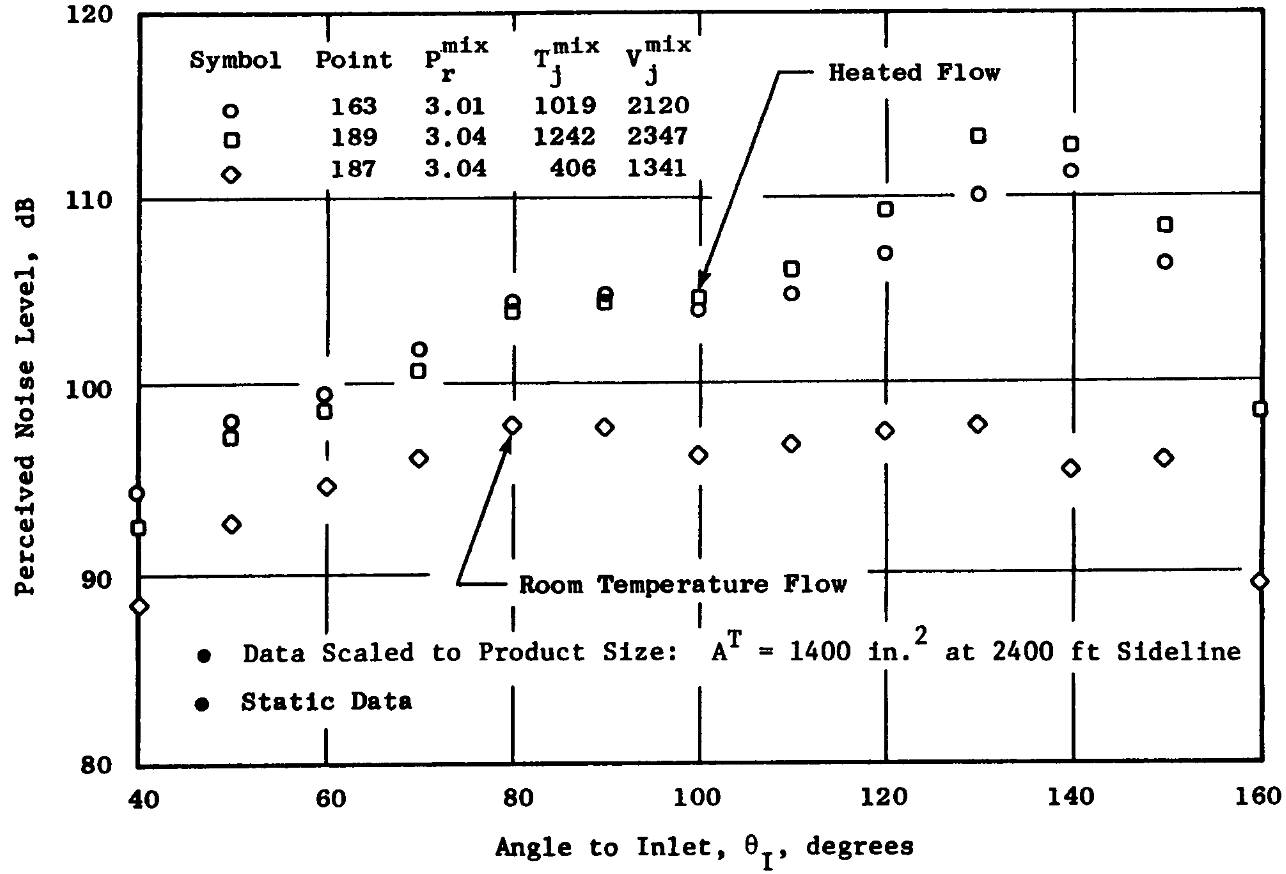

Figure 72. PNL Directivity for Coannular Plug Nozzle Tests with Heated and Room Temperature Flows.

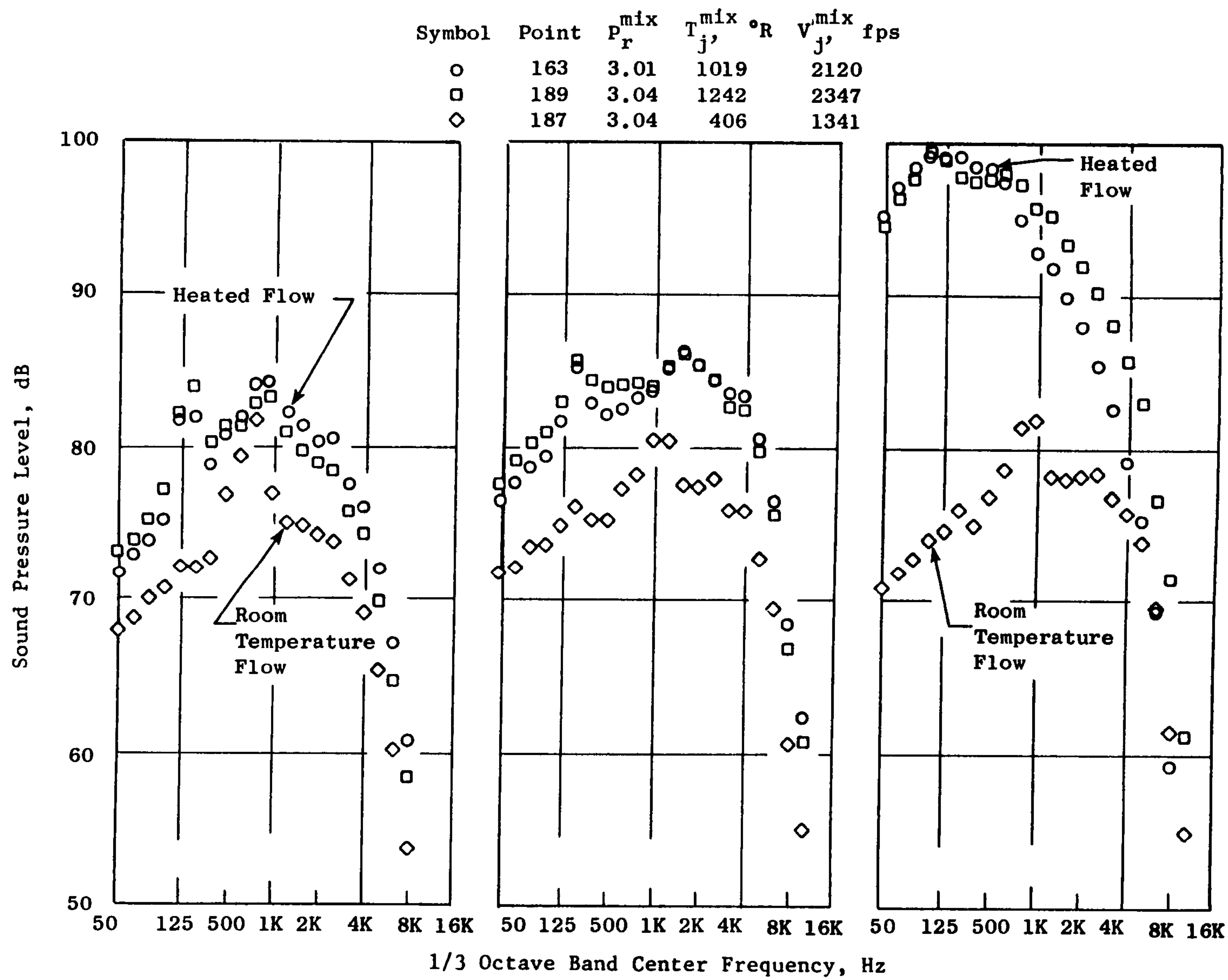

(a) Directivity Angle, $\theta_I = 60°$ (b) Directivity Angle, $\theta_I = 90°$ (c) Peak Noise Angle

Figure 73. SPL at $\theta_I = 60°$, $90°$, and Maximum Angle for Coannular Plug Nozzle Tests with Heated and Room Temperature Flows.

noise levels should be known. Earlier General Electric work (Reference 2) with coannular plug nozzles has indicated that the primary contribution to the shock cell noise may be due to the downstream shock cell structure. This is one reason why the coannular shock noise prediction procedure given in Section 5.3 uses D_{eq} as a characteristic dimension.

Test results obtained during the present investigation shed some light on this subject. Figure 74 shows GE laser velocimeter measurements of the axial mean velocity decay for two coannular plug nozzle experiments (Model 2). The first experiment is for LV measurements when the outer stream and inner streams of the coannular plug nozzle are operating at supercritical pressure ratios; the second experiment is for LV measurements when operating the outer annular plug nozzle at the same pressure ratio as the first experiment but with the inner stream operated at a subcritical pressure ratio. The laser velocimeter traces of the first experiment (both streams at supercritical conditions) show a strong series of shock cells, the second experiment (the inner stream subcritical) shows no downstream shock pattern -- although the mean velocity is measured to be fully supersonic (well above the inner stream velocity). The flow in the outer stream of both of these experiments was set at the same pressure ratio condition and therefore at equal outer stream shock structures and strength. Figures 75 and 76 illustrate companion static and simulated flight acoustic measurements. The static and simulated flight measurements show significant shock noise reduction or control in the forward and aft quadrant. Although the peak angle noise was not influenced by the observed phenomenon, the flight case duration correction was significantly reduced. For a level flyover calculation, a 2.6 EPNdB reduction was realized. The above results can be rationalized to make the following observations:

- The control of the downstream shock cell structure as well as the shock cell structure in the vicinity of the plug (not all of the shock noise was gone for the second experiment) is important to annular and coannular plug nozzle shock control. This may imply that for coannular plug or annular plug nozzles more than a C-D termination will be required for a total shock control.
- Flow visualization and laser velocimeter measurements will be important to further quantify the physical phenomenon.
- A significant additional flight noise benefit (2.6 ΔEPNdB for an unsuppressed annular/coannular nozzle) may be obtainable if total shock noise control can be achieved.

Test Point	V_j^o fps	P_r^o	T_T^o °R	V_j^i fps	P_r^i	T_T^i °R	V_j^{mix} fps	P_r^{mix}	T_T^{mix} °R
204	2555	3.78	1697	1644	3.21	794	2378	3.60	1521
216	2563	3.78	1708	1109	1.57	844	2416	3.42	1621

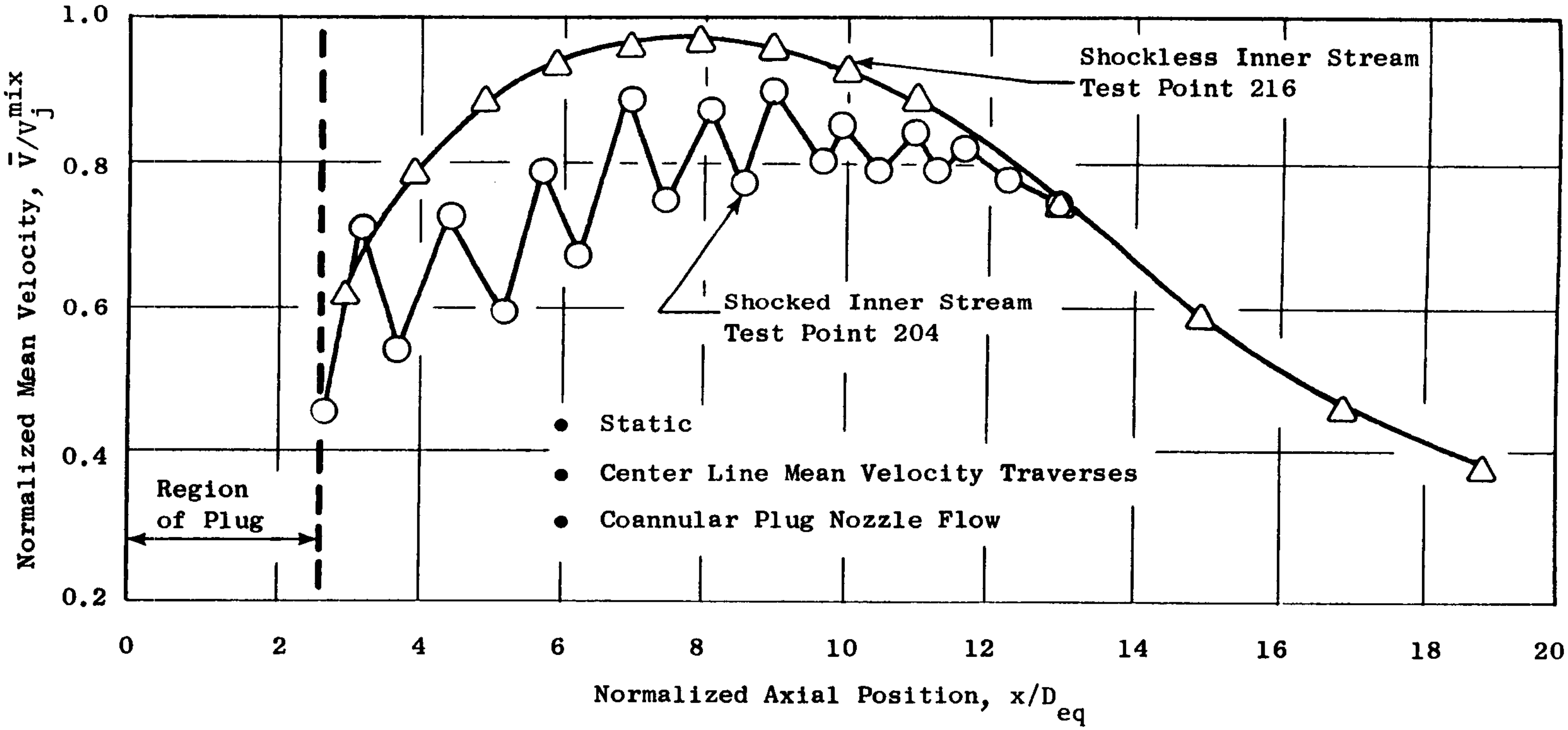

Figure 74. Laser Velocimeter Tests Showing Influence of Coannular Inner Stream on Downstream Shock-Cell Structure.

Test Point	V_j^o fps	P_r^o	T_T^o °R	V_j^i fps	P_r^i	T_T^i °R	V_j^{mix} fps	P_r^{mix}	T_T^{mix} °R
204	2555	3.78	1693	1644	3.21	794	2378	3.60	1521
216	2563	3.78	1708	1109	1.57	854	2416	3.42	1621

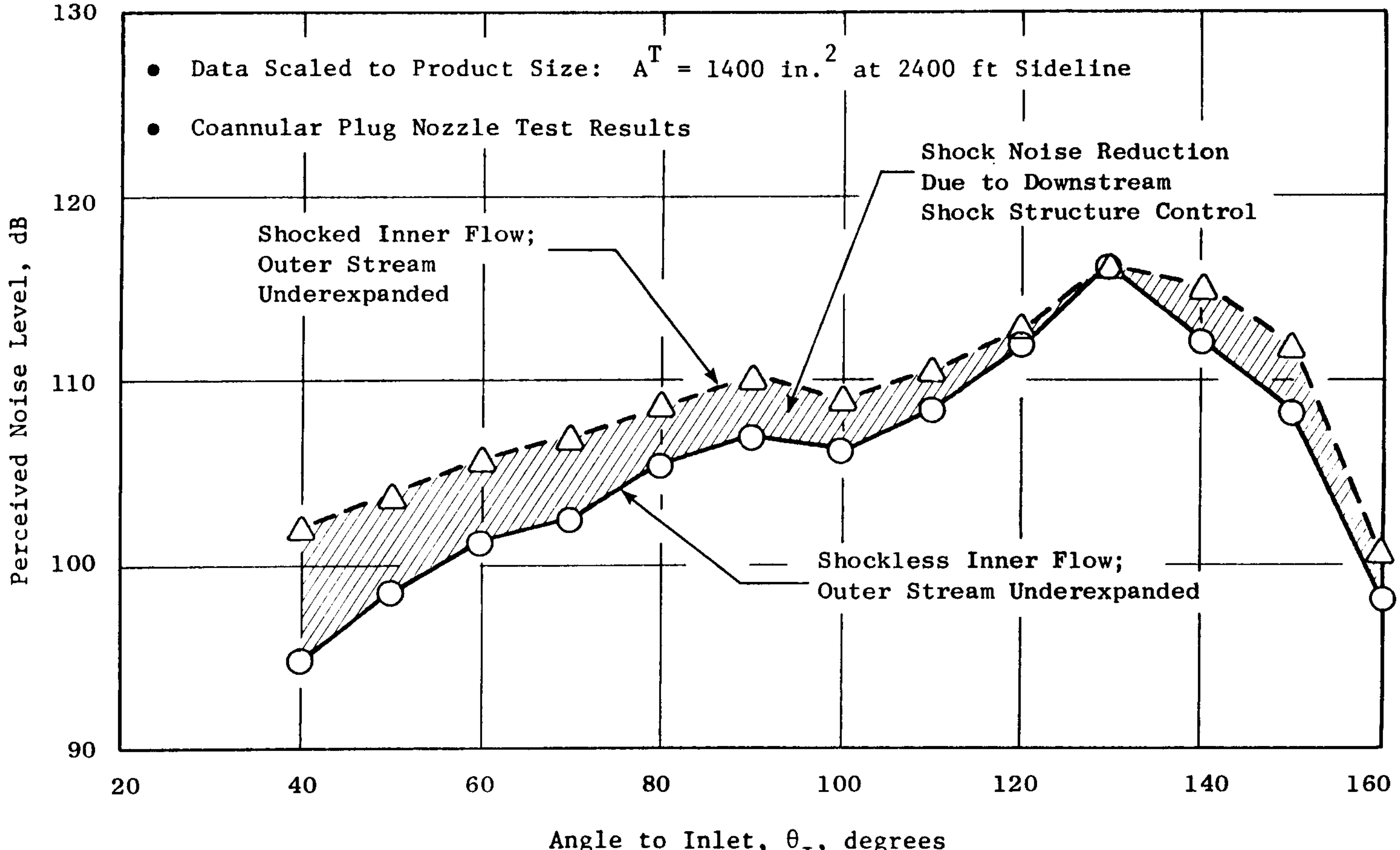

Figure 75. Influence of Coannular Plug Nozzle Shock-Cell Structure on PNL Directivity.

Test Point	V_j^o fps	P_r^o	T_T^o °R	V_j^i fps	P_r^i	T_T^i °R	V_j^{mix} fps	P_r^{mix}	T_T^{mix} °R
206	2558	3.81	1693	1659	3.22	807	2385	3.63	1523
218	2566	3.81	1703	1119	1.60	825	2416	3.45	1612

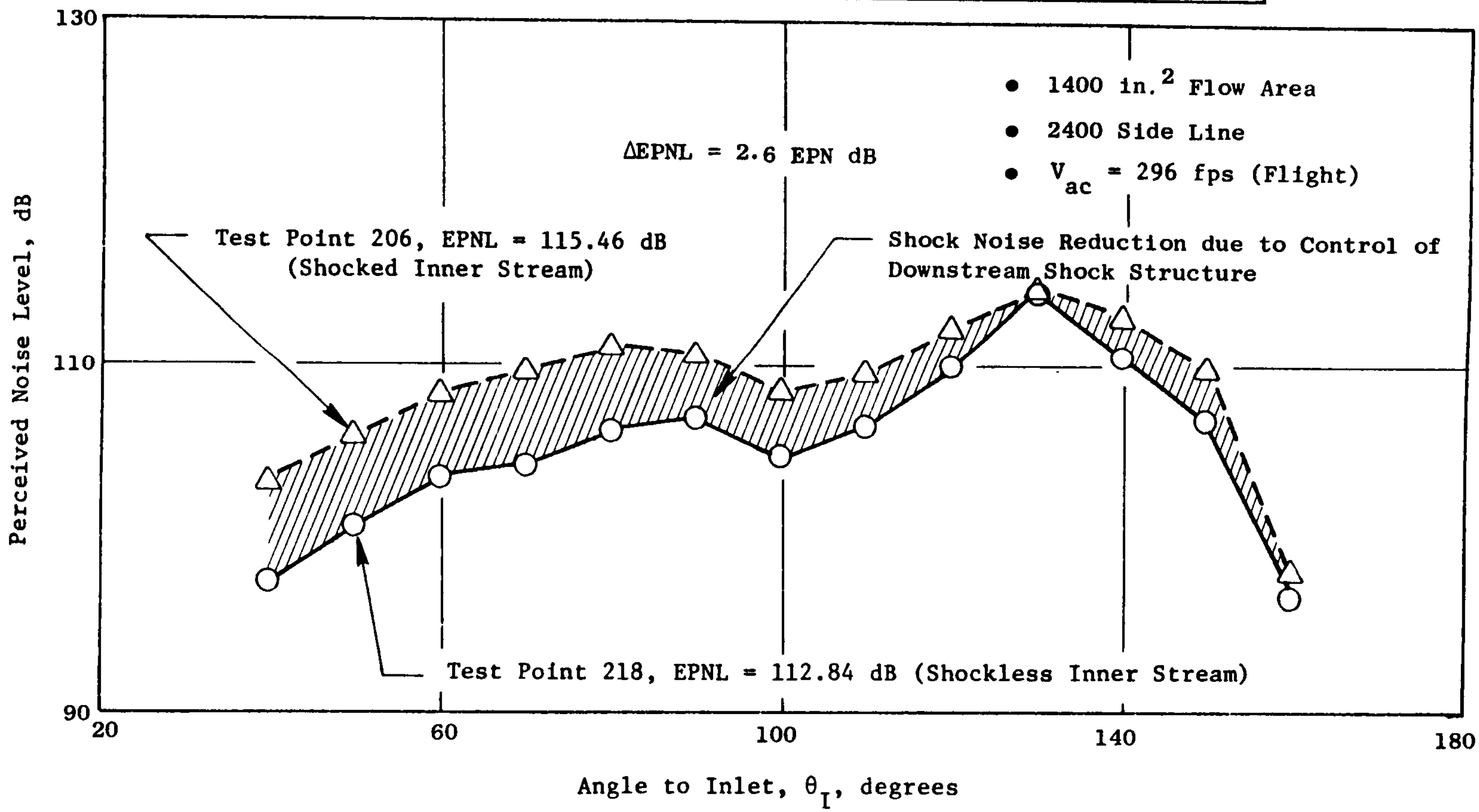

Figure 76. Influence of Coannular Plug Nozzle Downstream Shock Structure on PNL Directivity - Simulated Flight Acoustic Tests.

5.2 LASER VELOCIMETER TEST RESULTS

A laser velocimeter has been employed as a noninvasive diagnostic tool to measure the jet plume characteristics of conic and coannular plug nozzle models. A knowledge of the turbulent mixing characteristics of the jets gives an insight into the noise radiation from the jets. Extensive surveys of the mean and turbulent velocity measurements were performed for a wide range of flow conditions for the scale model nozzles. The following were the objectives for the LV measurements:

1. Determine the conic nozzle (Model 5) characteristics, at typical takeoff condition (viz, V_j = 2411 ft/sec, P_r = 3.17, T_T = 1700° R), at static and simulated flight conditions. This would serve as the baseline case for the purpose of comparison with other nozzles.

2. Determine the typical jet plume characteristics of an inverted velocity profile coannular plug nozzle operating at typical takeoff condition. Model 2 has been chosen for the purpose of illustration.

3. Evaluate the influence of the outer flowpath termination (i.e., convergent or convergent-divergent) on the shock cell structure of the plume and its influence on the shock cell noise.

4. Study the aerodynamic characteristics of the coannular plug nozzles operating at off-design pressure ratios (i.e., under- or over-expanded nozzles).

5. For a set of prescribed outer and inner stream conditions, evaluate the effect of nozzle area ratio and outer stream radius ratio on the plume development.

6. Determine the influence, if any, of the struts in the outer flowpath on the turbulent velocity levels and the mean velocity distribution.

7. Study the effect of geometric misalignment of the coannular plug nozzle on the plume asymmetry. This factor arose during the course of LV testing.

5.2.1 Exhaust Plume Characteristics of a Conic Nozzle

Figure 77 shows the shock cell pattern for the conic nozzle (Model 5) at two radial locations (viz, at the centerline and at the tip of the nozzle) for static condition. The aerodynamic test conditions represent typical take-off conditions. One observes that there are seven shock cells within the first 10 diameters of the nozzle at R/R_2^o = 0.0, but only one shock cell at R/R_2^o = 1.0 which is due to the deceleration by the ambient air. The location of velocity maxima and minima at R/R_2^o = 0.0 and 1.0 occurs at the same X/D location indicating that the Mach disks of the shock cells are fairly normal to

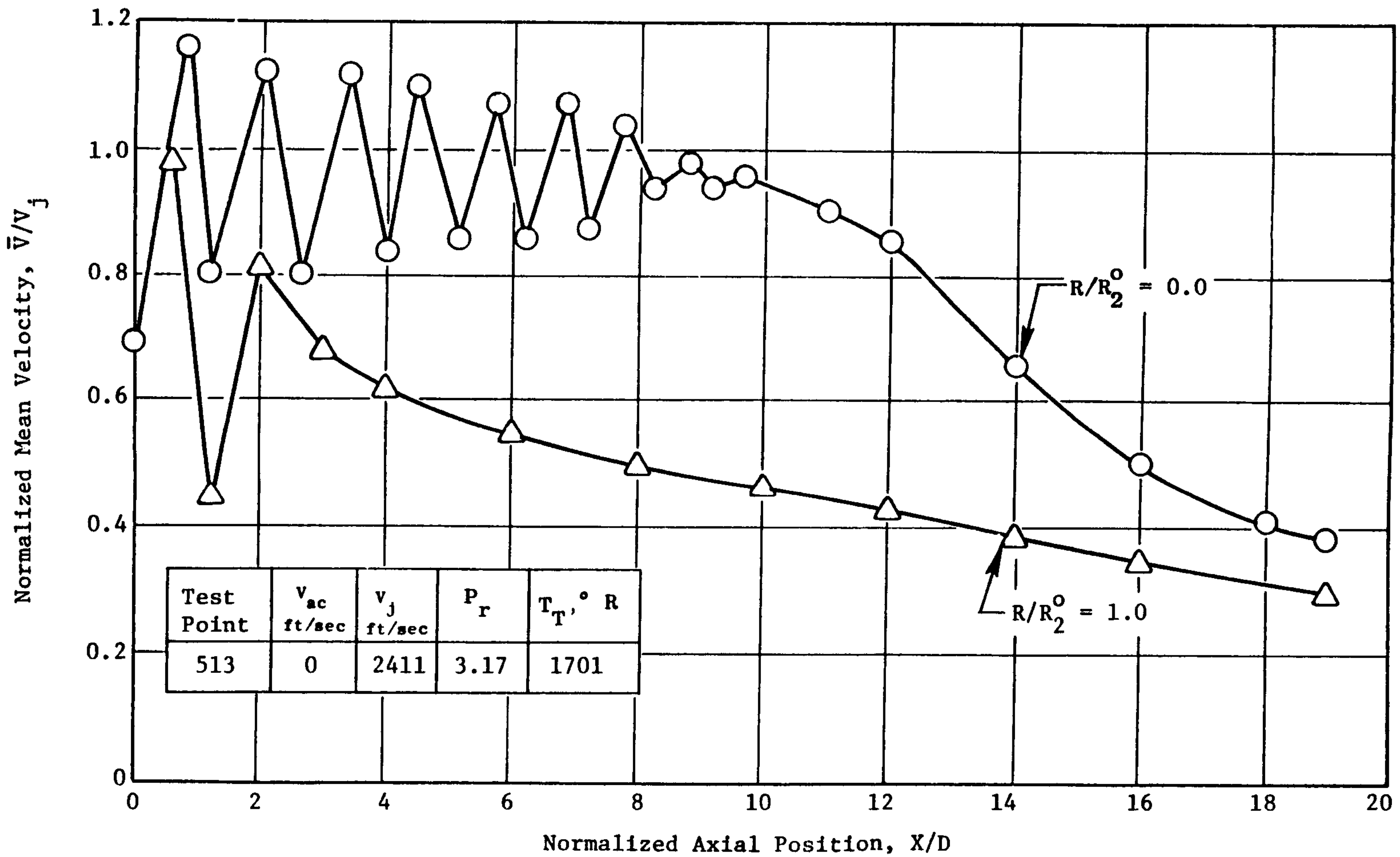

Figure 77. Mean Velocity Variation at Two Radial Locations for Conic Nozzle (Model 5) at Typical Takeoff Conditions (Static).

the jet axis. The shock strength parameter, β ($= \sqrt{M_j^2 - 1}$) is equal to 1.0 for P_r = 3.21. The average shock cell spacing for the first three cells equals 1.3 D, but equals only 1.03 D for the last three cells. The Fisher and Harper-Bourne model for shock noise (with L = 1.1 βD) yields an average shock cell spacing of 1.1 D, which seems to be a mean of the measured values.

Figure 78 shows the shock cell pattern for the conic nozzle operating at a typical takeoff condition at two radial locations for a free-jet velocity of 400 ft/sec. There are nine shock cells along the jet axis compared to seven shock cells in the static case, and there are two shock cells at $R/R_2^o = 1.0$ compared to one shock cell in the static case. This indicates the stretching of the shock cell pattern (i.e., the length of the jet plume over which the jet is locally supersonic) which is due to the reduced shear in simulated flight. Also, the average shock cell spacing for the first three cells equals 1.42 D compared to 1.3 D in the static case, indicating that the free jet has stretched each shock cell, as well. However, the Mach disks of the shock cells are still normal to the jet axis and do not seem to be influenced by the free jet. A slower decay is perceived in the mean velocity of the jet at both radial locations downstream of the shock cell pattern for the free-jet case as compared to the static case. Again, this is due to the reduction in shear by the free jet.

Next, the characteristics of turbulent velocity distribution for the conic nozzle for static and free-jet cases are studied. Figure 79 shows the axial variation of the turbulent velocity at two radial locations for the same static case as in Figure 77. Note that within the potential core (i.e., for X < 4D) the turbulent velocity remains within 4% of the jet exit velocity along the nozzle centerline and increases steadily through the transition and the fully developed regions of the jet to a peak value of 15% of V_j at X ≈ 14D. But, the turbulent velocity at $R/R_2^o = 1.0$ is about 12% of V_j at one diameter downstream of the nozzle exit plane and rises rapidly to a peak value of about 18% and remains within a variation of 2% for about 10 diameters, then drops after that. The turbulent velocity at the nozzle tip is fairly high compared to the centerline value, since it is in the middle of the shear layer of the jet where the turbulent shear stresses are maximum. Recall that the turbulent shear stress is directly proportional to the square of the turbulent velocity. As one moves downstream, the shear layer widens and, hence, the radial velocity gradients at $R/R_2^o = 1.0$ are reduced, resulting in lower turbulent velocity.

Figure 80 shows the axial variation of the turbulent velocity for the conic nozzle at two radial locations as in Figure 79, in the presence of a free jet at 400 ft/sec. It is worth mentioning that the turbulent velocities at the nozzle centerline are at about the same level as in the static case for locations within the potential core. Nevertheless, downstream of the potential core, the turbulent velocities are lower in simulated flight indicating a reduction in the turbulent shear stresses due to the free jet. At R/R_2^o = 1.0, the turbulent velocity reaches a peak value of 16% of V_j in comparison to 18% of V_j in the static case - yet another indication of reduced shear due to the free jet.

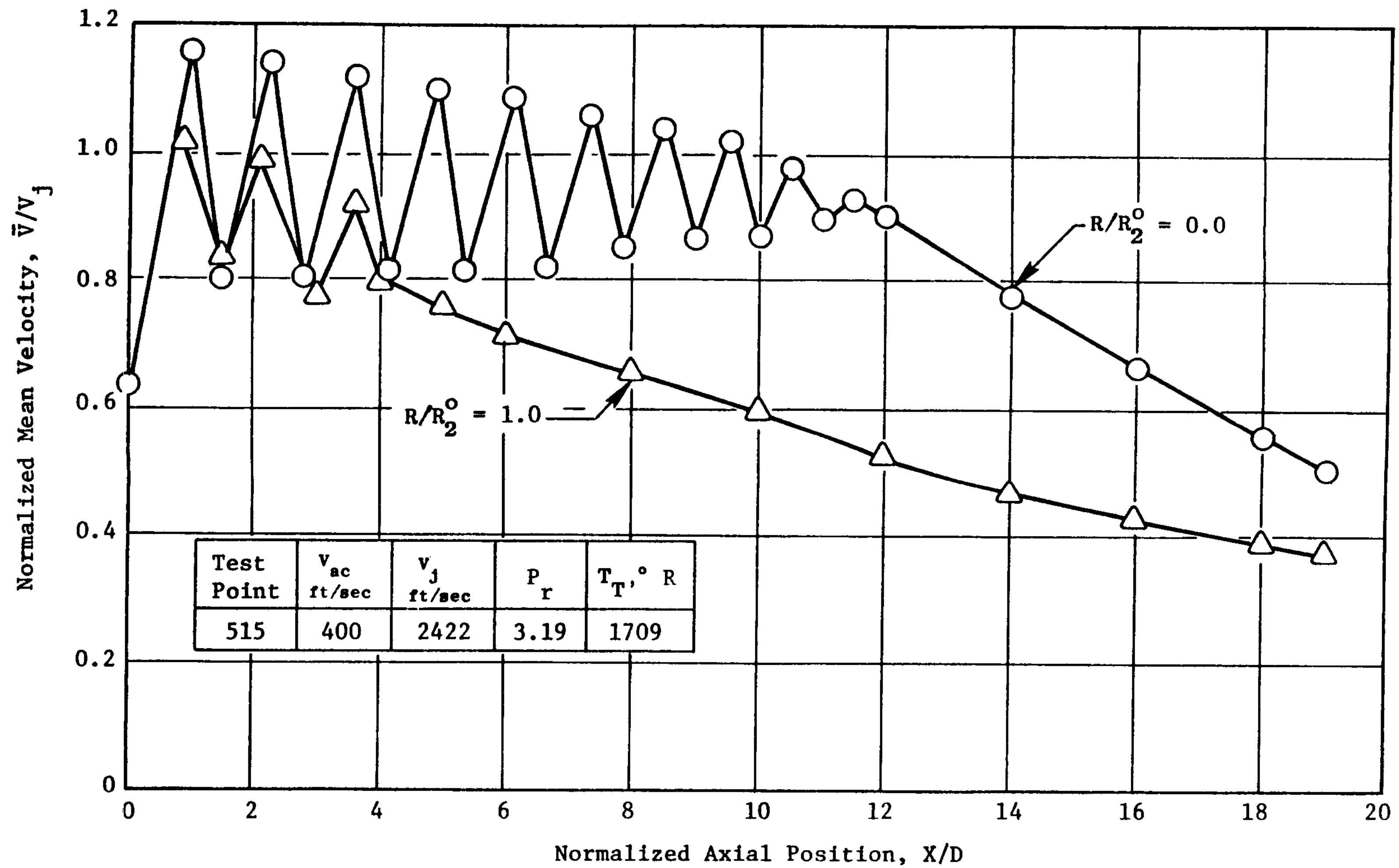

Figure 78. Mean Velocity Variation at Two Radial Locations for Conic Nozzle (Model 5) at Typical Takeoff Conditions (Flight, $V_{ac} \simeq 400$ Ft/Sec).

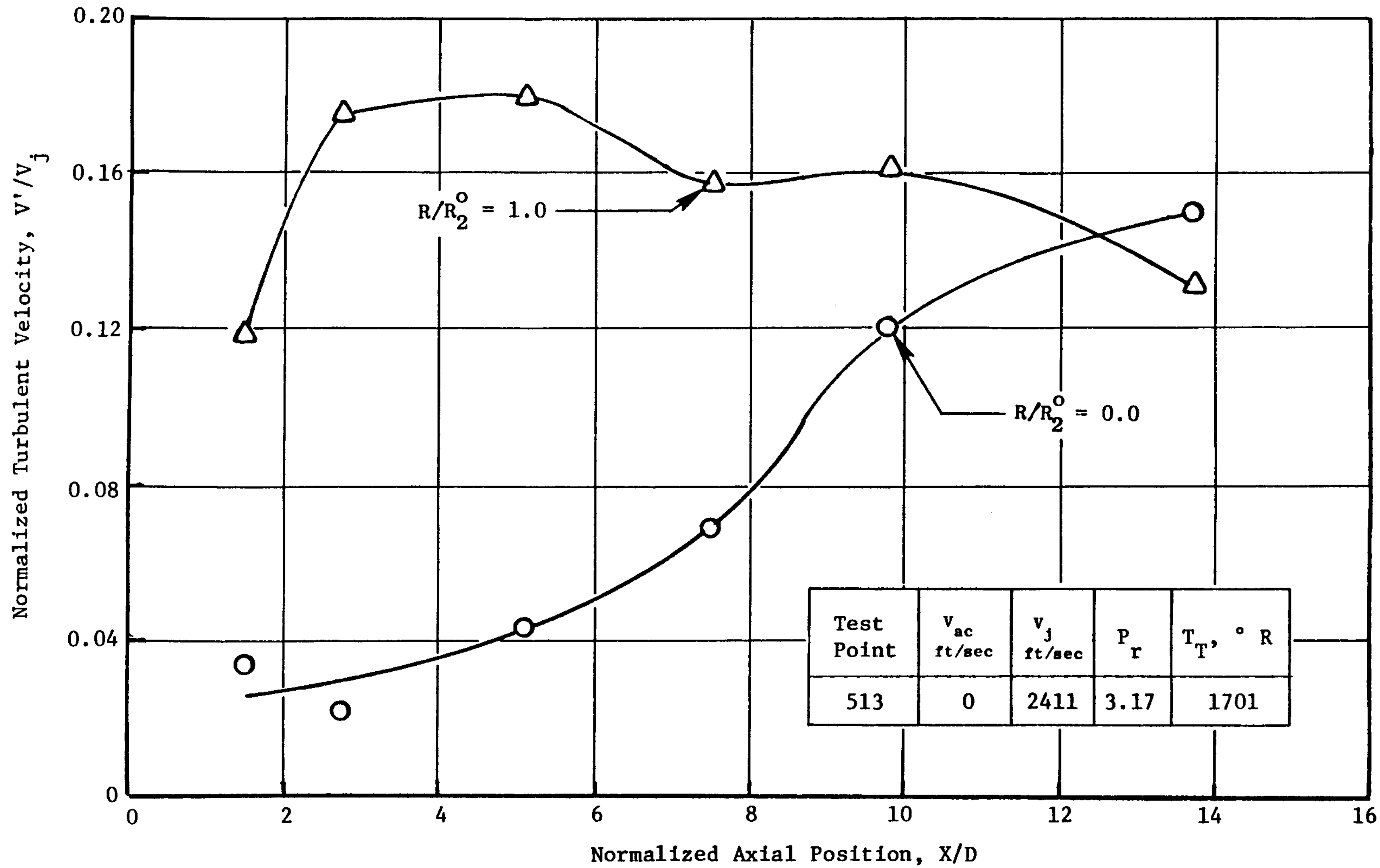

Test Point	V_{ac} ft/sec	V_j ft/sec	P_r	T_T, ° R
513	0	2411	3.17	1701

Figure 79. Turbulent Velocity Variation at Two Radial Locations for Conic Nozzle (Model 5) at Typical Takeoff Conditions (Static).

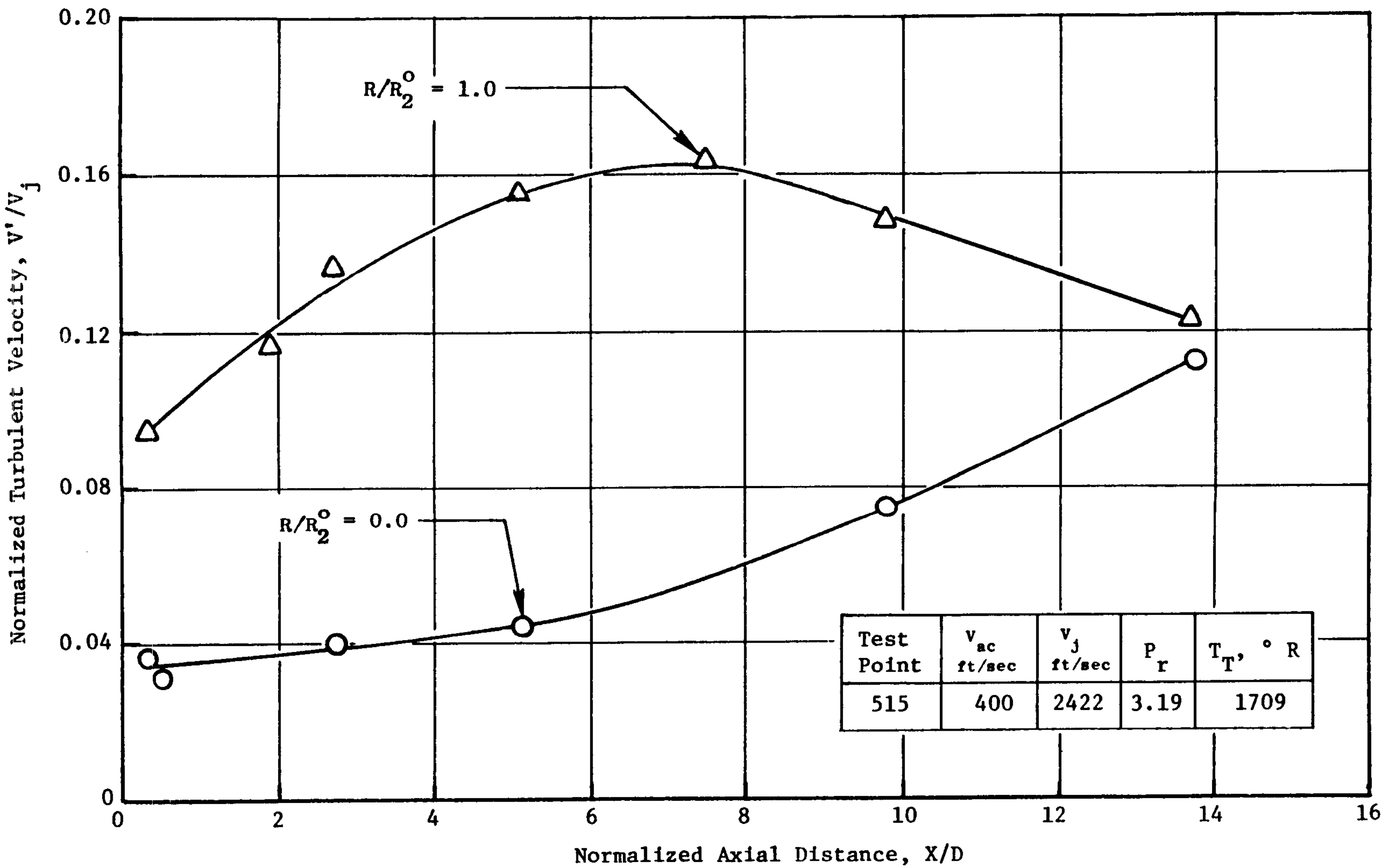

Figure 80. Turbulent Velocity Variation at Two Radial Locations for Conic Nozzle (Model 5) at Typical Takeoff Conditions (Flight, $V_{ac} \approx 400$ Ft/Sec).

Thus, Figures 77 through 80 indicate that a free jet reduces the shear, thereby reducing the decay of the mean velocity and at the same time reducing the turbulent eddy velocity. The noise radiated by the jet depends both on the mean velocity decay and on the levels of turbulent velocities. Since a free jet reduces both parameters, it cannot be definitely concluded whether a flight enhances noise production or reduces it.

5.2.2 Exhaust Plume Characteristics of a Coannular Plug Nozzle

Model 2 is a geometrically scaled version of an AST/VCE coannular plug nozzle ($A^i/A^o = 0.2$, $R_r^o = 0.853$) with a C-D termination on the outer flowpath and convergent termination on the inner flowpath but having no struts in the outer flowpath. Model 2 has been chosen to illustrate the typical plume characteristics of dual flow nozzles with an inverted velocity profile. Figure 81 shows the plume development for a typical takeoff condition (Test Point 201). The radial variation of the mean velocity at various axial stations is illustrated. Station A (at $X/D_{eq} = 0.243$) is upstream of the inner flow exit plane, and the presence of only the outer stream is noted. At Station C (at $X/D_{eq} = 0.678$), the inner flow has appeared. The inverted velocity profile is clearly demonstrated at Stations G, H, and J (respectively at $X/D_{eq} = 1.93$, 2.79 and 5.17). Also observed is the profile asymmetry about the jet axis at Stations H, J, and K (respectively at $X/D_{eq} = 2.79$, 5.17, and 7.56) which can be traced to the geometric misalignment of the nozzle (Section 5.2.8). For stations downstream of Station K (i.e., for $X/D_{eq} > 7.56$), the radial profile resembles that of a conic nozzle, thus indicating that the dual flow character is maintained up to an axial distance of approximately 7.5 D_{eq} from the nozzle exit plane.

Figure 82(a) shows the influence of the free jet on the centerline mean velocity distribution for Model 2. Unlike the conic nozzle, the shock pattern is not noticeably stretched by the free jet. This can be attributed to the differences in geometry and the resulting plume development of the two nozzles. There are seven shock cells under simulated flight conditions and eight at static conditions over the same distance, indicating that each shock cell is stretched slightly. For X greater than 10 D_{eq}, a slower decay for the simulated flight case is seen when compared to that of the static case. A similar observation was made earlier with the conic nozzle data.

The axial variation of the turbulent velocities of the coannular plug nozzle under static and simulated flight conditions are presented in Figure 82b. Similar to Figures 79 and 80 for the conic nozzle, the data of Figures 82b indicates that the free jet has reduced the fluid shear. Hence, in simulated flight, the turbulent velocities are lower for all axial locations, and the peak turbulent velocity reached is about 3% lower compared to the static case. As in the case of the conic nozzle, the centerline turbulent velocities reach their peak value at $X \simeq 14\ D_{eq}$.

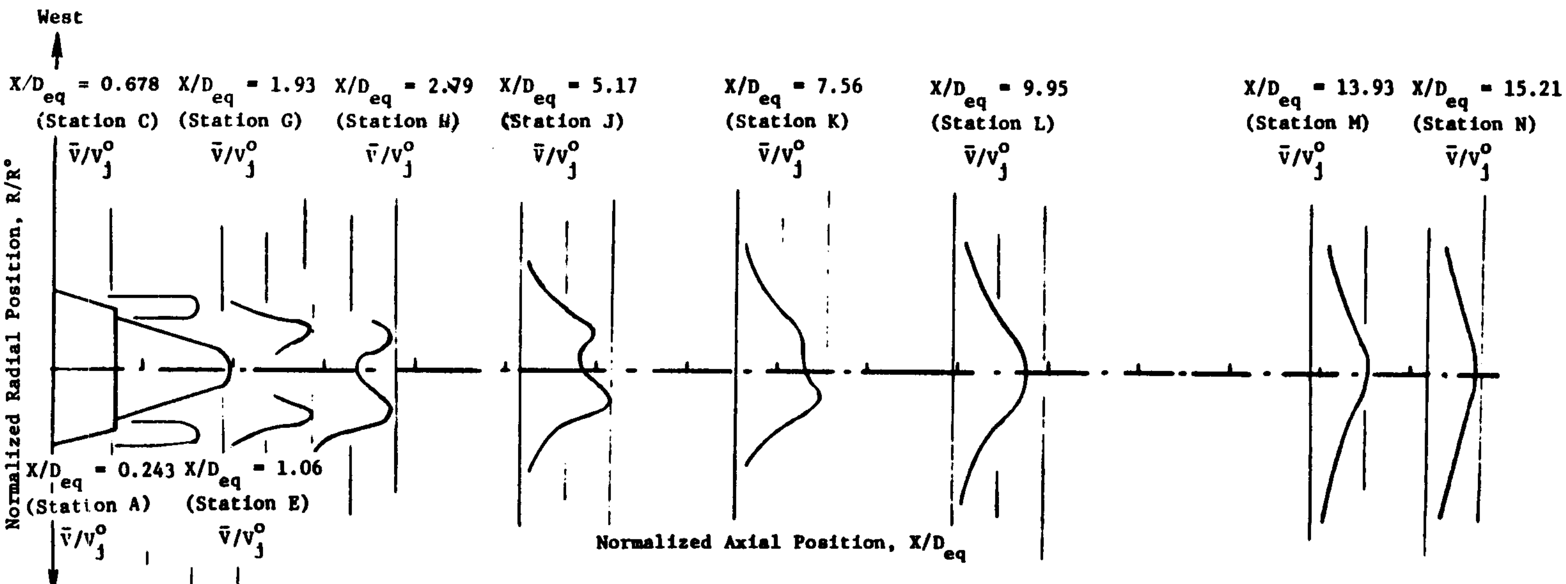

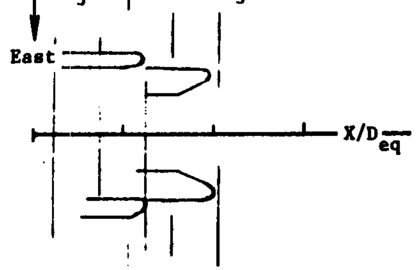

- Static
- D_{eq} = 5.178 inches, R_2^o = 4.593 inches

Test Point	V_j^o fps	P_r^o	T_T^o, °R	V_j^i fps	P_r^i	T_T^i, °R	V_j^{mix} fps	T_T^{mix}, °R	P_r^{mix}
201	2422	3.16	1720	1643	3.21	793	2246	1511	3.088

Figure 81. Radial Variation of Mean Velocity Profiles at Various Axial Locations Downstream of AST/VCE Model 2 Nozzle.

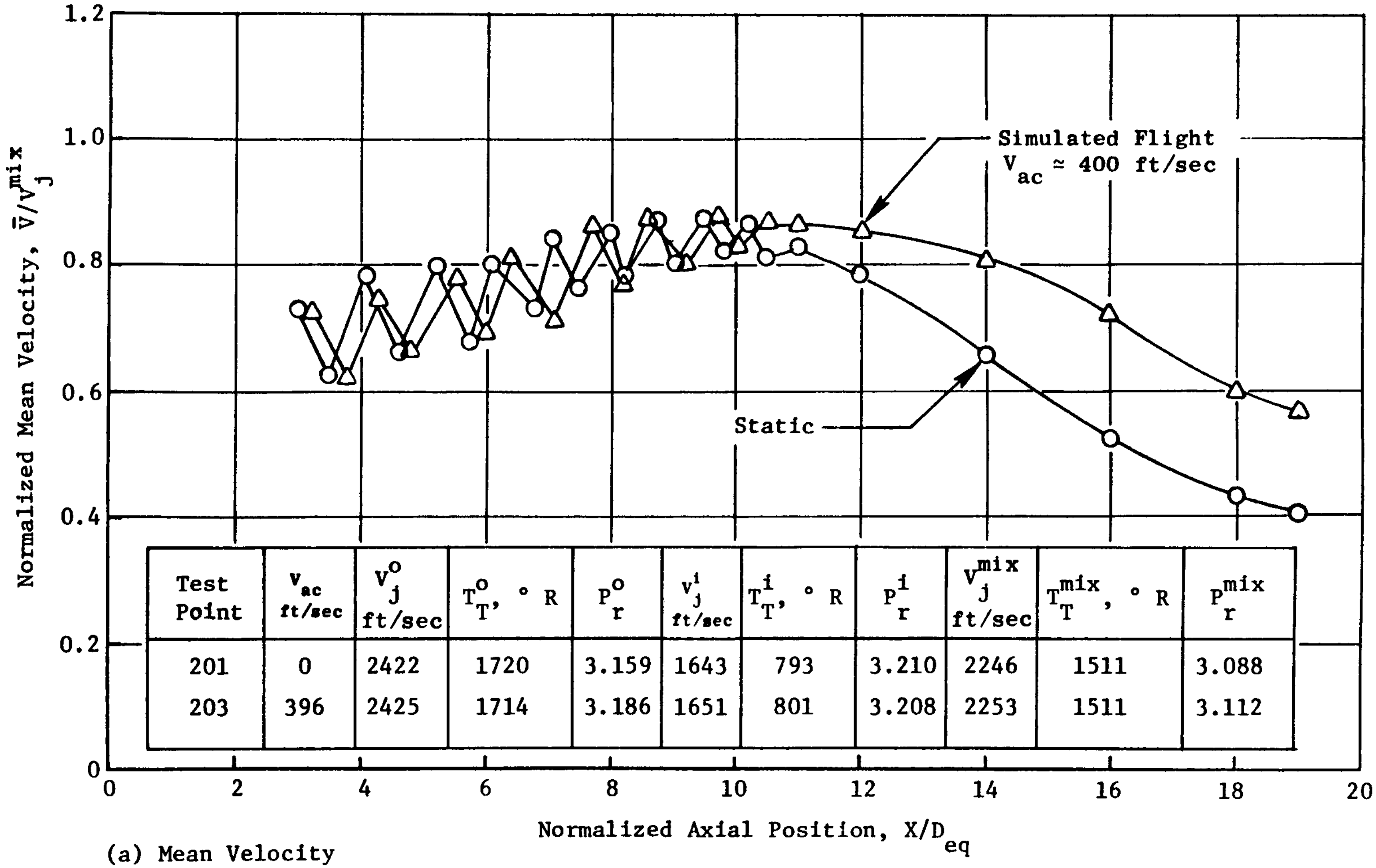

Test Point	V_{ac} ft/sec	V_j^o ft/sec	T_T^o, °R	P_r^o	V_j^i ft/sec	T_T^i, °R	P_r^i	V_j^{mix} ft/sec	T_T^{mix}, °R	P_r^{mix}
201	0	2422	1720	3.159	1643	793	3.210	2246	1511	3.088
203	396	2425	1714	3.186	1651	801	3.208	2253	1511	3.112

(a) Mean Velocity

Figure 82. Influence of Simulated Flight on the Centerline Mean and Turbulent Velocity Distribution for Coannular Plug Nozzle (Model 2) at Typical Takeoff Conditions.

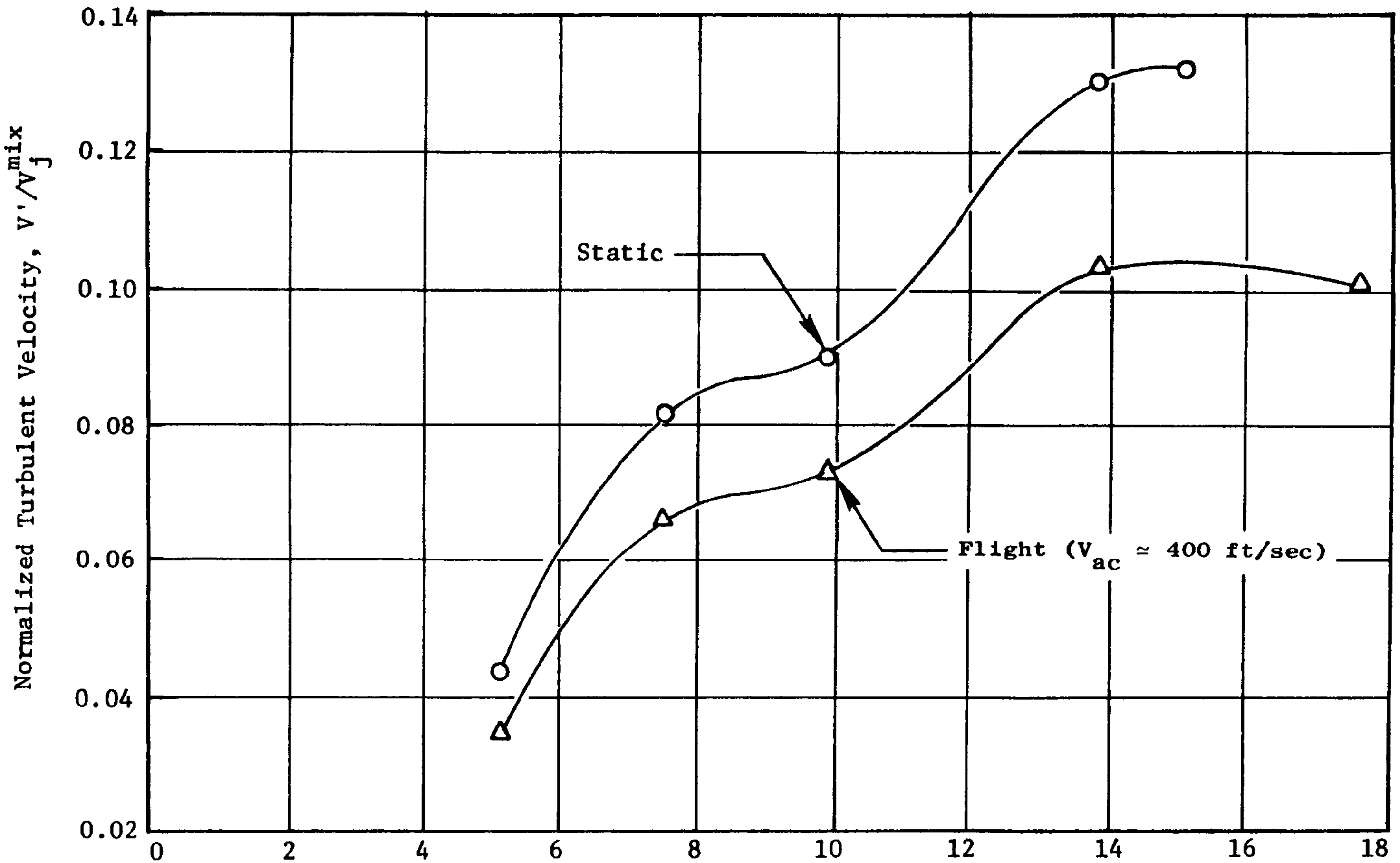

(b) Turbulent Velocity Normalized Axial Position, X/D_{eq}

Figure 82. Influence of Simulated Flight on the Centerline Mean and Turbulent Velocity Distribution for Coannular Plug Nozzle Model 2 at Typical Takeoff Conditions (Concluded).

5.2.3 Influence of Outer Flowpath Termination on the Flow Characteristics

AST/VCE Models 2 and 3 are compared in this section to isolate the effect of the outer flowpath termination on the shock structure and the resultant influence on shock cell noise. Models 2 and 3 are identical coannular plug nozzles, except that Model 2 has a convergent-divergent termination on the outer flowpath designed for $P_r^o = 3.20$ whereas Model 3 has a convergent termination on the outer flowpath.

Figures 83 and 84 compare the axial variation of the mean velocity and the shock cell structure for Models 2 and 3 for static and free-jet cases, respectively. The outer stream pressure ratio for both models equals 3.2 which corresponds to the design pressure ratio of Model 2. However, since the inner stream is supersonic ($P_r^I = 3.21$) and has a convergent termination for both models, the presence of a very strong shock cell pattern can be seen. As noted in Figure 81, the dual flow interaction exists for $X < 7.5\ D_{eq}$ over which most of the shock cell pattern exists. Thus, it is not possible to isolate the influence of the outer flowpath termination and only qualitative trends can be extracted. Table IV shows the peak SPL and the corresponding peak shock frequency at $\theta_I = 50°$ for a scaled total flow area of 1400 in.^{2} and an extrapolated sideline distance of 2400 ft. $\theta_I = 50°$ is chosen because shock noise is the dominant noise component in the front quadrant.

Table IV indicates that for the static and free-jet cases, Model 3 generates more shock noise than Model 2 indicating that, although a C-D termination on the outer flowpath did not eliminate shock noise, it resulted in a small reduction in the shock noise compared to a convergent termination on the outer flowpath.

Table IV. Shock Noise Characteristics of Models 2 and 3.

- Data scaled to 1400 in.^{2} flow area and 2400 ft sideline distance.
- $\theta_I = 50°$.

Model	Test Point	Outer Nozzle Termination	V_{ac}, ft/sec	SPL_p, dB	f_p, Hz
2	201	C-D	0	87.1	250/315
3	301	C	0	87.2	250
2	203	C-D	400	91.2	315
3	303	C	400	93.4	315

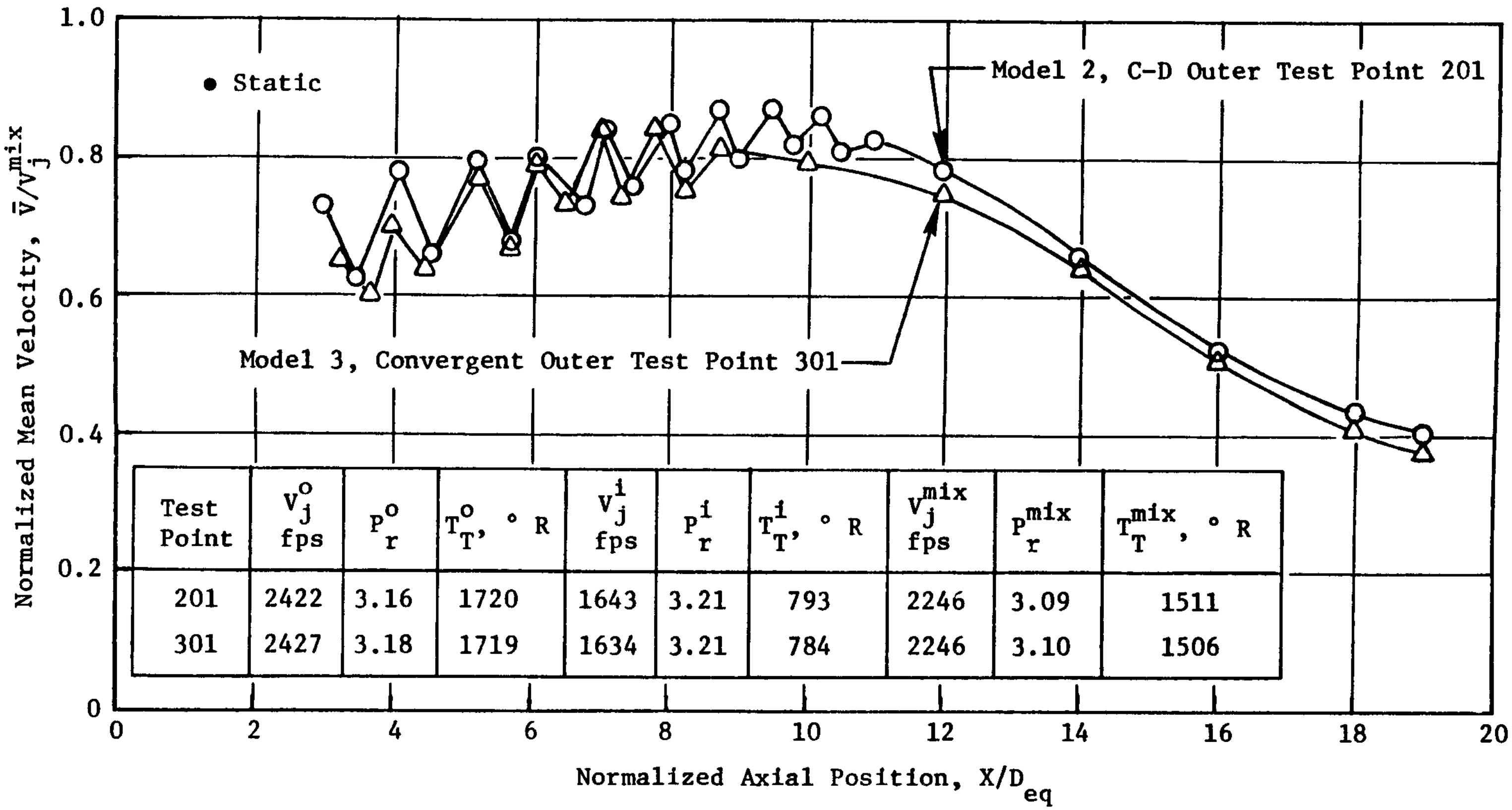

Test Point	V_j^o fps	P_r^o	T_T^o, °R	V_j^i fps	P_r^i	T_T^i, °R	V_j^{mix} fps	P_r^{mix}	T_T^{mix}, °R
201	2422	3.16	1720	1643	3.21	793	2246	3.09	1511
301	2427	3.18	1719	1634	3.21	784	2246	3.10	1506

Figure 83. Influence of Outer Flowpath Termination on the Centerline Mean Velocity at the Design Condition for the Outer Stream (Static).

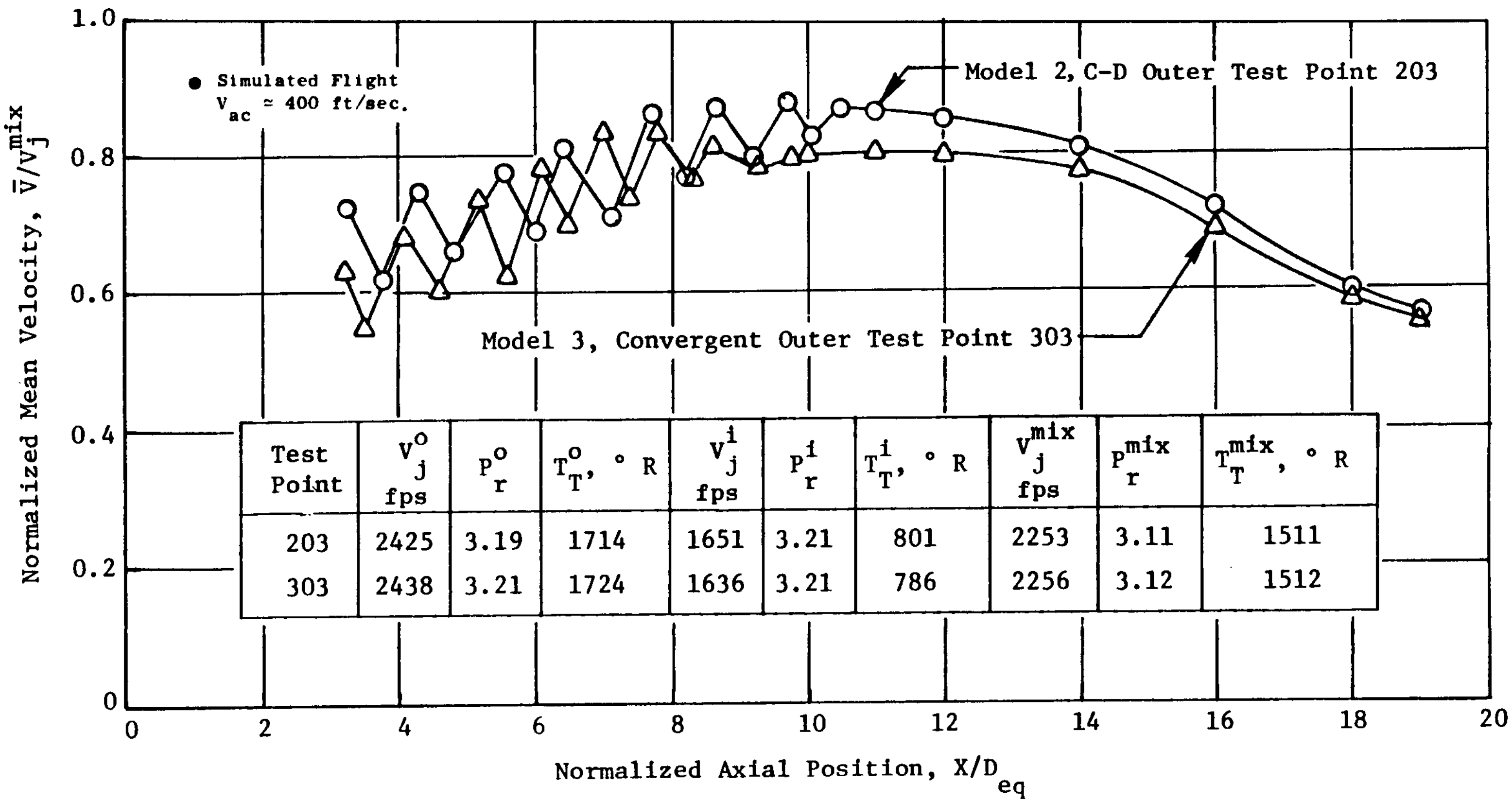

Test Point	V_j^o fps	P_r^o	T_T^o, °R	V_j^i fps	P_r^i	T_T^i, °R	V_j^{mix} fps	P_r^{mix}	T_T^{mix}, °R
203	2425	3.19	1714	1651	3.21	801	2253	3.11	1511
303	2438	3.21	1724	1636	3.21	786	2256	3.12	1512

Figure 84. Influence of Outer Flowpath Termination on the Centerline Mean Velocity at the Design Condition for the Outer Stream (Flight, $V_{ac} \simeq 400$ Ft/Sec).

5.2.4 Influence of Under/Overexpansion of Inner/Outer Streams On the Cell Structure

AST/VCE Model 2 has been employed in order to study the influence of off-design pressure ratios on the flow characteristics. Figure 85 compares the centerline mean velocity axial variation when the outer stream is operated at the design pressure ratio of 3.2 and then at an underexpanded pressure ratio of 3.78, keeping the inner stream pressure ratio at 3.21 for both cases. Since the inner stream is supersonic, it is observed that a strong shock cell pattern occurs for both cases. Yet, because of the difference in the outer stream pressure ratios, the inner stream senses a different static pressure in both cases. The inner stream shock cell pattern begins with a compression wave for $P_r^o = 3.2$ whereas it begins with an expansion wave for $P_r^o = 3.78$. There are eight shock cells for the two cases, but the average shock cell spacing when $P_r^o = 3.16$ equals 0.9 D_{eq} and equals 1.08 D_{eq} when $P_r^o = 3.78$. This indicates that an underexpanded outer nozzle effectively lengthens the supersonic region of the inner jet.

Figure 86 compares the centerline mean velocity variation when the inner stream is operated at subcritical and supercritical pressure ratios keeping the outer stream at an underexpanded pressure ratio (viz, $P_r^o = 3.78$). There is an absence of shock pattern on the centerline when the inner stream is subsonic (i.e., $P_r^i = 1.57$) and the outer stream is highly supersonic. And, when the inner stream is operated supersonically ($P_r^i = 3.21$), a shock pattern exists consisting of eight shock cells with an average shock cell spacing of 1.08 D_{eq}. For this reason, the inner stream pressure ratio is seen as a critical parameter in determining the occurrence of the shock cell structure of the jet plume and, consequently, the shock associated broadband noise.

To verify the above statement, the PNL directivities for the two test points are compared in Figure 87. Note that the front quadrant noise, which is dominated by shock noise (if present), for the case when $P_r^i = 3.21$ is higher compared to the case when $P_r^i = 1.57$. Also, the peak noise levels for both cases are seen to be identical, since the specific thrusts (i.e., V_{mix}) for both cases are about the same. At other aft angles, the PNL's are higher for $P_r^i = 3.21$. The spectral distribution is analyzed next. Figures 88 through 90 show the spectral content at $\theta_I = 60°$, 130° (peak angle), and 140°, respectively. Notice the effective broadband shock noise suppression obtained at $\theta_I = 60°$ by having a subcritical inner stream pressure ratio. At the peak angle (i.e., $\theta_I = 130°$), the PNL's agree and so do the spectra as seen in Figure 89. The tones observed at $\theta_I = 60°$ and 140° have been analyzed using narrowband data with a band width of 10 Hz and are attributed to shock screech and reflections off the exhaust stack of the facility. Acoustic data after removing these tones still showed about a 4-5 PNdB reduction in the front quadrant noise level by employing the inner stream shock control.

To further study the influence of the outer stream on the centerline mean velocity, variation of the centerline mean velocity is compared in Figure 91 for three outer stream conditions (viz., outer stream at design P_r^o, under-

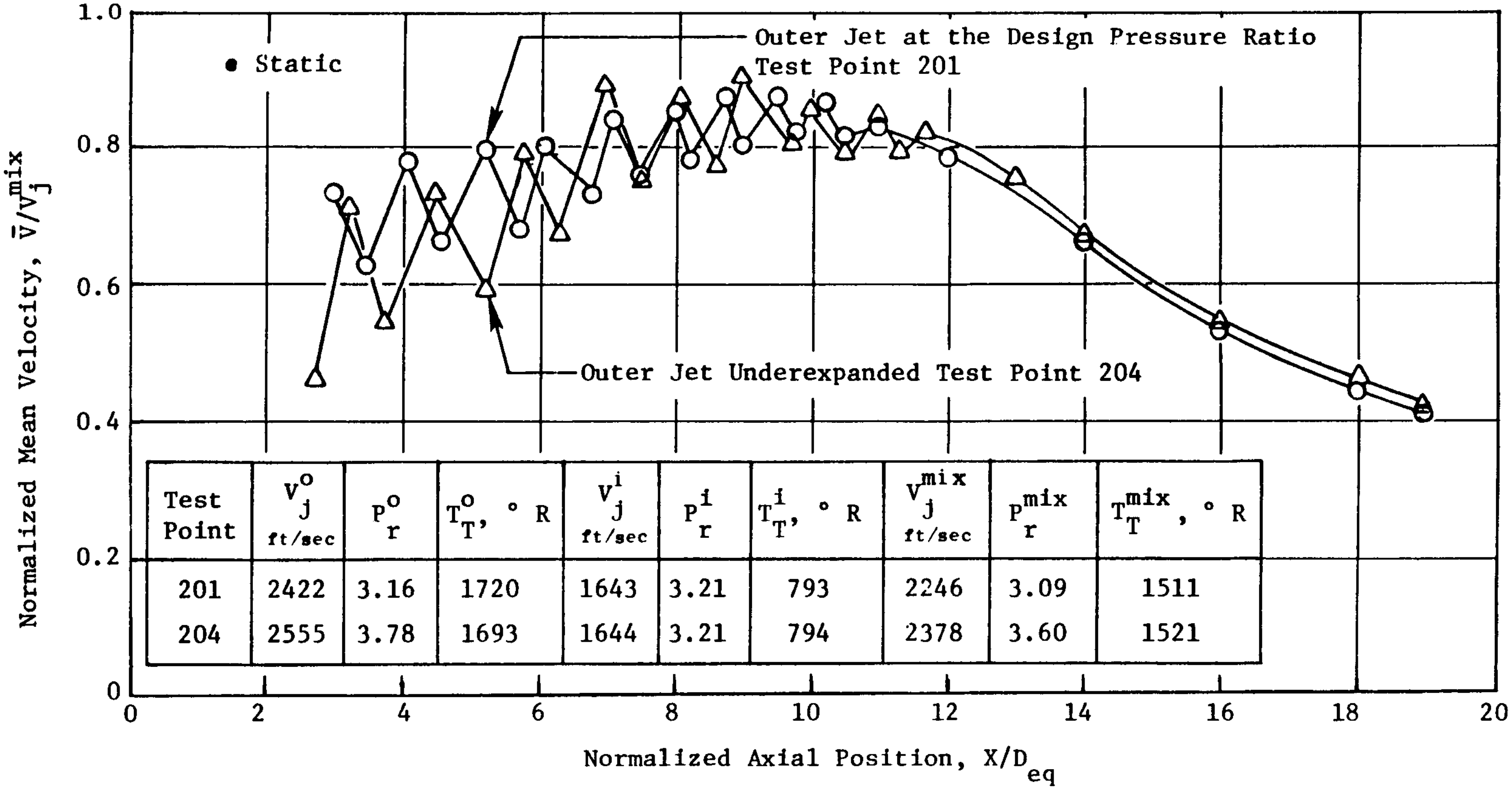

Test Point	V_j^o ft/sec	P_r^o	T_T^o, °R	V_j^i ft/sec	P_r^i	T_T^i, °R	V_j^{mix} ft/sec	P_r^{mix}	T_T^{mix}, °R
201	2422	3.16	1720	1643	3.21	793	2246	3.09	1511
204	2555	3.78	1693	1644	3.21	794	2378	3.60	1521

Figure 85. Effect of Underexpansion of the Outer Flow on the Mean Velocity Distribution Along the Centerline of Model 2 for Supersonic Inner Jet.

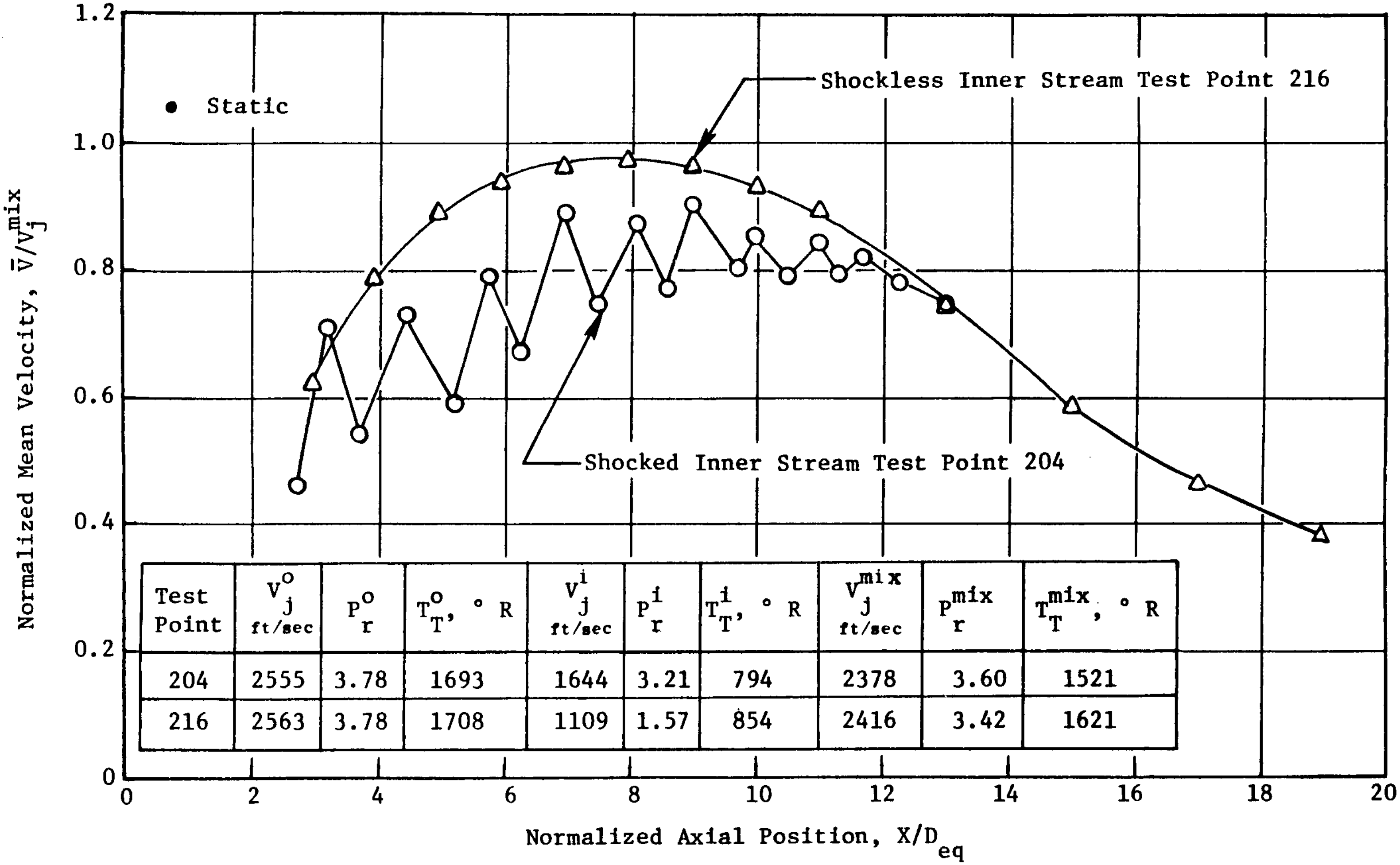

Test Point	V_j^o ft/sec	P_r^o	T_T^o, °R	V_j^i ft/sec	P_r^i	T_T^i, °R	V_j^{mix} ft/sec	P_r^{mix}	T_T^{mix}, °R
204	2555	3.78	1693	1644	3.21	794	2378	3.60	1521
216	2563	3.78	1708	1109	1.57	854	2416	3.42	1621

Figure 86. Effect of Inner Stream Pressure Ratio on the Degradation of Shock Cell Structure for Model 2.

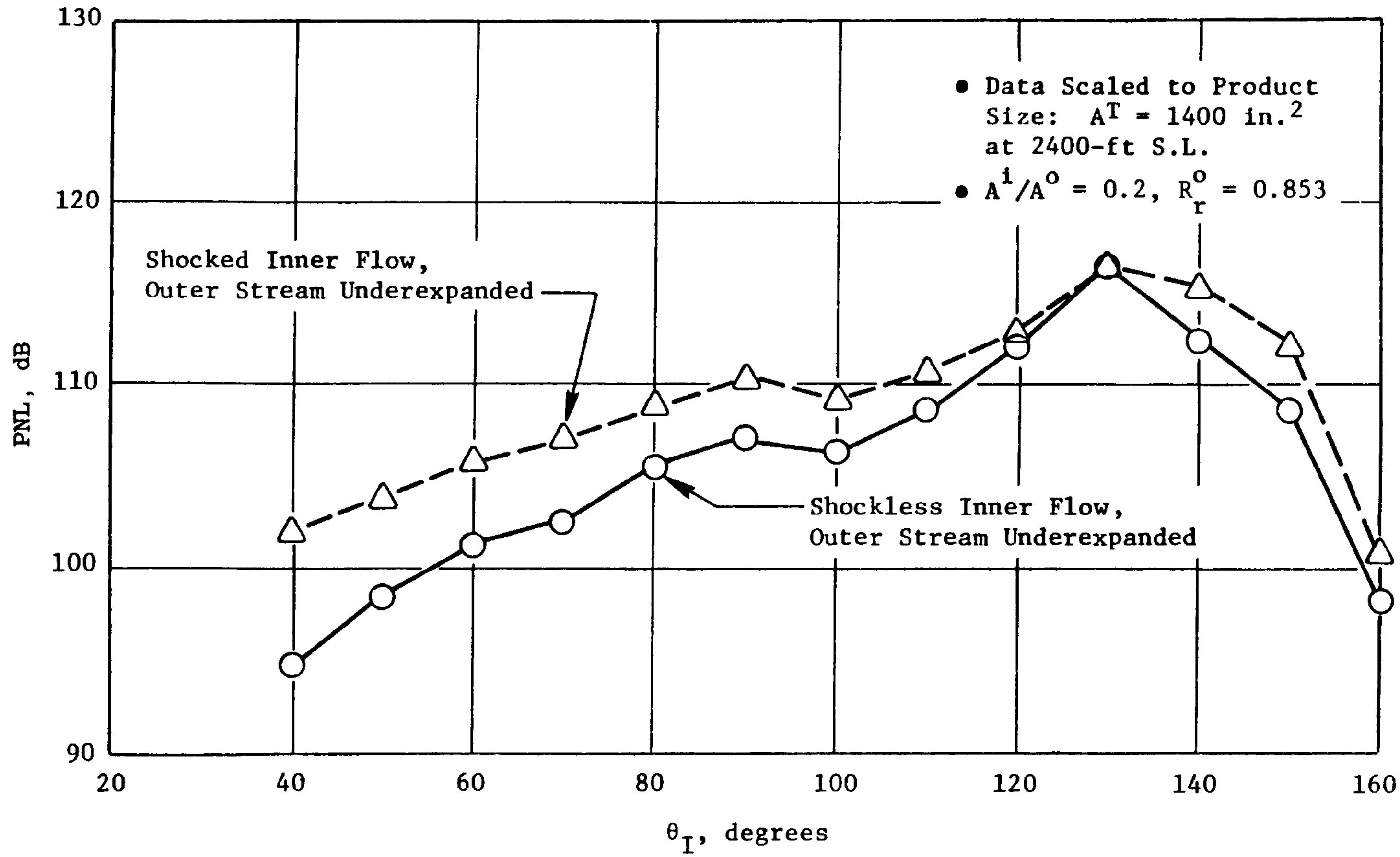

Figure 87. PNL Directivity Showing Front Quadrant Shock Noise Suppression By Inner Stream Control.

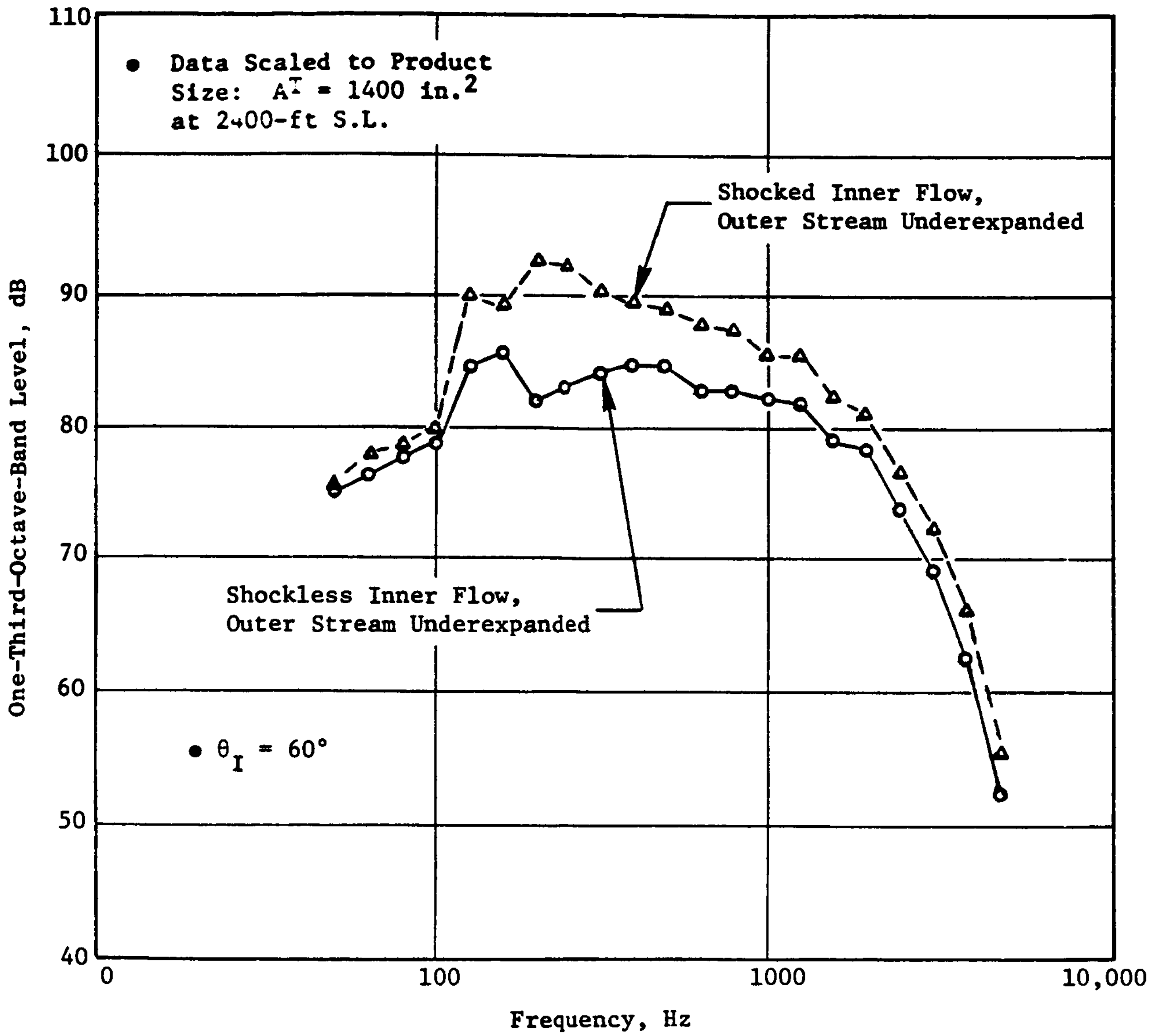

Figure 88. Front Quadrant (θ_I = 60°) Spectra Showing the Broadband Shock Noise Suppression By Holding the Inner Stream Pressure Ratio Subsonic.

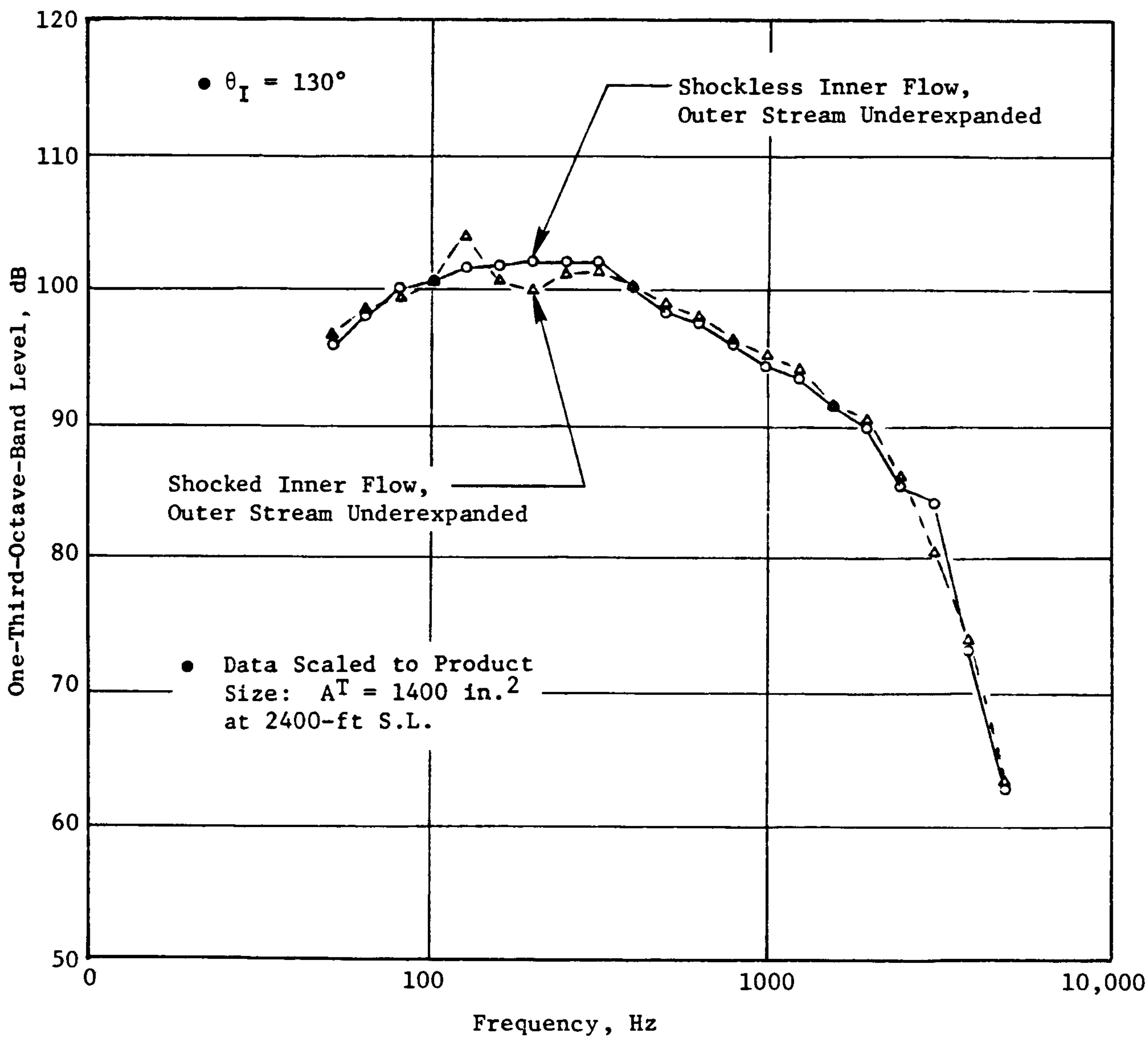

Figure 89. Peak Angle Spectra Showing Negligible Influence of the Variations in the Inner Stream Pressure Ratio.

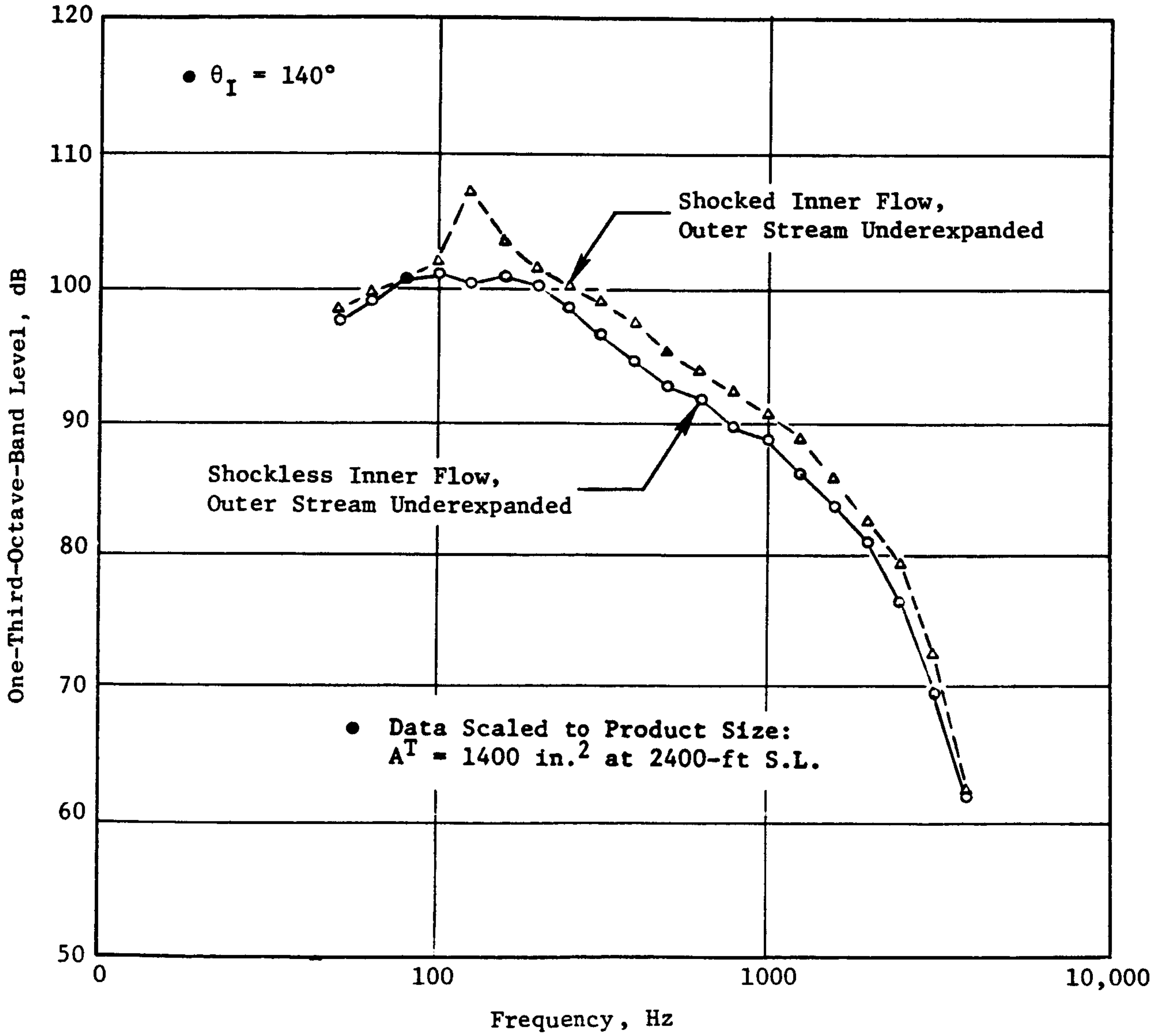

Figure 90. Aft Angle (θ_I = 140°) Spectra for Shocked and Shockless Inner Flow.

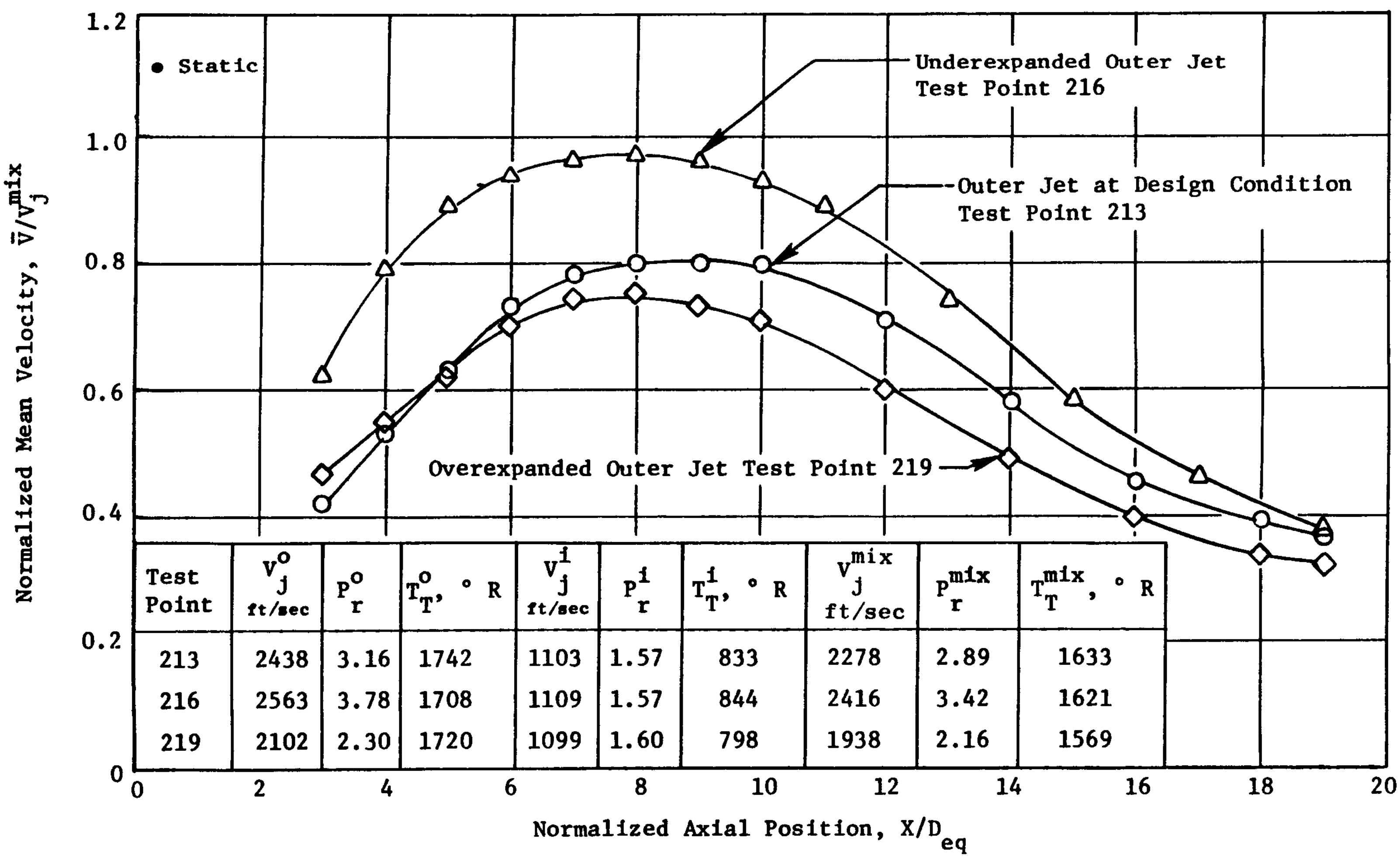

Test Point	V_j^o ft/sec	P_r^o	T_T^o, ° R	V_j^i ft/sec	P_r^i	T_T^i, ° R	V_j^{mix} ft/sec	P_r^{mix}	T_T^{mix}, ° R
213	2438	3.16	1742	1103	1.57	833	2278	2.89	1633
216	2563	3.78	1708	1109	1.57	844	2416	3.42	1621
219	2102	2.30	1720	1099	1.60	798	1938	2.16	1569

Figure 91. Influence of Operating the Outer Stream at the Design and Off-Design Pressure Ratios on the Centerline Mean Velocity; Inner Stream Subsonic.

expanded outer stream, and overexpanded outer stream), keeping the inner stream subsonic. On the normalized basis also (i.e., $\bar{V}(V_j^{mix})$, the centerline velocity is maximum when the outer jet is underexpanded and is followed by a fully expanded case and then by the overexpanded case. This is due to the higher momentum transfer possible when the outer jet is underexpanded (V_j^o = 2563 ft/sec) and is followed by the fully expanded case (V_j^o = 2438 ft/sec) and then by the overexpanded case (V_j = 2100 ft/sec).

5.2.5 Effect of Area Ratio and Outer Stream Radius Ratio on the Exhaust Plume Development

Nozzle area ratio and outer stream radius ratio are two important geometric parameters that determine the plume growth of coannular plug nozzles. AST/VCE Model 6 is a coannular plug nozzle with an area ratio (A^i/A^o) of 0.53 and an outer stream radius ratio (R_r^o) of 0.902, whereas AST/VCE Model 7 has an area ratio of 0.33 and an outer stream radius ratio of 0.853. As a result, a comparison of the plume characteristics of Models 6 and 7 will show the combined effect of A^i/A^o and R_r^o on plume growth.

Figure 92 shows the axial variation of the mean velocity at the radial location corresponding to the midpoint of the outer stream. The aerodynamic conditions of the outer and inner streams for both models are well matched and the mass-averaged conditions are obviously different due to the differences in the area ratio. It can be seen in Figure 92 that the traverse begins at $X/D_{eq} \approx 0$, since this traverse is at the midpoint of the outer stream. As soon as the inner stream appears (at $X/D_{eq} \approx 0.6$), the mean velocity for Model 6 drops below that of Model 7. As X/D_{eq} increases, the dual-flow character becomes prominent, and the differences between the two models increase. However, for $X > 10\ D_{eq}$, the two traverses approach one another, indicating the diminishing effect of individual stream geometric parameters. Figure 93 shows the mean velocity axial variation at the radial location corresponding to the midpoint of the inner stream, which emerges at $X = 0.6\ D_{eq}$. As seen in Figure 92, mean velocity for Model 6 drops in comparison to Model 7 for X between D_{eq} and 10 D_{eq}. For $X > 10\ D_{eq}$, the two models have identical mean velocity decays. These trends are explained below.

Model 6 has a higher area ratio and a higher outer stream radius ratio compared to Model 7. As R_r^o increases, the outer jet grows thinner and will suffer greater shear on either side due to the increased velocity gradient. Consequently, as R_r^o increases, the outer jet will decay faster and will radiate less noise. However, for a given outer stream flow area, increasing R_r^o would demand a larger engine diameter and subsequent weight and drag penalties. For this reason, a tradeoff between the potential noise benefit and weight and drag penalties has to be struck. Next, for given inner and outer stream flow conditions, as A^i/A^o increases, the amount of inner flow available to slow down the outer flow increases, causing the outer flow to decelerate faster and to radiate less noise. However, as the amount of inner flow increases, the mass-averaged velocity (which is also the specific thrust defined

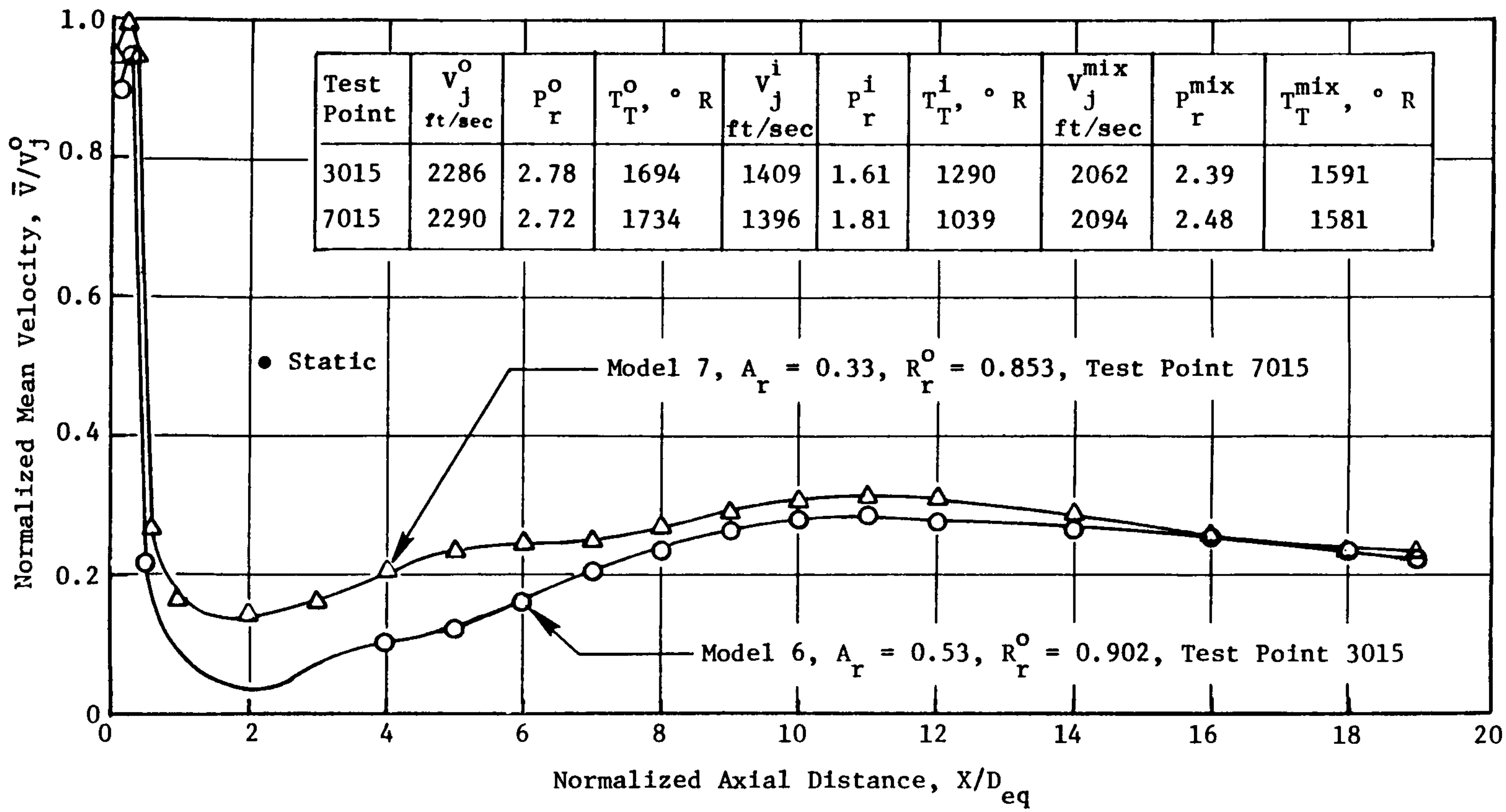

Test Point	V_j^o ft/sec	P_r^o	T_T^o, °R	V_j^i ft/sec	P_r^i	T_T^i, °R	V_j^{mix} ft/sec	P_r^{mix}	T_T^{mix}, °R
3015	2286	2.78	1694	1409	1.61	1290	2062	2.39	1591
7015	2290	2.72	1734	1396	1.81	1039	2094	2.48	1581

Figure 92. Influence of Area Ratio and Outer Stream Radius Ratio on the Mean Velocity Distribution at the Midpoint of the Outer Stream.

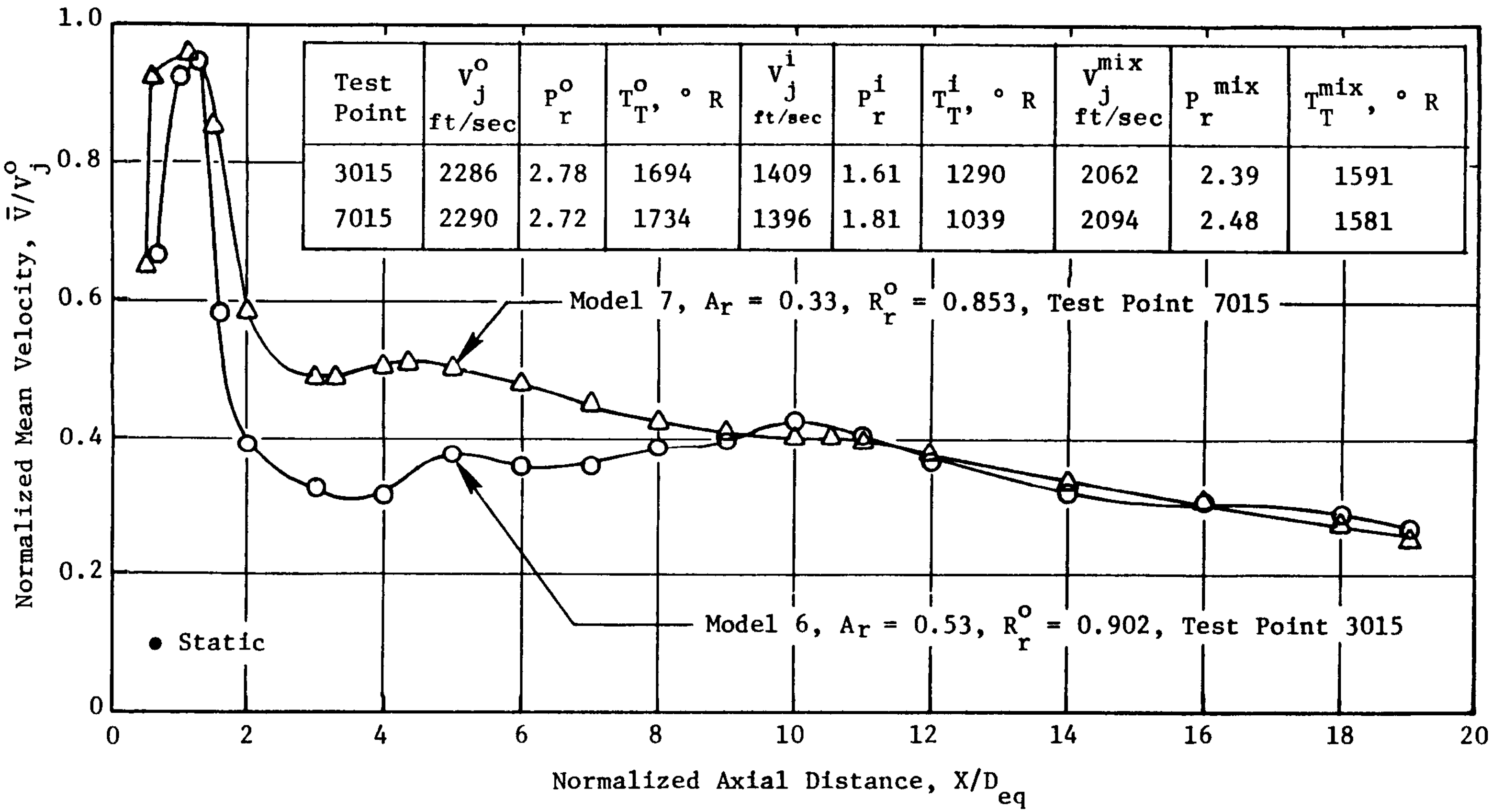

Figure 93. Influence of Area Ratio and Outer Stream Radius Ratio on the Mean Velocity Distribution at the Midpoint of the Inner Stream.

as thrust of the system per unit mass flow rate) decreases and hence the noise benefit has to be evaluated on an equal specific thrust basis.

5.2.6 Effect of Velocity Ratio on Plume Growth

Velocity ratio (V^i/V^o) is an important parameter which determines the velocity gradient between the inner and outer streams and, hence, determines the amount of shear exerted by the inner stream on the outer stream.

LV measurements were taken on Model 2 at two velocity ratios (V^i/V^o = 0.52 and 0.60), keeping the outer stream conditions the same. Figures 94 through 96 show the radial profiles at three X/D_{eq} stations. At X/D_{eq} = 1.0 (Figure 94), the inner stream has just appeared, and the inner streams at the two velocity ratios can be viewed distinctly; the outer streams do not show any effect due to the differences in the inner stream velocities. At X/D_{eq} = 1.81 (Figure 95), the plume has come closer to the jet centerline since the plug radius has been reduced. The peak outer velocities have remained at the same levels as at X/D_{eq} = 1.0, and again the inner streams have no influence on the outer streams. Instead, the inner streams have decelerated compared to their corresponding values at X/D_{eq} = 1.0. At X/D_{eq} = 2.54 (Figure 96), the absence of the plug is observed. The inner velocities have further reduced. Though the peak values of the outer velocities have not changed, the outer stream has grown wider indicating the momentum loss of the outer stream to the ambient.

The observations noted above can be explained by utilizing the principles of momentum transfer. It has been noted that the inner stream does not seem to have a noticeable influence on the outer stream, and the variation of velocity ratio does not alter the basic plume characteristics of the outer stream. Shear stress exerted by the inner stream on the outer stream is a dynamic quantity and depends on the ratio of the momentums of the two streams. Velocity ratio is a kinematic quantity which only determines the velocity gradient, not the shear stress.

One can define the momentum ratio as

$$\text{Momentum Ratio} = \frac{W^i\ V^i}{W^o\ V^o}$$

The pertinent aero conditions for the two test points considered are listed as follows:

Test Point	V_j^o ft/sec	P_r^o	T_T^o °R	V_j^i ft/sec	P_r^i	T_T^i °R	V_j^{mix} ft/sec	P_r^{mix}	T_T^{mix} °R
210	2085	2.29	1698	1258	2.07	701	1907	2.21	1484
219	2102	2.30	1720	1099	1.60	798	1938	2.16	1569

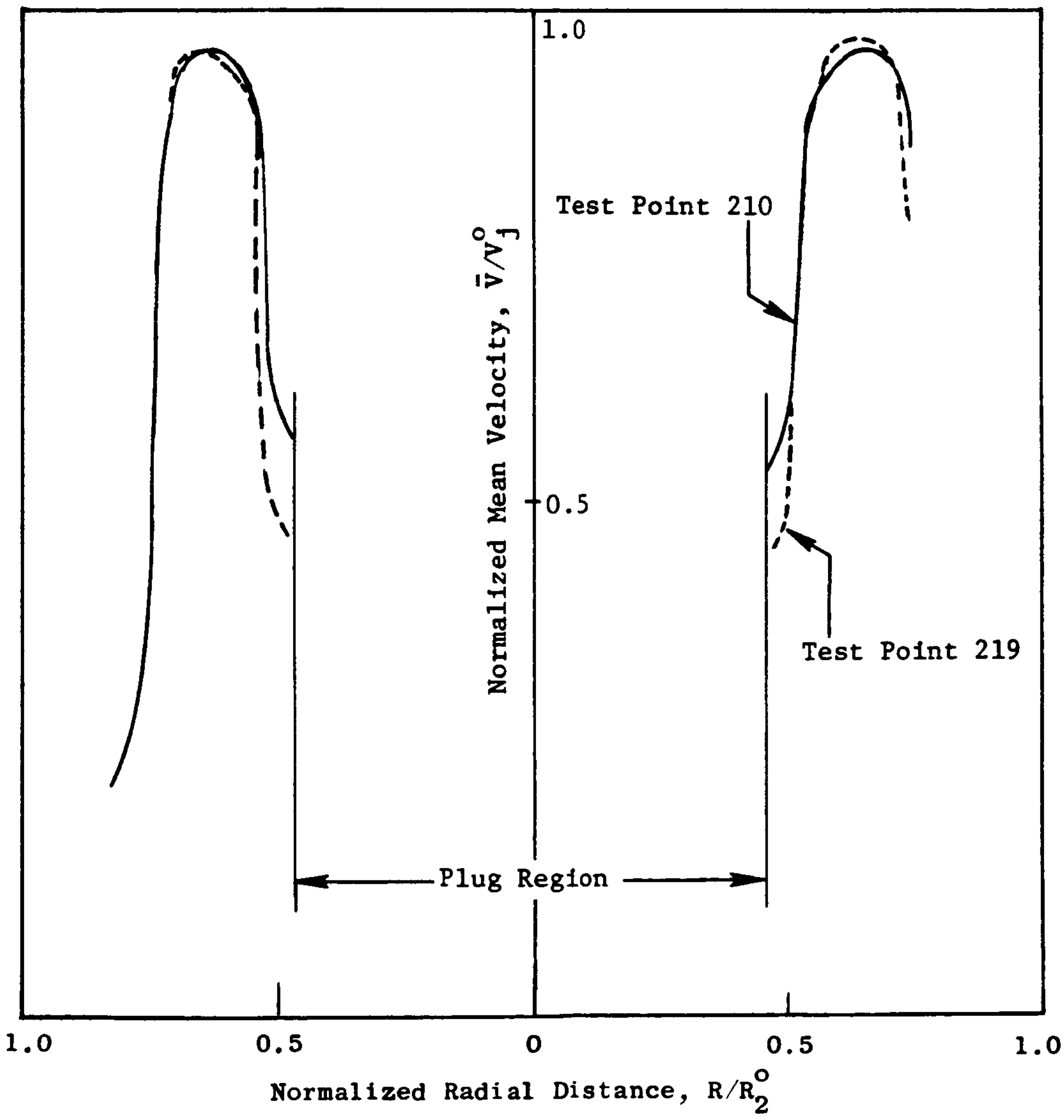

Figure 94. Radial Profile of the Mean Velocity at $X/D_{eq} = 1.0$ Showing the Appearance of the Inner Stream at Two Velocities.

Test Point	V_j^o ft/sec	P_r^o	T_T^o °R	V_j^i ft/sec	P_r^i	T_T^i °R	V_j^{mix} ft/sec	P_r^{mix}	T_T^{mix} °R
210	2085	2.29	1698	1258	2.07	701	1907	2.21	1484
219	2102	2.30	1720	1099	1.60	798	1938	2.16	1569

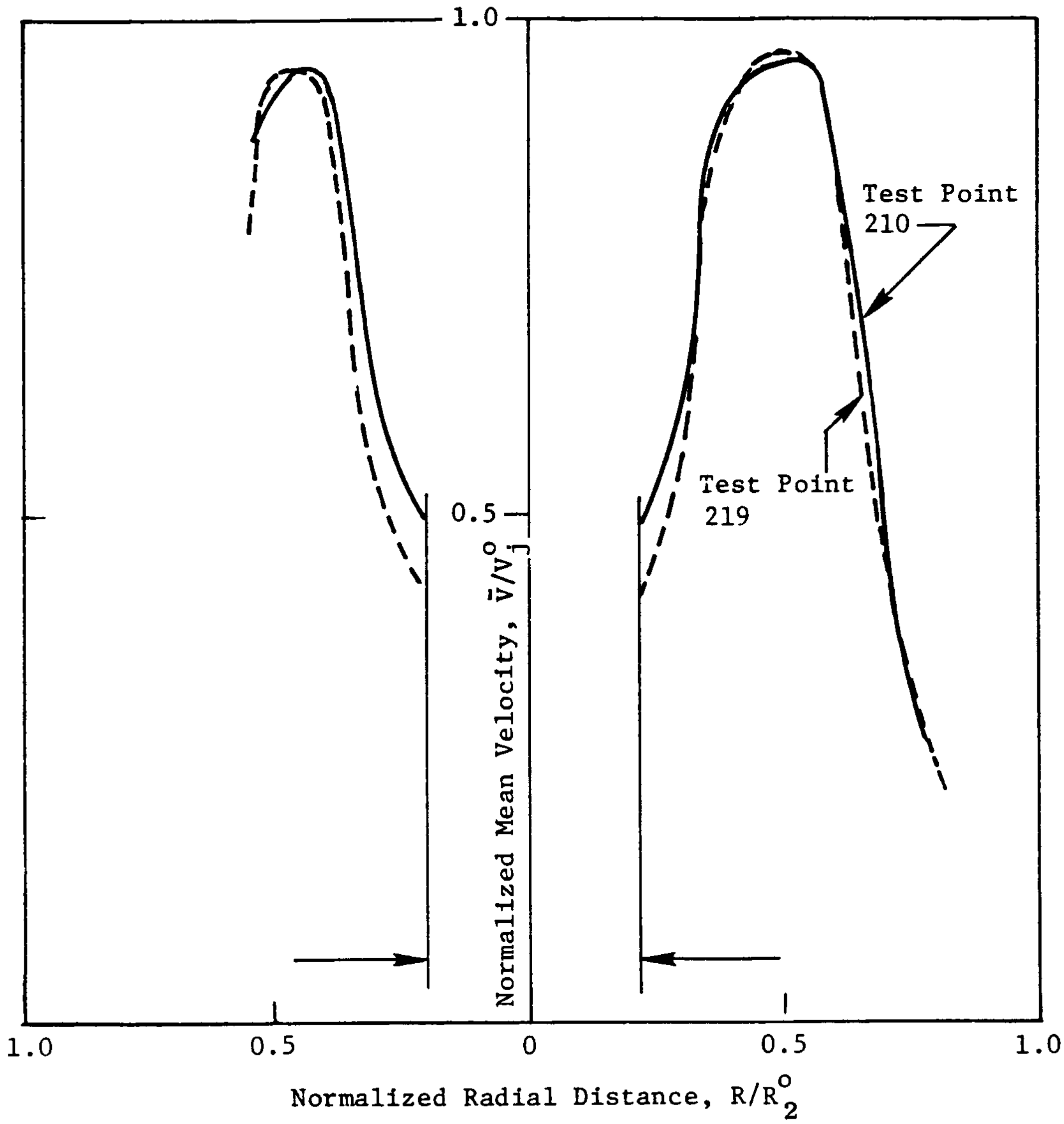

Figure 95. Radial Profile of the Mean Velocity at X/D_{eq} = 1.81 Showing the Deceleration of the Inner Streams Without Affecting the Outer Streams.

Test Point	V_j^o ft/sec	P_r^o	T_T^o °R	V_j^i ft/sec	P_r^i	T_T^i °R	V_j^{mix} ft/sec	P_r^{mix}	T_T^{mix} °R
210	2085	2.29	1698	1258	2.07	701	1907	2.21	1484
219	2102	2.30	1720	1099	1.60	798	1938	2.16	1569

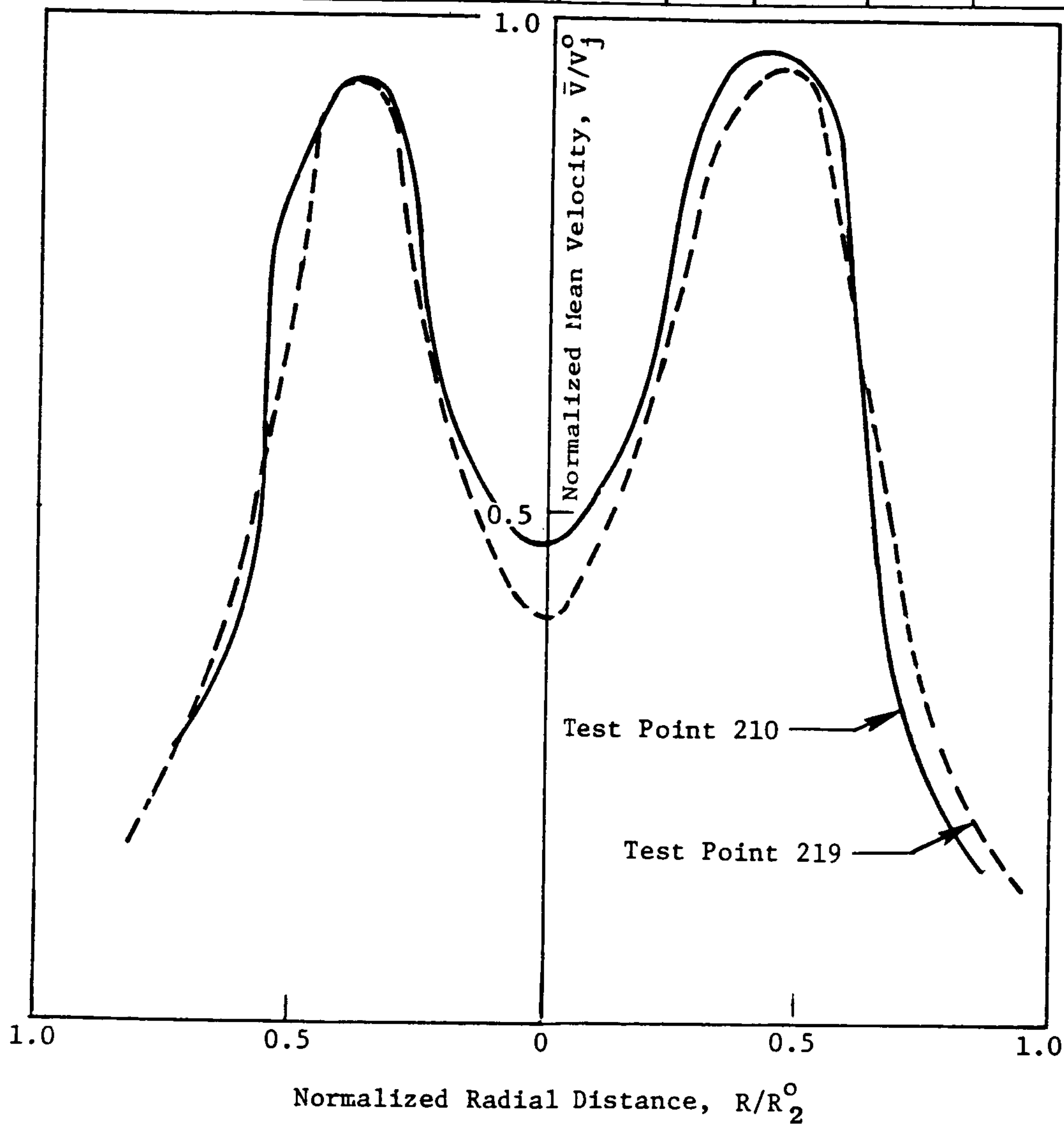

Figure 96. Radial Profile of the Mean Velocity at X/D_{eq} = 2.54 Showing the Disappearance of the Plug and Negligible Influence on the Outer Streams.

Test Point	V^o fps	W^o pps	V^i fps	W^i pps	V^i/V^o	$\frac{W^i V^i}{W^o V^o}$	V_j^{mix} ft/sec
210	2085	494	1258	135	0.603	0.165	1907
219	2102	492	1099	96	0.523	0.102	1938

Thus, the momentum of the inner stream available to retard the outer stream is small for both test points, but this fact is not evident when one looks at the velocity ratio only. In order to have the inner stream exert noticeable influence on the outer stream, the momentum ratio has to be increased without increasing the velocity ratio. This means the inner-to-outer stream area ratio has to be increased and/or the inner-to-outer stream density ratio has to be increased. When the inner-to-outer stream momentum ratio is increased, the mass-averaged velocity reduces. Therefore, the tradeoff between increased shear benefit and lowered specific thrust, due to the increase in the momentum ratio, has to be further evaluated.

5.2.7 Influence of Struts on Mean and Turbulent Velocities

AST/VCE Models 1A and 2 are identical coannular plug nozzles except that Model 1 has eight struts in the outer flowpath while Model 2 has none. So, a comparison of the LV measurements of the mean and turbulent velocities just downstream of the outer nozzle exit plane (i.e., before the inner flow emerges) would indicate the influence of the struts, if any. Figure 97 indicates the distribution of the mean and turbulent velocities at X/D_{eq} = 0.29 on either side of a strut location for Models 1A and 2. Because there are no significant differences in the mean velocity distribution and in addition, the levels of turbulent velocities are the same for both models, it can be concluded that the struts do not significantly alter the mean and turbulent velocity characteristics of the nozzle.

5.2.8 A Rationale for the Observed Flow Asymmetry

During the course of the LV testing, certain radial profiles of coannular plug nozzles showed asymmetric velocity distribution about the jet centerline. Figures 98 and 99 show the LV radial traverses at X/D_{eq} = 7.5 for AST/VCE Models 1A and 2, respectively. The asymmetry in peak velocity is 32% for Model 1 and 28% for Model 2. The measurement of the annular gap showed that the higher velocity occurred on the side with the larger annular height. Thus, the velocity profile asymmetry can be traced to the geometric misalignment of the nozzle hardware which results in unequal circumferential annular gap distribution. Since the outer nozzle in the two cases is operating at a supercritical condition, the velocity on the side of larger annular height is expected to be higher from a continuity consideration. An exactly opposite trend should be expected for subcritical exit conditions.

Symbol	Model	Struts	Test Point	V_j^o ft/sec	P_r^o	T_T^o °R	V_j^i ft/sec	P_r^i	T_T^i °R	V_j^{mix} ft/sec	P_r^{mix}	T_T^{mix} °R
○	1A	Yes	116	2177	2.47	1715	1332	2.14	755	2004	2.37	1518
△	2	No	222	2170	2.45	1718	1341	2.17	756	1999	2.35	1520

● Static

$D_{eq} = 5.238,\ R_2^o = 4.593$

(a) Turbulence Intensity Profiles from Histogram Data

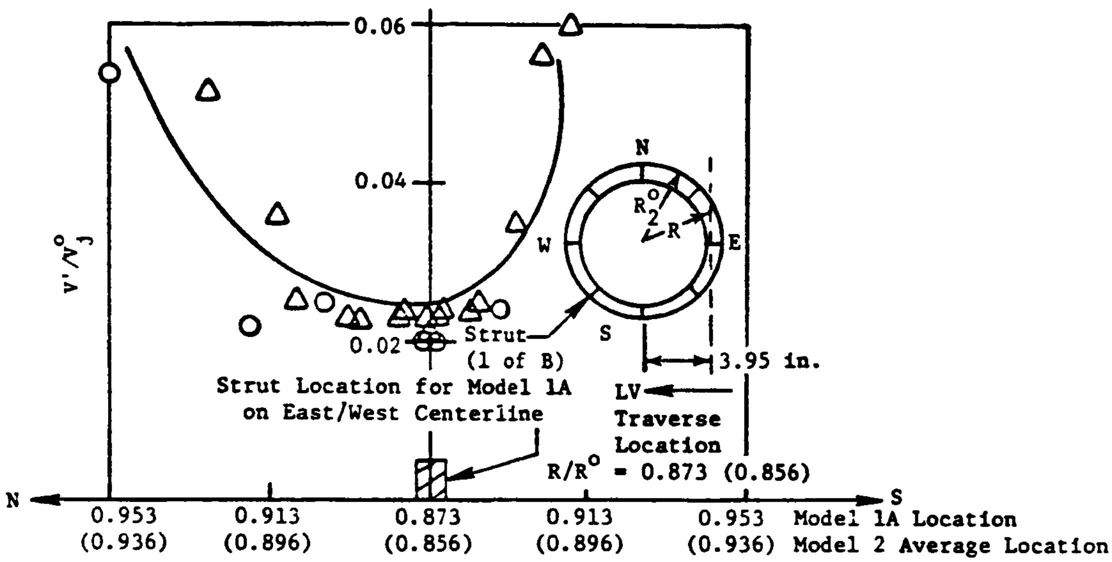

(b) Mean Velocity Profiles from Histogram Data

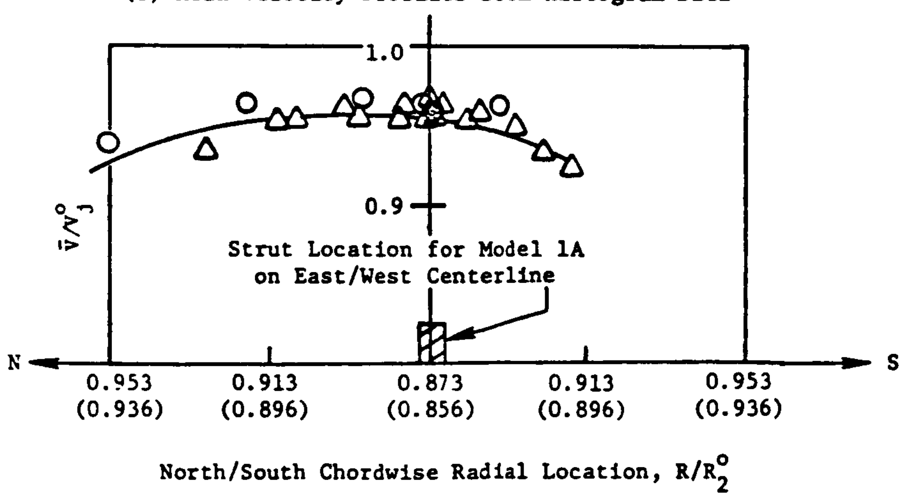

Figure 97. Strut Effect on Downstream Velocity Flow Profiles at $X/D_{eq} = 0.294$.

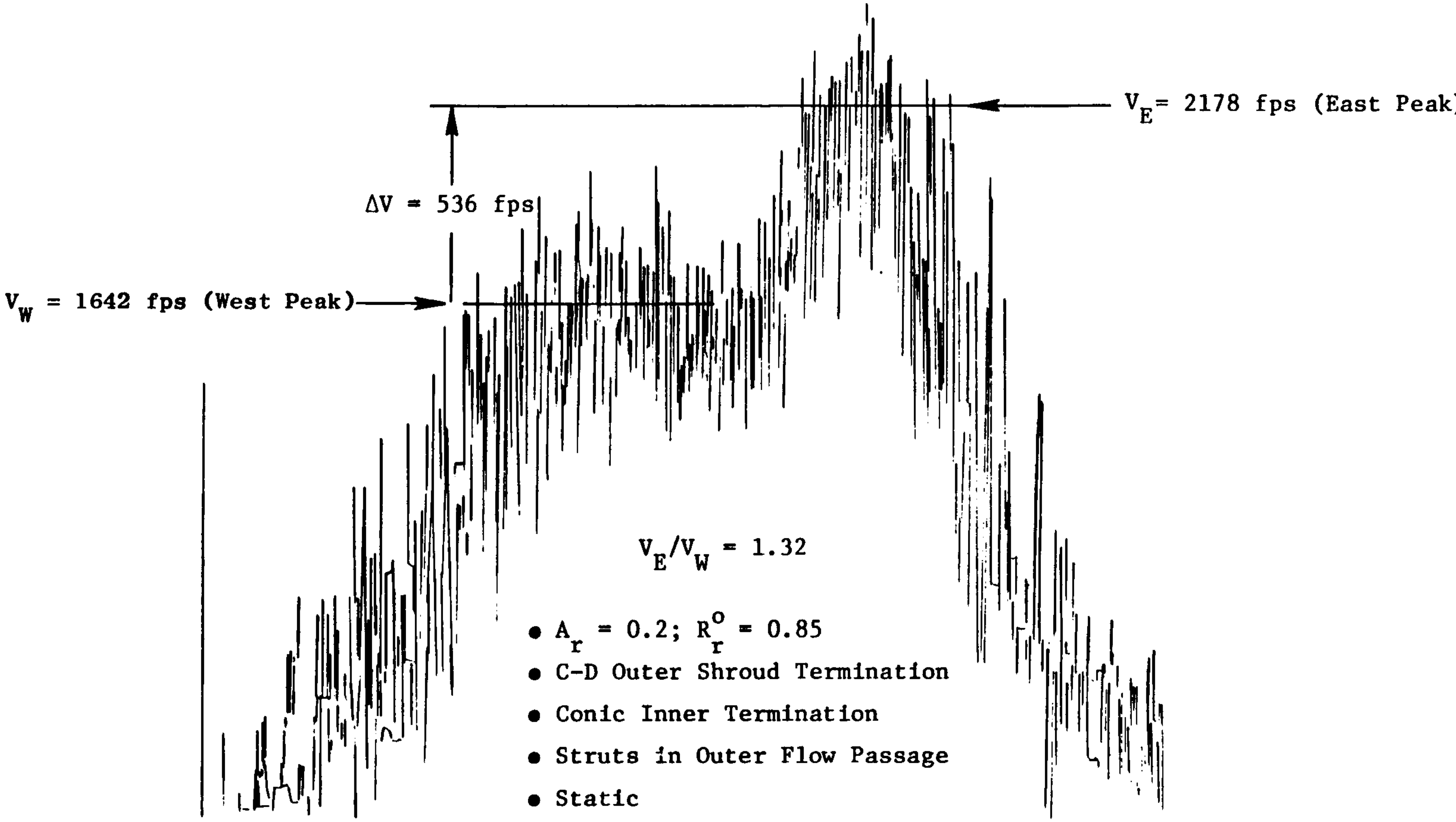

Test Point	V_j^o ft/sec	P_r^o	T_T^o °R	V_j^i ft/sec	P_r^i	T_T^i °R	V_j^{mix} ft/sec	P_r^{mix}	T_T^{mix} °R
101	2411	3.23	1678	1636	3.19	789	2239	3.15	1481

Figure 98. Radial Traverse Showing Mean Velocity Flow Asymmetry for Model 1A for $X/D_{eq} \simeq 7.5$ with Annular Gap Not Centered Before Test.

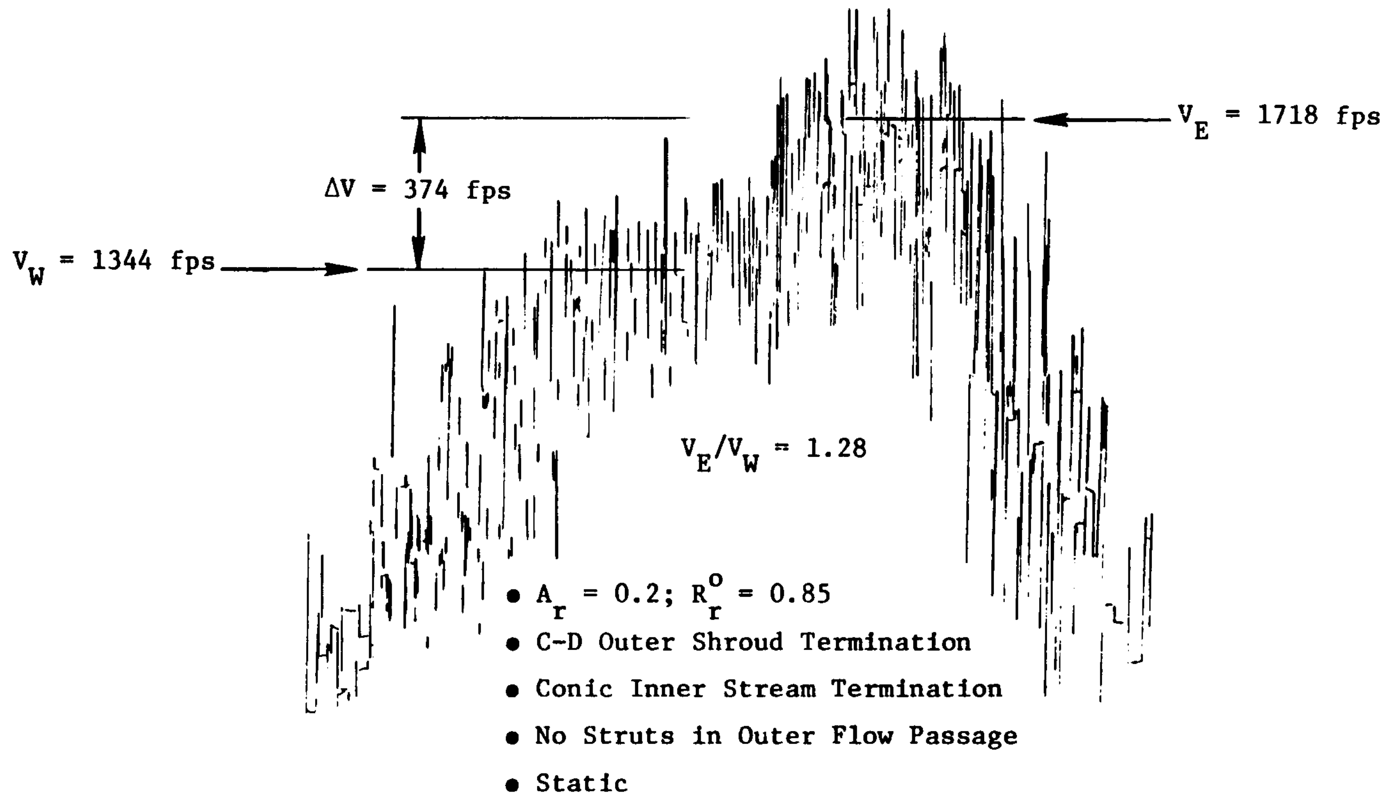

Test Point	V_j^o ft/sec	P_r^o	T_T^o °R	V_j^i, ft/sec	P_r^i	T_T^i	V_j^{mix} ft/sec	P_r^{mix}	T_T^{mix} °R
222	2170	2.45	1718	1341	2.17	756	1999	2.35	1520

Figure 99. Radial Traverse Showing Mean Velocity Flow Asymmetry for Model 2 for $X/D_{eq} \approx 7.5$ with Annular Gap Not Centered Before Test.

In order to minimize the velocity asymmetry, the above tests were rerun with the annular gap measured and monitored to within ±3% variation circumferentially. Figures 100 and 101 show the rerun LV radial traverses at X/D_{eq} = 7.5 for Models 1A and 2, respectively. Observe that for Model 1A, the velocity asymmetry now reduced from 32% to 21%. Similarly, for Model 2 the velocity asymmetry was reduced from 28% to 3%. The presence of struts in Model 1A and their absence in Model 2 could be the cause for the observed differences in the measured velocity asymmetry even after the gap was monitored. The annular gaps were measured and adjusted to within ±3% when the models were cold. It is hypothesized that an unequal thermal expansion of the struts could have caused Model 1A to be excessively misaligned during the rerun than Model 2 and thus account for the different reductions in the velocity asymmetry that were observed even after the nozzles were carefully aligned.

5.2.9 Summary of Observations

The extensive deployment of the laser velocimeter to measure the mean and turbulent velocities of the jet plumes of scale model conic and coannular plug nozzles has yielded valuable information regarding the mixing characteristics, which in turn has enabled one to understand the noise characteristics of these nozzles.

The principal conclusions of this study are summarized below:

1. The measured conic nozzle shock characteristics at typical takeoff condition agree well with those predicted by the empirical model of Fisher and Harper-Bourne. Due to reduction in shear, the free jet stretched the shock cell pattern and reduced the decay rate of the mean velocity, as well as the levels of the turbulent velocities. Thus it is not known whether a free jet reduces shock noise or enhances it.

2. The radial profile measurement at various axial stations for a coannular plug model showed that the dual-flow character is maintained for about 7 to 8 D_{eq} lengths downstream of the nozzle exit. The turbulent velocity distribution for a coannular plug nozzle shows similar characteristics to those of a conic nozzle.

3. Although a C-D flowpath for the outer stream did not eliminate shock cell pattern, it resulted in a small reduction in the shock noise when compared to a convergent flowpath for the outer stream.

4. A study of the under-/overexpanded nozzles showed that an underexpanded outer nozzle effectively lengthens the supersonic region of the inner jet. Even so, the outer stream pressure ratio does not significantly alter the basic aerodynamic characteristics of the inner jet which are mainly functions of the inner stream pressure ratio. The inner stream pressure ratio is a critical parameter in determining the shock cell distribution, as evidenced by the LV and

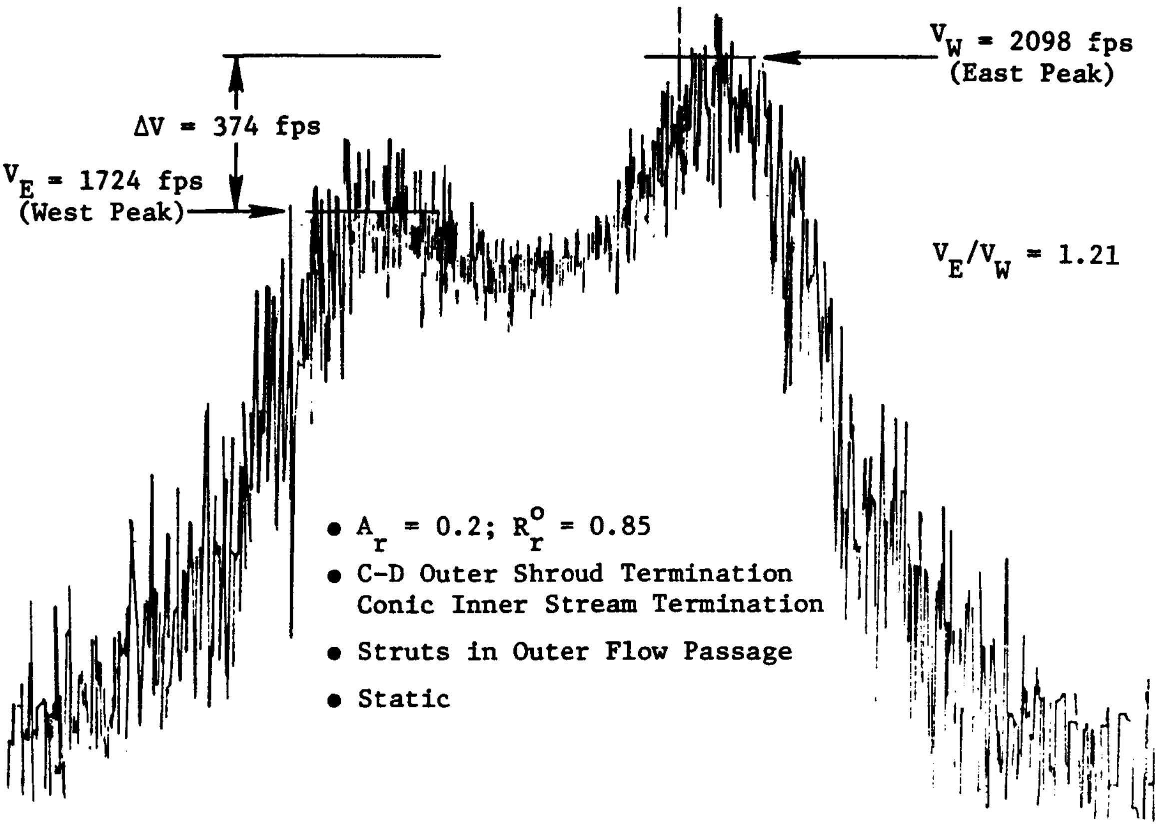

Test Point	V_j^o ft/sec	P_r^o	T_T^o °R	V_j^i ft/sec	P_r^i	T_T^i °R	V_j^{mix} ft/sec	P_r^{mix}	T_T^{mix} °R
101	2411	3.23	1678	1636	3.19	789	2239	3.15	1481

Figure 100. Radial Traverse Showing Mean Velocity Flow Asymmetry for Model 1A for $X/D_{eq} \approx 7.5$ with Annular Gap Centered Before Test.

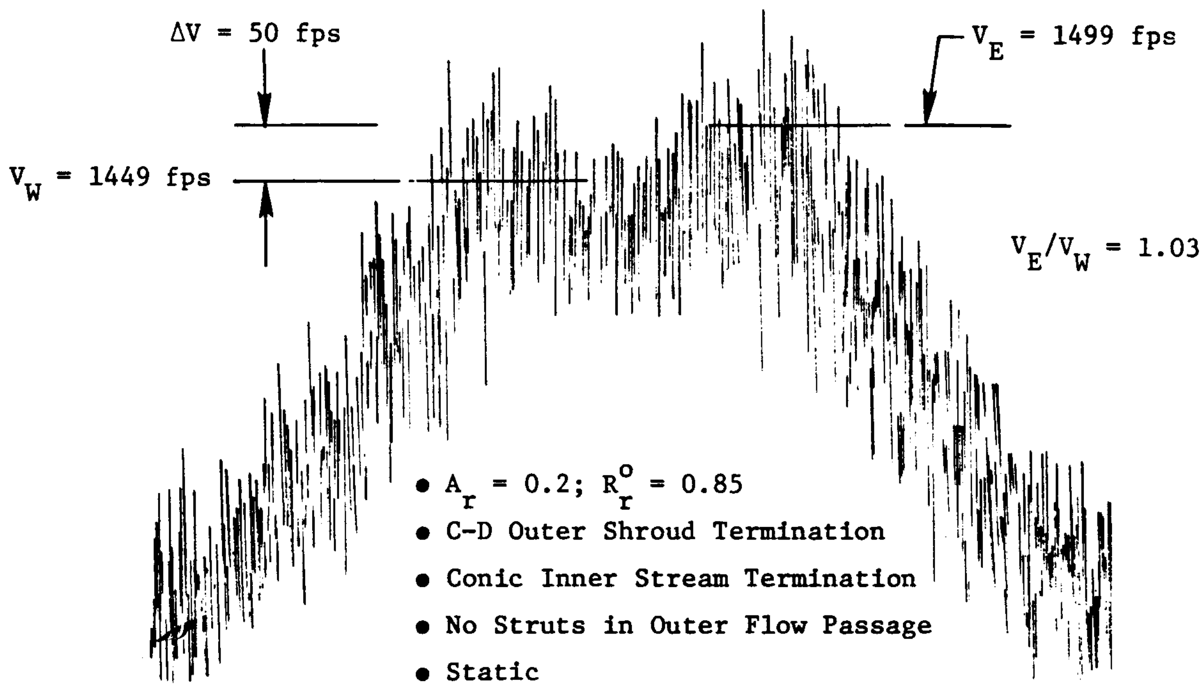

Test Point	V_j^o ft/sec	P_r^o	T_T^o °R	V_j^i ft/sec	P_r^i	T_T^i °R	V_j^{mix} ft/sec	P_r^{mix}	T_T^{mix} °R
222	2170	2.45	1718	1341	2.17	756	1999	2.31	1520

Figure 101. E-W Radial Traverse Showing Mean Velocity Flow Asymmetry for Model 2 for $X/D_{eq} \cong 7.5$ with Annular Gap Centered Before Test.

acoustic measurements. If the inner stream is operated at subcritical pressure ratios, considerable amount of shock noise can be eliminated with no loss of specific thrust.

The tones in the data are due to shock screech and reflections off of the exhaust stack of the facility. Acoustic data without the tones still show about a 4 to 5 PNdB reduction in the front quadrant noise level by employing a subcritical inner stream.

5. The combined influence of the area ratio (A^i/A^o) and the outer stream radius ratio (R_r^o) was studied using Models 6 and 7. With an increase in A^i/A^o and R_r^o, the outer jet is sheared more strongly which results in its faster decay. However, an increase in R_r^o and A^i/A^o would require a larger engine size and would reduce the specific thrust. Thus, an optimum value of R_r^o and A^i/A^o has to be found.

6. For the nozzle considered (Model 2, $A^i/A^o = 0.2$, $R_r^o = 0.853$), the inner stream does not have a noticeable influence on the outer stream, and a variation of the velocity ratio does not alter the basic plume characteristics of the outer stream. In order to have the inner stream exert a noticeable influence on the outer stream, the momentum ratio has to be increased without increasing the velocity ratio. There exists a tradeoff between the increased shear benefit and the lowered specific thrust due to the increase in the momentum ratio, which needs to be evaluated by further studies.

7. The struts in the outer flowpath of the coannular plug nozzle did not significantly alter distribution of the mean and turbulent velocities.

8. Due to a geometric misalignment, flow asymmetry was noted in some coannular plug nozzles. This was minimized in the nozzle having no struts by an accurate pretest alignment. For the case of the nozzle with struts, a careful alignment did not eliminate the asymmetry but did reduce it.

5.3 A UNIQUE COANNULAR PLUG NOZZLE JET NOISE PREDICTION PROCEDURE

5.3.1 The Basic Concept of the Procedure

An effort has been made to develop a semiempirical spectral prediction method for coannular plug nozzles operated in the inverted velocity profile mode that will account for the various noise-generating mechanisms. The effects of flight on coannular jet mixing and shock noise are also predicted. The guidelines for such a prediction method are that it be based on the physics of the flow and on its noise-radiating characteristics, and yet remain simple. The M*G*B model* (Reference 20) developed under a DOT contract incorporated the source spectrum, convective amplification, and fluid

*Mani, Gliebe, Balsa model

shrouding effects in order to predict the noise from eddies which are then integrated to obtain the jet mixing noise spectra for any jet/jets issuing from any given nozzle configuration. However, the M*G*B model calculates the aerodynamic properties at each slice of the jet before it can predict the radiated noise from that slice. This requires a verified aerodynamic model before verifying the acoustic model. As very little detailed aerodynamic data is available for coannular nozzles, it was considered useful to develop a semi-empirical model using the large acoustic data bank (References 2 and 9) but still use the same physical concepts incorporated in M*G*B.

5.3.2 An Outline of the Prediction Procedure

The prediction procedure consists of two modules:

- Coannular jet mixing noise prediction
- Coannular shock noise prediction.

Extensive details of these modules, the computer program, user's manual, sample input/output cases and comprehensive comparisons with the data can be found in Reference 21. Hence, only a brief description of the method is given here.

A. Coannular Jet Mixing Noise

The method developed to predict the jet mixing noise spectrum identified the noise spectrum as being made up of:

1. Source spectrum due to small-scale, random turbulence eddy fluctuations
2. Convective amplification and Doppler shift due to convecting eddies
3. Fluid shielding or flow shrouding of the eddies by the mean flow.

1. Source Spectrum

The first step in the prediction procedure was to determine the source spectrum. The spectrum at 90° is the source spectrum, as there are no convection effects or fluid shielding effects. The parameters needed to define this spectrum were the characteristic velocity and length scales at this angle of emission. From coannular plug nozzle acoustic data (Reference 2), the 90° spectrum (made "lossless," i.e., air attenuation added to the measured data) showed two distinct regions (Figure 102) which were appropriately defined as

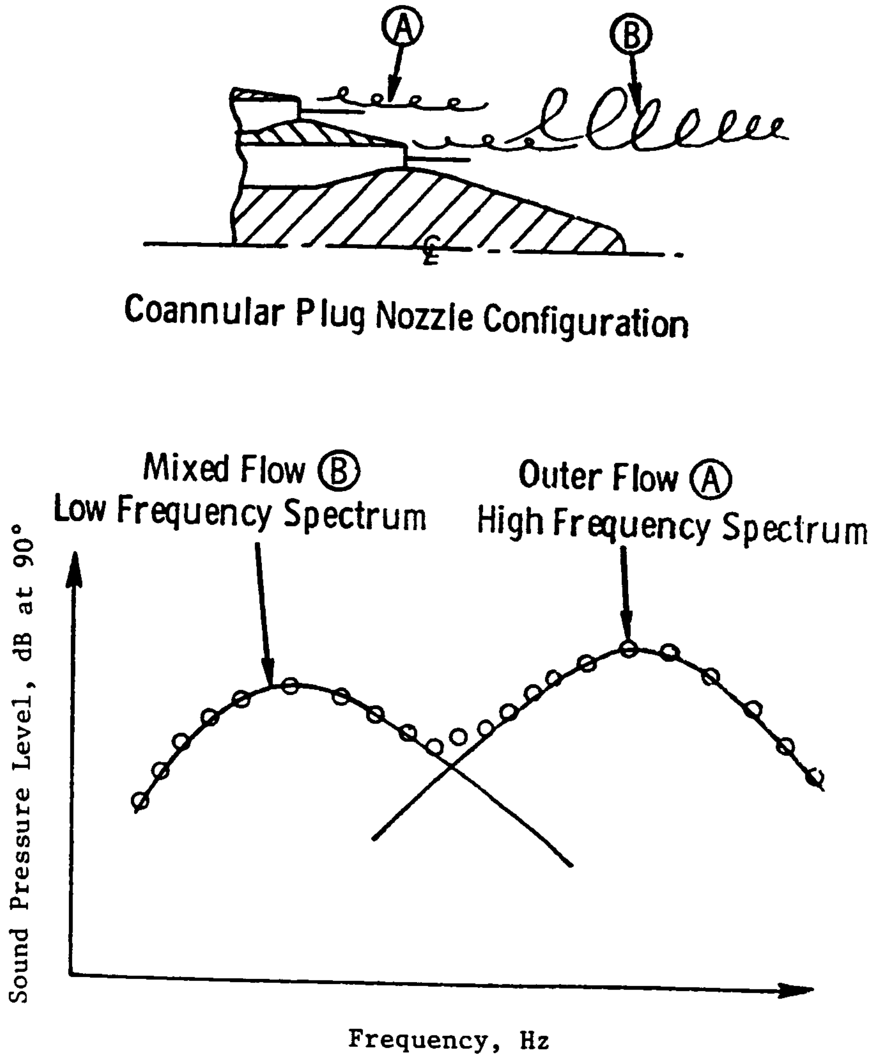

Figure 102. Source Spectrum Modeling of High and Low Frequency Regions of a Coannular Plug Nozzle.

the low and high frequency regions of the spectrum. The high frequency portion of the spectrum was identified as being generated by the outer flow before it merged with the inner flow, while the low frequency portion of the spectrum was identified as being generated by the mixed flow.

Having identified the outer jet as the probable source of the high frequency portion of the source spectrum, the fully expanded outer jet velocity and the hydraulic diameter as defined below were chosen as the characteristic velocity and length scales for this portion of the source spectrum (Figure 103).

$$D^{o}_{hyd} = \frac{4 \text{ x outer jet noise radiating area}}{\text{outer jet noise radiating perimeter}}$$

$$= 2\, h^{o} \left(1+R^{o}_{r}\right) \tag{1}$$

Similarly, for the low frequency portion of the source spectrum, the mass-averaged velocity and the diameter based on the total flow area as defined below were chosen as the characteristic velocity and length scales, respectively.

$$V^{mix}_{j} = \frac{Vj^{o}\, W^{o} + Vj^{i}\, W^{i}}{W^{o} + W^{i}} \tag{2}$$

$$D^{T}_{eq} = \frac{4}{\pi} \left(A^{o} + A^{i}\right)^{1/2} \tag{3}$$

Having chosen the characteristic velocity and length scales, the large acoustic data base for coannular jets was used once again to determine the normalized source spectrum (normalized sound pressure level as a function of the Strouhal number).

For the low frequency noise portion of the source spectrum, the peak Strouhal number was observed to be correlated by:

$$\left[\frac{f^{LF}_{p}\; D^{T}_{eq}}{V^{mix}_{j}}\right] \left[\frac{T^{mix}_{T}}{T_{a}}\right]_{eff} = 0.9 \tag{4}$$

where

$$\left[\frac{T^{mix}_{T}}{T_{a}}\right]_{eff} = 0.65\, \frac{T^{mix}_{T}}{T_{a}} + 0.35 \tag{5}$$

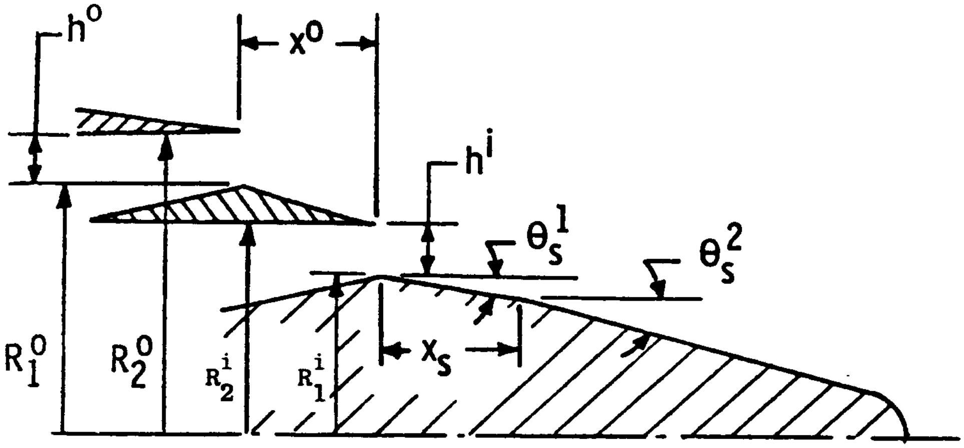

R_r = Radius Ratio (R_1/R_2)

h = Step Height

A = Area

D_{eq} = Equivalent Circular Diameter based on A

θ_s = Ramp Angle of Inner Plug

R = Radius

x = Distance

Superscripts

o = Outer Flow Region

i = Inner Flow Region

Figure 103. Schematic of Nozzle Configuration and Definition of Parameters.

and

$$T_T^{mix} = \frac{T_T^o \; W^o + T_T^i \; W^i}{W^o + W^i} \tag{6}$$

Equation 5 assumes that the total temperature profiles are similar, while Equation 4 was observed to predict the same peak Strouhal number for conic nozzles as did the SAE method (Reference 22).

However, for the high frequency portion of the source spectrum, the peak Strouhal number was found to correlate by

$$\left[\frac{f_p^{HF} \; D_{hyd}^o}{V_j^o}\right]\left[\frac{T_T^o}{T_a}\right]_{eff} = 1.18 \tag{7}$$

where

$$\left[\frac{T_T^o}{T_a}\right]_{eff} = 0.65 \; \frac{T_T^o}{T_a} + 0.35 \tag{8}$$

Normalization of the SPL's for the low frequency portion of the source spectrum was found to be best using the conventional Lighthill and Hoch velocity and density dependence laws (References 23 and 24),

i.e., $$SPLN^{LF}(f) = SPL^{LF}(f) - C_1 \log_{10}\left(V_j^{mix}/C_a\right) - 10 \log_{10}\left(\rho_j^{mix}/\rho_a\right)^{\omega} - 10 \log_{10} \frac{(A^T)}{\left(\frac{A^T}{R^2}\right)} \tag{9}$$

where

$$C_1 = \begin{cases} 75, \text{ for } V_j^{mix}/C_a \le 2.0 \\ 80, \text{ for } V_j^{mix}/C_a > 2.0 \end{cases}$$

The shape of the normalized low frequency portion of the spectrum was based on that of a conic nozzle, while the absolute level was based on coannular plug nozzle jet mixing noise data. Figure 104 shows the normalized low frequency source spectrum for coannular jet mixing noise.

Similarly, for the high frequency spectrum, normalized SPL's were determined in addition to the velocity, density, and area terms, the high frequency portion of the source spectrum was influenced by velocity ratio, radius ratio, and area ratio that are incorporated into the normalizing factor. These influences were empirically derived from the existing data base. The best correlation was obtained by

$$\begin{aligned} SPLN^{HF}(f) = SPL^{HF}(f) &- 80 \log_{10} (V_j^o/C_a) \\ &-10 \log_{10} (\rho_j/\rho_a)^{\omega} - 10 \log_{10} (A^o/R^2) \\ &+ 50 \log_{10} (R_r^o) - 10 \log_{10} \left(1+A_r^i\right) \\ &-15 \log_{10} (4.42\ V_r^2 - 4.56\ V_r + 2.15) \end{aligned} \qquad (10)$$

where

$$V_r = V_j^i/V_j^o \qquad \text{and} \qquad A_r = A^i/A^o$$

Figure 105 shows the normalized high frequency portion of the source spectrum. Using Figures 104 and 105, the low and high frequency portions of the source spectrum are determined, and the frequency (1/3-octave band) at which they intersect determines the end of the low frequency and the beginning of the high frequency portion of the source spectrum for any set of inner and outer jet flow conditions.

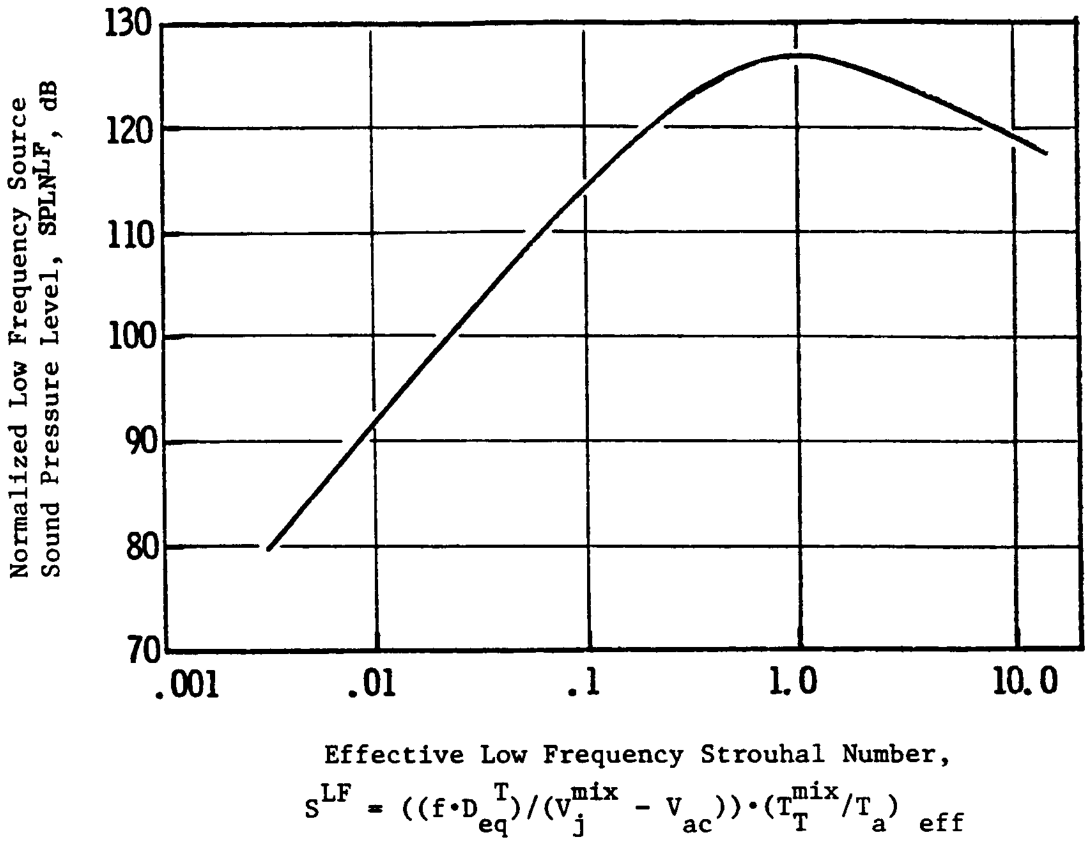

Figure 104. Normalized Low Frequency Spectrum at $\theta_I = 90°$.

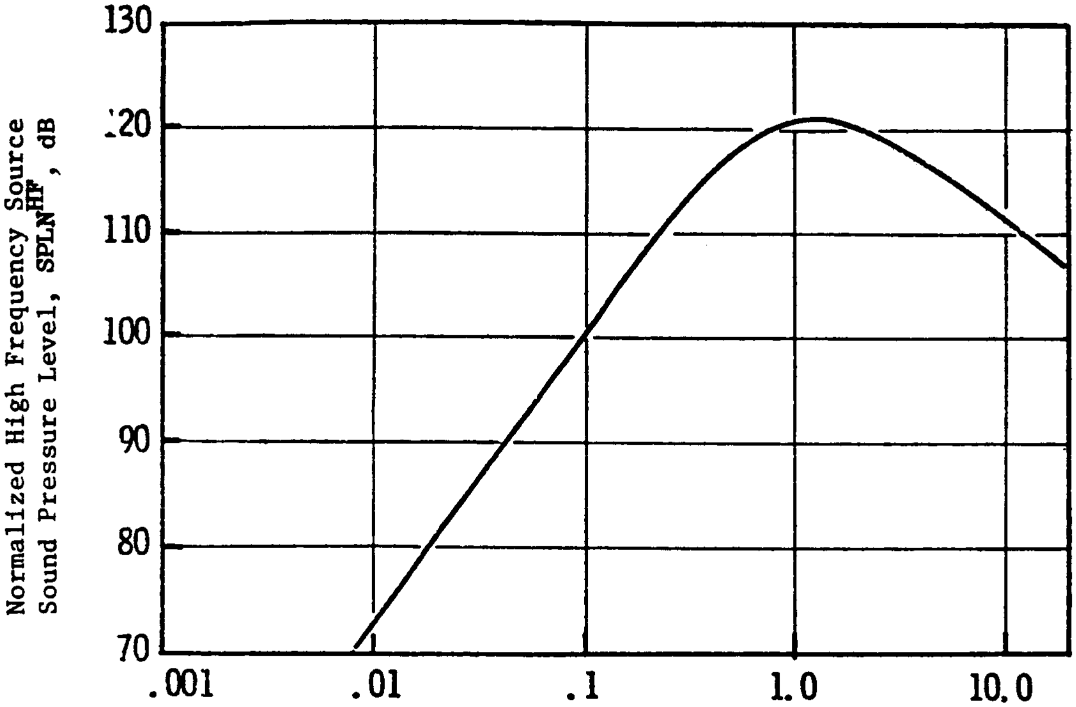

Effective High Frequency Strouhal Number,

$$S^{HF} = ((f \cdot D^{o}_{hyd})/(V^{o}_{j} - V_{ac})) \cdot (T^{o}_{T}/T_{a})_{eff}$$

Figure 105. Normalized High Frequency Spectrum at $\theta_I = 90°$.

2. Convective Amplification and Doppler Shift Due to Convecting Turbulence Eddies

As the turbulence eddies (that generate the mixing noise) are convected relative to the observer, there is an amplification of the source spectrum in the aft angles as well as an attenuation in the forward quadrant. The amplification/attenuation is a function of the eddy convection Mach number and the observer angle relative to the inlet. The convection Mach number of the turbulence eddies is given by

$$M_c = 0.5\left[0.55 + \frac{0.39}{V_r}\right]\left(V_j/a_o\right) \text{ for } V_r < 1.0 \tag{11}$$

$$= 0.55\, V_j/a_o \text{ for } V_r \geq 1$$

The above expression was derived from the M*G*B (Reference 10) prediction method as applied to inverted velocity profile coannular jets, though the constants are different because here the jet exit mean velocity is used in place of the local mean velocity.

The expression for the convective amplification is

$$\Delta\, SPL_{CA} = N\left(10\ \log_{10} C\right) \tag{12}$$

where

$$C = \left[\left(1 + M_c \operatorname{Cos} \theta_I\right)^2 + \alpha^2 M_c^2\right]^{1/2} \tag{12a}$$

and $\alpha = 0.325$ (from Reference 25).

Balsa's theory (References 26 through 28) for a conic jet suggests that the constant N, which is a function of θ_I, is 3 for angles to the inlet less than the cutoff angle for shielding and N = 7 for angles greater than the cutoff value. Based on these limits, the variation of N with θ_I was determined from the data base and is shown in Figure 106. The convection Mach numbers were calculated using V_j^{mix} and V_j^o for the low and high frequency portions of the spectrum, respectively.

The frequency shift associated with eddies moving relative to the observer is given by

$$f_{\theta_I} = \frac{f_{90°}}{C} \tag{13}$$

This shifts the peak frequency to lower frequencies in the front quadrant and to higher frequencies in the aft quadrant.

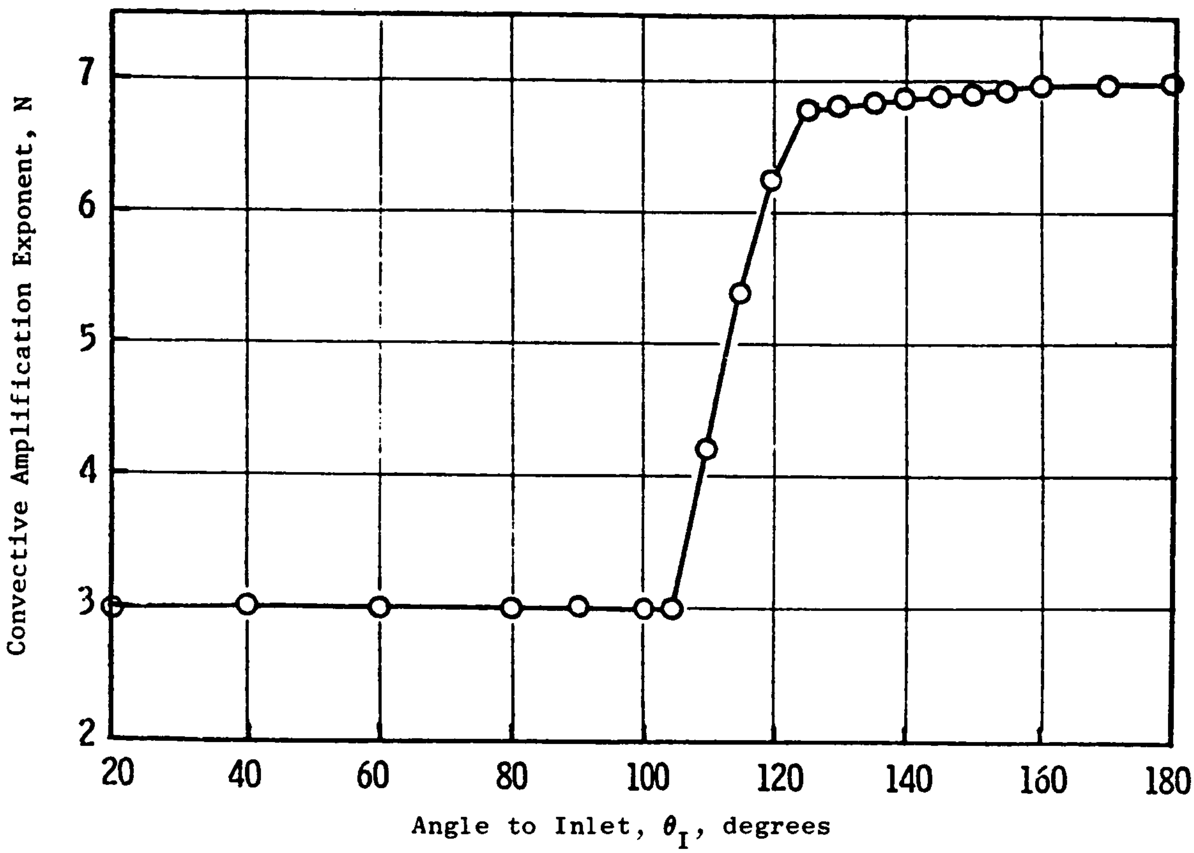

Figure 106. Variation of Convective Amplification Exponent with Angle.

3. Mean Flow Shrouding

Since Balsa's formulation (References 26 through 28) of the shielding function must be applied to each eddy in the flow depending on its location and the observer angle, a simplification is necessary for a semiempirical prediction procedure. Gliebe (Reference 29) derived such a simplification for conic nozzles by assuming average flow properties to replace the local flow properties, thereby determining the shielding function and shielding factor (defined later) as functions of observer angle, characteristic flow, geometric properties, and source frequency. Comparisons made by Gliebe with data based on these assumptions showed reasonable agreement. Based on the initial success of Gliebe, his expressions for shielding function and shielding factor were scrutinized, refined, and extended here to apply to coannular plug nozzles.

From Balsa's analysis, the reduction in noise level radiated by a single eddy (Figure 107) due to fluid shielding is given by

$$(\Delta dB)_{shielding} \approx -2K_1 g^2 \, (R)^{1/2} \, dR \tag{14}$$

where the shielding function is given by

$$\left\lfloor \frac{g^2}{C} \right\rfloor^{1/2} = \sqrt{\frac{\left| \left[(1+M_c \cos \theta_I)^2 \quad (C/C_a)^2 \right] - \cos^2 \theta_I \right|}{C^2}} \tag{15}$$

where

$$(C/C_a)^2 = 0.65 \, T_j/T_a + 0.35$$

Instead of defining the shielding function for each eddy, an average shielding function was defined where M_c and C are now based on the characteristic mean velocity of the flow rather than the local mean velocity. The constant of proportionality defined as the shielding factor is then given by

$$H\left(\frac{fD}{C_a}\right) = \frac{\Delta SPL\ (f)_{shielding}}{\left(\frac{fD}{C_a}\right)\left(2\pi C_a\right)\left(\frac{g}{C}\right)} \tag{16}$$

Using the data base on coannular jets (Reference 2), a curve of $H(fd/C_a)$ versus (fD/C_a) (Figure 107) was determined which could be used with the low and high frequency portions of the spectrum. From theory, it can be shown that shielding of the noise from the turbulence eddies by the mean flow occurs only for negative values of the shielding function g^2. So, the angle θ_C at

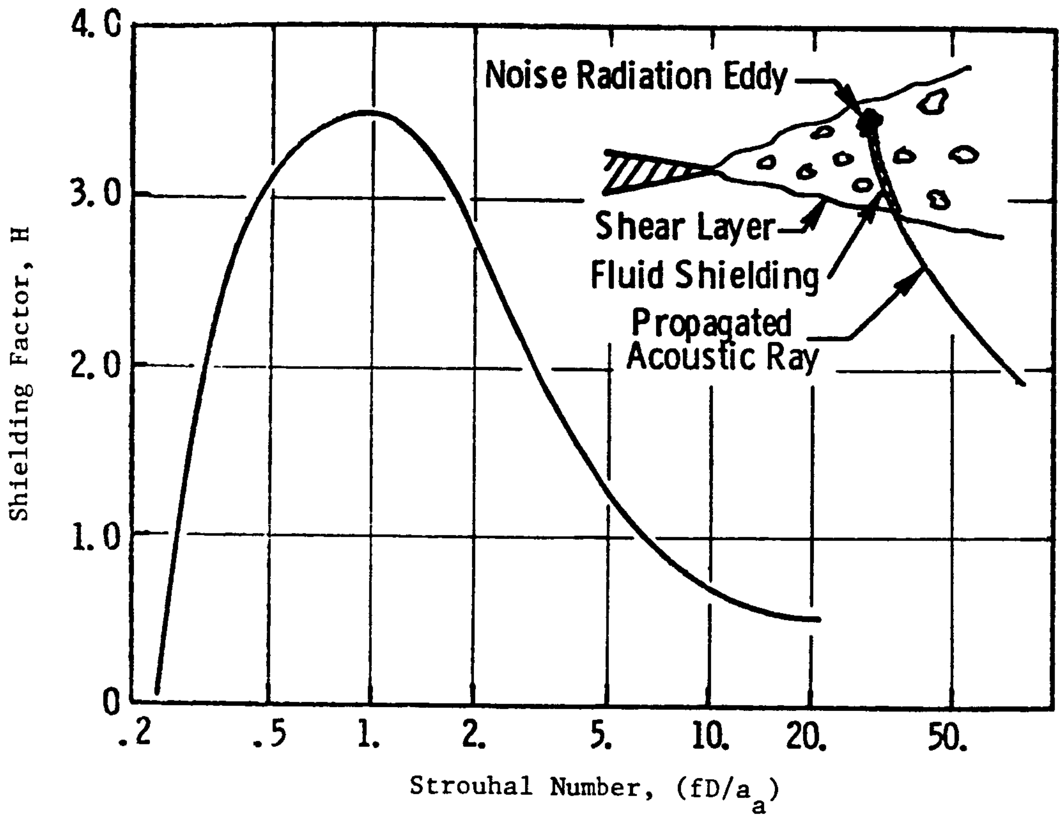

Figure 107. Variation of Shielding Factor with Strouhal Number for Coannular Plug Nozzles.

at which there will no longer be any shielding is obtained by equating the argument of Equation 15 to zero. This yields

$$\theta_C = \mathrm{Cos}^{-1}\left[\frac{-1}{(C/C_a) + M_c}\right] \tag{17}$$

Using Equations 14 through 17, the reduction in SPL as a function of frequency due to fluid shielding can be obtained for the low and high frequency portions of the spectrum at each angle.

Therefore, the procedure for predicting the jet mixing noise spectrum at any angle for coannular plug nozzles can be summarized as follows: the source spectrum is predicted using Equations 1 through 10 and Figures 104 and 105. Next, convective amplification effects on both noise level and frequency are added using Equations 11 through 13 and Figure 106. Finally, the fluid shielding effects are determined using Equations 14 through 17 and Figure 107. Then, the predicted sound pressure level at any frequency and angle is given by

$$\mathrm{SPL}\ (f) = \underbrace{\mathrm{SPL}_1\ (fs)}_{\substack{\text{Doppler shifted}\\ \text{due to convection}\\ \text{to } (f)}} - \underbrace{\Delta\mathrm{SPL}\ (f)}_{\text{fluid shielding}} \tag{18}$$

where

$$\mathrm{SPL}_1\ (fs) = \underbrace{\mathrm{SPL}\ (fs)}_{\substack{\text{source}\\ \text{spectrum}}} + \underbrace{\Delta\mathrm{SPL}\ (fs)}_{\substack{\text{convective}\\ \text{amplification}}}$$

The spectrum thus predicted is lossless (i.e., no air attenuation effects are included). It can then be scaled, extrapolated, or simply converted to standard day conditions using the appropriate procedures.

4. Extension of the Jet Mixing Noise Prediction Method to Flight

In order to apply the prediction method described above to engines in flight, the method had to be extended to include the effects of the flight velocity on the noise signature.

Based on comparisons of conic free-jet data transformed to flight with static data, the Strouhal numbers corresponding to peaks in the low and high frequency components of the coannular jet mixing noise source spectrum are modified from those for static predictions as follows:

$$\left(\frac{f_P^{LF}\ D_{eq}^T}{V_j^{mix}}\right)\left(\frac{T_T^{mix}}{T_a}\right)_{eff}\left(\frac{V_j^{mix} - V_{ac}}{V_j^{mix}}\right) = 0.9 \tag{19}$$

and

$$\left(\frac{f_P^{HF}\ \overset{o}{D}_{hyd}}{\overset{o}{V_j}}\right)\left(\frac{\overset{o}{T_T}}{T_a}\right)_{eff}\left(\frac{\overset{o}{V_j}-V_{ac}}{\overset{o}{V_j}}\right) = 1.18 \qquad (20)$$

where V_{ac} = aircraft velocity.

Also, the static source spectrum levels for the low and high frequency components of the spectrum are reduced, respectively, by

$$SPL^{LF} = 20\ \log_{10} \frac{V_j^{mix} - V_{ac}}{V_j^{mix}}$$

$$SPL^{HF} = 20\ \log_{10} \frac{\overset{o}{V_j} - V_{ac}}{V_j^{mix}} \qquad (21)$$

Hence, using Equations 19 through 21, the in-flight source spectrum can be predicted.

To predict the flight spectra at any other angle, the same procedure outlined for static prediction is used with the convection Mach numbers now based on relative velocity, i.e.,

$$M_c^{LF} = \frac{1}{2}\left[0.55 + \frac{0.39}{V_r}\right]\left(\frac{V_j^{mix} - V_{ac}}{a_a}\right) \text{for } V_r < 1.0$$

$$= 0.55\ (V_j^{mix} - V_{ac}/a_a) \text{ for } V_r \geq 1.0 \qquad (22)$$

$$M_c^{HF} = \frac{1}{2}\left[0.55 + \frac{0.39}{V_r}\right]\left(\frac{\overset{o}{V_j} - V_{ac}}{C_a}\right) \text{for } V_r < 1.0$$

$$= 0.55\ (\overset{o}{V_j} - V_{ac})/C_a \text{ for } V_r \geq 1.0$$

It must be noted that, except at $\theta_I = 90°$, this method of predicting flight noise spectra does not use the conventional method of applying flight-effect corrections to the static spectra in the form of a relative velocity exponent as used by several existing methods (References 30 and 31). As a result, the controversy of deciding the correct value of the exponent is avoided, as suggested in Reference 32.

B. Coannular Shock Noise Prediction

The spectral shock cell noise prediction method due to Fisher and Harper-Bourne (FHB) (Reference 33) for conic nozzles has been shown to adequately predict the shock noise from conic nozzles over a wide range of operating conditions. Therefore, the approach taken in formulating a shock noise spectral prediction method for coannular nozzles was to use the FHB method with appropriate modifications.

As the shock structure in any under- or overexpanded jet of a given cross-sectional area is a function of the operating pressure ratio and independent of the reservoir temperature, it would only seem logical to determine the effective pressure ratio of the coannular jet stream based solely on the pressure ratios of the two streams and not on the temperature at which they are operated. This is accomplished by equating the ideal thrust from an equivalent jet to the sum of the ideal thrusts produced by the inner and outer streams of a coannular plug nozzle configuration. By so doing, the effective pressure ratio P_r^{eff} of the equivalent jet can be determined and hence the effective (isentropic) Mach number. The effective shock strength parameter is then defined as:

$$\beta^{eff} = \sqrt{({M_j^{eff}}^2 - 1)} \tag{23}$$

where

$${M_j^{eff}}^2 = 2/\gamma-1 \left[(P_r^{eff})^{\gamma-1/\gamma} - 1\right] \tag{24}$$

and $P_r^{eff} = P_r^o + P_r^i \, A_r / 1 + A_r$

The equation used in the FHB method for the average shock cell length L is

$$L = K\beta D \tag{25}$$

where

D = Exit diameter of the nozzles

β = Shock strength parameter as defined by Equation 23

K = 1.1 for conic nozzles

For coannular jets, based on examining the data (Reference 17), the constant K was determined to be a function of β^{eff} and is given by

$$K = 0.48\,\beta^{eff} + 0.54 \tag{26}$$

Since the turbulence eddies convecting past the shock cells generate the broadband noise, the convection velocity associated with these eddies must be identified. The mass-averaged total temperature T_T^{mix}, and the effective jet Mach number, M_j^{eff}, are used to determine the effective jet velocity which is substituted in the FHB method in order to predict the peak frequency for the shock-associated broadband noise.

With these changes, the FHB method was used to predict shock noise for coannular jets. On comparing the predicted spectra with that measured, the shape was found to be satisfactory but the level was 6 dB too high. Since this was consistently observed for several operating conditions, the level was lowered by 6 dB and viewed as the noise from two shock cells instead of eight.

1. Extension of Shock Noise Prediction to Flight

The only difference between the static and flight shock noise is the dynamic effect and the Doppler shift. The dynamic effect is given by

$$(SPL_F - SPL_S) = 40 \log_{10} (1 + M_{ac} \text{ Cos } \theta_I) \tag{27}$$

which amplifies the shock noise in the front quadrant while it mitigates it in the aft quadrant. The Doppler shift is given by

$$f_F = f_S/(1 + M_{ac} \text{ Cos } \theta_I) \tag{28}$$

With these two changes, the flight peak noise spectra are predicted.

The coannular jet mixing noise and shock noise routines have been programmed, and the total spectra can be predicted for varying operation conditions and nozzle geometries.

5.3.3 Comparison of Data and Predictions

Comparison of the measured OASPL directivity and the 1/3-octave sound pressure spectra for a coannular plug nozzle configuration with $A_r = 0.2$ and $R_r^o = 0.853$ and mounted on a VCE engine (Reference 9) operating in the inverted velocity profile mode is shown in Figures 108 and 109. A good agreement is observed in both the noise level and in the shape of the directivity and sound pressure spectra. Additional verification is provided by Figures 110 through 112 that compare the measured and predicted variations of normalized PNL_{max} with 10 log V_j^{mix} for coannular nozzles of different area ratios and radius ratios.

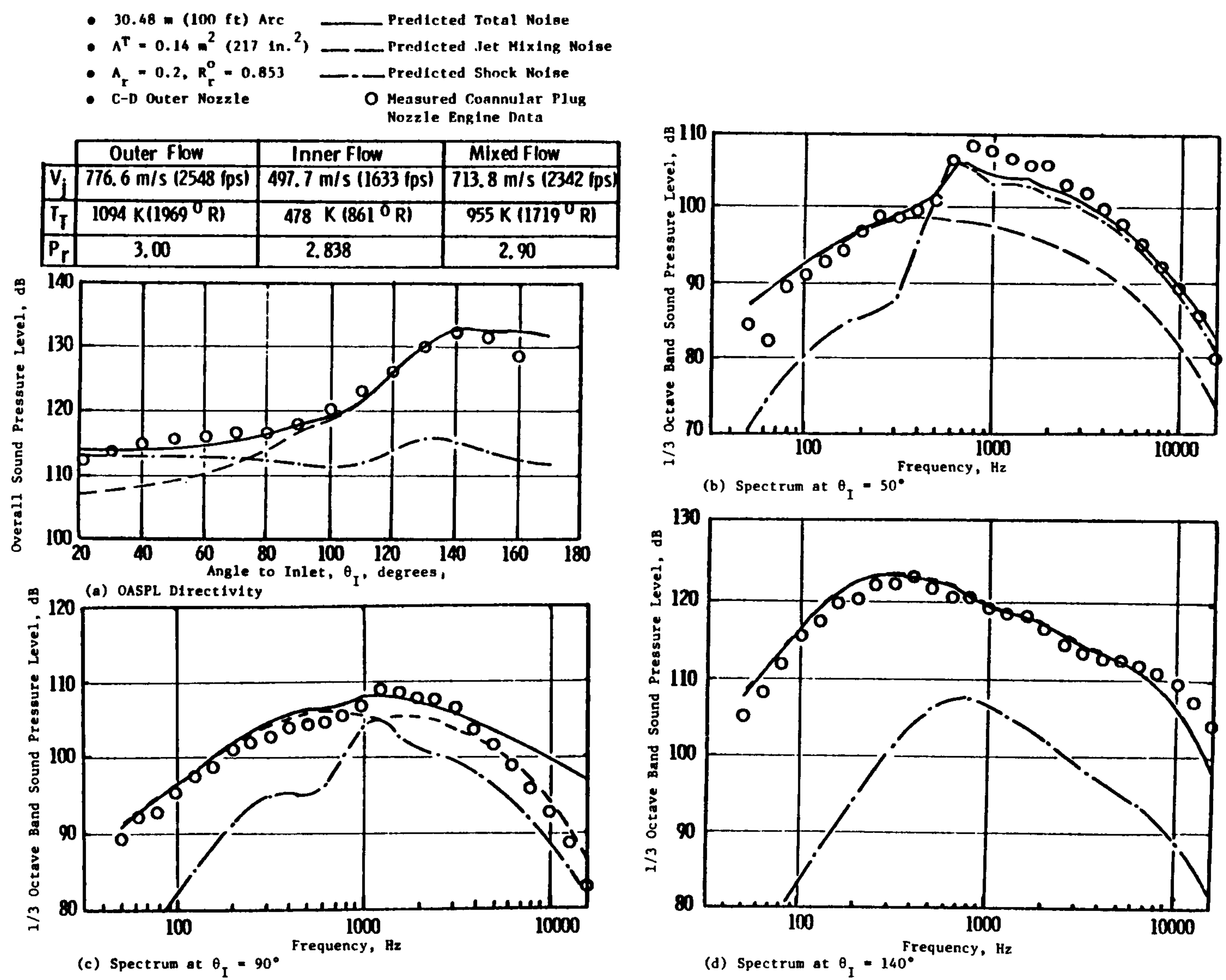

	Outer Flow	Inner Flow	Mixed Flow
V_j	776.6 m/s (2548 fps)	497.7 m/s (1633 fps)	713.8 m/s (2342 fps)
T_T	1094 K (1969 °R)	478 K (861 °R)	955 K (1719 °R)
P_r	3.00	2.838	2.90

Figure 108. Directivity and Spectral Comparisons of Measured Versus Predicted Jet Mixing and Shock Noise for a Coannular Plug Nozzle.

	Outer Flow	Inner Flow	Mixed Flow
V_j	547.7 m/s (1797 fps)	369.7 m/s (1213 fps)	507.8 m/s (1666 fps)
T_T	869 K (1564 °R)	415 K (747 °R)	767 K (1381 °R)
P_r	1.923	1.871	1.890

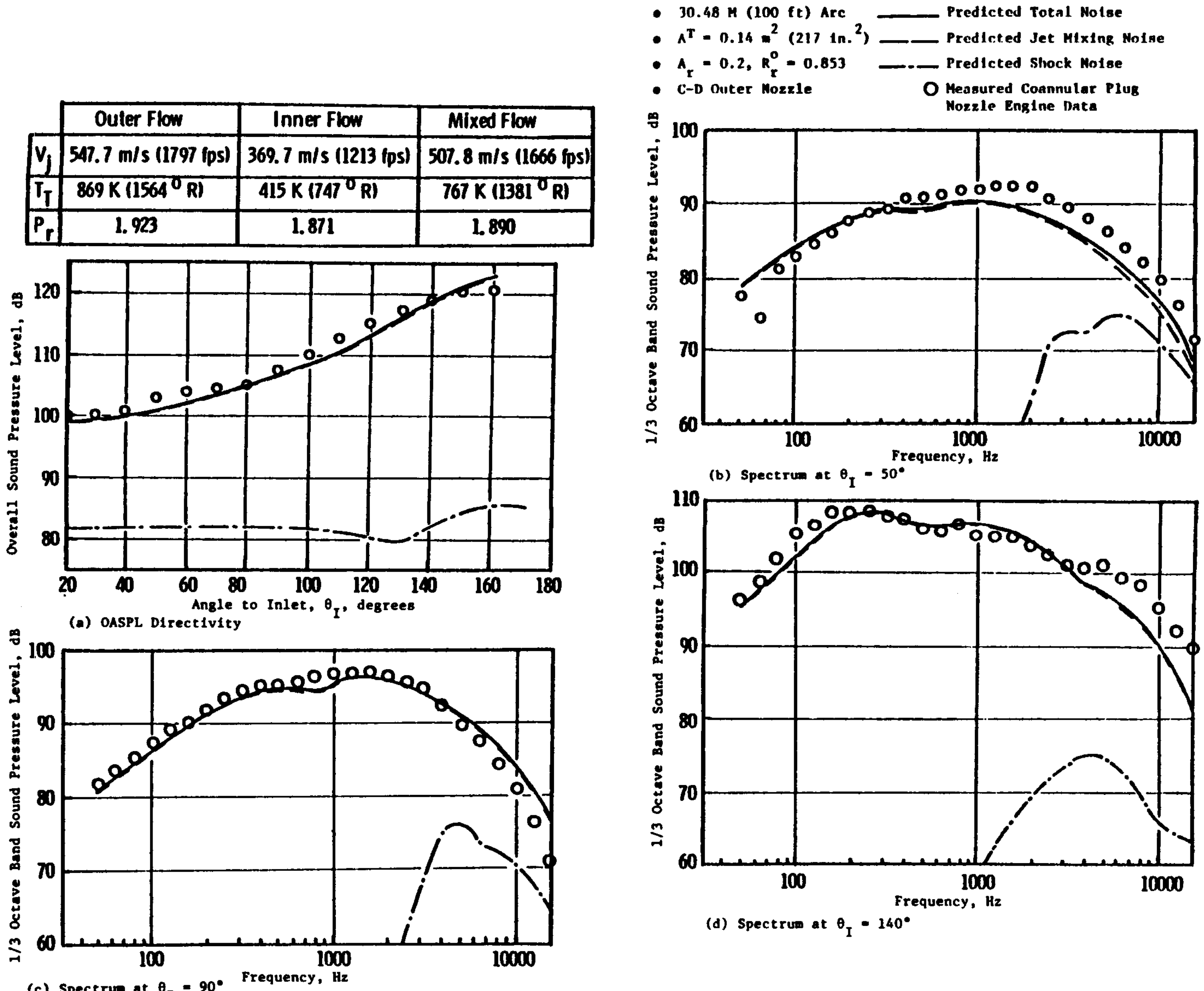

Figure 109. Directivity and Spectral Comparisons of Measured Versus Predicted Jet Mixing and Shock Noise for a Coannular Plug Nozzle.

- $A^T = 0.907\ m^2\ (1400\ in.^2)$
- 731.5 m (2400 ft) Sideline
- C-D Outer Nozzle
- F_{ref} = 22,819 N (5130 lb)
- ρ_a = 59° F

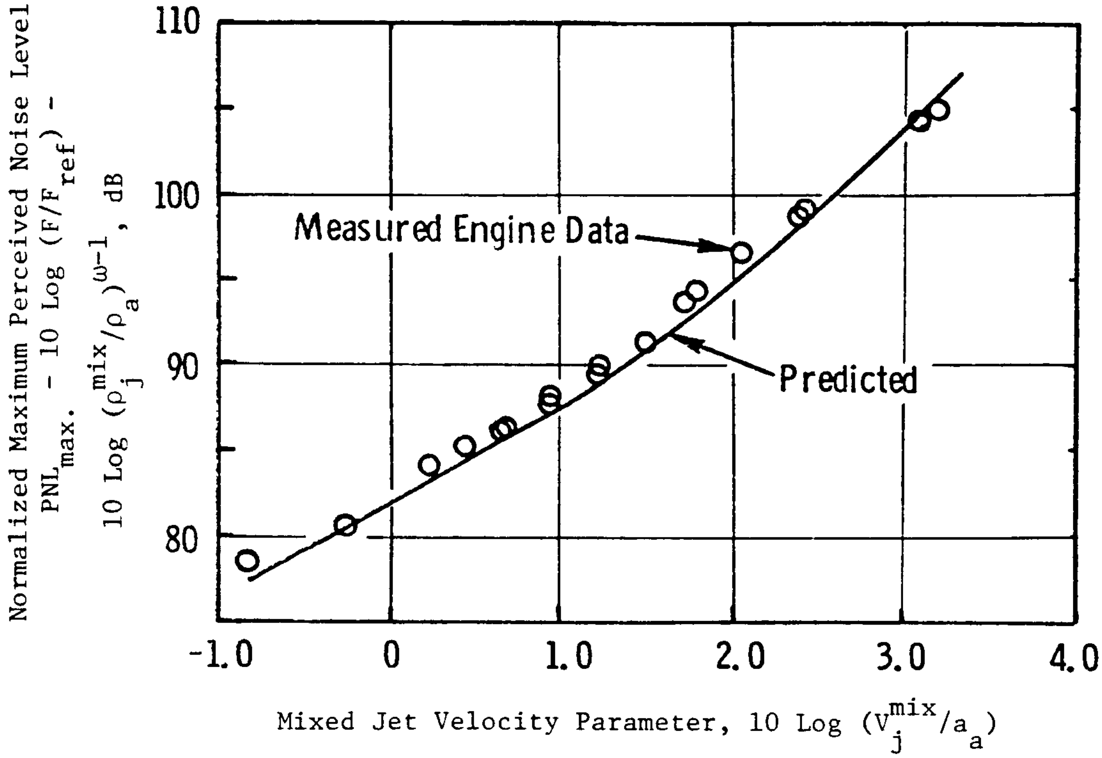

Figure 110. Comparison of Measured Versus Predicted Variation of Normalized PNL for a Coannular Nozzle, Area Ratio = 0.2, Outer Radius Ratio = 0.853.

- A^T = 0.907 m^2 (1400 in.^{2})
- 731.5 m (2400 ft) Sideline
- C-D Outer Nozzle
- F_{ref} = 22,819 N (5130 lb)
- ρ_a = 59° F

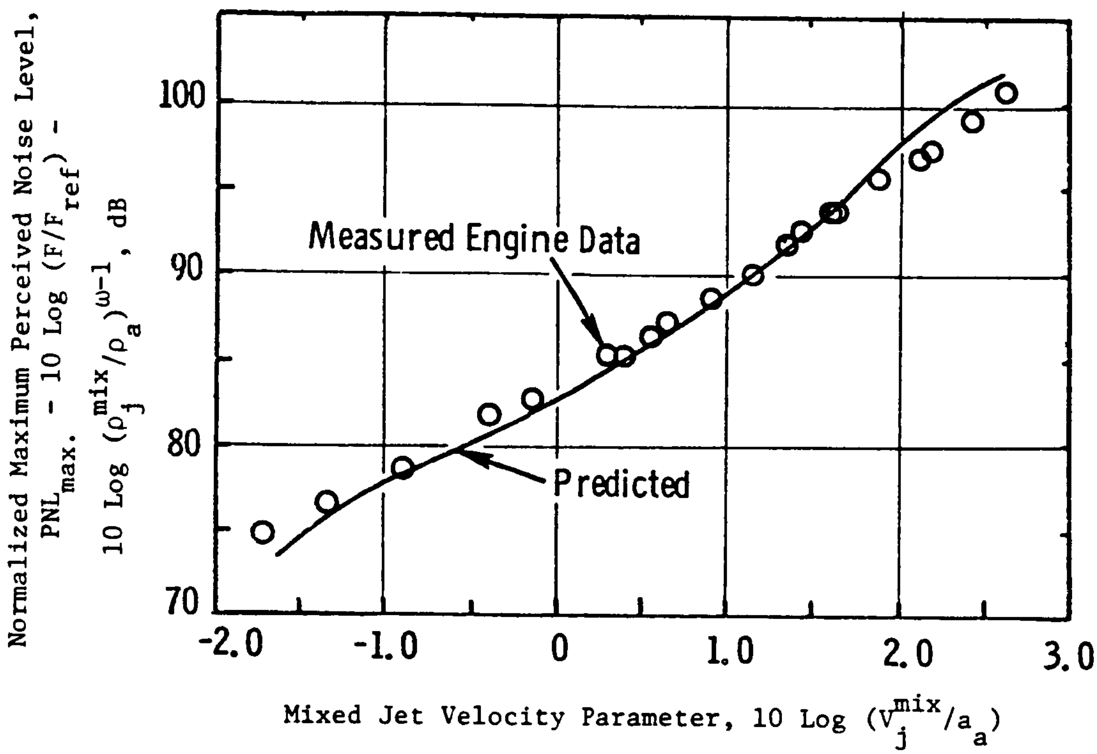

Figure 111. Comparison of Measured Versus Predicted Variation of Normalized PNL for a Coannular Nozzle, Area Ratio = 0.475, Outer Radius Ratio = 0.853.

- A^T = 0.907 m^2 (1400 $in.^2$)
- 731.5 m (2400 ft) Sideline
- C-D Outer Nozzle
- F_{ref} = 22819 N (5130 lb)
- ρ_a = 59° F

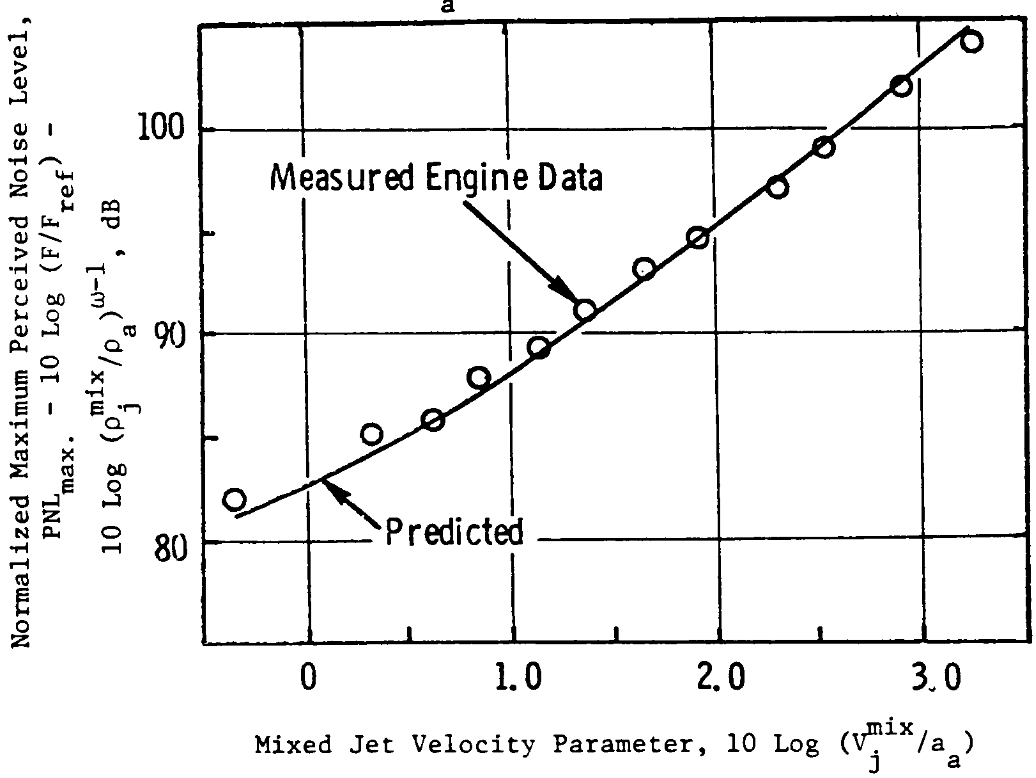

Figure 112. Comparison of Measured Versus Predicted Variation of Normalized PNL for a Coannular Nozzle, Area Ratio = 0.2, Outer Radius Ratio = 0.875.

To assess the in-flight prediction method, the free-jet data from coannular plug nozzles were flight transformed (Reference 28) and then compared with the predictions. This is shown in Figures 113 and 114. A good agreement is observed in both the spectrum shape and directivity. It must be indicated here that the data used for comparisons with the predictions were from engine and scale model tests, and they were not a part of the data base that was used during the development of the prediction method.

- $A^T = 0.907\ m^2\ (1400\ in.^2)$
- 731.5 m (2400 ft) Sideline
- $A_r = 0.2$, $R_r^o = 0.853$
- Static
- C-D Outer Nozzle

Legend:

—— Predicted

O Measured Coannular Plug Nozzle Engine Data

	Outer Flow	Inner Flow	Mixed Flow
V_j	739.4 m/s (2426 fps)	360.9 m/s (1184 fps)	690.1 m/s (2264 fps)
T_T	944 K (1700 ^{0} R)	452 K (814 ^{0} R)	880 K (1584 ^{0} R)
P_r	3.23	1.73	2.96

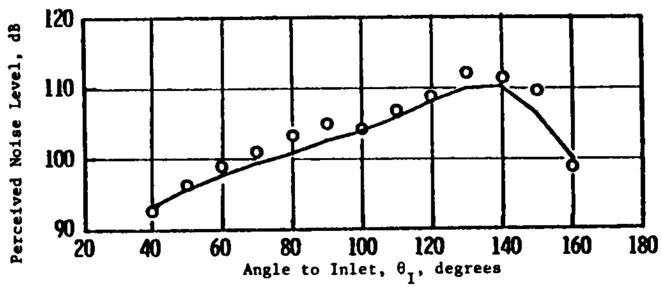

(a) PNL Directivity

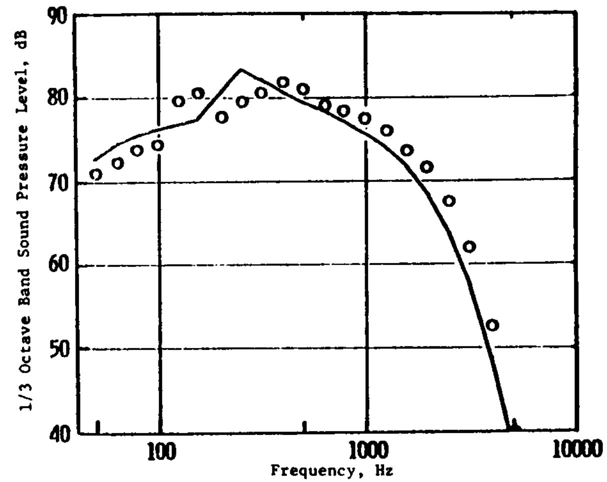

(b) Spectrum at θ_I = 50°

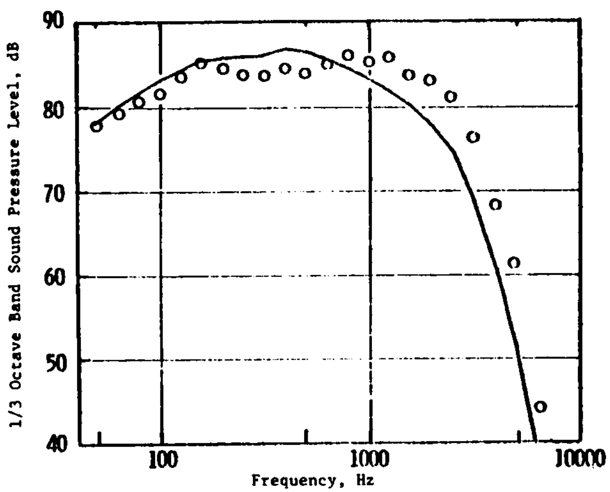

(c) Spectrum at θ_I = 90°

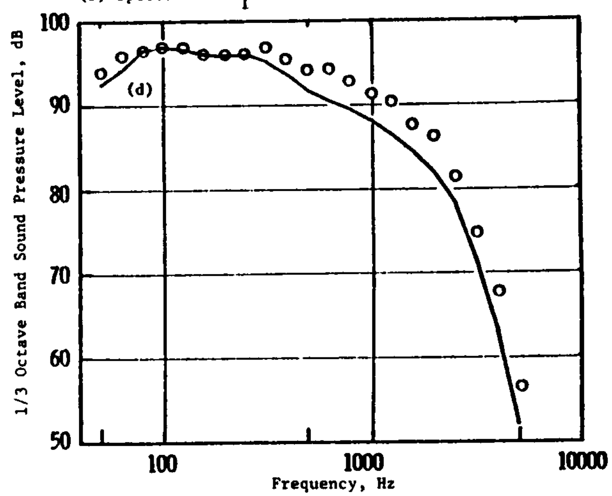

(d) Spectrum at θ_I = 130°

Figure 113. Directivity and Spectral Comparisons of Measured Versus Predicted Jet Mixing and Shock Noise for a Coannular Plug Nozzle (Static).

- A^T = 0.907 m^2 (1400 in.^{2})
- 731.5 m (2400 ft) Sideline
- A_r = 0.2, R_r^o = 0.853
- Flight, $V_{a/c}$ = 118.9 m/s (390 fps)
- C-D Outer Nozzle

Legend:

——— Predicted

O Measured Coannular Plug Nozzle Engine Data

	Outer Flow	Inner Flow	Mixed Flow
V_j	743.7 m/s (2440 fps)	361.4 m/s (1186 fps)	693.4 m/s (2275 fps)
T_T	953 K (1716 °R)	450 K (810 °R)	887 K (1597 °R)
P_r	3.23	1.73	2.96

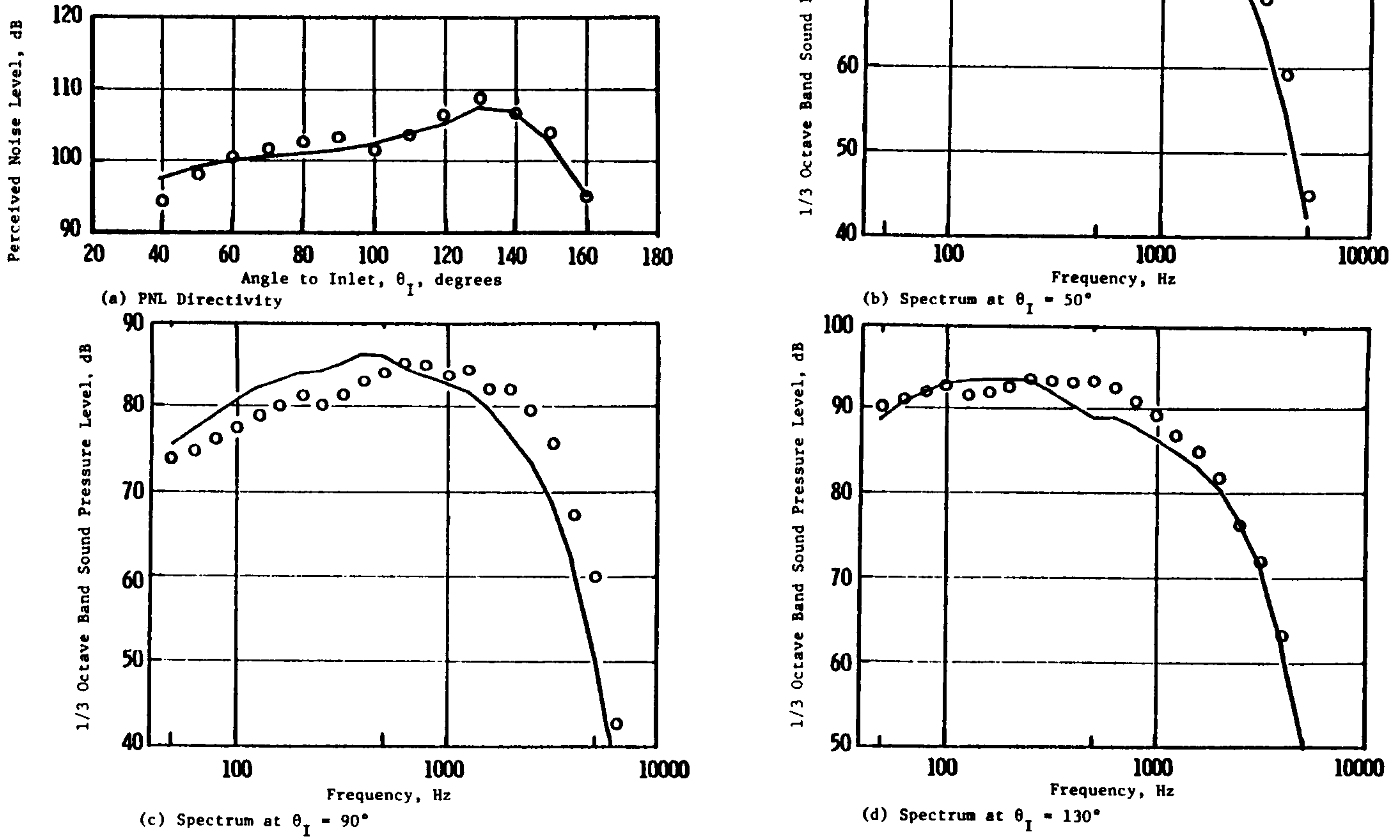

Figure 114. Directivity and Spectral Comparisons of Measured Versus Predicted Jet Mixing and Shock Noise for a Coannular Plug Nozzle (Flight).

6.0 CONCLUSIONS AND RECOMMENDATIONS

6.1 CONCLUSIONS

All six high-radius-ratio coannular plug nozzles, along with a reference conical nozzle, were successfully tested in a simulated flight environment. The nozzle models tested are candidate exhaust nozzle configurations for General Electric designs for VCE and AST applications. The nozzle geometric variables included: an outer nozzle radius ratio variation (0.853 and 0.902), an inner-to-outer nozzle area ratio variation (0.2 and 0.53), nozzles with and without struts, and a first simple attempt at a convergent-divergent termination on the outer stream nozzle for further shock noise control. Most of the tests were conducted at elevated exhaust nozzle temperatures (up to 1760° R) and at high nozzle pressure ratios (up to 3.6).

The significant results are:

- In a simulated flight environment, the unsuppressed coannular plug nozzle maintained its general favorable noise reduction features. At typical takeoff sideline engine operation, 5 PNdB jet noise reduction and 6 PNdB shock noise reduction were measured relative to a reference baseline conical nozzle at the same specific thrust and effective nozzle pressure ratios.

- Outer stream radius ratio and inner-stream-to-outer-stream area ratio nozzle geometry parameters were found to influence the simulated flight acoustic signature similar to what has been observed and reported from General Electric static acoustic test results (Reference 2):

  - A higher outer stream radius ratio results in greater noise on. reduction.
  - At low specific thrust values, an increase in area ratio will increase the jet noise.
  - Inner-stream-to-outer-stream velocity ratio is an important design parameter.

- The control of the downstream coannular shock structure can have a significant effect on the forward quadrant and aft quadrant radiated noise. Up to 2.5 ΔEPNdB noise reduction for a coannular plug nozzle configuration was estimated.

- To obtain shock control through the use of a convergent-divergent termination, great care will be necessary in the aerodynamic contour of the annular nozzle passages.

- A unique coannular plug nozzle spectral jet mixing and shock noise prediction method was evaluated. The method is based on the physics of the flow and its noise-radiating characteristics and is the first method to model the source spectrum, eddy spectrum, and fluid shrouding in a simplistic fashion. The predicted data were found to be in good agreement with measurements over a range of operating velocities. The general methodology might be easily extended to nozzles of other complex geometries.

6.2 RECOMMENDATIONS

Based on the studies conducted during this contract effort, the following items warrant future investigations:

- Continue systematic simulated flight acoustic experiments to evolve design criterion for shock control of coannular and annular plug nozzles using convergent-divergent terminations.

- Improve evaluation of the influence of temperatures on forward quadrant coannular plug nozzle shock noise.

- Evaluate the flight acoustic spectrum of a candidate multielememt, mechanically suppressed coannular plug nozzle.

- Further evolve the spectral acoustic prediction methodology of this study to other complex nozzle geometries for supersonic and subsonic exhaust nozzle applications.

7.0 NOMENCLATURE

A	Cross-Sectional Area
a	Radius of Free Jet
AST	Advanced Supersonic Transport
C	Convective Amplification Factor (see Equation 12a)
c	Speed of Sound
CDR	Comprehensive Data Report
$Corr_R$	Refraction Correction
$Corr_T$	Turbulent Absorption Correction
$Corr_{90°}$	Turbulent Absorption Correction at $\theta_I = 90°$
dB	Decibel
D	Diameter
D_R	Directivity Factor
D_I	Directivity Factor
EPNL	Effective Perceived Noise Level, EPNdB
F	Thrust
F_{ref}	Reference Thrust, 5130 pounds
f	Frequency
FTFSDR	Flight Transformed, Full-Scale Data Reduction Computer Program
g	Fluid Shielding Function (see Equation 15)
H	Shielding Factor
h	Annular Step Height
Hz	Hertz
I_o, I_i	Bessel Functions
J_o, J_i	Bessel Functions

K	Constant in Equation (25)
k	Wave Numbers, $2\pi\ f/c$
L	Shock Separation Distance
l	Path Length
M	Mach Number
M_c	Convection Mach Number
N	Convective Amplification Exponent
OAPWL	Overall Sound Power Level
OASPL	Overall Sound Pressure Level
P	Pressure
Pr	Defined = P_T/P_a
PNL	Perceived Noise Level
PNLN	Normalized PNL, Defined as PNL - 10 log $(F/F_{ref})\ (\rho/\rho_a)^{w-1}$
R	Radius
RH	Relative Humidity
R_r	Radius Ratio
S	Strouhal Number
SL	Side Line
SPL	Sound Pressure Level
SPLN	Normalized SPL
T	Temperature
U_c	Convection Velocity
$\acute{u}$	Turbulent Velocity
V	Ideally Expanded Velocity
VCE	Variable Cycle Engine
W	Weight Flow Rate

X	Axial Distance
X_s	Distance Along Plug (see Figure 103)
x	Geometric Acoustic Length, ka sin θ, see Figure 8
y	Geometric Acoustic Length, ka $\{\cos^2 \theta - (1 - M \cos \theta)^2\}^{1/2}$, see Figure 8
Y_o, Y_i	Bessel Functions
α	Turbulence Parameter
α_1, α_2	Linear Regression Coefficients
β	Shock Strength Parameter
γ	Specific Heat Ratio
ε	Eddy Viscosity
θ	Angle Measured Relative to Exhaust Centerline
θ_c	$\cos^{-1}$ [1/(1 x M)], see Figure 8
θ_I	Angle Measured Relative to the Inlet Centerline
θ_s^1, θ_s^2	Plug Angles, Defined in Table III
μ	Absolute Viscosity Coefficient
ρ	Density
σ_{yn}	Standard Error of Estimate, dB
ω	Density Exponent

Subscripts

1	Hub Dimension (defined in Table III)
2	Tip Dimension (defined in Table III)
ac	Aircraft
i	Initial
a	Ambient Conditions

Basic	Basic (Directivity)
c	Critical
E	East
eff	Effective
F	Flight
eq	Equivalent
fj	Free Jet
hyd	Hydraulic
max	Maximum
p	Peak
j	Based on Ideal Jet Conditions
r	Ratio
S	Static
T	Stagnation Condition
W	West
60°	Evaluated at $\theta_I = 60°$
θ	Value at Angle θ_I

Superscripts

eff	Effective
HF	High Frequency
i	Inner Stream
LF	Low Frequency
o	Outer Stream
mix	Fully mixed Conditions
T	Based on Total Area
$-$	Mean Quantity

REFERENCES

1. Knott, P.R., Stringas, E.J., Brausch, J.F., Staid, P.S., Heck, P.H., and Latham, D., "Acoustic Tests of Duct-Burning Turbofan Jet Noise Simulation," NASA CR-2966, July 1978.

2. Knott, P.R., Blozy, J.T., and Staid, P.S., "Acoustic and Aerodynamic Performance Investigation of Inverted Velocity Profile Coannular Plug Nozzles," NASA CR-3149, February 1981. Detailed data are on report titled "Acoustic and Aerodynamic Performance Investigation of Coannular Plug Nozzles: Comprehensive Data Report," NASA Contract NAS3-19777, GE Report R79AEG166, April 1979.

3. Dosanjh, D.S., Adelhamid, A.N., Yu, J.C., "Noise Reduction from Interacting Supersonic Jet Flows," NASA SP-207, Basic Aerodynamic Noise Research, 1969.

4. Dosanjh, D.S., Bhutiani, P.K., Ahuja, K.K., and Bassiouni, M.R., "Supersonic Jet Noise Suppression by Coaxial Cold/Heated Jet Flows," AIAA Paper No. 76-507, July 1976.

5. Dosanjh, D.S., Bhutiani, P.K., Ahuja, K.K., "Supersonic Jet Noise Reduction by Coaxial Cold/Heated Jet Flows," Final Report to DOT under grant DOT-OS-20094, March 1977.

6. Kozlowski, Hilary and Packman, Allan B., "Aerodynamic and Acoustic Tests of Duct-Burning Turbofan Exhaust Nozzles," NASA CR-2628, 1976.

7. Pao, S.P., "A Correlation of Mixing Noise from Coannular Jets With Inverted Flow Profiles," NASA Technical Paper 1301, April 1979.

8. Vogt, P.G., Bhutiani, P.K., and Knott, P.R., "Free Jet Acoustic Investigation of High-Radius-Ratio Coannular Plug Nozzles," GE Report No. R81AEG212, Comprehensive Data Report, Vols. I and II, January 1981.

9. Vdoviak, J., Knott, P.R., Ebacker, J.J., "Aerodynamic/Acoustic Performance of YJ101/Double Bypass VCE With Coannular Plug Nozzle," NASA CR-159869, January 1981.

10. Shields, F.D. and Bass, H.E., "Atmospheric Absorption of High Frequency Noise and Amplification to Fractional Octave Bands," NASA CR-2760, June 1977.

11. Knott, P.R., et al., "Supersonic Jet Exhaust Noise Investigation," AFAPL-TR-74-25, June 1974.

12. Knott, P.R., "Supersonic Jet Exhaust Investigation - Volume I Summary Report," AFAPL-TR-76-68, July 1976.

13. Knott, P.R. and Mossey, P., "Parametric Laser Velocimeter Studies of High Velocity, High Temperature, Turbulent Jets," Second International Workshop on Laser Velocimeter, 28 March 1974, AFAPL-TR-76-68 Vol. II, Chapter III.

14. Scott, P., Mossey, P., and Knott, P.R., "In-Jet Noise Source Location Studies - LV Developments," Chapter IV, AFAPL-TR-74-25, Knott, P.R., Ed., June 1974.

15. Scott, P., "The Theory and Implementation of LV Spectra Measurements," International Workshop on Laser Velocimeter, 23 March 1974.

16. Knott, P.R., "Noise Source Diagnostic Methods With a Laser Velocimeter," 1977 Independent Research and Development Technical Plan, Volume III, March 1977, R77AEG326.

17. FAA-RD-76-79, II "High Velocity Jet Noise Source Location and Reduction - Task 2," May 1978.

18. Schubert, "Numerical Study of Sound Refraction by a Jet Flow II Wave Acoustics," Journal of the Acoustical Society of America, September 1971.

19. Tanna, H.K., "An Experimental Study of Jet Noise - Part II: Shock Associated Noise," Journal of Sound and Vibration, (1977) 50 (3), pp. 429-444.

20. Stringas, E.J., et al., "High Velocity Jet Noise Source Location and Reduction," FAA-RD-76-79, Volumes I-IV.

21. Bhutiani, P.K., "A Unique Coannular Plug Nozzle Jet Noise Prediction Procedure," GE Report No. R79AEG481, October 1979.

22. Anon, "Jet Exhaust - Noise Prediction," AIR876, SAEA-21 Committee, N.Y., September 1975.

23. Lighthill, M.J., "On Sound Generated Aerodynamically: 1. General Theory," Proc. Royal, Soc. Lon., Vol. A211, 1952, pp. 564-587.

24. Hoch, R.G., Duponchel, R.P., Cocking, B.J., and Bryce, W.D., "Studies of the Influence of Density on Jet Noise," Journal of Sound and Vibration, Vol. 28, No. 4, 1973, pp. 649-668.

25. Ribner, H.S., "Aerodynamic Sound from Fluid Dilatations - A Theory of the Sound from Jets and Other Flows," UTIA Report No. 86, 1962.

26. Balsa, T.F., "Fluid Shielding of Low Frequency Convected Sources by Arbitrary Jets," Journal of Fluid Mechanics, Vol. 70. Part 1, 1975, pp. 17-36.

27. Balsa, T.F., "The Shielding of a Convected Source by an Annular Jet With an Application to the Performance of Multitube Suppressors," Journal of Sound and Vibration, Vol. 44, No. 2, 1976, pp. 179-189.

28. Balsa, T.F., "The Far Field of High Frequency Convected Singularities in Sheared Flows, with Application to Jet-Noise Prediction," Journal of Fluid Mechanics, Vol. 74, Part 2, 1976, pp. 193-208.

29. Gliebe, P.R., unpublished work.

30. Bushell, K.W., "Measurements and Prediction of Jet Noise in Flight," AIAA Paper No. 75-461, March 1975.

31. FAA-RD-76-79, VI, "High Velocity Jet Noise Source Location and Reduction - Task 6," April 1979.

32. Stone, J.R., "An Improved Method for Predicting the Effects of Flight on Jet Mixing Noise," NASA TM 79155, 1979.

33. Harper-Bourne, M. and Fisher, M.J., "The Noise from Shock Waves in Supersonic Jets," AGARD Conference, Paper No. CPP-131, 1973.

APPENDIX A

AERODYNAMIC TEST CONDITIONS FOR THE ACOUSTIC TESTS

NOZZLE - MODEL 1 AREA [MODEL SIZE - INNER = 2.47 , OUTER = 18.05 ; FULL SIZE - TOTAL = 1400.00] SQ.IN

TEST POINT	V_{ac} FT/SEC	P_r^o	T_T^o DEG R	V_j^o FT/SEC	W^o LB/SEC	P_r^i	T_T^i DEG R	V_j^i FT/SEC	W^i LB/SEC	P_r^{mix}	T_T^{mix} DEG R	V_j^{mix} FT/SEC	F LB	V_j^i/V_j^o
101	0	3.17	1721	2425	718.4	3.19	781	1628	149.4	3.11	1558	2287	61705	0.67
102	289	3.16	1723	2425	716.9	3.15	789	1628	146.4	3.10	1564	2289	61439	0.67
103	385	3.16	1733	2432	714.3	3.16	775	1616	148.4	3.09	1568	2291	61439	0.66
104	0	2.98	1695	2350	680.7	2.41	732	1398	116.3	2.86	1554	2211	54772	0.59
105	289	2.96	1693	2344	678.4	2.15	855	1421	96.2	2.84	1588	2229	53672	0.61
106	384	2.96	1687	2340	679.2	2.16	840	1413	97.6	2.84	1580	2223	53686	0.60
107	0	1.84	1605	1764	433.1	1.83	660	1121	93.0	1.82	1437	1650	26987	0.64
108	289	1.95	1488	1766	475.6	1.85	654	1125	94.4	1.91	1350	1659	29406	0.64
109	381	1.95	1473	1759	479.1	1.85	651	1122	94.5	1.91	1337	1654	29488	0.64
110	0	3.78	1684	2546	867.5	3.19	779	1625	149.1	3.64	1551	2410	76174	0.64
111	289	3.78	1715	2570	860.1	3.17	797	1639	146.7	3.64	1581	2434	76177	0.64
112	384	3.78	1697	2555	864.1	3.14	802	1639	144.8	3.64	1568	2423	75998	0.64
113	0	2.28	1738	2103	513.6	2.01	730	1261	97.5	2.21	1576	1968	37391	0.60
114	286	2.28	1724	2095	515.0	2.00	732	1258	96.6	2.21	1567	1962	37314	0.60
115	382	2.28	1728	2097	514.4	2.02	733	1267	97.5	2.21	1569	1964	37366	0.60
116	0	2.44	1715	2164	553.2	2.08	805	1352	95.9	2.36	1580	2044	41237	0.62
117	0	2.35	1678	2099	539.0	1.81	907	1305	78.6	2.27	1579	1998	38351	0.62
118	0	2.39	1732	2153	539.3	1.90	902	1346	82.5	2.31	1622	2045	39540	0.63
119	0	2.53	1677	2177	580.5	1.94	901	1367	84.5	2.44	1578	2074	42868	0.63

TEST POINT	T_{amb} DEG R	P_{amb} PSIA	RH %	NF dB	LVM	LBM	PNL (FULL SIZE, 2400 FT SIDE LINE), dB ANGLE RELATIVE TO INLET, DEGREES 50	70	90	110	120	130	140	OAPWL dB
101	476.0	14.58	43	-7.0	3.30	-0.10	101.2	104.1	107.4	108.5	111.7	114.3	112.7	186.0
102	473.7	14.59	56	-6.9	3.32	-0.12	105.4	106.3	108.1	107.4	110.6	111.4	110.2	184.4
103	474.6	14.59	56	-6.9	3.31	-0.12	106.7	106.8	108.0	106.9	110.9	111.1	109.3	184.3
104	477.3	14.58	43	-6.4	3.15	-0.53	96.2	99.5	104.1	105.9	110.5	112.2	111.3	184.4
105	479.5	14.60	49	-6.2	3.17	-0.61	97.6	100.9	103.7	104.1	108.3	109.1	107.7	181.4
106	479.5	14.60	49	-6.2	3.16	-0.61	99.3	101.2	103.6	103.5	108.5	108.6	106.8	180.9
107	473.7	14.59	46	-3.5	1.89	-10.00	85.8	90.3	95.4	97.1	100.0	99.1	97.0	173.0
108	481.8	14.57	48	-4.2	1.88	-7.18	88.5	92.1	95.3	95.1	98.2	96.4	91.6	169.5
109	482.3	14.57	48	-4.3	1.86	-7.01	89.5	91.9	94.9	94.3	97.7	95.6	89.9	169.1
110	476.6	14.58	43	-8.1	3.53	0.52	103.3	106.3	109.7	110.3	115.0	116.8	114.1	188.2
111	477.3	14.60	53	-8.0	3.57	0.52	104.8	106.7	109.0	109.0	114.0	115.4	114.0	187.2
112	477.7	14.60	53	-8.0	3.54	0.51	104.4	106.3	108.6	108.3	114.1	114.9	113.0	186.7
113	474.2	14.59	46	-4.3	2.66	-2.62	90.2	94.4	99.4	101.3	105.1	105.3	104.8	178.9
114	481.4	14.57	49	-4.4	2.61	-2.63	92.5	95.6	98.4	98.7	102.3	102.4	99.7	174.7
115	481.1	14.57	49	-4.4	2.62	-2.61	93.4	95.3	98.4	98.4	102.3	101.6	97.7	174.1
116	478.4	14.59	43	-4.8	2.80	-1.91	92.1	96.2	101.0	102.9	106.6	107.7	107.7	181.0
117	474.1	14.58	46	-4.4	2.72	-2.42	90.9	95.0	99.9	101.7	105.6	106.3	106.1	179.7
118	475.3	14.59	45	-4.5	2.82	-2.19	91.5	95.8	100.6	102.4	106.3	106.8	106.9	180.4
119	475.0	14.59	46	-5.0	2.88	-1.67	92.5	96.4	101.2	103.1	107.2	108.1	108.6	181.6

NOZZLE - MODEL 1A   AREA [MODEL SIZE - INNER = 3.50 , OUTER = 18.05 ; FULL SIZE - TOTAL = 1400.00] SQ.IN.

TEST POINT	V_{ac} FT/SEC	P_r^o	T_T^o DEG R	V_j^o FT/SEC	W^o LB/SEC	P_r^i	T_T^i DEG R	V_j^i FT/SEC	W^i LB/SEC	P_r^{mix}	T_T^{mix} DEG R	V_j^{mix} FT/SEC	F LB	V_j^i/V_j^o
101	0	3.23	1678	2411	703.4	3.19	789	1636	199.3	3.15	1481	2239	62844	0.68
103	390	3.23	1735	2453	691.6	3.22	804	1656	199.0	3.15	1527	2274	62969	0.68
104	0	2.99	1710	2364	644.0	2.28	738	1363	146.9	2.81	1529	2178	53543	0.58
106	390	2.98	1720	2369	640.8	2.27	761	1383	144.5	2.81	1543	2187	53393	0.58
107	0	1.96	1464	1758	457.7	1.83	681	1139	122.9	1.91	1298	1627	29359	0.65
108	290	1.96	1457	1757	460.4	1.83	681	1141	123.3	1.92	1293	1626	29514	0.65
109	390	1.96	1463	1759	458.8	1.83	677	1135	123.2	1.91	1296	1626	29432	0.65
110	0	3.84	1693	2564	831.5	3.19	793	1640	198.8	3.64	1519	2385	76398	0.64
112	390	3.81	1689	2556	827.7	3.21	787	1637	200.7	3.63	1513	2376	75963	0.64
113	0	2.31	1724	2110	495.5	2.08	716	1276	136.6	2.22	1506	1929	37916	0.60
115	390	2.30	1713	2099	495.4	2.04	728	1269	132.5	2.21	1505	1923	37545	0.60
116	0	2.47	1715	2177	530.7	2.14	755	1332	136.7	2.37	1518	2004	41568	0.61
117	0	2.40	1729	2157	514.8	2.13	753	1325	136.0	2.31	1525	1983	40114	0.61
118	0	2.51	1735	2207	536.4	2.22	753	1356	141.6	2.41	1529	2029	42762	0.61
119	0	2.50	1711	2190	539.5	2.19	721	1320	143.4	2.40	1503	2007	42606	0.60
121	0	3.23	1700	2426	697.5	1.72	814	1184	104.9	2.96	1584	2263	56449	0.49
122	390	3.23	1716	2440	696.3	1.73	810	1186	105.8	2.96	1596	2274	56706	0.49
123	0	3.23	1709	2433	695.9	1.18	837	678	52.4	2.96	1647	2310	53732	0.28
124	390	3.23	1730	2449	692.3	1.18	842	681	52.4	2.96	1667	2324	53808	0.28
125	0	3.22	1720	2440	826.9	1.00	858	1	0.0	3.22	1720	2440	62707	0.00

TEST POINT	T_{amb} DEG R	P_{amb} PSIA	RH %	NF dB	LVM	LBM	PNL (FULL SIZE, 2400 FT SIDE LINE), dB ANGLE RELATIVE TO INLET, DEGREES 50	70	90	110	120	130	140	OAPWL dB
101	513.7	14.51	34	-7.6	3.04	-0.03	98.4	102.3	105.9	107.5	109.2	113.0	112.1	185.4
103	517.8	14.51	13	-7.5	3.09	-0.02	101.5	104.0	104.8	104.1	107.5	110.0	108.8	182.9
104	514.0	14.51	29	-6.6	2.92	-0.60	94.1	99.1	103.2	105.5	108.2	111.6	111.0	184.5
106	518.0	14.51	13	-6.6	2.92	-0.61	96.7	100.1	102.2	102.3	105.5	107.7	105.7	180.0
107	514.2	14.52	14	-5.0	1.65	-7.08	84.3	89.5	93.9	96.1	97.1	98.0	95.8	172.2
108	512.0	14.52	21	-5.0	1.66	-6.84	86.5	91.0	93.9	94.1	94.8	95.0	90.2	168.1
109	512.2	14.53	14	-4.9	1.66	-6.99	87.7	90.4	92.7	92.7	94.0	93.5	88.3	167.2
110	514.0	14.51	29	-8.5	3.32	0.54	102.9	107.3	110.1	110.8	112.9	117.2	116.9	189.8
112	516.0	14.51	13	-8.5	3.29	0.53	108.0	112.2	109.4	108.6	111.5	113.7	111.5	187.2
113	513.7	14.52	14	-4.9	2.40	-2.47	88.7	93.6	97.9	100.7	102.4	104.5	102.8	178.5
115	518.3	14.52	13	-4.9	2.37	-2.55	91.4	94.6	96.6	97.1	98.9	99.8	96.0	172.7
116	515.3	14.51	22	-5.4	2.56	-1.83	90.6	95.5	99.5	101.7	103.6	106.0	105.6	180.4
117	512.8	14.52	15	-5.2	2.52	-2.06	90.1	94.7	98.9	101.4	103.5	105.4	105.2	179.9
118	513.3	14.52	15	-5.5	2.62	-1.66	91.0	95.4	99.8	102.3	104.7	106.9	106.8	180.9
119	513.3	14.52	15	-5.5	2.57	-1.68	90.8	95.2	99.6	102.2	104.2	107.0	106.9	180.9
121	517.3	14.50	40	-6.8	3.08	-0.40	96.4	101.1	105.0	106.6	108.7	112.0	111.3	185.0
122	519.1	14.51	13	-6.8	3.09	-0.39	98.1	101.2	103.2	103.4	106.3	108.8	106.8	181.1
123	511.5	14.51	45	-6.4	3.19	-0.55	95.6	100.8	104.7	106.2	108.5	112.1	111.6	185.1
124	518.2	14.51	13	-6.4	3.19	-0.55	97.9	101.3	103.1	103.1	106.6	109.3	107.8	181.7
125	523.6	14.51	49	-7.0	3.38	-0.03	96.7	101.5	105.2	107.5	110.1	115.5	112.9	186.9

NOZZLE - MODEL 1A CONTINUED

TEST POINT	V_{ac} FT/SEC	P^{o}_{r}	T^{o}_{T} DEG R	V^{o}_{j} FT/SEC	W^{o} LB/SEC	P^{i}_{r}	T^{i}_{T} DEG R	V^{i}_{j} FT/SEC	W^{i} LB/SEC	P^{mix}_{r}	T^{mix}_{T} DEG R	V^{mix}_{j} FT/SEC	F LB	V^{i}_{j}/V^{o}_{j}
126	390	3.23	1720	2442	829.3	1.00	972	1	0.0	3.23	1720	2442	62944	0.00
151	0	4.06	1694	2608	857.8	4.07	1733	2641	164.6	4.06	1700	2613	83046	1.01
152	390	4.02	1715	2618	853.9	4.00	1712	2612	164.8	4.02	1714	2617	82856	1.00
153	0	4.06	1698	2611	856.9	3.20	1642	2375	133.1	3.92	1690	2579	79361	0.91
154	390	4.02	1718	2620	852.7	3.16	1634	2359	133.2	3.89	1706	2584	79206	0.90
155	0	4.06	1695	2609	858.1	2.57	1556	2113	110.1	3.83	1679	2552	76810	0.81
156	390	4.02	1715	2618	853.5	2.56	1540	2099	111.5	3.80	1694	2558	76718	0.80
157	0	4.06	1694	2608	858.0	1.53	1284	1330	69.9	3.70	1663	2511	72436	0.51
158	390	4.03	1709	2615	856.5	1.53	1318	1346	69.5	3.68	1679	2519	72521	0.51
159	0	3.54	1728	2527	742.1	1.64	1435	1513	72.4	3.26	1701	2436	61691	0.60
160	390	3.61	1712	2531	766.9	1.64	1464	1524	72.0	3.32	1690	2444	63743	0.60
161	0	3.40	1731	2493	710.4	1.60	1476	1498	69.2	3.13	1708	2404	58268	0.60
162	390	3.41	1743	2505	715.8	1.62	1440	1499	71.9	3.14	1715	2413	59078	0.60
163	0	3.26	1397	2201	766.4	1.59	1174	1329	77.9	3.01	1376	2120	55648	0.60
164	390	3.27	1406	2211	762.1	1.56	1195	1313	74.7	3.02	1387	2130	55417	0.59
165	0	3.21	1051	1892	876.7	1.47	1008	1128	75.5	2.96	1047	1831	54206	0.60
166	390	3.30	1056	1915	895.0	1.49	1046	1161	74.7	3.04	1055	1856	55969	0.61
167	0	2.52	915	1596	738.0	1.41	794	945	79.6	2.35	903	1532	38944	0.59
168	390	2.54	922	1609	741.2	1.39	854	960	74.8	2.37	915	1549	39295	0.60
169	0	2.24	933	1517	647.2	1.32	821	867	69.0	2.10	922	1454	32375	0.57

TEST POINT	T_{amb} DEG R	P_{amb} PSIA	RH %	NF dB	LVM	LBM	PNL (FULL SIZE, 2400 FT SIDE LINE), dB ANGLE RELATIVE TO INLET, DEGREES 50	70	90	110	120	130	140	OAPWL dB
126	516.9	14.52	13	-7.0	3.41	-0.02	98.7	101.8	103.6	104.3	107.7	111.7	110.9	183.9
151	507.9	14.15	90	-8.5	3.74	0.82	102.0	105.7	109.1	110.0	113.3	118.3	112.8	188.7
152	511.1	14.31	77	-8.4	3.73	0.79	106.4	107.9	108.9	108.7	112.7	116.7	113.0	188.2
153	508.1	14.16	90	-8.3	3.68	0.71	102.7	106.4	109.2	110.1	113.0	118.4	112.9	188.7
154	510.6	14.31	75	-8.2	3.68	0.68	109.4	109.6	110.4	109.5	112.8	116.5	113.5	188.6
155	508.3	14.16	88	-8.1	3.64	0.62	102.8	106.4	109.2	110.4	112.8	118.2	113.9	188.7
156	510.6	14.30	76	-8.1	3.63	0.59	108.9	109.0	109.6	108.9	112.2	115.9	113.3	188.1
157	507.9	14.16	94	-7.9	3.57	0.46	99.7	103.3	107.1	109.0	112.5	117.4	112.8	187.9
158	510.1	14.29	78	-7.8	3.57	0.44	103.3	105.2	106.9	107.3	111.5	115.5	112.3	186.6
159	508.8	14.17	84	-6.9	3.43	-0.01	99.2	102.5	106.1	107.6	110.9	115.4	112.0	186.4
160	512.9	14.29	68	-7.1	3.43	0.06	102.4	104.8	105.9	105.9	109.6	113.1	111.2	185.1
161	508.8	14.17	84	-6.6	3.37	-0.20	97.9	101.9	105.7	107.2	110.3	114.4	112.9	186.2
162	512.0	14.28	69	-6.7	3.38	-0.18	100.9	103.4	105.1	105.1	108.9	112.1	111.1	184.2
163	508.8	14.22	84	-7.3	2.83	-0.38	98.1	101.9	104.8	104.8	106.9	110.0	111.3	183.9
164	512.0	14.14	92	-7.3	2.84	-0.38	101.5	103.9	104.3	102.8	105.8	107.4	106.5	181.3
165	508.8	14.23	84	-8.5	2.19	-0.49	98.1	101.3	103.6	102.2	103.6	105.1	106.8	181.1
166	512.4	14.17	90	-8.6	2.24	-0.36	102.4	103.9	104.4	101.0	103.1	103.0	100.8	179.3
167	508.6	14.23	84	-7.8	1.42	-2.15	90.5	94.5	96.5	95.7	96.5	97.7	96.3	172.9
168	459.7	14.21	90	-7.3	1.69	-2.08	94.3	95.1	95.0	89.1	90.5	88.8	84.8	170.3
169	508.6	14.18	84	-7.1	1.19	-3.86	87.2	91.9	93.8	92.6	93.9	94.9	93.2	170.0

NOZZLE - MODEL 1A CONTINUED

TEST POINT	V_{ac} FT/SEC	P^{o}_{r}	T^{o}_{T} DEG R	V^{o}_{j} FT/SEC	W^{o} LB/SEC	P^{i}_{r}	T^{i}_{T} DEG R	V^{i}_{j} FT/SEC	W^{i} LB/SEC	P^{mix}_{r}	T^{mix}_{T} DEG R	V^{mix}_{j} FT/SEC	F LB	V^{i}_{j}/V^{o}_{j}
170	390	2.22	942	1519	644.8	1.33	850	894	69.4	2.09	933	1458	32371	0.59
171	0	2.02	911	1413	593.1	1.29	789	816	67.2	1.91	898	1352	27753	0.58
172	390	2.04	921	1428	598.9	1.29	840	844	65.8	1.93	913	1370	28304	0.59
173	0	1.83	910	1314	534.7	1.26	799	777	62.7	1.74	898	1257	23352	0.59
174	390	1.81	916	1310	532.0	1.25	830	778	60.7	1.73	907	1255	23126	0.59
175	0	4.07	518	1434	1590.0	3.62	517	1382	274.0	4.00	517	1426	82635	0.96
176	390	3.99	523	1432	1551.0	3.56	521	1380	268.8	3.92	522	1424	80562	0.96
177	0	3.60	516	1378	1407.8	2.97	516	1287	225.0	3.50	516	1365	69299	0.93
178	390	3.55	523	1381	1380.0	3.05	521	1306	229.9	3.47	522	1370	68564	0.95
179	0	3.11	514	1307	1217.9	3.49	516	1364	264.3	3.17	514	1317	60680	1.04
180	390	3.06	522	1310	1192.3	3.53	522	1378	266.5	3.14	522	1322	59960	1.05
181	0	3.37	514	1346	1321.5	3.36	515	1346	255.0	3.37	514	1346	65951	1.00
182	390	3.28	522	1344	1278.9	3.18	533	1342	237.1	3.27	523	1343	63314	1.00
183	0	3.37	513	1345	1322.9	2.86	514	1266	217.2	3.29	513	1333	63848	0.94
184	390	3.29	523	1346	1279.3	2.70	546	1273	199.1	3.20	526	1336	61398	0.95
185	0	2.82	512	1256	1099.5	3.33	515	1342	250.9	2.91	512	1272	53388	1.07
186	390	2.82	520	1265	1099.9	3.29	521	1343	248.3	2.89	520	1279	53607	1.06
187	0	3.30	520	1344	1287.5	1.58	1159	1306	77.5	3.00	556	1341	56925	0.97
188	390	3.29	524	1348	1279.9	1.58	1160	1307	77.5	2.99	560	1345	56770	0.97
189	0	3.28	1673	2420	697.7	1.69	1581	1636	71.4	3.04	1664	2347	56112	0.68
190	390	3.26	1661	2407	696.4	1.68	1609	1638	70.0	3.02	1656	2336	55663	0.68

TEST POINT	T_{amb} DEG R	P_{amb} PSIA	RH %	NF dB	LVM	LBM	PNL (FULL SIZE, 2400 FT SIDE LINE), dB ANGLE RELATIVE TO INLET, DEGREES 50	70	90	110	120	130	140	OAPWL dB
170	511.9	14.29	76	-7.1	1.19	-3.97	90.0	92.2	91.9	88.8	90.8	90.1	85.8	167.0
171	508.3	14.18	84	-6.8	0.88	-9.86	82.5	87.7	90.8	91.0	92.3	92.7	89.9	166.9
172	512.6	14.28	74	-6.8	0.91	-8.17	84.8	87.3	88.7	87.4	89.4	88.6	83.9	164.3
173	508.3	14.18	84	-6.3	0.56	-10.00	81.1	86.0	89.5	89.4	90.6	90.5	87.7	164.7
174	512.8	14.28	70	-6.3	0.53	-10.00	83.7	86.1	87.7	86.2	87.7	86.5	81.2	162.7
175	511.5	14.25	79	-12.9	1.09	0.77	99.2	101.9	103.1	102.0	102.6	102.2	99.7	178.8
176	513.3	14.27	71	-12.7	1.08	0.71	103.8	105.3	104.6	101.2	102.0	101.3	97.3	179.0
177	511.5	14.25	82	-11.9	0.91	0.30	94.1	97.0	98.6	98.0	98.0	98.3	97.0	174.7
178	513.3	14.27	71	-11.8	0.91	0.27	100.1	98.9	97.8	94.5	95.6	95.5	91.0	173.6
179	511.5	14.25	82	-11.1	0.75	-0.11	95.9	99.4	102.8	98.2	98.0	97.7	95.1	175.2
180	513.3	14.26	71	-11.0	0.76	-0.15	101.9	101.6	99.3	95.8	96.7	95.9	90.6	175.0
181	511.5	14.25	82	-11.6	0.84	0.16	93.1	95.9	97.5	96.4	97.0	97.6	95.5	173.9
182	513.3	14.27	71	-11.3	0.83	0.03	99.3	98.1	96.7	93.4	94.8	94.4	90.0	172.6
183	512.2	14.24	81	-11.4	0.80	0.06	93.1	96.0	97.0	96.0	96.5	97.2	95.3	173.0
184	513.3	14.26	71	-11.2	0.80	-0.07	100.3	100.6	98.9	95.9	96.5	96.0	91.2	174.0
185	512.6	14.14	77	-10.4	0.59	-0.54	91.1	94.1	94.6	93.8	93.7	93.9	91.9	171.0
186	513.3	14.27	71	-10.4	0.61	-0.56	96.1	95.2	93.5	90.8	91.8	90.6	86.0	169.9
187	513.3	14.26	76	-10.8	0.82	-0.33	92.7	96.1	97.7	96.8	97.6	97.8	95.4	173.7
188	513.3	14.26	71	-10.8	0.83	-0.34	97.5	98.2	97.2	94.6	96.3	94.1	89.6	172.1
189	508.8	14.16	94	-6.5	3.27	-0.33	97.3	100.8	104.5	106.2	109.3	113.2	112.6	185.7
190	510.4	14.14	94	-6.5	3.24	-0.36	99.4	102.8	104.1	103.7	107.5	110.2	109.5	182.7

NOZZLE - MODEL 2 AREA [MODEL SIZE - INNER = 3.45 , OUTER = 18.05 ; FULL SIZE - TOTAL = 1400.00] SQ.IN.

TEST POINT	V_{ac} FT/SEC	P^o_r	T^o_T DEG R	V^o_j FT/SEC	W^o LB/SEC	P^i_r	T^i_T DEG R	V^i_j FT/SEC	W^i LB/SEC	P^{mix}_r	T^{mix}_T DEG R	V^{mix}_j FT/SEC	F LB	V^i_j/V^o_j
201	0	3.16	1720	2422	677.3	3.21	793	1643	196.4	3.09	1511	2246	61013	0.68
202	296	3.19	1716	2427	684.6	3.21	796	1646	196.2	3.11	1511	2253	61679	0.68
203	396	3.19	1714	2425	685.2	3.21	801	1651	195.6	3.11	1511	2253	61681	0.68
204	0	3.78	1697	2555	815.6	3.21	794	1644	196.2	3.60	1521	2378	74794	0.64
205	295	3.81	1687	2554	825.7	3.22	791	1642	197.1	3.63	1514	2378	75604	0.64
206	396	3.81	1693	2558	823.4	3.22	807	1659	195.3	3.63	1523	2385	75537	0.65
207	0	2.98	1713	2364	640.3	2.27	740	1363	143.9	2.81	1534	2180	53139	0.58
208	297	2.98	1723	2371	639.3	2.26	744	1362	142.8	2.80	1544	2186	53155	0.57
209	396	2.98	1732	2377	637.2	2.28	745	1371	144.3	2.81	1549	2191	53220	0.58
210	0	2.29	1698	2085	494.4	2.07	701	1258	135.0	2.21	1484	1907	37314	0.60
211	297	2.31	1709	2104	498.0	2.08	736	1291	132.0	2.23	1505	1933	37865	0.61
212	396	2.32	1709	2105	498.5	2.07	720	1276	133.3	2.23	1500	1930	37900	0.61
213	0	3.16	1742	2438	672.8	1.57	833	1103	91.6	2.89	1633	2278	54125	0.45
214	296	3.18	1741	2444	678.5	1.60	831	1122	93.9	2.91	1630	2283	54814	0.46
215	396	3.18	1743	2445	677.8	1.60	824	1118	94.4	2.91	1630	2282	54787	0.46
216	0	3.78	1708	2563	812.4	1.57	844	1109	90.8	3.42	1621	2416	67845	0.43
217	296	3.80	1702	2564	820.2	1.60	814	1110	94.8	3.44	1610	2413	68636	0.43
218	396	3.81	1703	2566	821.3	1.60	825	1119	94.4	3.45	1612	2416	68786	0.44
219	0	2.30	1720	2102	492.1	1.60	798	1099	95.7	2.16	1569	1938	35418	0.52
220	296	2.31	1697	2094	498.8	1.61	804	1106	95.8	2.17	1553	1934	35752	0.53

TEST POINT	T_{amb} DEG R	P_{amb} PSIA	RH %	NF dB	LVM	LBM	PNL (FULL SIZE, 2400 FT SIDE LINE), dB ANGLE RELATIVE TO INLET, DEGREES 50	70	90	110	120	130	140	OAPWL dB
201	514.4	14.44	62	-7.4	3.06	-0.11	99.8	102.8	106.8	107.6	109.6	113.5	112.2	185.8
202	507.0	14.45	83	-7.4	3.10	-0.08	101.7	104.3	106.7	105.4	108.6	111.2	110.4	184.2
203	506.8	14.46	82	-7.4	3.10	-0.08	103.8	105.4	106.9	105.2	108.4	111.0	110.1	184.0
204	514.6	14.44	62	-8.4	3.30	0.50	103.7	106.9	110.2	110.6	112.8	116.2	115.2	188.8
205	506.6	14.44	83	-8.4	3.34	0.53	105.9	109.8	110.7	109.5	112.3	114.7	113.0	188.0
206	506.5	14.44	83	-8.4	3.35	0.53	108.1	112.0	110.8	109.3	112.4	114.7	112.3	187.8
207	511.1	14.44	68	-6.6	2.94	-0.61	95.1	99.4	104.1	105.7	108.8	112.4	111.4	185.0
208	508.4	14.46	79	-6.5	2.96	-0.61	96.5	100.9	103.5	103.6	106.8	110.1	108.7	182.0
209	507.4	14.46	82	-6.5	2.98	-0.61	98.1	100.8	103.4	103.4	107.1	109.9	107.8	181.4
210	513.3	14.45	66	-4.9	2.35	-2.56	89.4	94.1	99.0	100.8	102.5	104.3	103.8	178.8
211	516.2	14.45	67	-4.9	2.40	-2.44	91.4	95.3	98.2	98.4	100.7	101.8	100.0	175.0
212	514.7	14.45	65	-5.0	2.39	-2.44	92.7	95.1	97.8	97.8	100.2	101.5	97.8	174.0
213	513.7	14.44	62	-6.4	3.12	-0.54	96.4	100.4	104.8	106.2	108.8	112.3	111.9	185.2
214	508.1	14.45	80	-6.4	3.15	-0.49	97.9	102.0	104.6	104.1	107.4	110.0	109.3	182.8
215	516.4	14.45	70	-6.5	3.12	-0.49	99.5	102.1	104.5	103.7	107.3	109.6	108.0	182.2
216	513.7	14.44	62	-7.6	3.38	0.22	98.6	102.6	107.1	108.6	112.0	116.3	112.2	187.0
217	507.9	14.45	76	-7.7	3.39	0.25	100.7	104.2	107.1	106.6	110.0	114.3	110.5	185.4
218	512.6	14.45	73	-7.7	3.38	0.26	102.0	104.6	106.8	106.0	110.2	114.4	110.4	185.4
219	511.0	14.44	64	-4.4	2.43	-3.00	89.4	93.6	98.6	100.4	102.1	104.0	102.7	178.2
220	511.0	14.45	69	-4.5	2.42	-2.92	91.6	95.2	98.3	98.6	100.6	101.8	99.5	174.7

NOZZLE - MODEL 2 CONTINUED

TEST POINT	V_{ac} FT/SEC	P_r^o	T_T^o DEG R	V_j^o FT/SEC	W^o LB/SEC	P_r^i	T_T^i DEG R	V_j^i FT/SEC	W^i LB/SEC	P_r^{mix}	T_T^{mix} DEG R	V_j^{mix} FT/SEC	F LB	V_j^i/V_j^o
221	396	2.31	1695	2094	499.7	1.61	812	1112	95.3	2.18	1553	1936	35815	0.53
222	0	2.44	1718	2170	524.6	2.16	756	1341	135.7	2.35	1520	1999	41040	0.62

TEST POINT	T_{amb} DEG R	P_{amb} PSIA	RH %	NF dB	LVM	LBM	PNL (FULL SIZE, 2400 FT SIDE LINE), dB ANGLE RELATIVE TO INLET, DEGREES 50	70	90	110	120	130	140	OAPWL dB
221	509.7	14.45	69	-4.5	2.43	-2.91	92.4	94.9	97.7	97.4	99.8	100.9	97.4	173.7
222	506.6	14.44	80	-5.2	2.58	-1.88	91.2	95.6	100.6	102.5	104.6	107.4	106.6	181.2

NOZZLE - MODEL 3 AREA [MODEL SIZE - INNER = 3.50 , OUTER = 18.05 ; FULL SIZE - TOTAL = 1400.00] SQ.IN.

TEST POINT	V_{ac} FT/SEC	P_r^o	T_T^o DEG R	V_j^o FT/SEC	W^o LB/SEC	P_r^i	T_T^i DEG R	V_j^i FT/SEC	W^i LB/SEC	P_r^{mix}	T_T^{mix} DEG R	V_j^{mix} FT/SEC	F LB	V_j^i/V_j^o
301	0	3.18	1719	2427	681.0	3.21	784	1634	200.3	3.10	1506	2246	61543	0.67
302	289	3.18	1717	2426	682.0	3.21	778	1628	201.2	3.10	1503	2244	61605	0.67
303	386	3.21	1724	2438	686.2	3.21	786	1636	200.2	3.12	1512	2256	62172	0.67
304	0	3.78	1694	2554	816.8	3.19	775	1620	199.9	3.59	1513	2370	74903	0.63
305	289	3.80	1691	2554	820.7	3.21	799	1649	198.4	3.61	1517	2377	75312	0.65
306	385	3.75	1706	2557	807.9	3.21	790	1640	199.6	3.58	1524	2375	74381	0.64
307	0	2.95	1715	2355	632.8	2.23	767	1373	140.7	2.78	1542	2176	52318	0.58
308	289	2.95	1739	2374	629.7	2.27	751	1374	145.1	2.78	1553	2186	52664	0.58
309	385	2.97	1730	2373	634.6	2.28	753	1377	145.1	2.80	1548	2187	53011	0.58
310	0	2.27	1715	2088	488.1	2.25	626	1248	157.4	2.20	1449	1883	37784	0.60
311	289	2.30	1711	2099	494.1	2.26	638	1263	156.5	2.23	1452	1897	38380	0.60
312	385	2.32	1699	2099	499.3	2.09	692	1256	138.7	2.23	1480	1915	37986	0.60
313	0	2.80	1705	2300	603.4	1.07	946	466	30.9	2.63	1668	2210	43583	0.20
314	385	2.80	1726	2315	599.3	1.07	906	466	32.3	2.62	1684	2220	43586	0.20
315	0	2.75	1712	2286	592.0	1.46	726	946	89.7	2.52	1582	2109	44702	0.41
316	386	2.72	1726	2287	582.7	1.45	767	962	85.9	2.50	1602	2116	43985	0.42
317	0	2.78	1695	2286	596.8	1.82	1067	1419	96.1	2.62	1607	2165	46641	0.62
318	377	2.74	1707	2280	592.3	1.81	1064	1415	97.2	2.58	1616	2158	46247	0.62

TEST POINT	T_{amb} DEG R	P_{amb} PSIA	RH %	NF dB	LVM	LBM	PNL (FULL SIZE, 2400 FT SIDE LINE), dB ANGLE RELATIVE TO INLET, DEGREES 50	70	90	110	120	130	140	OAPWL dB
301	500.7	14.46	32	-7.3	3.11	-0.08	99.1	102.7	105.5	107.0	108.5	112.4	111.2	184.3
302	500.2	14.46	33	-7.3	3.11	-0.08	103.1	104.9	106.2	104.9	107.3	109.2	108.3	182.4
303	501.2	14.47	31	-7.4	3.13	-0.05	105.5	105.8	106.4	105.2	107.4	108.9	107.3	182.4
304	500.9	14.45	31	-8.3	3.35	0.50	101.6	105.6	108.7	109.3	110.6	114.7	113.3	186.4
305	500.9	14.47	31	-8.4	3.36	0.51	105.4	107.5	108.6	107.6	110.1	111.8	111.6	185.2
306	500.9	14.46	31	-8.3	3.35	0.48	107.5	108.1	108.6	107.2	109.5	111.7	110.8	185.0
307	499.4	14.47	39	-6.4	2.98	-0.68	93.3	98.5	103.0	104.7	106.8	109.5	109.4	182.3
308	499.8	14.48	37	-6.4	3.00	-0.65	96.5	100.6	102.7	102.7	105.1	106.8	105.7	179.4
309	499.6	14.46	35	-6.4	3.00	-0.63	98.9	101.4	103.1	102.8	105.1	106.4	104.4	179.1
310	497.1	14.47	46	-4.9	2.36	-2.47	89.1	94.4	98.7	100.7	102.7	105.2	104.7	178.1
311	497.8	14.46	33	-5.0	2.39	-2.35	93.1	96.9	98.7	98.5	100.1	102.4	101.2	174.7
312	500.9	14.46	33	-4.9	2.42	-2.43	95.5	97.9	99.1	98.2	100.0	101.9	98.7	174.3
313	497.1	14.47	47	-5.1	3.06	-1.45	91.7	97.1	101.7	103.9	106.0	109.8	109.2	182.0
314	500.9	14.46	33	-5.1	3.06	-1.45	97.8	100.7	102.3	101.6	104.2	105.9	104.9	178.7
315	496.6	14.51	47	-5.4	2.86	-1.40	91.6	97.2	101.4	103.4	105.4	108.0	107.5	180.8
316	501.8	14.46	30	-5.3	2.85	-1.46	97.5	100.1	101.5	101.1	103.0	104.0	101.6	177.0
317	496.4	14.37	60	-5.6	2.97	-1.15	92.5	97.7	101.8	103.7	106.0	109.3	109.3	181.8
318	501.6	14.53	31	-5.5	2.94	-1.25	97.3	100.3	102.0	101.1	103.5	105.1	103.0	177.7

NOZZLE - MODEL 4 AREA [MODEL SIZE - INNER = 9.50 , OUTER = 18.05 ; FULL SIZE - TOTAL = 1400.00] SQ.IN.

TEST POINT	V_{ac} FT/SEC	P_r^o	T_T^o DEG R	V_j^o FT/SEC	W^o LB/SEC	P_r^i	T_T^i DEG R	V_j^i FT/SEC	W^i LB/SEC	P_r^{mix}	T_T^{mix} DEG R	V_j^{mix} FT/SEC	F LB	V_j^i/V_j^o
401	0	2.78	1736	2313	467.1	1.06	980	425	58.1	2.39	1652	2104	34344	0.18
402	387	2.79	1689	2285	469.1	1.06	1026	464	59.8	2.39	1614	2079	34182	0.20
403	0	2.78	1736	2313	464.9	1.18	1000	754	103.8	2.30	1601	2028	35858	0.33
404	387	2.78	1721	2303	462.4	1.18	968	742	104.5	2.30	1582	2015	35505	0.32
405	0	2.75	1730	2298	456.0	1.46	746	957	185.8	2.27	1445	1909	38094	0.42
406	387	2.75	1727	2297	457.0	1.46	762	965	183.4	2.27	1450	1915	38124	0.42
407	0	2.78	1727	2307	466.3	1.60	1312	1414	160.6	2.38	1620	2078	40492	0.61
408	387	2.79	1728	2311	462.9	1.62	1313	1425	160.3	2.39	1621	2083	40351	0.62
409	0	2.78	1742	2318	464.5	1.95	1258	1626	203.8	2.49	1594	2107	43763	0.70
410	387	2.80	1734	2319	463.9	1.95	1257	1625	201.7	2.50	1589	2108	43624	0.70

TEST POINT	T_{amb} DEG R	P_{amb} PSIA	RH %	NF dB	LVM	LBM	PNL (FULL SIZE, 2400 FT SIDE LINE), dB ANGLE RELATIVE TO INLET, DEGREES 50	70	90	110	120	130	140	OAPWL dB
401	499.2	14.58	28	-4.0	2.84	-3.01	90.4	95.5	100.4	102.0	104.7	109.1	107.8	180.8
402	493.2	14.37	60	-4.1	2.81	-2.93	95.9	99.8	101.8	100.7	103.0	105.6	103.0	177.7
403	499.2	14.52	29	-4.3	2.68	-2.71	89.6	95.2	100.1	102.0	104.1	106.7	105.6	179.5
404	493.2	14.37	57	-4.3	2.68	-2.71	95.5	99.4	101.3	100.2	102.6	104.3	101.3	176.7
405	492.7	14.37	64	-5.0	2.44	-2.31	90.2	96.0	100.6	102.4	103.8	106.1	104.9	178.6
406	492.7	14.37	63	-5.0	2.46	-2.30	95.3	98.8	101.2	100.3	102.5	103.7	99.3	176.0
407	499.2	14.52	33	-4.8	2.78	-1.99	91.0	96.4	100.8	102.6	104.7	107.5	107.5	180.7
408	493.7	14.37	53	-4.8	2.82	-1.94	96.2	99.7	101.6	100.6	103.1	104.5	101.7	177.0
409	499.2	14.52	37	-5.3	2.84	-1.54	91.9	96.8	101.2	102.9	105.0	107.9	108.7	181.4
410	493.7	14.37	50	-5.3	2.87	-1.50	96.0	99.4	101.6	100.7	103.1	104.8	102.6	177.3

NOZZLE - MODEL 6 AREA [MODEL SIZE - INNER = 5.85 , OUTER = 11.22 ; FULL SIZE - TOTAL = 1400.00] SQ.IN.

TEST POINT	V_{ac} FT/SEC	P_r^o	T_T^o DEG R	V_j^o FT/SEC	W^o LB/SEC	P_r^i	T_T^i DEG R	V_j^i FT/SEC	W^i LB/SEC	P_r^{mix}	T_T^{mix} DEG R	V_j^{mix} FT/SEC	F LB	V_j^i/V_j^o
3001	0	3.21	1699	2422	544.5	3.24	761	1615	433.6	3.08	1283	2064	62758	0.67
3002	388	3.20	1730	2440	533.2	3.27	778	1638	429.9	3.08	1305	2082	62318	0.67
3003	0	2.30	1685	2084	392.3	2.09	676	1241	296.6	2.15	1250	1721	36851	0.60
3004	302	3.20	1732	2441	532.6	3.25	789	1647	425.0	3.08	1313	2088	62166	0.67
3005	384	2.29	1707	2092	387.6	2.07	685	1242	291.9	2.13	1267	1726	36471	0.59
3006	0	2.78	1741	2316	465.8	1.07	637	371	77.4	2.35	1583	2038	34425	0.16
3007	299	2.78	1734	2312	467.0	1.03	681	271	52.4	2.43	1627	2106	33997	0.12
3008	388	2.80	1711	2302	468.9	1.03	709	272	50.1	2.45	1614	2106	33971	0.12
3009	0	2.29	1721	2098	385.8	1.37	604	792	187.3	1.92	1355	1671	29768	0.38
3010	299	2.28	1733	2104	383.8	1.36	625	792	180.5	1.92	1378	1684	29543	0.38
3011	388	2.28	1735	2106	383.9	1.36	609	783	183.2	1.92	1371	1678	29586	0.37
3012	0	2.75	1694	2274	466.6	1.43	747	935	180.5	2.27	1429	1900	38226	0.41
3013	298	2.75	1716	2291	464.8	1.47	719	949	192.0	2.27	1424	1898	38760	0.41
3014	384	2.76	1697	2279	468.0	1.46	726	943	188.5	2.28	1418	1895	38672	0.41
3015	0	2.78	1694	2286	472.4	1.61	1290	1409	161.6	2.39	1591	2062	40643	0.62
3016	298	2.79	1722	2307	469.6	1.62	1299	1420	162.0	2.39	1613	2079	40824	0.62
3017	389	2.80	1726	2314	467.4	1.62	1309	1423	159.7	2.40	1619	2087	40684	0.61
3018	0	2.75	1697	2276	463.0	1.95	1243	1616	201.8	2.47	1559	2075	42885	0.71
3019	301	2.76	1727	2301	461.0	1.97	1257	1634	202.3	2.48	1583	2097	43246	0.71

TEST POINT	T_{amb} DEG R	P_{amb} PSIA	RH %	NF dB	LVM	LBM	PNL (FULL SIZE, 2400 FT SIDE LINE), dB ANGLE RELATIVE TO INLET, DEGREES 50	70	90	110	120	130	140	OAPWL dB
3001	499.6	14.48	22	-8.1	2.75	-0.03	100.6	101.9	105.0	106.1	108.4	111.5	114.6	182.6
3002	499.3	14.39	21	-8.0	2.79	-0.03	104.3	103.7	104.8	103.9	107.6	109.2	108.3	179.3
3003	499.8	14.49	22	-5.7	1.96	-2.71	91.6	93.6	96.9	98.6	100.7	103.2	104.1	173.9
3004	499.1	14.39	21	-8.0	2.80	-0.04	102.6	103.6	104.9	104.0	107.4	109.4	110.2	179.5
3005	500.2	14.49	23	-5.6	1.97	-2.80	95.4	94.7	96.6	96.2	99.3	100.6	99.1	171.1
3006	497.6	14.52	23	-4.2	2.71	-2.96	93.3	96.3	100.7	102.2	104.3	108.6	108.1	177.4
3007	499.1	14.52	22	-4.1	2.84	-3.03	96.7	97.9	100.6	100.6	104.3	106.6	105.9	175.3
3008	498.9	14.39	22	-4.1	2.84	-2.96	98.0	98.5	100.5	100.7	103.8	105.9	104.6	175.0
3009	498.2	14.52	23	-4.5	1.84	-5.72	89.1	92.2	96.5	98.7	100.4	103.4	104.3	173.1
3010	498.9	14.52	22	-4.3	1.87	-5.92	93.3	94.0	96.3	96.6	99.8	101.8	101.6	170.8
3011	498.5	14.52	22	-4.4	1.86	-5.88	94.6	94.1	96.1	96.1	99.2	100.3	99.0	170.2
3012	500.0	14.48	22	-5.1	2.39	-2.33	94.8	96.6	100.2	101.7	104.1	108.0	108.1	177.3
3013	500.0	14.50	22	-5.2	2.39	-2.25	97.1	98.4	100.1	99.8	104.2	106.4	105.6	175.0
3014	500.3	14.49	22	-5.2	2.38	-2.26	98.1	98.1	100.1	99.7	103.3	105.2	104.0	174.5
3015	499.4	14.48	22	-4.9	2.75	-1.95	95.5	97.1	100.5	102.1	105.0	108.7	110.8	179.2
3016	499.8	14.50	22	-4.9	2.78	-1.93	97.9	98.7	100.3	100.6	104.2	106.7	106.7	175.9
3017	499.8	14.38	22	-4.9	2.80	-1.90	99.3	98.8	100.2	100.1	104.1	106.1	105.4	175.5
3018	499.3	14.38	22	-5.3	2.78	-1.60	95.0	96.9	100.5	102.3	105.1	108.9	111.5	179.7
3019	499.6	14.39	22	-5.3	2.82	-1.55	98.1	99.1	100.1	100.6	104.6	106.9	107.3	176.3

NOZZLE - MODEL 7 AREA [MODEL SIZE - INNER = 5.81 , OUTER = 18.05 ; FULL SIZE - TOTAL = 1400.00] SQ.IN.

TEST POINT	V_{ac} FT/SEC	P^o_r	T^o_T DEG R	V^o_j FT/SEC	W^o LB/SEC	P^i_r	T^i_T DEG R	V^i_j FT/SEC	W^i LB/SEC	P^{mix}_r	T^{mix}_T DEG R	V^{mix}_j FT/SEC	F LB	V^i_j/V^o_j
7001	0	3.14	1741	2431	600.4	3.05	815	1634	278.9	3.02	1447	2178	59534	0.67
7002	386	3.16	1741	2437	608.8	3.20	779	1627	301.9	3.05	1422	2168	61382	0.67
7003	0	2.28	1742	2109	437.1	2.06	679	1235	207.1	2.16	1400	1828	36602	0.59
7004	294	3.16	1730	2429	610.9	3.22	776	1627	304.1	3.06	1412	2162	61502	0.67
7005	386	2.29	1707	2093	447.5	2.07	683	1240	208.5	2.17	1381	1821	37145	0.59
7006	0	2.80	1736	2320	536.8	1.01	698	144	19.1	2.66	1700	2245	38792	0.06
7007	298	2.80	1714	2306	545.6	1.10	687	461	64.0	2.48	1606	2112	40022	0.20
7008	386	2.81	1705	2301	547.5	1.09	713	461	61.6	2.49	1604	2114	40042	0.20
7009	0	2.25	1715	2076	434.8	1.46	604	864	147.2	2.01	1434	1769	32010	0.42
7010	294	2.29	1717	2096	441.0	1.51	571	876	159.1	2.04	1413	1772	33058	0.42
7011	388	2.29	1731	2104	438.8	1.49	574	863	155.3	2.03	1428	1779	32859	0.41
7012	0	2.73	1721	2287	527.1	1.46	711	936	135.3	2.39	1514	2011	41402	0.41
7013	293	2.74	1701	2275	534.2	1.45	743	947	131.4	2.40	1511	2012	41644	0.42
7014	385	2.74	1713	2283	532.2	1.45	738	943	131.7	2.40	1519	2017	41624	0.41
7015	0	2.72	1734	2290	521.7	1.81	1039	1396	146.2	2.48	1581	2094	43474	0.61
7016	294	2.74	1726	2291	529.6	1.81	1053	1408	146.5	2.49	1580	2099	44124	0.61
7017	386	2.74	1724	2291	530.6	1.82	1063	1421	146.6	2.50	1580	2102	44254	0.62
7018	0	2.70	1745	2290	515.8	2.73	910	1652	236.7	2.65	1482	2089	48865	0.72
7019	294	2.71	1713	2273	527.1	2.72	901	1641	238.7	2.66	1459	2076	49408	0.72
7020	388	2.70	1729	2281	523.0	2.73	905	1647	238.9	2.65	1470	2082	49308	0.72

TEST POINT	T_{amb} DEG R	P_{amb} PSIA	RH %	NF dB	LVM	LBM	PNL (FULL SIZE, 2400 FT SIDE LINE), dB ANGLE RELATIVE TO INLET, DEGREES 50	70	90	110	120	130	140	OAPWL dB
7001	487.2	14.40	29	-7.2	3.04	-0.19	98.0	101.5	104.9	105.8	109.5	111.0	110.5	183.8
7002	489.7	14.51	42	-7.5	3.01	-0.11	103.4	105.0	107.4	105.4	109.2	108.7	106.5	182.5
7003	484.5	14.42	41	-4.8	2.29	-2.71	89.1	93.7	98.5	100.4	103.9	103.7	103.1	177.6
7004	488.8	14.51	42	-7.5	3.00	-0.10	102.2	104.9	107.2	105.6	109.1	108.9	107.9	182.7
7005	492.7	14.53	54	-5.0	2.24	-2.65	91.6	94.7	97.3	97.5	99.7	100.0	95.6	172.9
7006	484.0	14.42	39	-4.4	3.19	-2.03	92.9	97.2	102.2	103.2	108.1	109.5	107.3	181.4
7007	492.7	14.54	49	-4.8	2.88	-1.94	95.4	99.3	102.4	101.9	104.7	106.8	104.1	178.4
7008	492.7	14.53	51	-4.8	2.89	-1.93	96.5	99.3	102.4	101.5	105.0	106.4	102.9	178.2
7009	482.9	14.43	46	-4.1	2.16	-4.19	88.4	92.7	98.0	99.9	103.3	103.5	102.2	176.3
7010	497.7	14.40	54	-4.5	2.10	-3.73	89.7	94.3	97.4	97.8	99.8	100.7	97.3	172.7
7011	497.7	14.40	54	-4.4	2.12	-3.79	90.8	94.2	97.0	97.2	99.7	100.1	95.8	172.3
7012	483.6	14.42	41	-5.1	2.71	-1.79	92.1	96.8	101.4	103.2	107.2	107.9	106.7	181.2
7013	488.1	14.50	44	-5.2	2.69	-1.78	94.4	98.5	101.5	101.3	105.4	105.5	103.1	177.6
7014	489.5	14.50	44	-5.2	2.69	-1.79	96.0	98.3	101.6	100.9	105.3	105.2	101.1	177.2
7015	485.0	14.41	39	-5.2	2.88	-1.53	92.3	97.0	101.3	103.3	107.2	108.3	108.0	181.3
7016	488.3	14.50	43	-5.3	2.87	-1.49	94.3	98.3	101.7	101.6	105.9	106.4	104.6	178.5
7017	489.2	14.50	43	-5.3	2.88	-1.47	95.5	98.6	101.5	101.1	105.7	106.0	103.2	178.0
7018	487.6	14.41	29	-6.1	2.86	-0.95	93.5	97.5	101.7	103.4	107.8	108.5	109.2	182.2
7019	488.8	14.51	42	-6.2	2.82	-0.94	94.4	98.8	101.8	101.5	105.3	106.2	104.9	178.6
7020	488.5	14.51	42	-6.2	2.84	-0.94	95.6	98.7	101.8	101.6	105.6	105.8	103.8	178.3

NOZZLE - MODEL 7 CONTINUED

TEST POINT	V_{ac} FT/SEC	P^o_r	T^o_T DEG R	V^o_j FT/SEC	W^o LB/SEC	P^i_r	T^i_T DEG R	V^i_j FT/SEC	W^i LB/SEC	P^{mix}_r	T^{mix}_T DEG R	V^{mix}_j FT/SEC	F LB	V^i_j/V^o_j
7101	0	2.53	1523	2076	519.9	1.73	845	1214	154.7	2.32	1367	1878	39384	0.58
7102	387	2.56	1517	2080	530.9	1.72	856	1217	154.4	2.33	1368	1885	40164	0.59
7103	0	2.58	1532	2100	527.8	2.57	1065	1740	205.0	2.56	1401	1999	45540	0.83
7104	386	2.56	1515	2079	531.6	2.50	1097	1743	198.2	2.53	1401	1987	45089	0.84
7105	0	1.91	1428	1710	407.2	1.21	654	643	95.8	1.74	1280	1506	23556	0.38
7106	386	1.91	1404	1694	413.3	1.22	696	680	96.1	1.75	1270	1502	23790	0.40
7107	0	1.91	1396	1691	411.3	1.78	954	1318	149.8	1.87	1278	1591	27751	0.78
7108	386	1.91	1395	1688	414.4	1.76	965	1316	148.8	1.87	1281	1589	27827	0.78
7109	0	3.42	1671	2454	669.6	1.38	639	821	129.9	2.91	1503	2188	54389	0.33
7110	389	3.53	1668	2479	691.8	1.50	591	883	154.6	2.99	1471	2187	57542	0.36
7111	0	3.53	1672	2481	689.5	2.51	961	1635	211.6	3.24	1505	2282	63921	0.66
7112	387	3.53	1678	2486	694.9	2.57	973	1662	216.9	3.26	1510	2290	64900	0.67
7113	0	3.52	1670	2478	688.5	3.63	1221	2129	269.6	3.53	1543	2379	70866	0.86
7114	387	3.55	1666	2481	701.3	3.62	1217	2122	271.4	3.54	1540	2380	71978	0.86
7201	0	2.85	1658	2284	559.6	3.03	1358	2110	212.4	2.89	1575	2236	53650	0.92
7202	148	2.91	1653	2300	578.0	3.08	1355	2121	218.3	2.95	1571	2250	55711	0.92
7203	326	2.86	1651	2282	568.1	3.07	1357	2120	217.4	2.90	1569	2237	54624	0.93
7204	387	2.85	1674	2294	561.0	3.00	1355	2100	212.5	2.88	1586	2240	53873	0.92
7205	0	3.08	1702	2385	595.1	2.27	1184	1727	171.3	2.87	1586	2237	53311	0.72
7206	148	3.09	1693	2383	605.7	2.29	1153	1713	177.2	2.88	1570	2231	54295	0.72

TEST POINT	T_{amb} DEG R	P_{amb} PSIA	RH %	NF dB	LVM	LBM	PNL (FULL SIZE, 2400 FT SIDE LINE), dB ANGLE RELATIVE TO INLET, DEGREES 50	70	90	110	120	130	140	OAPWL dB
7101	489.9	14.39	20	-5.4	2.38	-2.14	90.7	95.2	99.2	100.7	104.4	104.7	104.2	178.4
7102	486.3	14.54	46	-5.4	2.42	-2.07	94.0	96.7	99.2	98.5	102.0	101.2	97.2	174.4
7103	489.9	14.39	20	-6.0	2.65	-1.28	92.0	95.9	100.0	101.4	105.4	106.3	107.6	180.6
7104	487.0	14.54	46	-5.9	2.64	-1.39	93.4	96.0	99.1	98.9	103.0	102.6	100.7	175.9
7105	482.5	14.43	43	-4.1	1.46	-10.00	83.1	86.7	91.8	93.8	97.4	96.1	94.4	170.1
7106	492.7	14.53	52	-4.4	1.40	-10.00	83.4	86.5	89.3	89.2	91.3	90.9	85.9	164.1
7107	489.5	14.39	21	-4.6	1.67	-10.00	83.1	87.6	92.6	94.5	98.4	97.6	95.3	171.9
7108	489.0	14.53	44	-4.6	1.66	-10.00	84.5	86.9	90.0	90.0	93.5	91.5	87.2	165.4
7109	482.3	14.42	46	-6.6	3.08	-0.50	98.0	102.1	105.8	106.2	110.4	111.0	110.7	184.1
7110	498.7	14.40	54	-7.1	3.01	-0.30	103.1	106.2	108.1	106.5	109.2	109.3	105.8	182.5
7111	488.1	14.39	22	-7.4	3.24	0.05	98.6	102.0	105.8	106.5	110.6	113.2	112.2	185.1
7112	489.9	14.52	45	-7.5	3.24	0.07	102.5	105.0	107.7	106.1	110.3	111.0	109.5	183.7
7113	488.6	14.39	22	-7.9	3.42	0.36	102.3	105.4	107.8	107.8	111.8	115.5	112.1	186.5
7114	489.0	14.53	45	-8.0	3.42	0.38	106.2	107.1	109.3	107.2	111.8	113.4	111.2	186.0
7201	488.8	14.39	20	-6.3	3.15	-0.56	97.3	100.2	103.5	104.5	108.8	112.6	110.5	184.1
7202	492.7	14.53	60	-6.6	3.16	-0.45	98.0	101.1	104.1	104.2	106.4	110.6	110.9	183.2
7203	492.7	14.53	60	-6.5	3.13	-0.52	99.8	102.4	104.4	103.0	106.0	109.5	109.1	182.3
7204	489.0	14.52	45	-6.3	3.15	-0.57	99.6	101.4	103.8	102.7	107.5	109.3	108.2	181.7
7205	487.2	14.39	25	-6.3	3.16	-0.58	95.3	98.8	103.2	104.5	109.5	112.3	110.2	183.5
7206	492.7	14.53	61	-6.4	3.12	-0.55	96.1	100.5	103.6	104.2	107.1	110.8	110.2	182.9

NOZZLE - MODEL 7 CONTINUED

TEST POINT	V_{ac} FT/SEC	P^{o}_{r}	T^{o}_{T} DEG R	V^{o}_{j} FT/SEC	W^{o} LB/SEC	P^{i}_{r}	T^{i}_{T} DEG R	V^{i}_{j} FT/SEC	W^{i} LB/SEC	P^{mix}_{r}	T^{mix}_{T} DEG R	V^{mix}_{j} FT/SEC	F LB	V^{i}_{j}/V^{o}_{j}
7207	299	3.09	1696	2384	604.1	2.32	1178	1743	177.3	2.89	1578	2238	54364	0.73
7208	386	3.09	1684	2377	607.8	2.32	1186	1747	176.3	2.89	1572	2235	54478	0.73
7209	0	3.32	1740	2481	636.4	1.49	811	1022	130.1	2.86	1582	2233	53206	0.41
7210	151	3.35	1737	2487	643.0	1.50	811	1029	131.2	2.89	1580	2239	53902	0.41
7211	298	3.35	1741	2490	642.0	1.49	812	1026	130.5	2.89	1584	2242	53848	0.41
7212	389	3.36	1722	2477	646.5	1.49	813	1025	130.1	2.89	1569	2233	53917	0.41
7301	0	2.21	1615	1993	439.5	2.26	1089	1649	177.9	2.21	1463	1893	36343	0.83
7302	386	2.20	1643	2005	437.4	2.22	1089	1633	176.3	2.19	1483	1898	36208	0.81
7303	0	2.37	1628	2076	468.5	1.78	904	1282	153.8	2.20	1449	1879	36354	0.62
7304	386	2.38	1647	2093	471.9	1.80	911	1300	156.7	2.21	1463	1895	37030	0.62
7305	0	2.53	1700	2196	492.0	1.21	596	619	101.3	2.21	1511	1926	35525	0.28
7306	386	2.56	1682	2193	498.2	1.22	565	610	105.2	2.22	1487	1916	35950	0.28
7402	148	3.55	1664	2479	700.9	1.46	594	857	149.3	3.00	1476	2194	57978	0.35
7403	300	3.55	1675	2487	698.1	1.44	572	825	148.6	2.99	1481	2195	57771	0.33
7406	148	3.55	1662	2478	701.6	2.49	973	1638	210.1	3.26	1503	2284	64736	0.66
7407	304	3.56	1655	2474	704.5	2.56	974	1659	215.5	3.28	1495	2283	65286	0.67
7410	148	3.55	1669	2483	699.8	3.66	1226	2139	273.7	3.55	1544	2386	72203	0.86
7411	327	3.55	1665	2480	701.2	3.65	1223	2133	272.9	3.55	1541	2382	72140	0.86
7501	0	3.05	1178	1968	724.9	2.02	825	1342	185.5	2.80	1106	1840	52076	0.68
7502	386	3.07	1180	1973	725.6	2.02	849	1361	182.3	2.81	1113	1850	52205	0.69

TEST POINT	T_{amb} DEG R	P_{amb} PSIA	RH %	NF dB	LVM	LBM	PNL (FULL SIZE, 2400 FT SIDE LINE), dB ANGLE RELATIVE TO INLET, DEGREES 50	70	90	110	120	130	140	OAPWL dB
7207	492.7	14.52	57	-6.4	3.13	-0.54	96.9	101.2	103.8	103.3	106.8	109.8	108.4	181.6
7208	492.7	14.53	55	-6.4	3.13	-0.54	97.8	100.8	103.8	103.1	106.8	109.3	107.9	181.3
7209	484.5	14.41	39	-6.2	3.16	-0.59	96.6	101.1	105.0	106.2	110.3	112.7	110.7	184.2
7210	496.7	14.41	51	-6.4	3.12	-0.54	97.8	102.6	106.0	105.5	107.6	110.5	110.5	183.2
7211	496.7	14.40	54	-6.4	3.12	-0.55	99.8	103.9	106.6	105.4	108.0	109.1	109.1	182.4
7212	496.7	14.40	54	-6.4	3.11	-0.54	101.1	104.6	106.9	105.5	108.6	109.3	107.4	182.1
7301	490.3	14.39	18	-4.7	2.42	-2.76	89.0	92.6	97.0	98.9	103.0	103.2	104.2	177.9
7302	488.6	14.52	43	-4.6	2.44	-2.88	90.1	92.8	96.1	96.0	99.8	99.2	96.0	172.2
7303	489.9	14.39	19	-4.7	2.39	-2.76	89.2	93.6	98.0	99.7	103.5	103.9	103.7	177.8
7304	489.4	14.52	44	-4.7	2.43	-2.68	91.9	94.8	97.7	97.3	101.2	100.9	97.2	173.5
7305	482.7	14.43	46	-4.4	2.53	-2.82	90.2	94.9	100.0	101.8	105.6	105.7	104.4	178.6
7306	497.7	14.40	56	-4.6	2.44	-2.71	93.4	96.4	99.7	99.3	101.9	102.5	97.7	174.6
7402	490.7	14.52	64	-7.0	3.06	-0.30	99.7	103.8	107.2	106.4	108.3	110.1	109.2	183.5
7403	490.7	14.52	64	-7.0	3.06	-0.31	101.6	106.0	108.1	106.0	108.5	110.0	107.2	182.6
7406	491.7	14.51	64	-7.5	3.23	0.06	99.2	103.3	106.6	106.4	108.9	111.9	112.0	184.6
7407	490.7	14.52	64	-7.6	3.23	0.09	101.3	105.3	107.0	105.6	108.8	111.0	110.1	183.7
7410	491.7	14.52	63	-8.0	3.41	0.39	103.1	106.4	109.1	108.3	110.3	114.9	112.2	186.3
7411	491.7	14.52	62	-8.0	3.41	0.38	105.5	107.8	109.4	107.5	110.4	113.7	111.7	186.0
7501	487.7	14.55	24	-7.8	2.31	-0.74	96.8	100.2	102.8	102.0	104.8	105.6	106.3	180.3
7502	489.0	14.52	43	-7.8	2.32	-0.72	99.9	102.1	103.9	100.4	103.4	102.4	100.0	177.9

NOZZLE - MODEL 7 CONTINUED

TEST POINT	V_{ac} FT/SEC	P^o_r	T^o_T DEG R	V^p_j FT/SEC	W^o LB/SEC	P^i_r	T^i_T DEG R	V^i_j FT/SEC	W^i LB/SEC	P^{mix}_r	T^{mix}_T DEG R	V^{mix}_j FT/SEC	F LB	V^i_j/V^o_j
7503	0	2.08	1734	1996	399.9	2.02	832	1349	183.2	2.03	1450	1792	32490	0.68
7504	386	2.10	1732	2004	405.8	2.03	845	1363	183.7	2.04	1455	1804	33058	0.68
7505	0	1.46	1726	1458	265.8	1.50	578	873	156.5	1.44	1300	1241	16290	0.60
7506	387	1.47	1716	1471	269.8	1.53	568	881	161.1	1.45	1286	1250	16748	0.60
7601	0	2.91	1686	2322	565.5	2.28	791	1413	211.9	2.69	1442	2074	50122	0.61
7602	387	2.93	1677	2321	575.6	2.31	810	1438	213.6	2.71	1442	2082	51070	0.62
7603	0	2.80	1676	2279	546.1	2.64	893	1611	230.3	2.71	1443	2080	50213	0.71
7604	387	2.80	1641	2254	557.0	2.59	893	1598	228.3	2.70	1423	2063	50364	0.71
7605	0	2.70	1672	2240	526.7	2.90	957	1737	244.8	2.70	1445	2080	49887	0.78
7606	387	2.69	1660	2228	531.5	2.91	985	1764	243.9	2.70	1447	2082	50179	0.79
7607	0	3.11	1707	2398	601.8	1.60	617	968	165.6	2.67	1471	2089	49841	0.40
7608	386	3.10	1707	2397	600.4	1.68	567	968	182.3	2.66	1441	2064	50217	0.40
7609	0	3.11	1700	2392	601.2	2.87	915	1692	248.1	2.99	1470	2187	57739	0.71
7610	298	3.14	1732	2425	602.5	2.90	934	1716	248.1	3.02	1499	2218	58644	0.71
7611	387	3.14	1713	2411	605.8	2.88	926	1704	247.5	3.01	1484	2205	58506	0.71
7612	0	3.23	1744	2460	618.6	2.58	816	1526	236.5	2.99	1487	2201	58517	0.62
7613	298	3.25	1725	2452	626.1	2.57	830	1534	232.7	3.01	1482	2203	58807	0.63
7614	387	3.25	1723	2450	625.9	2.56	834	1537	231.9	3.01	1482	2203	58740	0.63
7615	0	3.33	1770	2505	632.3	2.22	757	1363	211.5	2.98	1516	2218	58186	0.54
7616	298	3.36	1734	2486	644.3	2.26	751	1368	215.1	3.01	1487	2206	58931	0.55

TEST POINT	T_{amb} DEG R	P_{amb} PSIA	RH %	NF dB	LVM	LBM	PNL (FULL SIZE, 2400 FT SIDE LINE), dB ANGLE RELATIVE TO INLET, DEGREES 50	70	90	110	120	130	140	OAPWL dB
7503	484.5	14.42	39	-4.1	2.21	-4.07	87.2	90.9	96.3	98.4	102.2	101.8	100.6	175.6
7504	489.5	14.51	43	-4.2	2.21	-3.91	89.4	92.1	95.4	95.2	99.1	98.0	94.0	171.1
7505	482.9	14.43	45	-4.4	0.62	-10.00	79.9	84.1	88.7	88.7	91.5	89.1	85.7	163.7
7506	498.7	14.40	55	-4.6	0.58	-10.00	80.5	83.6	86.1	84.8	86.0	84.5	79.1	161.0
7601	487.2	14.39	25	-6.3	2.83	-0.84	93.8	97.9	102.0	103.3	107.6	109.0	108.5	181.9
7602	488.5	14.52	44	-6.4	2.84	-0.80	96.8	100.4	103.1	102.4	106.7	106.9	104.3	179.2
7603	489.3	14.39	20	-6.4	2.83	-0.83	93.7	97.7	101.5	103.1	107.3	108.5	108.9	181.9
7604	489.9	14.52	44	-6.4	2.79	-0.86	96.2	98.9	102.0	101.5	105.4	105.6	103.6	178.3
7605	490.1	14.39	19	-6.3	2.83	-0.86	93.8	97.7	101.7	103.0	107.1	108.8	108.9	181.9
7606	490.6	14.52	44	-6.4	2.83	-0.87	96.6	99.2	102.1	101.6	105.7	105.8	104.2	178.7
7607	482.2	14.42	45	-6.2	2.88	-0.87	94.5	99.5	103.9	104.9	108.9	110.9	109.3	182.7
7608	498.7	14.40	54	-6.4	2.75	-0.84	99.3	102.5	104.9	103.3	106.4	107.3	104.6	180.1
7609	487.6	14.39	27	-7.0	3.06	-0.29	97.5	100.5	104.1	105.0	109.5	111.6	110.6	183.7
7610	497.7	14.40	54	-7.1	3.07	-0.24	101.9	84.0	105.6	104.8	107.3	109.2	108.7	182.2
7611	497.7	14.40	54	-7.1	3.05	-0.25	101.1	103.0	105.3	104.3	107.2	108.8	107.1	181.6
7612	484.3	14.41	39	-7.0	3.10	-0.25	97.7	101.3	105.2	106.5	110.4	111.9	110.5	184.1
7613	497.7	14.41	55	-7.1	3.04	-0.23	99.7	103.8	105.5	105.0	107.7	108.6	107.7	181.8
7614	497.7	14.40	55	-7.1	3.04	-0.23	100.6	103.4	105.7	104.7	107.9	108.5	106.8	181.6
7615	484.7	14.41	39	-6.9	3.13	-0.27	97.1	100.9	105.4	106.6	110.5	111.1	110.7	184.1
7616	496.7	14.41	55	-7.1	3.05	-0.22	99.4	104.0	106.4	105.5	107.7	109.3	107.0	181.7

NOZZLE - MODEL 7 CONTINUED

TEST POINT	V_{ac} FT/SEC	P_r^o	T_T^o DEG R	V_j^o FT/SEC	W^o LB/SEC	P_r^i	T_T^i DEG R	V_j^i FT/SEC	W^i LB/SEC	P_r^{mix}	T_T^{mix} DEG R	V_j^{mix} FT/SEC	F LB	V_j^i/V_j^o
7617	387	3.36	1742	2492	642.8	2.27	752	1372	215.9	3.01	1493	2210	58991	0.55
7618	0	3.02	1691	2360	586.1	3.11	1004	1828	256.0	2.99	1482	2198	57534	0.77
7619	294	3.02	1693	2362	590.8	3.13	990	1819	261.4	3.00	1477	2195	58150	0.77
7620	387	3.01	1722	2381	584.5	3.15	1001	1833	261.5	3.00	1499	2211	58155	0.77

TEST POINT	T_{amb} DEG R	P_{amb} PSIA	RH %	NF dB	LVM	LBM	PNL (FULL SIZE, 2400 FT SIDE LINE), dB ANGLE RELATIVE TO INLET, DEGREES 50	70	90	110	120	130	140	OAPWL dB
7617	496.7	14.40	55	-7.1	3.06	-0.22	100.7	104.1	106.5	105.1	108.2	108.9	105.6	181.4
7618	487.7	14.39	27	-6.9	3.08	-0.30	98.9	101.5	104.6	105.5	109.8	112.6	110.0	183.8
7619	487.6	14.50	43	-7.0	3.07	-0.29	101.7	104.2	106.2	104.6	108.5	109.3	108.7	182.6
7620	488.3	14.51	44	-6.9	3.10	-0.29	104.3	104.4	105.9	104.3	108.5	109.6	108.3	182.7

APPENDIX B

AERODYNAMIC TEST CONDITIONS FOR THE LASER VELOCIMETER TESTS

Table B-I. Aerodynamic Test Matrix for Laser Velocimeter Tests.

Model	Test Point	$V_{a/c}$ ft/sec	Outer P_r^o	Outer V^o ft/sec	Outer T_T^o °R	Outer T^o °R	Outer W^o lbm/sec	Inner P_r^i	Inner V^i ft/sec	Inner T_T^i °R	Inner T^i °R	Inner W^i lbm/sec	Mixed V^M ft/sec	Mixed T^M °R	Mixed V^i/V^o
1	101	0	3.17	2416	1708	1263	10.52	3.19	1636	790	567	2.16	2283	1146	0.677
	101A	0	1.00	0	592	592	0	3.21	1635	785	563	2.18	1635	563	—
	103	400	3.17	2427	1722	1274	10.47	3.19	1633	787	565	2.17	2291	1155	0.673
	113A		1.00	0	571	571	0	1.62	1104	784	683	1.08	1104	683	—
	116	0	2.43	2175	1735	1381	8.00	2.08	1348	801	650	1.40	2051	1276	0.620
	119A	0	2.26	2092	1733	1406	7.44	1.02	262	1013	1008	0.18	2050	1403	0.125
	1505	0	1.45	1447	1720	1567	4.53	1.45	898	666	599	1.01	1348	1393	0.621
	1506	400	1.45	1653	1733	1579	4.51	1.63	899	693	626	0.97	1355	1413	0.619
1A	101A	0	3.19	2453	1722	1272	10.54	3.22	1648	789	565	3.09	2270	1114	0.672
	116A	0	2.45	2184	1721	1366	7.96	2.20	1338	735	587	2.15	2003	1511	0.613
2	201	0	3.17	2435	1733	1283	10.44	3.24	1629	774	553	3.10	2250	1118	0.669
	203	400	3.18	2425	1716	1268	10.52	3.20	1630	782	561	3.04	2247	1112	0.672
	204	0	3.79	2551	1688	1186	12.65	3.23	1638	784	561	3.06	2372	1069	0.642
	206	400	3.76	2559	1707	1203	12.48	3.24	1635	780	557	3.08	2376	1080	0.639
	210	0	2.28	2088	1710	1384	7.56	2.09	1264	700	567	2.10	1909	1210	0.605
	212	400	2.28	2084	1704	1379	7.57	2.11	1265	693	560	2.13	1904	1203	0.607
	213	0	3.15	2430	1734	1286	10.37	1.58	1097	817	717	1.43	2268	1229	0.451
	215	400	3.18	2429	1722	1273	10.50	1.61	1104	789	696	1.49	2265	1213	0.455
	216	0	3.79	2551	1689	1187	12.65	1.59	1098	808	708	1.45	2402	1151	0.430
	219	0	2.27	2085	1713	1388	7.52	1.59	1092	800	701	1.46	1924	1283	0.524
	221	400	2.29	2089	1704	1377	7.61	1.61	1094	783	683	1.50	1925	1270	0.524
	222	0	2.42	2165	1727	1376	7.98	2.18	1324	731	585	2.14	1987	1213	0.612
	222A	0	2.45	2184	1713	1360	8.12	2.18	1334	739	591	2.13	2000	1510	0.611
3	301	0	3.17	2434	1732	1282	10.44	3.22	1634	782	560	3.10	2250	1119	0.671
	303	400	3.17	2433	1731	1281	10.44	3.21	1634	784	562	3.09	2251	1119	0.671
5	513	0	3.14	2428	1735	1288	11.67	—	—	—	—	—	2428	1288	—
	515	400	3.19	2431	1720	1270	11.90	—	—	—	—	—	2431	1270	—
6	3009R	0	2.26	2088	1726	1401	4.64	1.37	795	611	558	2.26	1664	1145	0.381
	3011	400	2.23	2070	1722	1402	4.58	1.39	796	587	534	2.37	1636	1127	0.385
	3015R	0	2.78	2292	1704	1306	5.74	1.63	1438	1317	1156	1.98	2073	1278	0.628
	3016	300	2.73	2290	1727	1332	5.60	1.63	1426	1294	1136	2.00	2063	1290	0.623
	3017	400	2.74	2293	1726	1329	5.62	1.63	1431	1303	1144	1.99	2068	1291	0.624
	3018	0	2.70	2285	1736	1343	5.52	1.98	1630	1259	1049	2.47	2082	1258	0.713
	3020	400	2.70	2281	1730	1338	5.53	1.95	1622	1255	1047	2.46	2078	1254	0.711
7	7009	0	2.25	2085	1730	1406	7.46	1.48	868	592	529	2.59	1772	1195	0.416
	7011	400	2.25	2090	1737	1412	7.45	1.48	869	593	530	2.59	1775	1199	0.416
	7015	0	2.73	2295	1735	1338	9.04	1.83	1406	1036	874	2.54	2100	1244	0.613
	7016	300	2.71	2287	1734	1340	8.98	1.83	1411	1043	881	2.53	2094	1247	0.617
	7017	400	2.70	2292	1746	1351	8.91	1.83	1410	1042	880	2.53	2097	1255	0.615
	7018	0	2.67	2269	1729	1341	8.86	2.73	1643	901	676	4.08	2072	1134	0.724
	7019	300	2.68	2267	1721	1333	8.91	2.74	1650	905	679	4.08	2073	1130	0.728
	7020	400	2.67	2274	1736	1347	8.84	2.78	1644	888	663	4.18	2071	1129	0.723

1. Report No. NASA CR-3818	2. Government Accession No.	3. Recipient's Catalog No.

4. Title and Subtitle
Free-Jet Acoustic Investigation of High-Radius-Ratio Coannular Plug Nozzles

5. Report Date
October 1984

6. Performing Organization Code

7. Author(s)
P. R. Knott, B. A. Janardan, R. K. Majjigi, P. K. Bhutiani, and P. G. Vogt

8. Performing Organization Report No.
R83AEB574

10. Work Unit No.

9. Performing Organization Name and Address
General Electric Company
Aircraft Engine Business Group
Cincinnati, Ohio 45215

11. Contract or Grant No.
NAS3-20619

13. Type of Report and Period Covered
Contractor Report

12. Sponsoring Agency Name and Address
National Aeronautics and Space Administration
Washington, D.C. 20546

14. Sponsoring Agency Code
505-31-3B (E-2177)

15. Supplementary Notes
Final report. Project Manager, Orlando A. Gutierrez and James R. Stone, Fluid Mechanics and Instrumentation Division, NASA Lewis Research Center, Cleveland, Ohio 44135.

16. Abstract

This report summarizes the experimental and analytical results of a scale-model simulated flight acoustic exploratory investigation of high-radius-ratio coannular plug nozzles with inverted velocity and temperature profiles. In all, six coannular plug nozzle configurations and a baseline convergent conical nozzle were tested for simulated flight acoustic evaluation in General Electric's Anechoic Free-Jet Acoustic Test Facility. The nozzles were tested over a range of test conditions that are typical of a Variable Cycle Engine for application to advanced high speed aircraft. The outer stream radius ratio for most of the configurations was 0.853, and the inner-stream-to-outer-stream area ratio was tested in the range of 0.2 to 0.54. Other variables investigated were the influence of bypass struts, a simple noncontoured convergent-divergent outer stream nozzle for forward quadrant shock noise control, and the effects of varying outer stream radius ratios and inner-stream-to-outer-stream velocity ratios on the flight noise signatures of the nozzles. It was found that in simulated flight, the high-radius-ratio coannular plug nozzles maintain their jet noise and shock noise reduction features previously observed in static testing. The presence of nozzle bypass struts will not significantly affect the acoustic noise reduction features of a General Electric-type nozzle design. A unique coannular plug nozzle flight acoustic spectral prediction method was identified and found to predict the measured results quite well. Special laser velocimeter and acoustic measurements were performed which have given new insights into the jet and shock noise reduction mechanisms of coannular plug nozzles with regard to identifying further beneficial research efforts.

17. Key Words (Suggested by Author(s))
Coannular plug nozzle jet noise; Supersonic jet noise reduction; Variable cycle engine; Acoustic flight noise simulation; Laser velocimeter measurements

18. Distribution [redacted]

19. Security Classif. (of this report)	20. Security Classif. (of this page)	21. No. of pages	22. Price
Unclassified	Unclassified	217	

NASA-Langley, 1984